ELECTROSPRAY ION BEAM DEPOSITION AND MASS SPECTROMETRY OF NONVOLATILE MOLECULES AND NANOMATERIALS

THÈSE N^{O} 3958 (2007)

PRÉSENTÉE LE 13 DÉCEMBRE 2007

À LA FACULTÉ DES SCIENCES DE BASE
LABORATOIRE DE SCIENCE À L'ÉCHELLE NANOMÉTRIQUE
PROGRAMME DOCTORAL EN PHYSIQUE

ÉCOLE POLYTECHNIQUE FÉDÉRALE DE LAUSANNE

POUR L'OBTENTION DU GRADE DE DOCTEUR ÈS SCIENCES

PAR

Stephan RAUSCHENBACH

Diplom-Physiker, Universität Augsburg, Allemagne
et de nationalité allemande

acceptée sur proposition du jury:

Prof. R. Schaller, président du jury
Prof. K. Kern, directeur de thèse
Prof. J. Barth, rapporteur
Prof. M. Mayor, rapporteur
Prof. T. Rizzo, rapporteur

ÉCOLE POLYTECHNIQUE
FÉDÉRALE DE LAUSANNE

Suisse
2008

ABSTRACT

The vacuum deposition of complex functional molecules and nanoparticles by thermal sublimation is often hindered due to their extremely low vapor pressure. This especially impedes the application of ultrahigh vacuum (UHV) based analytical and surface modification techniques for the investigation of these extremely interesting systems. On the other hand, specimen prepared under ambient conditions or in solution are typically not sufficiently well-defined and clean to allow a thorough and precise characterization.

In order to bridge this technological gap, a novel ion beam source for controlled soft landing deposition in ultrahigh vacuum is constructed. The ion beam of nonvolatile particles is created by electrospray ionization (ESI). The deposition apparatus consists of six differential pumping stages designed to overcome the pressure difference of 13 orders of magnitude between the ambient pressure side, where ionization occurs, and the high or ultrahigh vacuum, where the deposition takes place. A variety of ion optical devices is employed to form, mass select and guide the ion beam through the pumping stages onto the deposition target. The ion beam is sampled from a supersonic expansion by a skimmer, collimated in a high pressure quadrupole ion guide, mass selected in a low pressure quadrupole ion guide and focused by electrostatic lenses. In order to have full control over all relevant parameters, the ion beam is characterized before the deposition by a linear time-of-flight mass spectrometer and a retarding grid energy detector. The flux, the composition and the kinetic energy of the ion beam can thus be measured and adjusted.

The concept of ion beam deposition in high and ultrahigh vacuum is demonstrated by extensive mass spectrometric and deposition experiments. Many different types of ion beams, for instance composed of organic molecules, organic and inorganic ionically bound clusters, polymers and proteins, are created by ESI. Their properties are analyzed by mass spectrometry, with special focus on their behavior upon energetic collisions with a neutral gas, since these processes bear many similarities to collisions with a solid surface.

Some of the ion beams are used for deposition. Ion beams of the protein **BSA**, of the dye molecule Rhodamine 6G (**Rho6G**), of organic ionic surfactant clusters composed of sodium-dodecyl sulfate (**SDS**) and of inorganic nanoparticles (gold colloids, carbon nanotubes, CdS nanorods and $\mathrm{V_2O_5}$ nanowires), are deposited onto graphite and silicon oxide ($\mathrm{SiO_x}$) surfaces in high vacuum. The fluorescence of **Rho6G** is detected after its deposition, which is a proof for the destruction-free ion beam deposition, i.e. of a successful soft landing. For the other classes of deposited particles, diffusion on the surface and sometimes formation of nanostructures is observed. **BSA** forms fractal agglomerations on graphite, while it does not show any diffusion on $\mathrm{SiO_x}$ surfaces. **SDS** forms flat, two dimensional islands on graphite and silicon. Finally it is demonstrated that large, inorganic nanoparticles (up to $10^6\,\mathrm{u}$) can be ionized and soft landed by the developed apparatus.

Having proven the principle of low energy ion beam deposition for a wide variety of nonvolatile particles, the technique is now ready for being integrated with in-situ characterization techniques such as scanning tunneling and atomic force microscopy (STM, AFM). For this purpose, the ion beam deposition setup has been expanded by two vacuum chambers for sample preparation and analysis. Future experiments aim at the deposition and analysis of complex organic molecules in UHV, and at gaining a more detailed understanding of the soft landing process.

Keywords: Electrospray, Ultrahigh Vacuum, Ion Beam, Deposition, Soft Landing, Mass Spectrometry, Scanning Probe Microscopy, Organic Molecule, Protein, Nanoparticle, Cluster

ZUSAMMENFASSUNG

Nanopartikel und grosse funktionelle Moleküle haben keinen Dampfdruck, was ihre Anwendung bei der Vakuumdeposition durch Verdampfen unmöglich macht. Zudem ist die Verwendung von Ultrahochvakuum (UHV) basierter Analytik bei Proben, die an Luft oder in Lösung hergestellt werden, nicht möglich, da diese für UHV Techniken meist nicht sauber genug sind.

Um diese technologische Lücke zu schliessen, wurde eine neuartige Ionenstrahlanlage zur sanften Deposition (*soft landing*) im UHV konstruiert. Ein Ionenstrahl aus nicht volatilen Teilchen wird durch Elektrospray Ionisation (ESI) erzeugt. Die Anlage besteht aus sechs aufeinanderfolgenden, durch Blenden verbundenen Pumpstufen. Dieser Aufbau ist in der Lage, die Druckdifferenz von 13 Grössenordungen zwischen Umgebungsdruck und Hoch- bzw. Ultrahochvakuum zu überwinden.

Verschiedene Ionenoptiken werden eingesetzt, um einen Ionenstrahl zu erzeugen, seine Masse einzustellen und ihn durch die Pumpstufen auf eine der Proben zu leiten. Der Ionenstrahl wird aus einer Überschallexpansion von einem Skimmer abgetrennt und in einem Hochdruckquadrupol gebündelt. In einem weiteren Quadrupol im Hochvakuum wird die Masse des Ionenstrahls eingestellt. Im weiteren Verlauf leiten elektrostatische Linsen den Ionenstrahl und fokussieren ihn auf die Probe. Um eine kontrollierte Deposition zu gewährleisten, wird der Ionenstrahl vor der Deposition von einem linearen Flugzeitmassenspektrometer und Faradaybecher mit einem Bremsfeld analysiert. Teilchenstrom, Zusammensetzung und kinetische Energie können auf diese Weise bestimmt werden.

Massenspektrometrische Untersuchungen und Depositionsexperimente wurden ausgeführt, um die Tragfähigkeit des Konzepts der Ionenstrahldeposition im Hoch- und Ultrahochvakuum unter Beweis zu stellen. Viele verschiedene Ionenstrahlen konnten hergestellt werden, darunter solche von organischen Molekülen, von organischen und anorganischen Salzclustern, von Polymeren und von Proteinen. Die Eigenschaften dieser Strahlen sind mit Massenspektrometrie untersucht worden, wobei insbesondere ihr Verhalten bei Kollisionen mit einem neutralen Gas im Mittelpunkt steht, die Parallelen zu Kollisionen mit Oberflächen aufweisen.

Einige der untersuchten Ionenstrahlen sind für die Deposition verwendet worden. Das Protein **BSA**, der Farbstoff Rhodamine 6G (**Rho6G**), das metall-organische, ionische Tensid Natrium Dodecyl Sulfat (**SDS**) sowie inorganische Nanopartikel (Gold Kolloide, Kohlenstoff Nanoröhrchen, CdS Nanostäbchen und $\mathrm{V_2O_5}$ Nanodrähte) wurden auf $\mathrm{SiO_x}$ - und Graphitoberflächen im Hochvakuum deponiert. Die charakteristische Fluoreszenz von Rhodamine konnte nach der Deposition nachgewiesen werden, was beweist, dass es möglich ist, Moleküle aus einem Ionenstrahl sanft zu deponieren. Dieser Vorgang wird als *soft landing* bezeichnet. Die anderen deponierten Teilchen diffundieren nach der Deposition, woraus das Wachstum von Nanostrukturen auf einigen Oberflächen resultiert. Fraktale Inseln konnten für **BSA** auf Graphit beobachtet werden, während auf $\mathrm{SiO_x}$ keine Diffusion festgestellt werden konnte. **SDS** bildet abhängig von der Beschaffenheit der Oberfläche molekulare Einzel- oder Doppelschichten auf Graphit und $\mathrm{SiO_x}$. Ausserdem ist gezeigt worden, dass sehr grosse Nanopartikel mit Massen bis zu $10^6\,\mathrm{u}$ ionisiert und deponiert werden können.

Da die Experimente in dieser Arbeit zeigen, dass das Prinzip der Ionenstrahldeposition für nicht verdampfbare Moleküle und Cluster funktioniert, wird der experimentelle Aufbau derzeit um eine Einheit zur in-situ Charakterisierung erweitert. Zwei weitere UHV Kammern, eine für die Probenpräparation, die andere enthält ein UHV Rastertunnel- und Rasterkraftmikroskop, werden gegenwärtig in Betrieb genommen. Weitere Experimente, die das Verhalten von komplexen organischen Molekülen auf Oberflächen im UHV untersuchen sollen und dazu beitragen, den Depositionsprozess von hyperthermischen organischen Ionen besser zu verstehen, werden zurzeit vorbereitet.

Schlagworte: Electrospray, Ultrahoch Vakuum, Ionenstrahlen, Beschichtung, Soft Landing, Massenspektrometrie, Rastersondenmikroskopie, Organische Moleküle, Proteine, Nanopartikel, Cluster

Contents

1 INTRODUCTION

Nanoscience and Nanotechnology

Nanotechnology is an expression of advancing technology. The desire to have more effective and efficient tools and machines has led to increasingly stronger efforts to understand, control and exploit matter at the nanoscale.

On one side, the bundling of many functions into a single device, the increase of actuation speed and parallelization and the decrease of energy consumption has driven the production of ever smaller objects. In general, these are able to serve the same purposes of their larger counterparts but do this faster, cheaper and more effectively. On the other hand, research of the last fifty years has demonstrated that nanometer size objects very often behave completely different than macroscopic ones. When the size of matter reaches the nanometer range, its properties do not follow anymore a simple downscaling but start to obey to different physical laws and new phenomena can emerge. The exploitation of these novel properties of matter is one of the most relevant aspects of nanotechnology.

Calculating machines are distinctly one of the most prominent examples of a technology whose miniaturization has crossed the nanoscale border. The integration density in nowadays computer processor has reached such high levels that their elementary building parts have sizes of few tens of nanometers [1]. Biological structures are a further example of highly complex systems whose behavior is entirely determined by processes occurring at the level of single atoms or molecules, thus in every respect at the nanoscale. Nowadays it is generally believed that a profound knowledge of biological processes at the nanoscale combined with the development of technologies able to use this knowledge, will open the way to extremely powerful and long-reaching applications into the fields of medicine, pharmacology, agriculture, energy, etc.

At present nanotechnology is becoming an interdisciplinary effort which combines several traditional sciences including physics, chemistry, material science, biology and medicine. Its principal efforts are directed towards the fabrication of new materials and the development of new tools able to analyze and precisely characterize matter at the nanoscale.

Recent advances in synthetic macromolecular chemistry have resulted in complex organic compounds, that are capable to perform a pre-designed specific function at the single molecular level. For instance, molecules designed to behave as bridges [2], propellers [3, 4], circuits for persistent currents [5], switches [6, 7], wheelbarrow [8] or even *nanocars* [9] have been recently successfully synthesized.

However, functional molecules do not need to be necessarily fabricated exnovo. Billions of years of evolution have selected incredibly smart molecular units able to perform very complex tasks. DNA for example is today studied not only due to its function as the genetic information storage medium, but also due to its programmable and * Main.TWikiUsers * TWiki.TWikiRegistration * Bureaucracy.WebHome * Documentation.LibraryKK * Ideas.WebHome * Laboratory.EsiLab * Fun.WebHome

extremely selective binding properties. Since only complementary single strands of DNA will form a stable double strand, selected sequences of DNA can be used in order to self-assemble 3 dimensional nanometer structures [10]. Another important topic in biological nanotechnology is the exploration of the active sites of proteins [11]. Although being made out of a catalogue of only 20 basic units, these nanoscale molecules are able to specifically catalyze all types of reactions necessary for life while working under physiological conditions at room temperature.

Since the fundamental processes governing the behavior of all these functional molecules occur at the nanoscale, the ability of characterizing them on the same lengthscale has become equally essential. Scanning probe microscopy represents an exquisite imaging technique with nanometer resolving capabilities that can be employed if molecules are adsorbed on a surface. Scanning tunneling (STM) and atomic force microscopes (AFM) use the interaction between a sharp tip and a surface to locally measure the height and create an image when scanned across a certain area. Used in ultra-high-vacuum under very clean and controlled conditions, these imaging techniques can reach unprecedented levels of spatial resolution [12].

Some of the molecules mentioned above have indeed been characterized by STM at molecular and sub-molecular resolution [13]. However, the fact that complex functional molecules and nanoclusters do not typically have a high vapor pressure, represents a major problem for their analysis by means of scanning probe microscopy (SPM) and other UHV-based advanced characterization techniques. In fact, such molecules decompose before being sublimed and therefore cannot be transferred onto clean surfaces in UHV by traditional molecular beam evaporation techniques.

Thus several alternative approaches of bringing molecules to surfaces in UHV have been explored. These include pulsed value techniques [14, 15], pulsed evaporation [16] and printing of molecules. These techniques are able to deposit nonvolatile molecules to a surface in vacuum, but they also bear major disadvantages.

Pulsed valves are used to inject small amounts of solution, sometimes dispersed in a carrier gas, containing nonvolatile molecules into the UHV. The solvent, typically chosen to be very volatile, evaporates before the molecules reach the surface. Major problems of this methods are the temporary strong contamination of the vacuum – the pressure raises in the $10^5\,\mathrm{mbar}$ range – and the high kinetic energy of the molecules when they hit the surface, which is determined by the supersonic expansion of the gas entering the vacuum chamber. Although nonvolatile molecules can be deposited this way, the deposition is often very inhomogeneous, the surface is contaminated by solvent residues and the parameters of the deposition, especially the kinetic energy of the molecules cannot be controlled.

Printing of molecules bears similar disadvantages. The surface can be damaged or contaminated by the stamp and the transfer of the molecules is very inhomogeneous and certainly not reproducible. The pulsed evaporation technique employed heat pulses rather than continues heating [16]. It can be used to evaporate molecules that are fragmented partially upon normal evaporation. However, always a certain fraction of the molecules is fragmented by this evaporation technique and molecules that do not evaporate at all, cannot be transferred into the gas phase with this technique either.

On the other hand, extremely versatile mass spectrometric tools are available in analytical chemistry and biochemistry that are able to detect and identify large and complex molecules as gas phase ions. Electrospray ionization (ESI) [17] and matrix assisted laser desorption ionization (MALDI) [18] have opened and greatly advanced the field of analytical applications in these fields, due to the fact that biological molecules, despite their sensible nature, can be ionized and brought into the gas phase while staying intact.

Recent attempts on vacuum deposition of nonvolatile molecules have been made in combining soft ionization and deposition in vacuum. A modified MALDI mass spectrometer has been used for vacuum deposition of graphene molecules on graphite surfaces [19]. Others attempt to use an electrospray ionization source in vacuum (and not at ambient pressure as usual) and have shown to be able to deposit polymer droplets and carbon nanotubes from a solution on surfaces in vacuum [20, 21]. Since rather a beam of small charged droplets than a gas phase ion beam is deposited, this technique has to be compared to pulsed valve techniques, since solvent contamination is present also here.

How to Combine Nanoscale Objects and Ultrahigh Vacuum – Outline of the Work

The work presented in this thesis focuses on the combination of the technologies of electrospray ionization mass spectrometry (ES-MS) and ultrahigh vacuum scanning probe microscopy (UHV-SPM) in order to create a novel tool for nanotechnology. A molecular or nanoparticle ion beam created by ESI is used for controlled vacuum deposition on a solid substrate. A fundamental requirement of such an apparatus is the ability to set and monitor the key parameters of the deposition, the ion flux, kinetic energy, charge state and mass. Therefore, the setup needs to combine an electrospray ion beam source in which the beam composition can be determined and a time-of-flight mass spectrometer to analyze it.

The deposition takes place at a solid sample where it must be possible to position the ion beam, to measure the ion flux and to adjust the ion energy. The resulting sample needs then to be analyzed in situ with SPM or transferred through a loadlock for further ex situ analysis.

In order to reach these goals, several milestones have to be achieved. Since the soft landing ion beam deposition in ultra high vacuum requires a custom made source, an integral part of the work deals with the development and testing of this novel apparatus.

In chapter 2 the basics of electrospray ionization and time-of-flight mass spectrometry as well as some aspects of ion beam interactions with gases and solids are outlined. There the main aspect is the ionization process itself and the energy transfer in the collision processes. These phenomena determine the type of particle which is deposited, by ionization and fragmentation.

Chapter 3 mainly deals with the ion beam deposition setup as it is designed, constructed and used. A special focus is on the development of the ion beam optics, that plays a crucial role in the deposition process. The correct design of quadrupoles and electrostatic lenses determines the two most important parameters for ion beam soft landing: the ion flux which can be achieved for deposition and the kinetic energy of the ion beam. In addition some analytical techniques that have been used for sample analysis are outlined.

Chapter 4 and 5 present and discuss experiments performed on the ion beam deposition source. Mass spectrometric measurements and ion beam deposition in high vacuum is performed in order to characterize the performance of the ion beam source and address current topic in ion beam deposition.

Ion beams of ionic salt clusters, organic molecules, biological molecules and nanoparticles are created and analyzed by mass spectrometry. The investigations focus on the charge state of the ion and on its fragmentation behavior. Both properties play an important role for the ion beam deposition. The charge state determines the kinetic energy and depends on the structure of the particle, the collisions with gas molecules results in fragmentation which can be compared with surface collisions.

Deposition experiments are performed with proteins, dye molecules, organic salts and nanoparticle. For four distinctly different classes of molecules, ion beam deposition and also soft landing is investigated by different techniques. Proteins, organic salt layers and nanoparticles are analyzed morphologically, while the dye molecules are studied by fluorescence spectroscopy.

2 BASICS

The controlled deposition of molecular or cluster ions at a solid surface in ultrahigh vacuum requires an experimental setup which combines several techniques from different areas of expertise. To put this general idea into practice, knowledge about the creation, manipulation, detection and deposition of ions, as well as about other technical aspects, like vacuum generation, mass spectrometry, ion optics, electronics and software are required(which are treated in chapter 3).

Within this chapter the generation of molecular or cluster ions by electrospray ionization is discussed in section 2.1, page 13. The mechanisms of electrospray ion generation are outlined in section 2.1.2, page 14, while section 2.1.3, page 17 is devoted to properties of the ions that are created. A short overview on the principles of time-of-flight mass spectrometry is given in section 2.2, page 20. This technique is employed in order to control the ion beam before the actual vacuum deposition.

The collision of ions with a surface and with gas molecules is finally treated in section 2.3, page 24. The involved phenomena, collision induced dissociation (CID) and surface induced dissociation (SID) are discussed and compared based on literature on the topic. In this context, a simple model is developed by which it is possible to qualitatively understand the energy transfer due to ion-gas-collisions and its dependence on the main experimental parameters.

2.1 ELECTROSPRAY IONIZATION

2.1.1 Introduction

Many methods are available to produce gas phase ions. Depending on the desired properties of the resulting ion beam, a specific ion source is selected. Electron impact ionization (EI), fast atom bombardment (FAB) or laser ionization in different forms (LDI, MALDI) are used for mass spectrometry, while RF or microwave sources generate high fluency beams for applications like surface modification [22, 23, 24, 18].

The electrospray ionization source (ESI) for the use in mass spectrometry (MS) was invented in the 1980s [25, 17, 26, 27, 28], the electrospray effect which is the dispersion of a liquid into an aerosol by a high electric field has been known since a long time [29, 30, 31]. ESI-MS rapidly became a widely used technique due to its unique property to softly ionize even very sensitive organic and biological molecules, which thus became quickly and easily to detect [11, 32, 33].

Today ESI-MS is widely used for medical, biological and biochemical applications. A major advantage of this solution based ionization technique is the capability of directly coupling a mass spectrometer to a (high pressure) liquid chromatography (LC) system, which allows a high throughput analysis of very small amounts of sample. [34] These developments have made LC-ESI-MS the technique of choice in biochemistry for mapping the proteomic expression of living organisms. For this complex task automated mass measurements and database coupled automated data analysis is employed. [35, 33].

Moreover, electrospray mass spectrometers are a very important and versatile tool in analytical chemistry, where they are used to identify all kinds of compounds. Additionally, many specialized applications employ electrospray ionization. Electrosprays are used to disperse solution in various ambient pressure deposition applications [36, 37, 38, 39, 40, 41, 42, 43, 44, 45], in the ion mobility analysis of the interaction of large molecules and gases [46, 47, 48], for ion trapping and spectrometry [49] and finally when electrosprayed ions are deposited at surfaces in vacuum for the purpose of preparative mass spectrometry [50, 51, 52, 53, 54, 47, 55, 56, 57, 58, 59, 60, 61, 62]. The scope of this work has many common aspects with the latter application, since both techniques employ electrospray ion beams for the soft landing deposition of matter. The difference lies in the purpose of the deposition. Preparative mass spectrometry is used to purify and enrich materials, like a rare isotope or a protein [63, 53], while the UHV deposition of large organic molecules and clusters aims at the creation of functional nanostructures on surfaces under highly controlled vacuum conditions.

The following section describes the principles of electrospray ionization and outlines some of the properties and considerations relevant for its use in mass spectrometry and in ion beam deposition experiments. In particular section 2.1.2, page 14 describes the creation of charged droplets and how they evolve into gas phase ions. In section 2.1.3, page 17 the properties of ion produced by ESI are reviewed.

2.1.2 The Electrospray Ionization Process

Instability Driven Creation of Gas Phase Ions

Electrospray ionization is a technique to create gas phase ions from a solution containing charged particles. A voltage applied between a capillary and a counter electrode results in a strong field at the needle's apex which leads to the polarization of the liquid. If the field is strong enough, the charged surface of the liquid is destabilized and a cone (Taylor cone [30]) forms which emits a jet of charged droplets [64, 65, 25].

The emitted current I_{drop} depends on the flow rate of the liquid f and on the conductivity of the solvent $\sigma_{\mathrm{solvent}}$. The power law $I_{\mathrm{drop}} \propto (f\sigma_{\mathrm{solvent}})^x$ for $x < \frac{1}{2}$ is found experimentally [66, 67]. In a typical ESI source the needle is positioned in a distance of $1 - 10\,\mathrm{mm}$ away from the counter electrode. The electric field is created by a voltage in the range of $0.5 - 5\,\mathrm{kV}$ applied to either the needle or the counter electrode.

Figure 2.1 sketches the electrospray needle with the Taylor cone, the droplet formation and the consecutive droplet evolution, which leads to the creation of gas phase ions. In the electric field the droplets are accelerated towards the counter electrode. On their way they interact with the surrounding gas, which leads to the evaporation of the solvent, which is further supported by a heated gas flow in counter direction (curtain gas).

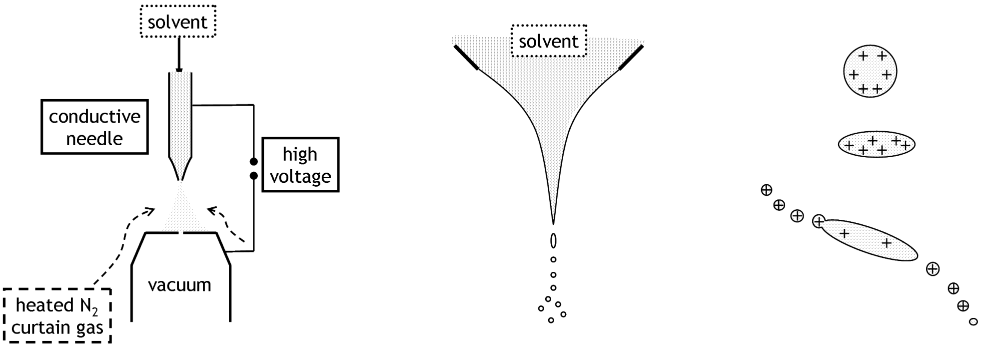

Figure 2.1 – **[left]** Setup of the atmospheric part of an electrospray source contains a conductive needle and a capillary entrance. **[middle]** Sketch of a Taylor cone emitting droplets **[right]** Destabilization and fission of a charged droplet.

The solvent evaporation increases the charge-per-volume ratio which finally destabilizes the droplet. The Rayleigh limit gives the critical size (radius R) of a charged droplet as a function of its charge Q, the material properties of the solvent, the electric permittivity ϵ and the surface tension γ [67].

$$Q = 8\pi\sqrt{\epsilon\gamma R^3} \tag{2.1}$$

Equation (2.1) shows that for a constant volume many small charged droplets are more stable than few large ones. Instable droplets therefore fission or emit small, highly charged droplets when they become unstable [65]. The iteration of solvent evaporation and fission finally results in desolvated charge carriers, which are molecular ions, cluster ions or just atomic ions.

Two mechanisms of the final desolvation of the charge carriers are possible. The *charged residue model* proposes that the solvent continuously evaporates until it is completely gone, leaving behind a charged particle [68, 69]. The alternative *ion evaporation model* is based on the fact that when a charged droplet is close to being unstable, it can gain energy by emitting charged particles in the form of desolvated ions [69, 70, 71].

Independently of the model, only a small amount of the ions or molecules in solution become gas phase ions. Not all droplets are charged highly enough to undergo successive droplet fissions that finally creates ions. Other molecules might just be desolvated as neutrals. Most importantly, all particles in a droplet are competing in the ionization process. Besides the analyte molecules also solvent molecules can be ionized, which typically happens in the form of solvent clusters. Every electrospray therefore contains a certain amount of charged clusters of solvent molecules or contaminations. The relative abundance of two ion species thus depends on the concentration ratio and on how easy a certain molecule can be charged.

Supersonic Expansion: Transfer into Vacuum

Electrospray ionization creates a cloud of charged and uncharged particles in air, which is sucked into vacuum. There, the ion cloud has to be transformed into an ion beam that can be used for the purpose of mass spectrometry or deposition. The assembly which creates the ions and transforms them into an ion beam in vacuum in general is referred to as an ion beam source. In the special case of atmospheric ionization for mass spectrometry, the term atmospheric interface (AI) is often used, due to its function to couple the mass spectrometer in high vacuum to the ionization in air.

A defined leak in a vacuum chamber connects the atmospheric pressure ionization to the vacuum assembly which is needed for the handling of an ion beam. To limit the pumping speed necessary to maintain the pressure in this first vacuum chamber, the leak is designed as small as possible by employing a long capillary of a diameter of less than one millimeter through which the ions can enter. In this way, a pressure ratio of $2-5$ order in magnitude can be achieved. In figure 2.2 [left] a typical atmospheric interface containing the spray needle, counter electrode, capillary, skimmer and quadrupole is sketched.

The difference in pressure leads to an expansion of the gas entering the vacuum chamber by which gas molecules, neutrals and gas phase ions are cooled and accelerated to supersonic speeds. This process happens in a way which is determined by the carrier gas. The maximal terminal velocity of the expansion is only a function of characteristics of the carrier gas (heat capacitance C_p, mass m, temperature T) [72]:

$$v_{\mathrm{terminal}} = \sqrt{\frac{k_B T}{m} C_p} \tag{2.2}$$

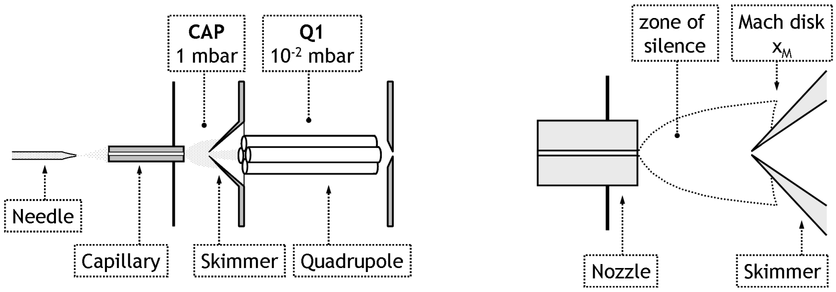

Figure 2.2 – **[left]** Atmospheric Interface. **[right]** Sketch of a supersonic expansion.

Depending on the pressure, the expanding gas interacts with the background gas in the vacuum chamber by which it is heated due to collisions. The position x_M of the Mach disk marks the transition from supersonic to subsonic speeds, which is equivalent to the transition from a molecular beam (directed motion) to a gas cloud (random motion).

$$x_M = d_{\text{capillary}} \sqrt{\frac{p_0}{p_1}} \tag{2.3}$$

The transfer of the ions into the next vacuum chamber at lower pressure is done using a skimmer to minimize turbulence. In order to achieve an ion beam of high intensity and good collimation, the skimmer should be placed in the region before the Mach disk, where it can sample particles still characterized by a directed motion [67, 72].

Alternatively an ion funnel can be used, to collimate the expanding gas cloud and transfer the ions to the next pumping stage []. Since ion funnels are RF ion optical devices that consist of many components, such a solution means a much larger effort, then the use of a skimmer.

2.1.3 Ions Produced by an Electrospray Source

Electrospray ionization is possible in positive and negative mode, which relates to the polarity of the applied voltage and hence of the created ions[1]. Which ions are created from a solution depends on the solvent, the properties of the dissolved molecules, their concentration and the settings of the source parameters. In order to create an ion beam for a specific purpose the solution needs to be prepared accordingly. For instance, a solution for mass spectrometry should give a clean, low background signal, while for deposition a high current is most desirable. What ions are to be expected from a certain solution is discussed in the following section.

---

[1] Within this work only the more popular positive electrospray mode is used. Since both modes are equivalently described, only the positive mode will be discussed in the following.

Type of Charging

Since not every particle of an electrosprayed solution gets charged the question arises if there are molecules that are charged preferably and whether this depends on specific conditions. Most solutions used for electrospray contain ions in solution. Water is autoprotolyzed in H^+ and OH^-, other solutions are contaminated with small amounts of salt ions. These ions are typically also present in the electrospray ion beam, especially when no competing ionization pathway exists.

Solutions containing molecules can be ionized under certain conditions characterized by pH value, salt concentration or the electrochemical potential. The most prominent example relevant for positive mode ESI is the amino functional group in organic molecules which is protonated for acidic pH [73, 69, 74, 32]. This way of charging is used for proteins since it requires only a very mild acid like acetic or formic acid which does not decompose the protein [32]. The addition of the acid raises the concentration of H^+ by which the equilibrium in the reaction $\mathrm{H}^+ + \mathrm{H_2N{-}R} \leftrightarrow (\mathrm{H_3N{-}R})^+$ is shifted to the right side. As a consequence, the fraction of protein ions in the electrospray is increased.

A similar effect can be achieved by the addition of low concentrations of salts for instance through contaminations. Ions like H^+, Li^+, Na^+,K^+ and to a lower extend Mg^{2+} and Ca^{2+} can attach to organic molecules in solution and form gas phase ions in the electrospray [67]. By this mechanism charged clusters of many particles are formed, whose building units can be ions or non-ionic molecules. Charged solvent clusters are a common example [75, 76, 77].

The charging of salt cluster ions formed from concentrated salt solutions represents a special case of this mechanism. Sodium chloride, for example, creates singly and doubly charged cluster ions of the type $\mathrm{mNa}^+(\mathrm{NaCl})_\mathrm{n}$ ($m = 1, 2$) [78, 79, 80, 81]. A high concentration of salts in a solution leads to the dominant creation of cluster ions which suppresses other ionization paths.

Finally non-ionic molecules can be ionized in an electrospray besides the attachment of H^+ or Na^+ by an electrochemical reaction. Due to the high voltage used for the electrospray, the potential drop at the metal-liquid interface of the spray needle can be sufficient to oxidize molecules. These molecules are then ionized in solution and can become gas phase ions. Complex compounds and aromatic or highly conjugated molecules with electron donating groups like $-\mathrm{OH}$, $-\mathrm{OCH_3}$, $-\mathrm{N(CH_3)_2}$ or $-\mathrm{CH_3}$ are typical candidates [67].

Mass-to-Charge-Ratio Range

Both charging mechanisms proposed for electrospray ionization, either the *charge residue model* [68, 69] or the *ion evaporation model* [69, 70, 71] predict that large molecules can be highly charged. In fact, this has been observed in experiments on the ionization of molecules with very high masses, up to $10^5\,\mathrm{u}$

[74, 27]. The mass-to-charge-ratio of electrospray ions is almost always found in the range of $0 - 6000\,\mathrm{Th}$, which implies a strong multiple charging for heavy molecules [40].

This phenomenon is one of the major advantages of ESI. Firstly, multiple charging means low mass-to-charge-ratios which makes simple quadrupole mass spectrometers available for high mass detection. Secondly, multiple charge states give direct access to the real mass of a particle. The identification of ions based on their mass-to-charge-ratio is possible if more than one charge state is observed. From the mass-to-charge-ratios of two neighboring charge states z and $z + 1$, $M_z = m/z$ and $M_{z=1} = m/(z + 1)$, the mass can be directly calculated as [35](section 4.3.1, page 106)

$$m = \frac{M_{z+1} M_z}{M_z - M_{z+1}} \tag{2.4}$$

Finally, the charge state gives additional information about the conformation of the ions in solution, which can be the native environment for functional biological molecules, which exist in different conformational states. These can be related to different charge states of their gas phase ions (section 4.3.2, page 108).

In general, the charge state of a particle depends on the energetics of the ionization process and how many ionization sites are available. Highly charged particles can be created and will be stable if the charging sites are far enough from each other so as to minimize the Coulomb repulsion. The energy that is needed to charge two sites in a gas phase ion is gained by lowering the charge of the droplet, the gas phase ion is originating from. The ion evaporation model proposes that the emission of a multiply charged gas phase ion from a highly charged unstable droplet is energetically favorable. The energy gained by the emission is needed to compensate desolvation and the charging energy.

The picture in the charged residue model starts with a multiply charged droplet which is stable and will remain stable also when all the solvent is gone, since the particle inside is big enough to bind all the charges in solution. In this case no further fission occurs. Also in this case the result is a multiply charged gas phase ion.

As a consequence of either electrospray ionization charging mechanism, highly charged particles will be created by an electrospray source, if many charged particles are present in solution due to a high concentration of ions and when no low charged competitor is available at the same time.

2.2 TIME-OF-FLIGHT MASS SPECTROMETRY

2.2.1 General Aspects of Mass Spectrometry

The term mass spectrometry refers to a group of techniques which are used to determine the mass of ions. The first mass spectrometer has been constructed by J. J. Thomson in 1913 [23].

Since then, several types of mass spectrometers have been developd. Among the most popular are quadrupole mass spectrometers (QMS) [82], magnetic sector mass separators, fourier transform ion cyclotron resonance mass spectrometers (FTICR-MS) [83], orbitrap mass spectrometers [84] and the time-of-flight mass spectrometer (TOF-MS) [85] that is used in this work.

In mass spectrometry the measured quantity is mass-to-charge-ratio and not mass since all techniques employ electromagnetic fields in such way that the particles are separated by $\mathrm{m/z}$. The unit of this quantity is Thomson, named after J.J. Thomson [23] and is defined as $1\,\mathrm{Th} = 1\,\frac{\mathrm{u}}{\mathrm{e}}$. The mass-to-charge-ratio M of a particle with mass m and charge state $z = Q/e$, where Q is its total charge, is defined as [86]:

$$M = \frac{m}{z} \quad . \tag{2.5}$$

A time-of-flight mass spectrometer separates ions due to the fact that, accelerated by the same electric field, light ions reach a detector earlier than heavy ones. A TOF measurement starts with an extraction voltage pulse which acts on the ions belonging to a certain position of the ion beam (the so called extraction volume) and accelerates them towards a detector. The ion current generated at the detector is recorded as a function of time. A time-of-flight spectrum results from the integration of this $I(t)$ signal over many cycles, each of which lasts a few 100 microseconds. The final mass-to-charge spectrum is obtained after the calibration of the time-of-flight-spectrum.

Due to its mode of operation, a time-of-flight mass spectrometer immediately gives the full mass range for each cycle, which makes measurements very quick, even for a large mass-to-charge-ratio range. The TOF's mass-to-charge-ratio range of up to $10^5\,\mathrm{Th}$ is very large, compared to other mass analyzers. The resolution that can be achieved by TOFs ranges from 100 to 1000 for linear spectrometers and up to 20000 for reflectrons [87, 88, 89, 90]. The device itself is very robust, since it contains no movable mechanical parts and only moderate manufacturing precision is needed. Moreover, the electronics necessary for an average performance TOF-MS is off the shelf today.

2.2.2 Ion Motion in the Linear TOF Mass Spectrometer

An orthogonal extraction linear time-of-flight mass spectrometer is characterized by a switchable extraction region, an acceleration region (length a), a field free drift region (length d) and finally the detector. In figure 2.3 the characteristic parameters of these components and the potential landscape they generate are sketched. In fact, the ions fly to the detector under a certain angle $\Theta = \arctan(\sqrt{v_x/v_y}) \approx \arctan(E_{\mathrm{kin}}/U_a)^{\frac{1}{4}}$ which is determined by the initial kinetic energy of the beam E_{kin} and the acceleration potential potential U_a.

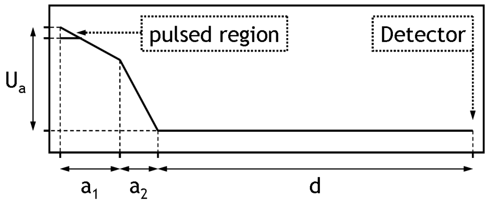

Figure 2.3 – Potential landscape of a linear time-of-flight mass spectrometer, ($a = a_1 + a_2$-acceleration length, d - drift length, U_a - acceleration potential)

Starting with the extraction pulse, the charged particles are accelerated by an electric field $\mathcal{E}$, which changes their direction towards the detector. Particles of mass m and charge $Q = ze$ are accelerated by a potential U_a along a distance a into the y direction (the additional drift length d is neglected for simplicity). From Newton's equation of motion follows

$$m\frac{d^2y}{dt} = \mathcal{E}Q = \frac{U_a ez}{a} \tag{2.6}$$

For a flight distance $y = a$ the flight time t is be derived to be

$$t = a\sqrt{\frac{2}{U_a e}\frac{m}{z}} \quad , \tag{2.7}$$

which shows the dependence of the flight time on the mass-to-charge-ratio .

This relation is exact only for a linear acceleration region and for particles with no initial velocity. Nevertheless, it illustrates two facts that are valid also for a more elaborate calculation. Firstly, particles of different mass-to-charge-ratio (not mass) are separated by the acceleration in the electric field so that they arrive at different times at the detector.

Secondly, variations in the kinetic energy[2] or in the flight distance will result in unprecise measurements. These errors are caused by a non-uniform initial velocity, by field distortions related to mechanical and electrical imperfections and by the spread in the initial position of the ion.

In the linear TOF mass separator the error in flight time for particles of the same mass-to-charge-ratio but different initial positions can be partly compensated by designing a suitable potential landscape [85]. To compensate errors

---

[2] Strictly speaking, variations in E_{kin} are not reflected in equation (2.7), but will result from a more elaborate treatment of a time-of-flight mass spectrometer

caused by the spread in the initial velocity a reflectron type setup is needed [91]. This operates on the principle that an initially different starting position in y direction is compensated by the effect that particles closer to the detector are less accelerated in the electric field and thus are slower in the drift region. Therefore, the faster particles catch up. There is a certain point, where both particles are at the same y-position, which is called *Wiley-MacLaren-Focus*. At this point, where the detector has to be positioned, the initial error in position is compensated.

2.2.3 Instrumental Resolution

Errors in time measurement, inherent in the technique or imposed by the experimental equipment, limit the precision of a flight time measurement which is quantified in terms of time resolution:

$$R_t = \frac{t}{\Delta t} \tag{2.8}$$

All errors in time are reflected in errors in mass-to-charge-ratio measuremnts, due to the connection stated in equation (2.7):

$$R_m = \frac{M}{\Delta M} \approx 2R_t \tag{2.9}$$

A constant resolution across the whole mass range, which is 4 orders of magnitude for a typical TOF, means that features in the mass spectrum at higher mass-to-charge-ratio have to be further separated from each other in order to be distinguished. At a mass resolution of 300 the peaks $300\,\mathrm{Th}$ and $301\,\mathrm{Th}$ can be distinguished from each other, while the peaks at $3000\,\mathrm{Th}$ and $3001\,\mathrm{Th}$ would overlap into one feature.

2.2.4 Calibration and Calibration Error

The measured time-of-flight spectra have to be converted into mass spectra in order to be interpreted. This is done with a calibration relation which is derived from the integration of equation (2.6).

$$M = A(t - t_0)^2 \tag{2.10}$$

The parameters A and t_0 are determined by a fit to a known mass spectrum as demonstrated in section 4.1.2, page 71.

Just as the measurement it is derived from, a calibration is limited in precision, which is important to know when mass spectra are interpreted. The error ΔM on the mass-to-charge-ratio M results from errors in the calibration parameters and in the time measurement:

$$\begin{aligned} \Delta M &= \left|\frac{\partial M}{\partial A}\right| \Delta A + \left|\frac{\partial M}{\partial t_0}\right| \Delta t_0 + \left|\frac{\partial M}{\partial t}\right| \Delta t \qquad (2.11) \\ &= (t - t_0)^2 \Delta A + 2A(t - t_0)(\Delta t_0 + \Delta t) \quad . \qquad (2.12) \end{aligned}$$

The relative error $\frac{\Delta M}{M}$, which is a resolution in mass-to-charge-ratio , can be understood as a limitation in mass resolving power imposed by precision of the calibration. This is derived from equation (2.12) and equation (2.10) using the approximation $t_0 << t$

$$\frac{M}{\Delta M} = \left[\frac{\Delta A}{A} + \frac{2\Delta t_0}{t} + \frac{2\Delta t}{t}\right]^{-1} \tag{2.13}$$

$$= \left[\frac{\Delta A}{A} + \frac{2\Delta t_0}{t} + R_m\right]^{-1} \tag{2.14}$$

The resolution in mass resulting from errors in calibration and the instrumental mass resolution are connected by a reciprocal sum. Therefore the lowest value determines the final resolution of the instrument. In section 4.1.2 the effect of the precision in calibration is considered on the example of CsI. It is shown that for high resolution mass spectra a calibration over many peaks is necessary to be able to reach the instrumental resolution.

An unprecise calibration can also be the result of systematic errors such as the use of peaks for which the detector is saturated. These peaks typically appear for very strong signals and can be identified by their asymmetrical shape. Due to the intense current for this specific mass, the detector is saturated and further events are not detected for a dead time depending on the detector type. This results in a shift of the peak center to lower flight times and thus in a wrong calibration if this peak is used.

2.3 ION BEAM INTERACTIONS WITH GASES AND SOLIDS

2.3.1 General Properties of Ion Beams

An ion beam, per definition, is a cloud of charged particles, atoms or molecules, with a non zero average velocity. Each particle in the beam is fully described by its coordinates in phase space (x, y, z, p_x, p_y, p_z) and its mass m and charge state $Q = ze$ with z the number of unit charges.

To describe the shape and motion of an ion beam in a more useful way than by the phase space coordinates of each particle, integral quantities are defined. The directed axial momentum of the ion beam $p_{\|}$ is given by the average of the momentum over all particles, since the randomly distributed components Δp add up to zero. The average kinetic energy per ion can be written as

$$
\begin{aligned}
E_{\text{kin}} &= \frac{1}{2m}(p_{\|}^2 + \Delta p^2) && (2.15)\\
&= E_{\text{kin}}^{\|} + k_B T \quad . && (2.16)
\end{aligned}
$$

The temperature T or energy $k_B T$ relates to the spread in momentum and energy of the ion beam. An ion beam at $0\,\mathrm{K}$ thus would be perfectly collimated. In fact, the ion beam can be considered a gas at this temperature. An ion beam can be heated, for instance by radiation from an RF field in a quadrupole[92], or cooled when in contact with a cold gas (section 3.2.1, page 52)[93, 94, 95, 96].

A conservative system presumed, this temperature is conserved [97]. Ion optical devices such as an electrostatic lens of a time-of-flight mass spectrometer do not affect the beam temperature. Since the energy spread is coupled to the particles momentum, the spread of a heavy particle ion beam is lower compared to a light particle beam of the same energy.

A beam of charged particles finally can be described as an electrical current and as a flux of mass at the same time. Both are defined as the amount of charge or mass passing through a surface in unit time. The current of an ion beam is often directly measurable, for instance by a faraday cup [98, 99] (see section 3.1.4, page 42). The mass flux can be calculated when the mass-to-charge-ratio of the ions is known. It is the product of electrical current and mass-to-charge-ratio .

2.3.2 Ion-Gas-Interactions

Introduction: Beam Cooling and Collision-Induced-Dissociation

Ion-gas-interactions play a key role in ion beam applications and can be utilized as an additional tool for ion beam manipulation. In order to investigate an ion beam by means of mass spectroscopy, the phase space volume of the beam should be as small as possible to reach a high mass resolution. However in perfect vacuum an ion beam can only be influenced by electromagnetic fields or by collisions with a solid wall. The use of electromagnetic fields typically creates a framework in which the total phase space volume of the system is constant. This leads to tradeoffs that can be unfavorable for a certain application. For instance, the selection of one value for the kinetic energy will reduce the ion beam flux. The more narrow the width of the energy distribution of the ion beam gets, the lower the current. Another example is, that good focusing results in either a broadening of the energy distribution or in loss of current.

Ion gas collisions can be used to overcome these limitations. Collisional focusing or buffer gas cooling in ion traps are typical examples [93, 94, 95, 96]. These techniques are based on the effect, that many low energy collisions of fast ions with a relatively cold buffer gas lead to the equilibration of the ions and the buffer gas. Such thermalized ion beams have an energy spread related to the temperature of the buffer gas, which is typically lower than the beam temperature (equation (2.16)) of an ion beam emitted from a supersonic nozzle, for instance.

Collision induced dissociation (CID) is another major application of ion-gas-interactions besides cooling. This collective term relates to the disintegration of clusters and molecules upon collisions with a neutral gas target, independent of the mechanism. Energetic collisions are the cause of this fragmentation due to the transfer of kinetic energy into internal energy [100]. The specific excitation or destruction of molecular ions or clusters is widely used in mass spectrometry in order to obtain more information about an ion by analyzing its fragments [101, 102, 74]. The most prominent technique employing CID is product ion mass spectrometry (PIMS) in which a precursor ion is mass selected and fragmented (for apparative details see section 3.4.4, page 66).

The fragmentation of the precursor molecule or cluster only takes place if the collision energy is higher than a certain threshold value. This phenomenon is widely researched for very diluted gases, typically at low temperatures [92]. For organic molecules a great variety of fragmentation reactions with different threshold energies can be observed. The reason for the existence of this threshold collisions is that the cross section for collisions at chemical energies strongly depends on the collision energy and the chemical properties of the molecule and the collision partner.

Skimmer-nozzle fragmentation, the method to create ion-fragments used within this work, is one other possible method to implement CID in a mass spectrometer besides using a collision cell (see section 3.4.4, page 66 for tandem MS using a collision cell). Skimmer-nozzle fragmentation takes place in the first pumping stage of an atmospheric pressure ionization source (API). It is less commonly used than fragmentation in a collision cell, since it generates less mass spectrometric information due to the lack of mass selection before the CID [67]. Nevertheless this technique is used widely within this work, since it is a good way to gather more mass-spectrometric information with the present apparatus which is optimized for deposition of ions on a surface and thus lacks an additional collision cell.

Collisional focusing and nozzle-skimmer-fragmentation are both employed in the ion beam deposition setup developed. Based on the kinetic gas theory, a simple model is developed, which can be used to understand the mentioned processes and interpret the results. This model is presented below and can be used to estimate the number and energy transfer of the ion-gas collisions under the influence of an electric field, and is thus a helpful tool for the design of the atmospheric interface (see section 3.2.1, page 52).

Aspects of Kinetic Gas Theory

The kinetic theory of gases provides a framework within the kinetic processes involved in ion-gas interactions can be described. Chemical processes during a collision, which are described by quantum mechanics are not included in the model. In the following the collisions between an ion beam and a neutral gas are investigated with the kinetic gas theory [103, 104].

A beam of ions with radius R, mass m_i and charge z is considered to move with velocity v in a volume of gas. The neutral gas of mass m and particle radius r is characterized by thermal equilibrium at temperature T, pressure p and its molar density $n = \frac{pN_A}{RT}$. The average velocity of a molecule in the gas is then given by

$$\bar{v} = \sqrt{\frac{8k_BT}{\pi m}} \tag{2.17}$$

which is $471\ \frac{\mathrm{m}}{\mathrm{s}}$ for nitrogen at room temperature. This velocity corresponds to a kinetic energy of $32\,\mathrm{meV}$.

An ion which is moving in this gas undergoes multiple collisions. The mean free path λ is the average distance that an ion can travel between two collisions and is given by:

$$\lambda = \left[n\pi\sigma\sqrt{\frac{m_i}{m}}\right]^{-1} \tag{2.18}$$

Here $\sigma = \pi(r+R)^2$ is the collision cross section of the hard sphere model.

The energy loss of the ion due to a buffer gas collision is called collision energy and can be calculated from energy- and momentum conservation. Without knowledge of the exact collision parameters it is useful to calculate the maximum collision energy in order to compare the calculated values to experimentally found fragmentation threshold energies.

$$E_c = \frac{\mu}{2}(\bar{v} - v)^2 \tag{2.19}$$

The maximum collision energy E_c depends on the velocities and the reduced mass $\mu = \frac{mM}{m+M}$.

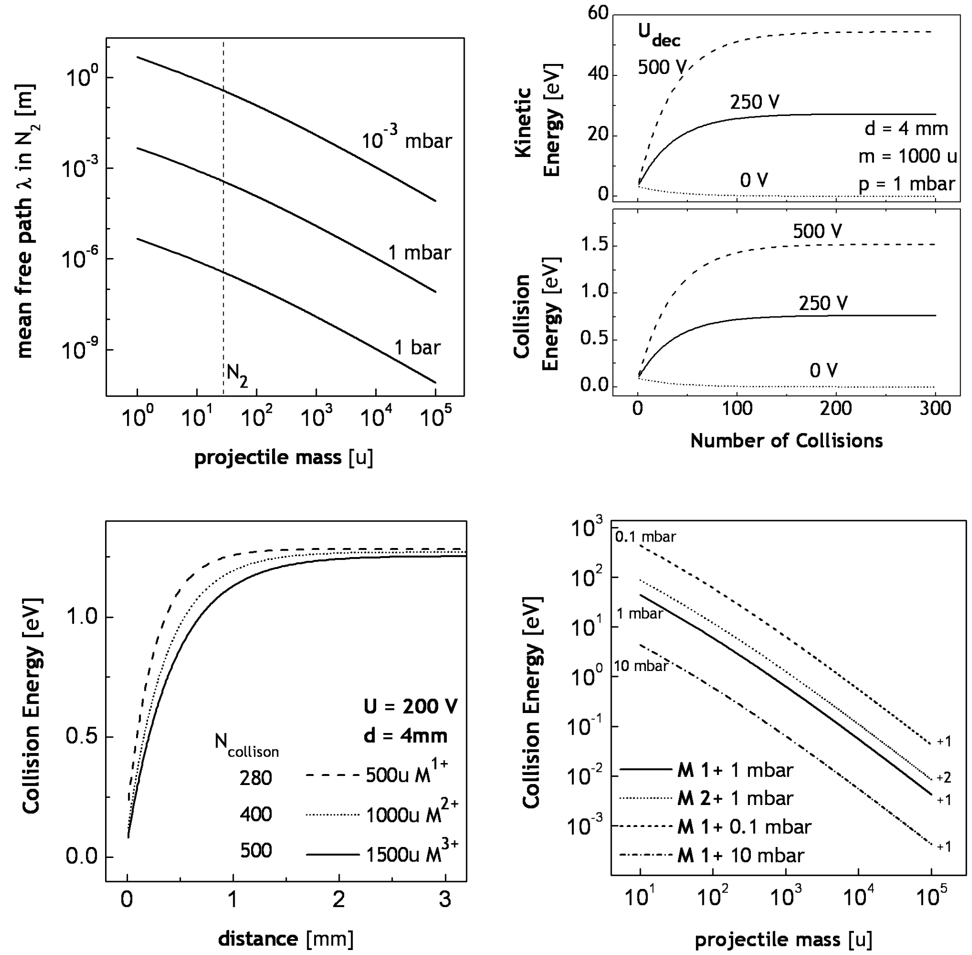

Figure 2.4 – **[top left]** Mean free path of a particle as function of mass in $\mathrm{N_2}$ at $293\,\mathrm{K}$ and various background pressures, calculated from equation (2.18). **[top right]** Kinetic energy and collision energy as a function of the collision number for a $1000\,\mathrm{u}$ particle accelerated by declustering potentials of $0 - 500\,\mathrm{V}$ in $\mathrm{N_2}$ at $1\,\mathrm{mbar}$. (equation (2.26)) **[bottom left]** Collision energy for three particles of the same mass-to-charge-ratio as a function of path traveled in $1\,\mathrm{mbar}$ $\mathrm{N_2}$ at $200\,\mathrm{V}$ declustering potential. The number of collisions $N_{\mathrm{collision}}$ is given. **[bottom right]** Collision energy as a function of particle mass for $p = 0.1 - 10\,\mathrm{mbar}$ and charge states of $1+$ and $2+$ at $250\,\mathrm{V}$.

The relations presented above allow to estimate important characteristics of ion optical devices that employ ion-gas-collisions for fragmentation or cooling. Equation (2.17) gives the drift velocity of a thermalized ion beam, allows to estimate how many collisions occur on such a way and equation (2.19) shows how intense these collisions are.

Kinetic Model for Skimmer-Nozzle Fragmentation

The collision energy between two particles can be estimated by equation (2.19), the average distance between two collisions by equation (2.18). For nozzle-skimmer-fragmentation the framework in which kinetic gas theory is applied, is more complicated. The same ion collides many times while it is constantly accelerated. Due to the energy transferred through these collisions, the molecule eventually fragments, either when a certain threshold energy is exceeded in a single collision or by accumulation during many events. In order to calculate the collision energy and to find how this energy depends on parameters like pressure, electric field and what particles are involved, a simple model to approximate the accelerated motion of the ion is developed.

In the first pumping stage, gas containing molecular ions leaves the capillary and enters a region of low pressure, typically $1\,\mathrm{mbar}$. As already shown in section 2.1.2, page 14 a supersonic expansion of the gas into vacuum is the result, which accelerates the gas molecules to supersonic speeds.

The terminal velocity of this expansion, given in equation (2.2), is assumed as starting velocity. The declustering potential between the fragmentor electrode and the skimmer $U_{\mathrm{dec}} = U_{\mathrm{frg}} - U_{\mathrm{skimmer}}$ is further accelerating the ions once they leave the nozzle. On their way the ions undergo intense collisions with the background gas that can lead to the fragmentation of the molecular or cluster ions, as described in section 4, page 67. The number of collisions is estimated by the mean free path equation (2.18) and their maximal energy transfer by equation (2.19).

The thermal energy of the buffer gas is much smaller than the relevant binding energies between the molecules or clusters. Therefore, in order to simplify the calculation, the buffer gas is assumed to be at rest, which is suitable for the average over many collisions, since the velocity of the gas particles is low compared with the velocity of the ion. Between the collisions the ions can travel freely.

The change in kinetic energy per collision, as given by equation (2.19) can then be written as the quotient of the kinetic energy of the ion before (E_1^{kin}) and after (E_2^{kin}) the event. This quotient is the kinematic factor

$$\kappa = \frac{E_2^{\mathrm{kin}}}{E_1^{\mathrm{kin}}} = 1 - \frac{2\mu}{m_i} \tag{2.20}$$

which is constant for given collision partners. Between two collisions an ion can travel freely in the electric field $\mathcal{E} = U_{\mathrm{dec}}/d_{\mathrm{NS}}$ of skimmer and fragmentor electrode (distance $d_{\mathrm{NS}} = 4\,\mathrm{mm}$). The energy W gained therefore depends on the mean free path λ equation (2.18) and the charge state of the particle ze.

$$W = \mathcal{E}\lambda ze \tag{2.21}$$

For a number of collisions k the kinetic energy can thus be written as

$$\begin{aligned} E_{\mathrm{kin}}(k) &= E_0\kappa^k + W\sum_{i=1}^{k}\kappa^i & (2.22) \\ &= E_0\kappa^k + W\frac{\kappa(\kappa^k - 1)}{\kappa - 1} & (2.23) \end{aligned}$$

where E_0 is the kinetic energy of the particle after the supersonic expansion.

The kinetic energy of the ions that leave the nozzle-skimmer area can be estimated from equation (2.23). For low pressures $k_{\mathrm{NS}} = d_{\mathrm{NS}}\lambda$ has to be calculated. For high pressures the exit energy is the limit for $k \to \infty$

$$E_{\mathrm{Exit}} = W\frac{\kappa}{\kappa - 1} \tag{2.24}$$

which then mainly depends on the declustering potential, mass and charge state of the particles. It is important to know this energy for the further design of the apparatus, since it is the energy of the particles entering the next pumping stage (see section 3.2, page 52).

Since the one main interest is the nozzle-skimmer fragmentation in the first pumping stage, the collision energy E_c is of special interest. The energy loss $E_c(k)$ of the k^{th} collision is the factor $(1 - \kappa)$ of the kinetic energy of the ion right before the collision. This energy is $E_{\mathrm{kin}}(k-1) + W$, the energy after the last collision plus the energy gained during the free flight period between the two subsequent collisions.

$$\begin{aligned} E_c(k) &= (1-\kappa)(E_{\mathrm{kin}}(k-1) + W) & (2.25) \\ &= (1-\kappa)\left[E_0\kappa^{k-1} + W\frac{\kappa^k - 1}{\kappa - 1}\right] & (2.26) \end{aligned}$$

Figure 2.4 [top right] shows the kinetic energy and the collision energy E_c for typical parameters.

A stationary condition is attained after approximately 100 collisions for a pressure of $1\,\mathrm{mbar}$. At this point the energy gained in the electric field equals the energy loss through the collisions. The evaluation of equation (2.26) shows that the predominant number of collisions and the more intense ones occur after stationary conditions are reached. Thus equation (2.21) is a good estimate for the collision energy. In figure 2.4 [bottom left] the collision energy is shown as a function of traveled path in the gas. The stationary state is reached within the dimensions of the skimmer nozzle distance. The calculated value has to be seen as an average, since epically the free traveled path during which the ion is accelerated is not constant as assumed. This results in a rather wide distribution of collision energies around the calculated value.

Results from the Kinetic Model

Relation 2.26 describes the ion gas collisions as a function of the main experimental parameters. Mass and charge of the incident ion, temperature, pressure, buffer gas mass, cross sections, declustering potential and geometry of the apparatus all have an influence on number and intensity of the collisions. Since the model describes the collisions only as hard-sphere interactions, the complex chemical behavior of the involved molecules is not reflected, which are for instance the formation of intermediate compounds or the excitation of internal degrees of freedom. Both effects can cause a fragmentation of a molecule: an intermediate compound can disaggregate into products that are different from the original substances, while the continued excitation of internal degrees of freedom by many collisions is equivalent to a heating of the particle by which it can be destroyed. Nevertheless the influence of the variation of the parameters on the system can be studied by the kinetic model developed in this section and compared with the experiment, as shown in section 4, page 67.

Figure 2.4 [top right] displays the kinetic and collision energy as a function of the number of collisions. Both functions show the same behavior, because they are directly connected by the kinematic factor. The graphs illustrate the influence of the most important parameter in nozzle-skimmer-fragmentation, the declustering potential, on which the kinetic and collision energy depends linearly.

In figure 2.4 [bottom left] it is shown that for the same mass-to-charge-ratio the collision energies are the same, once the stationary condition has been reached. Depending on the particles mass, the stationary condition is reached for a different number of collisions, but approximately after the same flight path. The slight deviation is caused by the mass dependency of the mean free path equation (2.18).

Variations in the charge state change the collision energy drastically since they have a direct influence on the acceleration in the electric field. A doubly charged molecule collides with twice the energy of a singly charged ion (see figure 2.4 [bottom right]). The number of collisions is unaffected, since the mean free path does not depend on the charge.

Finally the pressure has an influence on the collision energy. As shown in figure 2.4 [bottom right] an increase in pressure by factor 10 decreases the collision energy by the same factor. This effect is due to the changed mean free path. A change in pressure also results in a changed number of collisions. For instance at a higher pressure the number of collisions increases, whereas the collision energy decreases.

The question if a single or multiple collision events are responsible for the fragmentation is not answered by the kinetic model presented. Since the hard-sphere collision is only a rough estimation of the collision energy and the energy transfer into internal degrees of freedom, such as the excitation of rotational and vibrational states, are not included in the model, only the order of magnitude of the calculated energies can be compared with binding energies. Thus a fragmentation onset at a certain value for the declustering potential, which can be related to a collision energy is not given by the model. However since the calculated collision energy is a key parameter in either single or multiple collision fragmentation, parameters that influence the collision energy will also influence the fragmentation behavior.

The knowledge of how these experimental parameters influence the collision energy helps to interpret the experimental results. For instance the charge state dependent fragmentation of **BSA** (section 4.3.1, page 106) and salt clusters of **SDS** (section 4.1.3, page 74) is related to the change in kinetic energy due to the stronger acceleration in the electric field. Another example are the typical fragmentation patterns of organic molecules observed in mass spectrometry that are interpreted by the subsequent fragmentation of first weak and later strong bonds with increasing acceleration field (section 4.2, page 82).

2.3.3 Ion-Solid-Interactions: Surface-Induced-Dissociation and Soft Landing

The controlled ion beam deposition of molecules on solid surfaces requires knowledge about the interaction of solids with energetic ion beams. In particular the effects that occur in the very low energy range, ion beam soft landing and surface induced dissociation (SID), are of interest when molecular or cluster ions are concerned.

Ion-surface-interactions can be classified by the kinetic energy of the ion beam, since this parameter determines how the solid and the ions interact [105, 66]. In table 2.1 these ranges and typical processes are summarized. The thermal and hyperthermal energy range is relevant for soft landing deposition of polyatomic ions. In the same energy range surface induced dissociation occurs [105]. Higher energy ranges are characterized by destructive processes. Therefore typically only monoatomic ion beams are found in ion beam applications in this energy range, since they are easier to produce and the result after the impact is the same.

Surface Interaction of Molecular Ions

Inelastic collisions of a polyatomic ion with a surface leads to an energy transfer from kinetic energy into vibrational modes of the molecule or cluster ion and into the surface. The excitation of the molecule can cause various processes including fragmentation, which is referred to as surface induced dissociation (SID) [106].

	Energy Range (eV)	**Characteristic Processes**
thermal	$0-1\,\mathrm{eV}$	physisoption, chemisorption, (soft landing)
hyperthermal	$1-100\,\mathrm{eV}$	soft landing, surface induced dissociation (SID), elastic scattering
low energy	$100\,\mathrm{eV}$ - $10\,\mathrm{keV}$	sputtering
high energy	$>10\,\mathrm{keV}$	ion implantation, sputtering

Table 2.1 – Energy range classification of ion beams [105]. For thermal energies an ion beam with a directed motion and therefore soft landing often cannot be defined.

Just like collision induced dissociation (CID), surface induced dissociation (SID) typically occurs above a threshold of energy transferred. Below this energy, the molecular ion will stay intact. Upon a non destructive collision, the ion can be adsorbed at the surface. This is called soft landing. Once on the surface, the particle can be neutralized.

Ion-surface interactions with molecules are studied by means of surface induced dissociation within the framework of tandem mass spectrometry [107]. In contrast to collisions induced dissociation (CID), the gain in internal energy by the collision of an ion with a surface is larger. The energy distribution found for ion surface collisions is more narrow than for corresponding ion-gas-collisions. Since ion-surface reactions can be performed at high vacuum conditions, the corresponding experimental setup for mass spectrometry becomes more simple. These favorable properties have led to the application of SID in mass spectrometry as an alternative to the fragmentation at gas targets [100].

For an ion beam deposition experiment, the whole kinetic energy has to be converted into binding energy and internal energy of the ion or the surface, in order for the molecule to stick to the target. Generally speaking, the physical and chemical properties of the surface, the stability of the ion and the incidence energy are the key parameters in the processes upon which the fate of the particle between dissociation or soft landing is decided [106, 105].

The conversion of the kinetic energy into vibrational energy is found to be almost linear for molecules up to a mass of $250\,\mathrm{u}$ [106, 105, 108]. For small ions, the substrate takes up a large fraction (up to 80%) of the kinetic energy, which decreases as the ion becomes bigger and thus offers more vibrational and rotational degrees of freedom to be excited.

For energies in the chemically relevant range ($<10\,\mathrm{eV}$), several studies show that the incident ion takes a larger fraction of the kinetic energy than for high energy collisions [106, 108, 109]. Ions with high kinetic energy interact with the surface mostly via the repulsive coulomb interaction. For decreasing kinetic energy the attractive interactions, like van-der-Waals or dipole forces, becomes more important, which is the reason for the observed change in energy conversion ratio.

If the amount of energy transferred into the vibrational modes is lower than the activation energies of the dissociation, the molecule is soft landed. A review of the literature shows that a kinetic energy up to $15\,\mathrm{eV}$ is found to be suitable for the soft landing of molecules [107]. The values vary depending on the study, since molecular ions and surfaces are varied throughout all experiments conducted so far [57, 58, 59, 61, 62, 19, 106, 110]. To relate the kinetic energy of $15\,\mathrm{eV}$ to a threshold value for fragmentation is complicated, since often just the recovery of intact molecules is considered as soft landing. Additionally, for the soft landing of multiply charged protein ions, values in the same range are reported as collision energy per charge.

The soft landing ratio, which expresses the relation between intact deposited material and destroyed molecules, has not been quantified for many experiments described in literature. Moreover, the definition of soft landing ratio varies, depending on what is considered as the amount of initially deposited particles, what can be particles in solution, particles in the beam or particles that hit the surface. A few estimations show that the number of molecules that can be recovered is in the order of $1\,\%$ to $5\,\%$ of the molecules that have been used in the spray solution [110, 53].

It is further shown that intact deposition of the molecules can be assisted by a modification of the substrate surface. Liquid surfaces and organic self assembled monolayers increase the fraction of energy taken by the substrate. This results in an increase of the threshold energy for the dissociation of the molecules and thus in a higher soft landing ratio. Energies up to $20\,\mathrm{eV}$ are reported for polyatomic ions of mass-to-charge-ratio in the range of $100-200\,\mathrm{Th}$ landed on liquid glycerol surfaces and self-assembled monolayers [52, 58, 106].

The few studies conducted so far on ion beam soft landing focus on the recovery of material in order to reuse it. Typically, the goal is to create an array of biological relevant substances, like antibodies or enzymes, by mass selection and deposition, which can be used for sensor applications. Therefore only few information about the structure formation of molecules on the surface upon ion beam molecular deposition is available. One work known is the deposition of graphene molecules ionized by MALDI, which are found to form islands by 2D growth on a graphite surface [19].

Soft Landing of Cluster Ions

The soft landing deposition of clusters is substantially different to that of molecules. A specific threshold energy after which the clusters disintegrate cannot be given independently of the particle size. In contrast to a molecule in which one or two bonds need to break in order to create fragments, in a cluster many bonds need to break. Furthermore clusters, which are small crystallites, have many more degrees of freedom. In order to dissipate collision energy, they can incorporate defects and can be deformed.

These properties of clusters lead to the observation that a kinetic energy of approximately $1\,\mathrm{eV/atom}$ is a general threshold for the soft landing deposition of clusters [111, 112]. For higher energies the cluster deposition is accompanied by the creation of defects at the surface or the cluster itself [113]. The clusters themselves are deformed and pining sites are created [72]. Borderline between clusters and molecules are particles like proteins, fullerenes (C_{60}) or the above mentioned graphene. These particles combine properties from both groups: the well defined structure of the molecule and the large size and high amount of degrees of freedom of the cluster.

Proteins, for example, are chain molecules with a covalently bound molecular structure. At kinetic energies relevant for soft landing, their specific biological function can be left aside. Upon a collision with a surface a protein can unfold, which can be compared to the defect formation in a cluster or it can be fragmented like a molecule.

Fullerenes like C_{60} consist of carbon in a state similar to sp_2 hybridized carbon. Their covalently bound structure is well defined like a organic molecules. The cluster property is expressed by the fact that many different sizes and defect structures exist besides C_{60} and that many defects can be incorporated before the molecule fragments.

The soft landing of these particles from ion beams is demonstrated up to energies of $10\,\mathrm{eV}$ for the fullerenes on graphite and $10\,\mathrm{eV}$ for proteins on a liquid surface [51, 60, 53, 114]. These results indicate that the fragile nature of the molecules is still the dominating limitation for soft landing.

3 MATERIALS, METHODS and EXPERIMENTAL SETUP

As described in the introduction, an important goal of this work is the design and setup of an apparatus for low energy ion soft landing deposition in ultra high vacuum. To achieve this goal a wide variety of techniques and equipment have been used.

The principles of the creation, detection and manipulation of ion beams have been introduced in section 2, page 13. In the first part of this chapter (section 3.1, page 35) the setup of the ion beam deposition apparatus is outlined. The design considerations for the ion optics are described in section 3.2, page 52 in more detail. Experimental procedures like the preparation of samples and the alinement of the beam are described in section 3.3, page 57. This part is supposed to provide guidelines for future users of the instrument and to give the supplementary information necessary for the detailed understanding of the experimental results. Techniques for advanced mass spectrometry and for the characterization of the ion beam deposited samples have been used. Besides the ion beam deposition setup, they are briefly explained in section 3.4, page 64.

3.1 THE ION BEAM SOFT LANDING DEPOSITION SETUP

The controlled deposition of nonvolatile molecules and clusters on surfaces in ultrahigh vacuum (UHV) is one aim of this thesis and thus the purpose of the ion beam deposition apparatus which has been developed. Figure 3.1 schematically shows the general concept of the ion beam source. In the following sections, the various components are described in detail.

Electrospray ionization is chosen as the method to transfer nonvolatile particles into the gas phase (3.1.1). The ionization process is nondestructive and applicable to all soluble molecules with very few exceptions like small nonpolar compounds. The choice of atmospheric pressure ionization as source of gas phase particles necessarily fixes a certain number of other characteristics of the deposition source. Differential pumping (3.1.3) is absolutely necessary

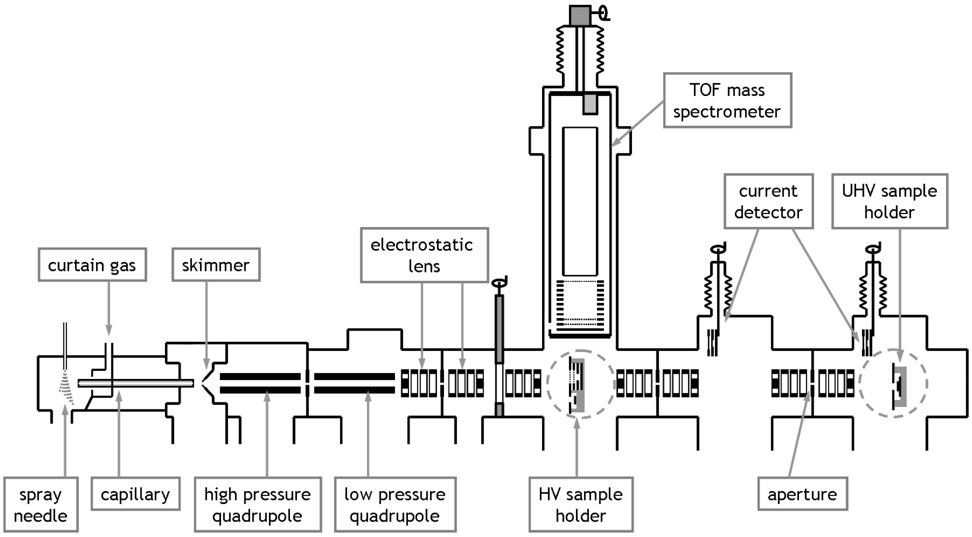

Figure 3.1 – Scheme of the ion beam deposition setup.

to bridge the pressure gap of 13 orders in magnitude between ambient pressure and UHV. Ion optics (see section 3.1.2, 3.1.7) are needed to transfer the beam trough the different vacuum chambers. Finally sample holders which need to be suitable for ion beam deposition have to be developed (3.1.6).

The controlled deposition requires mass spectrometry (3.1.5), current measurement and retarding grid energy analyzers to characterize the ion beam (3.1.4). The operation of the complete ion beam source is done with a computer system with software written for the purpose of instrumental control, monitoring and data acquisition (3.1.8).

Especially critical is the layout of the ion optical components. The atmospheric interface, the quadrupoles, the lenses and the mass spectrometry have very different requirements, but finally all have to be able to function with the same ion beam for which a certain range of parameters is given. On the other hand the design of the ion optics has a strong influence on the design of other components such as the size of the chambers or the voltages of the power supplies. Due to their key role, the design considerations for the high- and low pressure quadrupole, the electrostatic lenses and the ion beam detection are explained in more detail in section 3.2, page 52.

3.1.1 Atmospheric Interface

The atmospheric interface (AI) (figure 3.2) is the part of the ion beam source where the ions are actually created and formed into a beam. The principles of electrospray ionization explained in section 2.1.2, page 14 and the ion beam collimation by collisional cooling described in section 2.3, page 24 are applied here in order to achieve this goal. Furthermore, the AI provides the bridge between ambient pressure and high vacuum.

An electrospray is generated from a liquid in a spray needle by applying a voltage between the needle an the capillary entrance (section 2.1.2, page 14). This process can be assisted by a nebulizer gas. The gas phase ions created from the spray enter the first vacuum chamber through a capillary. Their in-vacuum expansion generates a supersonic beam characterized by the zone of silence in which the gas moves directed at supersonic speed. The ion beam is sampled from this area at a distance of $3-5\,\mathrm{mm}$ from the nozzle by a skimmer. Afterwards, in the second pumping stage, a high pressure quadrupole thermalizes the ion beam. Finally the beam is extracted from the AI through an aperture (Q1Q2Ap) in the high vacuum part of the ion beam deposition source.

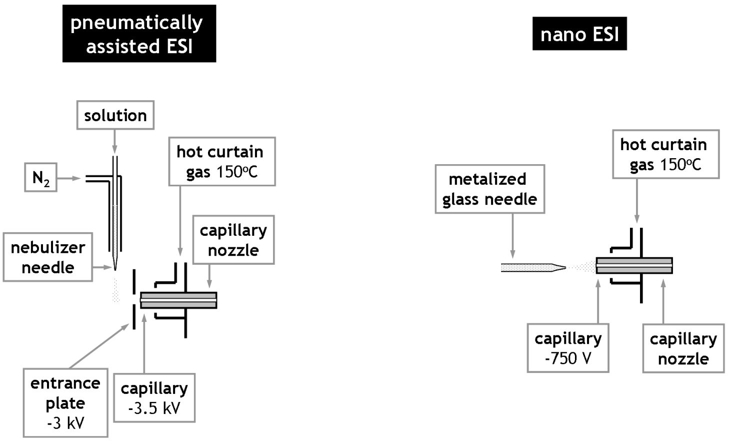

Figure 3.2 – Sketch of the **[left]** gas assisted orthogonal electrospray and the **[right]** nanospray assembly.

The atmospheric interface consists of the spray assembly (figure 3.2), the nozzle-skimmer chamber (NOZ-chamber) and the high pressure quadrupole chamber (Q1-chamber). The spray assembly (*Agilent Technologies NR, Weinheim, Germany*) can be used with a pneumatically assisted spray needle (*Agilent Techn.*) or with an emmiter mode nanospray needle (*Proxeon Biosystem, Odense, Denmark*). The spray needle is either a metal capillary of $50\,\mu\mathrm{m}$ diameter or a metalized pulled glass needle. The first type is covered by a concentric metal tube that carries the nebulizer gas when the pneumatically assisted spray source is used. In the nanospray source metalized glass needles are used and no nebulizer gas is needed. During operation the tip of the nanospray needle is placed at a distance of $2-4\,\mathrm{mm}$ to the stainless steel entrance cap of the capillary. The curtain gas (typically $\mathrm{N_2}$) is heated to $20-300\,^{\circ}\mathrm{C}$ and injected in the spray assembly in opposite direction to the gas flow into the vacuum.

The glass capillary of $0.4-0.6\,\mathrm{mm}$ diameter and $18\,\mathrm{cm}$ length has metalized ends so that voltages can be applied at its air side (entrance plate) and at its vacuum side (nozzle or fragmentor electrode) independently. The vacuum side is the nozzle from which the supersonic expansion originates. This end is covered by the fragmentor electrode. A skimmer with an opening diameter of $1 - 2\,\mathrm{mm}$ is placed at a distance of $3 - 5\,\mathrm{mm}$ of the fragmentor. Downstream to the skimmer the quadrupole Q1 of $10\,\mathrm{cm}$ length, $6\,\mathrm{mm}$ inner diameter and $5\,\mathrm{mm}$ rod diameter completes the atmospheric interface. Q1 is separated from the following high vacuum chamber by the aperture Q1Q2Ap with an opening diameter of $2\,\mathrm{mm}$.

3.1.2 Ion Optical System

The purpose of all ion optical components is the formation and guiding of the beam throughout the whole source. Electrostatic lenses, quadrupole ion guides and apertures are the components that are used. In this section the function and assembly of the ion optical components within the framework of the source is outlined, while a detailed discussion of their design principle is left to section 3.2, page 52.

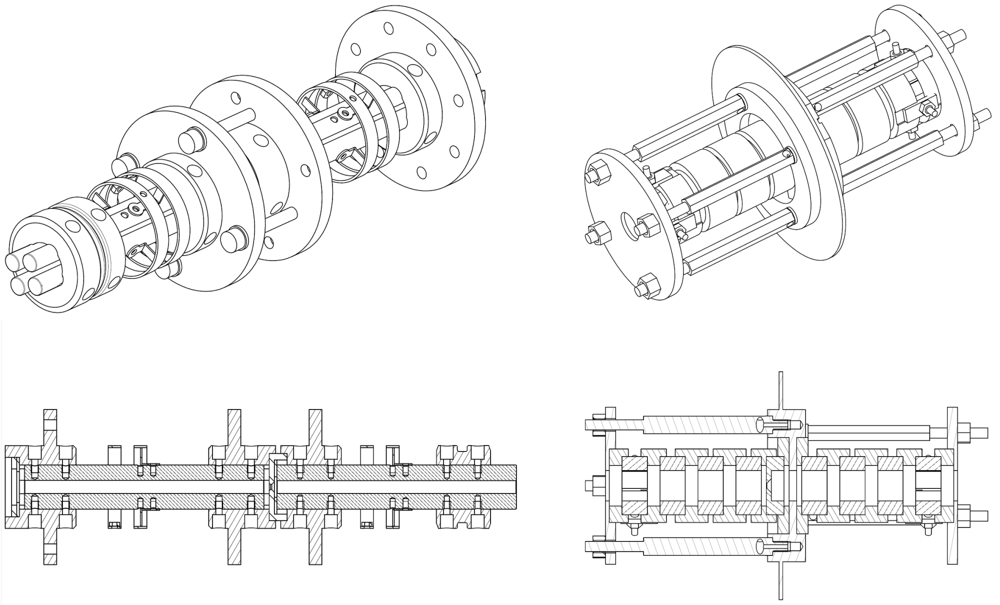

Figure 3.3 – Ion optical system components: **[left]** Quadrupole system consisting of two quadrupole ion guides. **[right]** Double electrostatic lens with aperture separating two successive pumping stages.

Figure 3.3 shows the two main ion optical components within the source, the quadrupole assembly [left]and an electrostatic lens [right]. In the high pressure part the skimmer and the quadrupole Q1 are used for beam collimation as described in section 3.1.1, page 36. In the high and ultrahigh vacuum parts first the mass selecting quadrupole Q2 and then seven electrostatic lenses (LA-LG) continuously guide the ion beam.

The quadrupole Q2 has the same dimensions as Q1. They are connected via the aperture Q1Q2Ap, which marks the boundary to high vacuum. At this pressure Q2 can be used as mass selecting quadrupole. Depending on the drive frequency, amplitude and DC offset voltage the transmitted mass range can be selected (see section 3.2.1, page 52).

The purpose of the lens is to focus the ion beam at a certain desired point in space, for example onto the sample surface in the last vacuum chamber, into the extraction volume of the mass spectrometer or through an aperture. Each lens consists of three concentric rings enumerated in beam direction (e.g. LA-1, LA-2, LA-3) to which voltages can be applied. The lenses B,E and G are additionally equipped with an aperture of $2\,\mathrm{mm}$ diameter. This aperture serves as separation of two successive pumping stages. The lens upstream of the aperture is used to focus the ions through the hole into the next chamber, the lens downstream is used to restore the beam collimation. All lenses are endowed with a 4-fold segmented ring constituting a set of steering plates (e.g. LA-SU, LA-SD, LA-SL, LA-SR), which can be used to correct eventual misalignments of the beam.

Lenses and quadrupoles are mounted on base plates which are themselves mounted onto base flanges between two chambers. The position of the baseplate on the base flange is aligned during the assembly of the system using a laser beam as reference. Lens rings and steering plates are mounted in stacks on the base plates. They are aligned by insulating rings made of PEEK, which define the axis and mutual distances. The stacks are pressed onto the baseplate by a closing plate which is at ground potential and has a opening of the same size as the lens rings.

A lens group containing steering plates, lens rings and possibly an aperture is connected via Kapton insulated 9-fold sub-D vacuum feedthrough to the power supplies. On the air side a corresponding 9-fold sub-D cable is used to bundle the connection for each lens group (see section 3.8, page 49).

3.1.3 Vacuum System

The vacuum system of the differentially pumped ion beam source has to work under a high gas load. While the ionization takes place at ambient pressure, the ions are deposited either at $10^{-7}\,\mathrm{mbar}$ or at $10^{-10}\,\mathrm{mbar}$, which corresponds to a ratio of 10^{10} or 10^{13} in pressure, respectively. With an approximate conductivity of the capillary of $10^{-4}\,\frac{\mathrm{l}}{\mathrm{s}}$, the leak rate through the capillary is about $0.1\,\frac{\mathrm{mbar\,l}}{\mathrm{s}}$. To reach UHV with this gas load a speed of $10^{9}\,\frac{\mathrm{l}}{\mathrm{s}}$ would be necessary, which is most probably impossible and certainly impractical when STM measurements are to be performed in the same room.

Moreover, there are several other reasons to use a multiple stage differential pumping system to create an ion beam starting from an atmospheric pressure ionization. The formation of the ion beam in fact depends to a great extent on the ion-gas interaction. As described in section 2.3.2, page 24 the nozzle-skimmer-fragmentation is needed to create ions that are free of solvents or to produce specific fragments ions. Moreover ion gas collisions in the first quadrupole at a pressure of $10^{-1} - 10^{-2}\,\mathrm{mbar}$ are used to thermalize the beam in order to achieve a narrow energy distribution.

Additional constrains have to be mentioned that are valid for the selection of the pumps and the dimensioning of the pumping stages. An aperture connecting two consecutive pumping stages generates a gas load q_{in} in the downstream chamber proportional to the conductivity of the aperture L and the pressure difference: $q_{\mathrm{in}} = L(p_1 - p_2)$. This gas load is pumped by the turbopump (pumping speed S) that maintains the lower pressure p_2. In the static case the gas load flowing out $q_{\mathrm{out}} = Sp_2$ equals the inflowing gas load q_{in} and since a pressure difference of several orders in magnitude is needed, also $p_1 \gg p_2$ is given. Then the pumping speed necessary to reach the pressure difference is

$$S = L\frac{p_1}{p_2} \quad . \tag{3.1}$$

An aperture of $2\,\mathrm{mm}$ in diameter has a gas conductivity of approximately $L = 1\,\frac{\mathrm{l}}{\mathrm{s}}$. Equation (3.1) thus implies that the pumping speed approximately equals the pressure ratio that can be achieved by this combination of pump and aperture.

This rule of thumb applies very well for pressures lower than $10^{-3}\,\mathrm{mbar}$. In three pumping stages with small turbopumps of $100\,\frac{\mathrm{l}}{\mathrm{s}}$ thus 6 orders of magnitude in pressure are gained. Starting at $10^{-3}\,\mathrm{mbar}$, which is obtained in the Q2 chamber $10^{-9}\,\mathrm{mbar}$ can be reached. Considering that turbo pumps lower their pumping speed when they reach the limit of their compression ratio, either three pumps with a pumping speed much higher than $100\,\frac{\mathrm{l}}{\mathrm{s}}$ or a fourth pumping stage are necessary.

Finally, the use of an UHV-STM as in-situ analytical technique requires two contradictory conditions. On the one hand, the vacuum-pumps of the UHV deposition stage of the ion beam source cannot be switched off if the UHV pressure has to be maintained. On the other hand, as few vibrational sources as possible should run during STM measurements to ensure low disturbance and thus high resolution of the microscope.

The vacuum system sketched in figure 3.4 is designed to deal with all the mentioned conditions and to supply UHV for the ion beam deposition. It consists of two parts: the ion beam deposition part and the STM part, which rest on separate decoupled frames and are separated by flexible vacuum pipes.

The STM part itself is separated internally into a preparation chamber (PREP) and the actual STM chamber, which also rest on separate frames and are decoupled using corrugated, flexible tubes (bellows). The STM is pumped with

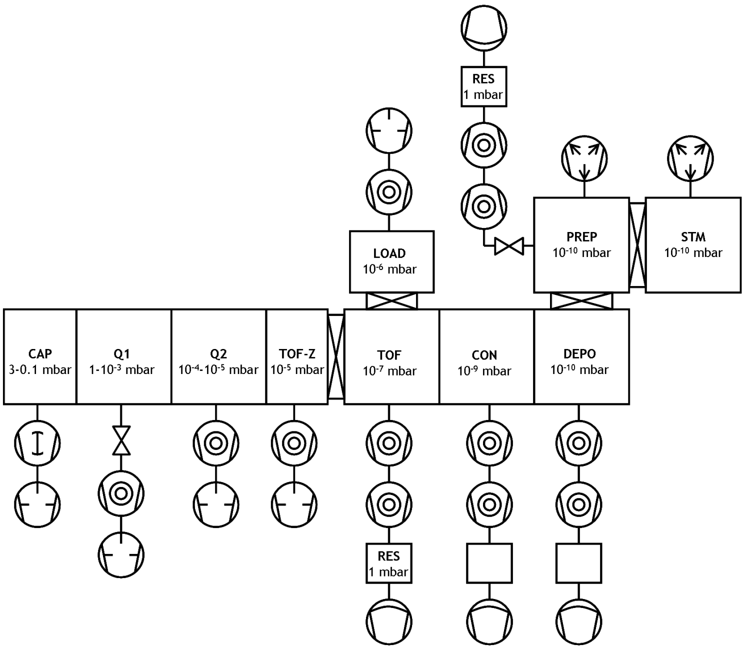

Figure 3.4 – Vacuum system of the ion beam deposition setup. The STM, PREP and the DEPO chambers are kept at ultra high vacuum. The ion beam deposition source is differentially pumped through the chambers CAP, Q1, Q2, TOF-Z, TOF, CON down to $10^{-10}\,\mathrm{mbar}$ at DEPO.

a vibration free ion getter pump only (*Varian Starcell*). The preparation chamber can be pumped via a turbopump (*Leybold TurboVac 340M*) or an ion-getter pump (*Varian Starcell*) as well. When measuring STM, only the ion-getter pump is running.

The ion beam deposition part is separated into six pumping stages which are all, except the first, evacuated by turbo molecular pumps. The system is controlled by a specially designed control computer to synchronously switch on, shut down or vent the coupled chambers. Additionally, it provides power fail, emergency shutdown and restart procedures whose handling become increasingly complicated, if many vacuum chambers are coupled.

The interconnected differential pumping stages require high pumping speeds in order to reach the pressure needed for each pumping stage with the corresponding ion optics. Especially the first pumping stage has a high gas load and is thus evacuated by a roots blower (*Balzers Pfeiffer WKP500A*). Permanent running of these big pumps, which is not only a noise but also a maintenance issue, is avoided by separating the ion beam source between the third and the fourth pumping stage. A gate valve at this position can be closed and the first three stages can be switched off. The last three high vacuum stages are permanently pumped to sustain the UHV. The high compression ratio needed is achieved using two stages of turbopumps, a combination of Leybold (*Ley-*

bold TurboVac 340M) and *Pfeiffer TMU 071P* which are backed by a vacuum reservoir. The reservoir ($0.1 - 10\,\mathrm{mbar}$) is pumped by a membrane pump. Its pressure is monitored through the power consumption of the connected turbopump. A too high value triggers the pumping of the reservoir, which thus occurs only when necessary. This reduces vibrations and maintenance of the membrane pumps, since they run only once a week for a few minutes.

Since the ion gas collisions in the first two pumping stages are very important processes in the creation of the ion beam and depend strongly on the pressure, valves are introduced between these chambers and their pumps to adjust the pumping speed by changing the cross section of the pipe. The pressure in the first pumping stage is variable between $0.1\,\mathrm{mbar}$ and $3\,\mathrm{mbar}$ and in the Q1 chamber pressures between $1\,\mathrm{mbar}$ and $10^{-3}\,\mathrm{mbar}$ can be set. Typically the CAP chamber is operated at $1.4\,\mathrm{mbar}$ and the Q1 chamber at $2{\times}10^{-2}\,\mathrm{mbar}$. Such an adjustment also has an effect on the downstream chambers, but due to the high number of pumping stages it is only observed up to the fourth pumping stage.

3.1.4 Current Measurement

The current of an ion beam is an electrical current but at the same time it represents a mass flux of molecular or cluster ions. In contrast to a mass current, an electrical current can be measured very precisely by relatively simple means with an ampmeter. Therefore, current measurements are the main tool for monitoring and adjusting the ion beam source.

Since the current of a typical electrospray ion beam is very low, electrometers (Keithley 616) that can detect currents as low as $0.1\,\mathrm{pA}$ are used. When an ion beam hits a conductive plate inside the vacuum chamber, an according electron current is generated in a wire connecting to a electrode. Mechanisms which lead to a current flow involve the neutralization of the particles or the creation of mirror charges[106]. Besides these effects, other processes can lead to errors in the current measurement, such as secondary electron or secondary ion emission. However, in the low hyperthermal energy range where soft landing takes place, these processes only play a minor role.

During an experiment currents are measured at various electrodes. For the nanospray source the first monitored current is the spray current flowing into the needle. For the pneumatically assisted source this is not possible since the needle is grounded but it is also not necessary since this source provides a much more stable current over a long time in respect to the nanospray source.

Following the ion beam on its way to the deposition target, the current can then be measured at the skimmer, at the apertures between the pumping stages and on the sample holders and current detector in the HV and UHV chambers. In table 3.1 the current measurement points are summarized.

The sample holders contain spatially resolved detectors with retreading grid

Electrode	**Chamber**	**Purpose** (alignment / monitoring)	**Typical Current** (pA)
spray needle	air	(monitoring)	$0.1 - 50\,\mathrm{nA}$
skimmer	CAP-Q1	(monitoring)	$100 - 1000\,\mathrm{pA}$
Q1-Q2 aperture	Q1-Q2	alignment	$20 - 200\,\mathrm{pA}$
LB aperture	Q2-TOF	monitoring	$5 - 150\,\mathrm{pA}$
HV sample holder	TOF	monitoring	$1 - 100\,\mathrm{pA}$
LE aperture	TOF-CON	monitoring	$1 - 50\,\mathrm{pA}$
CON detector	CON	alignment	$1 - 20\,\mathrm{pA}$
LG aperture	CON-DEPO	monitoring	$1 - 15\,\mathrm{pA}$
DEPO detector	DEPO	alignment	$1 - 10\,\mathrm{pA}$
UHV sample holder	DEPO	monitoring	$1 - 10\,\mathrm{pA}$

Table 3.1 – Electrodes used for current measurements. Some electrodes are always monitored, others sometimes and several are only used when the source parameters are adjusted. The current given for the apertures refers to the net current, which consists of the current from ion hitting the aperture and ions that pass it.

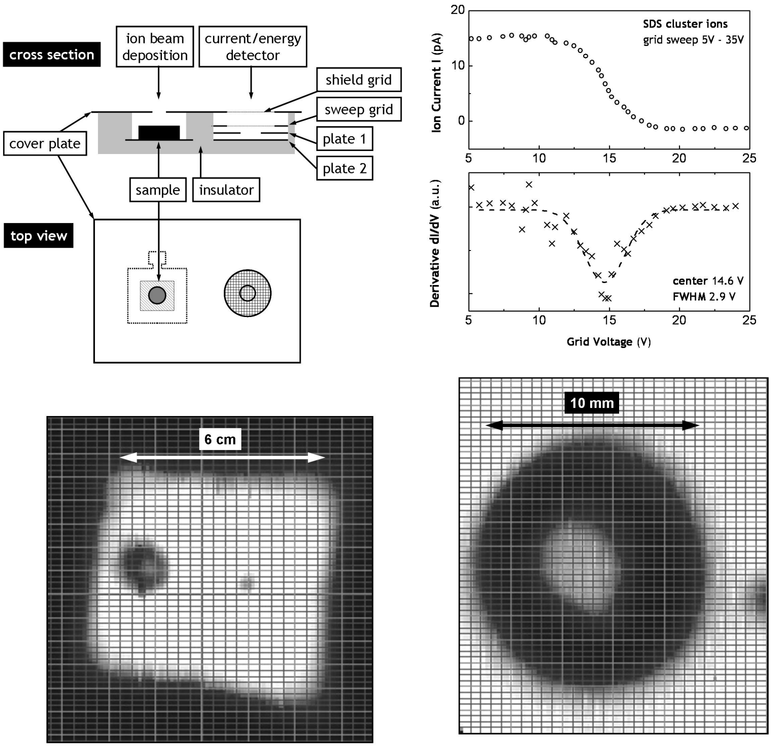

Figure 3.5 – **[top left]** Scheme of a retarding grid energy analyzer and sample holder **[top right]** Kinetic energy distribution measurements: detector current (plate 1 and 2) as function of the grid voltage and corresponding first derivative. **[bottom left]** Current image of the cover plate ($6\,\mathrm{cm}\times 6\,\mathrm{cm}$). Bright regions indicate a high current measured on the plate. **[bottom right]** Magnification of the spacial resolving current detector imaged with cytochrome c protein ions with $250\,\mu\mathrm{m}$ beam spot size.

energy analyzers (TOF chamber only) in order to determine the shape and the kinetic energy of the ion beam. Figure 3.5 shows a scheme of such a device. Two grids ($0.5\,\mathrm{mm}$ pitch, $50\,\mu\mathrm{m}$ tungsten wires) are used to create a linear potential slope with low disturbance to minimize the error in energy measurement to $0.1\,\mathrm{eV}$ per charge[115]. The voltage is applied at the inner grid and swept using the *ESI-control software* (section 3.1.8, page 50). The absolute value of the first derivative of the current as a function of the grid voltage corresponds to the kinetic energy distribution of the ion beam.

The spacial detector consists of two concentric round plates, one ring shaped (plate 1) and one disk (plate 2). They are placed behind the grids. The topmost plate 1 thus lets the current pass through the hole that hits plate 2. If the ion beam hits the center of this current detector, a current is measured on both plates. The finer the focus is, the higher a current is found on plate 2.

By simultaneous scanning the voltages applied to the x and y steering plates, such a focused ion beam can be scanned across the sample holder/current detector electrodes. The current at the electrodes displayed as a function of the steering plate voltage results in ion beam images, as displayed in figure 3.5 [bottom]. Since the geometry of the electrode is known, the result gives an indication about the focusing of the beam. This technique is also used to adjust the beam on the sample or feed it through an aperture. Figure 3.5 [bottom left] shows the ion beam image of the complete sample holder. The current is measured at the front plate and the detector plate 2, which appear bright. Dark in contrast is the deposition spot (left) and the donut shaped plate 1 (right). In order to demonstrate the resolution, which can be reached with a focused and very low energy ion beam, the current detector is magnified. Plate 1 (light, middle), plate 2 (dark) and the cover plate (light, outside) are clearly distinguished by sharp edges of less than $0.5\,\mathrm{mm}$ width, which is the size of the focal spot.

3.1.5 Orthogonal Extraction Linear TOF Mass Spectrometer

The linear time-of-flight mass spectrometer is placed in the forth pumping stage of the ion beam source and thus operates at a pressure of $10^{-7}\,\mathrm{mbar}$. It is mounted onto a vertical manipulator with a travel of $20\,\mathrm{cm}$ by which the spectrometer can be moved into the beam axis for mass spectrometric measurements. When other experiments are performed, the spectrometer is moved upwards and the ion beam axis in the TOF chamber is free. This enables the use of the HV sample holder or to let the beam cross the TOF chamber.

Figure 3.6 shows a sketch of the time-of-flight mass spectrometer which creates a potential landscape as displayed and discussed in section 2.2, page 20. The TOF is mounted between a base and a top plate and is surrounded by a shield to prevent the field from spreading into the chamber, where it could disturb the ion path. Its lower part is constructed of a number of stainless

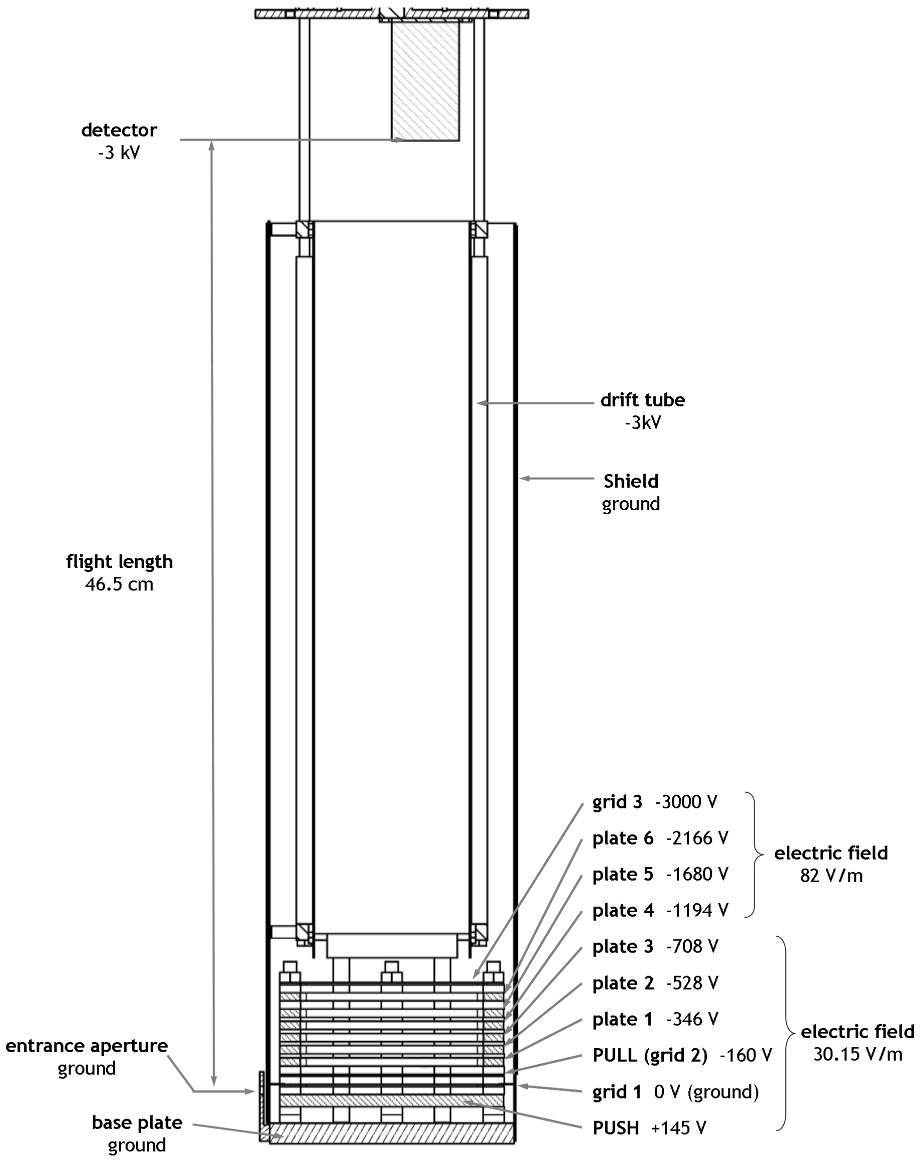

Figure 3.6 – Scheme of the time-of-flight mass spectrometer cut across the beam axis and along the drift tube.

steel plates shaped like rectangular frames, which create a linear acceleration potential when the appropriate voltages are applied. The drift tube and the detector constitute the middle and upper parts.

The acceleration region consists of the push and pull plates which are separated from each other by the grid 1 which is at ground potential, by the plates 1 to 6 and by the grid 3. Push and pull are pulsed in order to extract the ion beam from the extraction into the acceleration region. Constant voltages are applied to the frame plates 1 to 6 and to the the grid 3, which is the next electrode along the TOF axis. The voltages given in figure 3.6 rise from $-300\,\mathrm{V}$ for P1 to $-3\,\mathrm{kV}$ for grid 3. The successive drift tube and the detector (*ETP, fast dynode detector 14480*) are at the same potential.

The TOF-MS measurement is controlled by a time-to-digital-converter (TDC) card which initiates a cycle and collects the data (TOF-1 TDC, *Blue Sky Electronics*, Houston, Texas, USA). The start pulse for a flight time measurement cycle is sent from the TDC card to a delay generator (PCI delay generators BME G03), which generates two synchronous pulses of $75\,\mu\mathrm{s}$ length and $\pm 2.5\,\mathrm{V}$ amplitude. These pulses trigger high voltage switches (*Behlke HTS*) that apply the voltage to the push ($+145\,\mathrm{V}$) and pull ($-160\,\mathrm{V}$) electrodes within a rise time of $5\,\mathrm{ns}$.

During the $75\,\mu\mathrm{s}$ in which the high voltages are applied to the push and pull electrodes an electric field is generated in the extraction volume between grid 1 and the push plate that starts the ions motion towards the detector. Further accelerated, the ions eventually reach the detector, which thereby produces a current pulse upon each impact event. The current pulse is amplified and discriminated (F-100 amplifier/discriminator*Advanced Research Instruments Corp.*, Boulder, Colorado, USA) and the resulting signal (TTL standard) is sent to the TDC card for recording. Each complete cycle has a length of $131\,\mu\mathrm{s}$, what corresponds to a repetition rate of $7.6\,\mathrm{kHz}$. The data from the preamplifier is integrated by the TDC card's on-board histogramming memory with a resolution of $1\,\mathrm{ns}$. The card is read by the TOF software after the spectrum has been collected for a given time, which typically amounts to a few seconds.

3.1.6 Deposition Setup

The final step in the ion beam deposition experiment is the actual deposition onto a sample put in a holder in the TOF chamber at $10^{-7}\,\mathrm{mbar}$ or in the UHV sample holder at $10^{-10}\,\mathrm{mbar}$.

Both sample holders, which are constructed in a similar way, are displayed in figure 3.7. The sample is placed behind the opening of an aperture with a diameter of $4\,\mathrm{mm}$. The aperture and the sample itself are electrically connected by separate wires, so that a current flowing due to incident ions can be measured as described in section 3.1.4, page 42. At the same time a voltage can be applied to the sample in order to adjust the collision energy of the ion beam.

The sample holder in the HV chamber serves multiple purposes. Its use

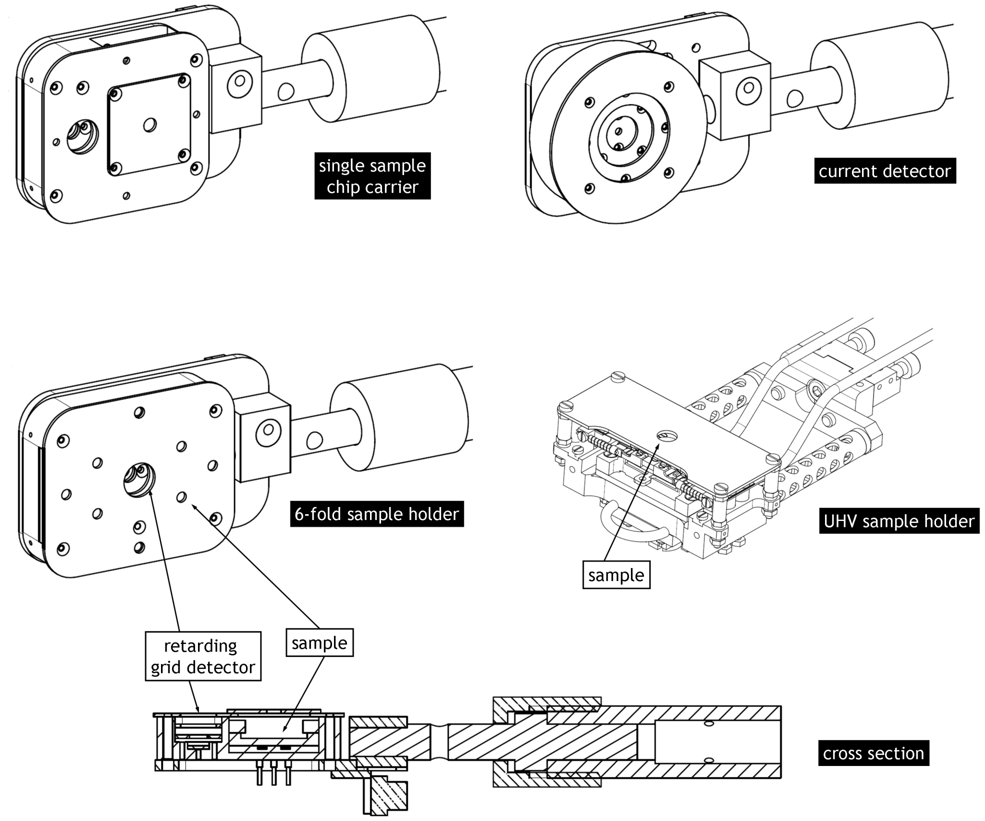

Figure 3.7 – Schemes of the different sample holders used in the deposition setup in high- and ultrahigh vacuum. **[bottom]** Cross section of the single sample holder.

for the detection of the beam energy and spacial distribution is described in section 3.1.4, page 42. Three different kinds of sample holders can be mounted in the loadlock and transferred into the beam axis for deposition: a sample holder containing a single sample on an *Omicron*-type base plate, a sample holder containing a sample in a chip carrier and a six-fold sample holder.

The UHV sample holder is mounted on a manipulator at the DEPO chamber which allows the exchange of samples between the STM preparation chamber and the ion beam deposition chamber. The sample can be cooled and heated within a range of $100 - 1000\,\mathrm{K}$. This is done with a specially developed sample holder based on the *Omicron* design that contains an electron bombardment heating stage and an integrated thermocouple for temperature measurements.

3.1.7 Power Supplies

Electrostatic lenses and quadrupole ion guides are used for the guiding of the ion beam (section 3.1.2, page 38). The characteristics of the power supplies like voltage range, maximal load or voltage stability depend on type and geometry of the ion optics used. All power supplies can be controlled with a low voltage signal ($\pm 10\,\mathrm{V}$) and can thus be connected to the *ESIcontrol* computer and be driven by the corresponding software (see section 3.1.8, page 50).

Name	Type	Channels	Voltage	Connected Ion Optics
CGC-RFG10	high power RF generator, $500\,\mathrm{kHz}$, $1\,\mathrm{MHz}$ or $2\,\mathrm{MHz}$	2×2	$0 \ldots 1000\,\mathrm{V}$	quadrupoles Q1 and Q2
HV200	precision DC high voltage generator	2×2	$\pm 100\,\mathrm{V}$	quadrupoles Q1, Q2 $\pm 100\,\mathrm{V}$ bias offset
5kV	HV amplifier	5	$\pm 5000\,\mathrm{V}$	athmospheric interface, TOF-MS
1kV(ABC)	HV amplifier	A:1×3 B: 1×4 C: 1×3	$\pm 1000\,\mathrm{V}$	athmospheric interface, TOF-MS
135V(AB)	HV amplifier	A:1×16 B: 1×8	$\pm 135\,\mathrm{V}$	electrostatic lenses
40V	stab. power supply	1×16	$\pm 40\,\mathrm{V}$	electrostatic lenses and steering plates
20V	stab. power supply	2×16	$\pm 20\,\mathrm{V}$	steering plates
10V	stab. power supply	1×8	$\pm 10\,\mathrm{V}$	control of other power supplies

Table 3.2 – Power supplies used for the electrospray ion beam source.

Table 3.2 summarizes the power supplies and their characteristics used for the ion beam deposition setup. Figure 3.8 shows how the power supplies are connected with the other components of the source.

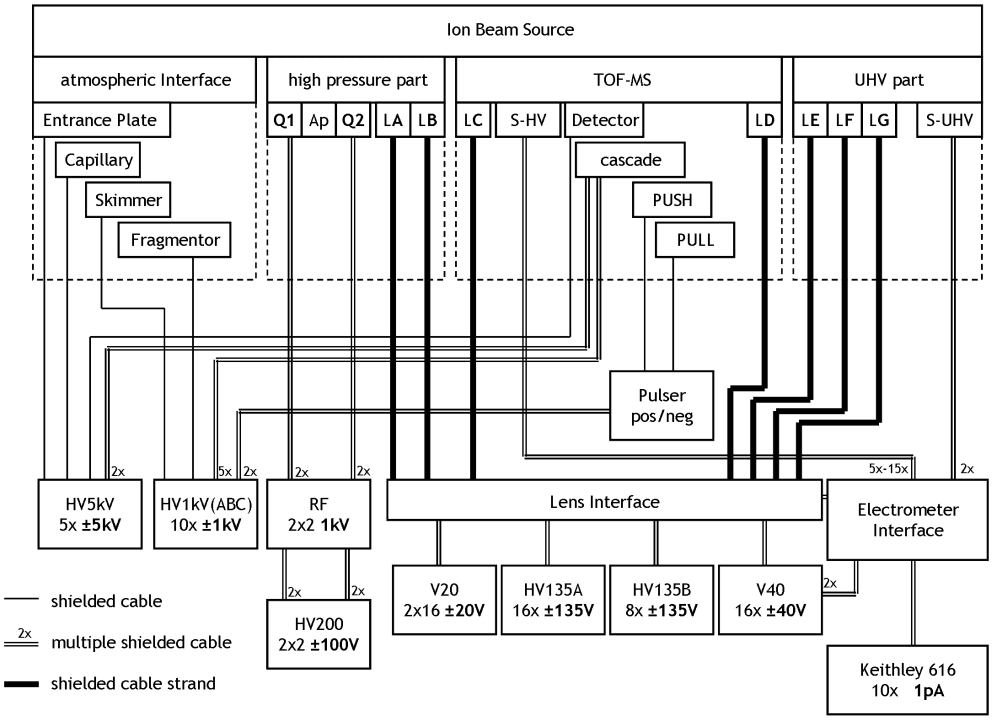

Figure 3.8 – Bloc diagram of the connections between the electrospray ion beam source, interface panels, power supplies and electrometers. S-HV and S-UHV are the high vacuum and ultrahigh vacuum sample holders, respectively.

The connections between the terminals at the source and the appropriate power supplies can become very complex when their number becomes high, especially when rewiring is needed, even if infrequently. To overcome this possible source of errors, an interface is provided in which ion optical elements are grouped. For each lens only one cable strand connects to the interface panel. The wiring of the individual power supplies and ampmeters to the terminals of the lenses is only done via the interface panel using shielded cables (BNC and MHV) in order to minimize crosstalk to the current measurement lines.

3.1.8 Computer System and Software

Software Concept

The setup of a low energy ion beam deposition experiment involves many tasks related to device control, data acquisition and visualization.Due to the vast amount of parameters that need to be set correctly in order to create an ion beam, and the great amount of data gathered, the source is entirely controlled by a computer system. The software for this unique applications is custom made, developed only for the present setup using the LabView programming language (*National Instruments Corp.*).

The key challenge for the software development is to provide tools which allow the control and monitoring of all parameters and all measured data. Special effort was made to achieve an ergonomic handling of a rather abstract object such as an ion beam.

Experimental Control (ESI-control)

The main experimental workstation is running a program to control the experiment (*ESIcontrol v0.47*) and a program to calibrate the output voltage of the power supplies used for the ion beam optics with respect to the $\pm 10\,\mathrm{V}$ input signal (*ESIcalib v1.3*). Both programs are developed in LabView 8 (*National Instruments Corp.*).

The computer contains analog-digital/digital-analog (AD/DA) converter hardware (4x PIO-DA16 DA, 1xA-822PGH, 1xA812PG, 1xA626, *ICP-DAS*) to control the power supplies and to read the current measurements. Altogether this hardware is able to control 72 channels which are used for power supplies and it can read up to 24 channels for current measurements.

The output channels are calibrated with the *ESIcalib* program using a two point linear fit. The resulting calibration data, a calibration factor, an offset voltage and the voltage range is stored (.cal files) and recalled in the *ESIcontrol* program in order to calculate the $\pm 10\,\mathrm{V}$ control signal.

The applied voltages are stored separately from the calibration data (.cal files) and from the wiring information (.chn files) in terminal table files (.ter).

Terminal tables contain the layout and the settings (min./max voltage, applied voltage) of the ion optical system in the source. The wiring file (.chn) contains information on which electrode is connected to which power supply. This means that the settings in the terminal tables can be for different wirings, while the voltages that are applied at the source are the same. In fact, the user does only have to change the wiring information file, when a rewiring had to be done, to use the last terminal table again.

The program further offers tools to conveniently tune and monitor the ion optical system such as voltage sweeps, ion beam imaging (figure 3.5), soft-linking of channels via functions, virtual channels that can be used like variables and quick browsing of the terminal table. All parameters and all obtained data can be stored for further analysis.

Mass Spectrum Acquisition (ESI-TOF)

In order to operate the time-of-flight mass spectrometer (section 3.1.5, page 44) a time-to-digital-converter (TDC) card (Blue Sky Electronics TOF1), a delay generator (Bergmann G03 and G03s) and two software programs are used. One program, *setDelay v0.1* developed in LabView 6 (National Instruments Corp.), runs the delay generator which supplies the trigger signal of the extraction pulse upon the start signal of the TDC card. The pulses length and delay can be set with a precision of less then 1 ns.

The TDC card is operated with a second program (*TOF Acquisition*) developed by *Laboratory of devices and methods of ecological monitoring, Institute for Analytical Instrumentation, Russian Academy of Sciences, St. Petersburg, Russia*. With this program mass spectra can be acquired, calibrated according to equation (2.10) and stored. For later use the data is stored as raw time-of-flight and counts data and can be further analyzed using a calibration programm (*MSC v1.0*) developed by using Java JDK6 (*Sun Microsystems*).

Vacuum Monitoring (ESI-VacSys)

Two computers are used to monitor and store relevant parameters of the vacuum system (see section 3.1.3, page 39). The program *ESIPressure v0.7* has been developed using LabView 6.0i (National Instruments Corp.). It reads the vacuum gauge controllers (12 channels Pfeiffer Activeline, 9 channels Pfeiffer Digiline), displays the pressures over time and stores them if further analysis if necessary. Commercial software for the Pfeiffer Prisma quadrupole mass spectrometer for gas analysis is running on a second computer.

Separate computers are used to avoid the interference of the software applications and their data acquisition hardware components with each other or with the main software for the ion beam source and the time-of-flight mass spectrometer.

3.2 DESIGN AND PERFORMANCE OF THE ION OPTICAL ELEMENTS

Historically, the first devices that manipulated charged particle beams were cathode ray tubes where an electron current is switched by applying a voltage to a grid[116]. Since then the number of devices that operate on charged particle beams has grown enormously. Ion beam devices exist for acceleration , focusing and steering[117], collimation , energy selection or mass dependent deflection[118] and are studied in great detail.

The following section is thus only outlining the fundamental physics of the devices which are utilized in the developed ion beam deposition apparatus. Different applications of quadrupole ion guides are discussed in section 3.2.1, page 52 based on the adiabatic approximation for RF-traps[92]. The design of electrostatic lenses which can be used to guide an ion beam through several pumping stages is reviewed in section 3.2.2, page 56.

3.2.1 Quadrupoles at Different Pressures for Different Purposes

Radio frequency quadrupoles are widely used as mass spectrometer up to a mass-to-charge-ratio of $2000\,\mathrm{Th}$ [119], but they are also used as ion traps [92], ion guides or ion coolers. RF-quadrupoles for ion beam applications have the important feature of trapping ions perpendicularly to the quadrupole axis, while along the axis a flat potential allows them to move freely.

Collimation in a High Pressure Quadrupole Ion Guide

For the ion beam deposition setup presented, two quadrupoles of the same geometry are used, which serve a different purpose that is determined by the operating pressure. Quadrupole Q1 is used at a pressure of $10^{-1} - 10^{-2}\,\mathrm{mbar}$ where the energetic ions, coming from the atmospheric interface, are laterally trapped in the RF-field and thermalized by buffer gas collisions. A potential difference at the exit aperture (Q1Q2Ap) extracts the thermalized ions into high vacuum. From this point no more ion-gas collisions occur. The potential at this point thus is the reference point for the kinetic energy of the ion beam throughout the following high vacuum stages.

Depending on the declustering potential, ions arrive in the quadrupole Q1 with kinetic energies of $0 - 100\,\mathrm{eV}$ that can be derived from the kinetic model for ion gas collisions in section 2.3.2, page 28. The mean free path for the relevant mass-to-charge-ratio range of $50 - 5000\,\mathrm{Th}$ at the typical pressure of $2 \times 10^{-1}\,\mathrm{mbar}$ is $0.5 - 0.005\,\mathrm{mm}$, respectively. The corresponding kinematic factors are in the range between 0.8 and 0.995 (see Equation (2.20)).

For the given values, the number of collisions necessary for thermalization is between 50 for the light particles with the long free path and 5000

for the heavy particles with the short free path. As a consequence, the minimal length of Q1 necessary for the complete thermalization of all mass-to-charge-ratios results to be of $2.5\,\mathrm{cm}$. The RF-amplitude and frequency needed for this quadrupole is estimated to be equivalent to that of the low pressure quadrupole, since the trapping efficiency of a high pressure device is always better than that one of the corresponding low pressure.

Mass Selection in a Low Pressure Quadrupole

Quadrupole Q2 operates in high vacuum ($10^{-4} - 10^{-6}\,\mathrm{mbar}$) and is used for the definition of the desired mass-to-charge-ratio range. In order to determine the design of Q2, the required mass selecting precision, the mass-to-charge-ratio transmission window and the power consumption have to be considered. These three parameters force a trading of the priorities. A quadrupole with very good mass resolution and a big transmission window will need a big trap radius, which will require a high power RF generator[120].

A low mass resolution is enough for the ion beam deposition application since only the cutoff of unwanted ions like solvent clusters or molecule fragments in a certain mass-to-charge-ratio range is required. The quadrupole is not used for mass-spectrometry, because the mass analysis in TOF-MS can be done faster and at higher resolution. A precise mass selection like for tandem MS is simply not needed (see section 3.4.4, page 66). As a consequence the first priority for the design of Q2 is to have a big mass-to-charge-ratio transmission window in order to achieve high deposition currents for different molecules.

The method of the adiabatic approximation can be used to estimate the performance of a RF quadrupoles, or RF ion traps in general[92]. In contrast to stability evaluation of the Mathieu differential equations [82], this method only gives a stability mass-to-charge-ratio range for the trap operated in RF-only mode. Within this range, mass selection can be done by applying a differential DC potential to the quadrupole rods.

In the adiabatic approximation the stability of an ion is estimated by time averaging its displacement and energy gain in the inhomogeneous RF-field. The effect of the RF-field on charged particles is described by an effective potential $\Phi(x)$ that traps the charge carriers and an adiabaticity parameter η which can be used to estimate the ions energy gain by the RF-field[92].

$$\Phi = \frac{x^2}{r_0^2}\frac{V_{\mathrm{RF}}^2}{(2\pi f)^2}\frac{z^2e^2}{m} \tag{3.2}$$

$$\eta = \frac{4}{r_0^2}\frac{V_{\mathrm{RF}}}{(2\pi f)^2}\frac{ze}{m} \tag{3.3}$$

Effective potential and adiabaticity depend on the RF amplitude V_{RF}, the trap radius r_0, the RF frequency f and on the particle mass m and charge ze.

From equation (3.3) the minimal and maximal transmitted mass-to-charge-ratio M_{min} and M_{max} can be derived.

$$M_{\mathrm{max}} = \frac{x^2}{r_0^2} \frac{V_{\mathrm{RF}}^2}{(2\pi f)^2} \frac{ze}{E^{\perp}} \tag{3.4}$$

$$M_{\mathrm{min}} = \frac{4}{r_0^2} \frac{V_{\mathrm{RF}}}{(2\pi f)^2} \frac{1}{0.3} \tag{3.5}$$

For a given ion (m, z) to be stable in the RF-field two conditions need to be fulfilled. First, the effective potential needs to be larger than $E^{\perp} = kT^{\perp} = \Delta p_{\perp}^2$, which is the lateral part of the ion beam kinetic energy (section 2.3.1, page 24). Otherwise the particle overcomes the trapping barrier and leaves the quadrupole. The effective potential is evaluated at the relative trap radius $x = r/r_0 = 0.8$. This value is commonly accepted to provide the limit for stable trajectories. Ions that move further away from the trap center, gain more energy in the RF-field due to increased field inhomogeneities, which will cause them to leave the trapping potential well.

Second, the adiabaticity needs to be smaller than 0.3. This parameter is related to the heating of the ion beam, the energy gain of the particle in the RF field. For values higher than 0.3 the kinetic energy of the particles rises during its presence in the RF-field, until the perpendicular part is eventually higher than the trapping potential and the trapping is lost.

The expressions for the minimal and maximal transmitted mass-to-charge-ratio equation (3.5) can be used to determine the parameters of the quadrupole Q2. The main parameters are RF-voltage range, frequency and trapping radius. To guarantee transmission of all incoming ions, the trap radius should be equal to the beam diameter, which is defined by the apertures in the ion optics. Large traps transmit light ions preferably and have a high power consumption, small traps rather transmit heavy ions but have the disadvantage of a low resolution when used in mass selecting mode.

For a fixed trap radius of $2.5\,\mathrm{mm}$ the mass-to-charge-ratio transmission ranges are calculated and displayed in figure 3.9 for $E^{\perp} = 1\,\mathrm{eV}$ which correspond to measured energy spreads of the ion beam. For the described quadrupole the mass-to-charge-ratio range between $20\,\mathrm{Th}$ and $10^5\,\mathrm{Th}$ is covered with frequencies of $2\,\mathrm{MHz}$, $1\,\mathrm{MHz}$ and $500\,\mathrm{kHz}$, when RF voltages with amplitudes of up to $500\,\mathrm{V}$ are applied.

According to these results, the frequency of the RF-generators is switched depending on the mass-to-charge-ratios relevant for deposition. For example, if particles at $1000\,\mathrm{Th}$ are deposited, the $1\,\mathrm{MHz}$ RF-generator is the appropriate choice in order to minimize the RF-voltages that have to be applied.

The mass selection within the mass-to-charge-ratio range calculated by the adiabatic approximation can be estimated from a stability diagram originating from the Mathieu differential equations. Equation (3.6) gives the relation be-

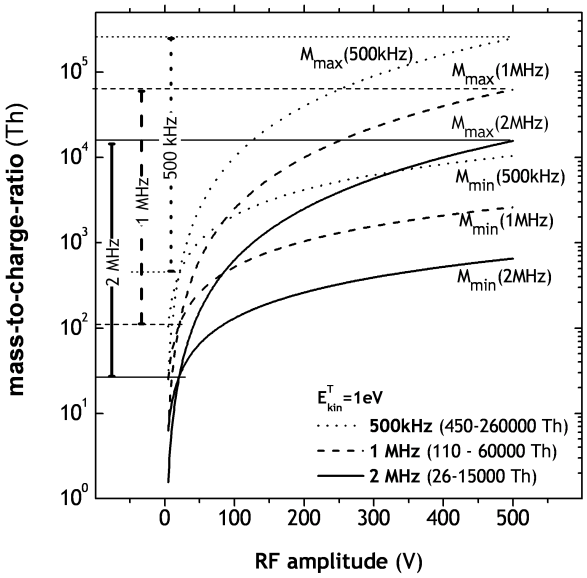

Figure 3.9 – Transmission of Q2, the low pressure quadrupole in RF-only mode calculated by the adiabatic approximation for several frequencies.

tween the RF-amplitude and the differential DC voltage that has to be applied in order to limit the transmission to a certain mass-to-charge-ratio M.

$$U_{\mathrm{DC}} = 0.1678 \cdot V_{\mathrm{RF}} = 0.1678(4.11\times10^{-12} \cdot r_0^2 f^2 M) \qquad (3.6)$$

In contrast to the adiabatic approximation, this simple estimation does not tell whether the ion with mass-to-charge-ratio M is transmitted, instead it just gives the voltages which have to be applied for a mass selection if the quadrupole is laid out correctly.

The length of Q2 does not show up explicitly in the equations equation (3.5) for the mass selection properties. Since the adiabatic approximation is a time average it is based on the assumption that many oscillation cycles pass while the ion is trapped in the RF-field of the quadrupole. Generally, a minimum of ten cycles is assumed in order to reach stationary conditions. For the lightest and fastest particles to be transmitted at each frequency, this corresponds to a length of $5\,\mathrm{cm}$ at an axial kinetic energy of $10\,\mathrm{eV}$.

With respect to the mass-to-charge-ratio range that has to be achieved, the design requirements of the Q2 quadrupole are similar to Q1. Due to the better trapping and the lower drift velocity and at high pressures, a quadrupole designed as ion guide for low pressure will certainly work at high pressure as well. Thus, in order to simplify the construction and manufacturing of the quadrupoles and their power supplies, both quadrupole ion guides have the same geometry. Finally, the length of $10\,\mathrm{cm}$ has been chosen for both quadrupoles in order to have additional tolerance against pressure changes which affect the mean free path in Q1.

3.2.2 Electrostatic Lenses

Electrostatic lenses are electrodes of a special geometry to which dc-voltages are applied in order to form a potential landscape which focuses an ion beam. There are several types of electrostatic lenses, which typically employ a certain number of concentric ring electrodes of different length, diameter and pitch.

In the present electrospray ion beam deposition source the functions of the electrostatic lenses are to extract the beam from the Q2 quadrupole, to focus the beam through several $2\,\mathrm{mm}$ diameter apertures positioned between the successive pumping stages and finally to focus ions onto the deposition target.

Figure 3.10 shows the geometry and the potential landscape of an Einzel lens together with the trajectories of a parallel ion beam traveling from left to right. The specific design feature of the Einzel lens are the three identical rings of which the outer two are at the same potential. The geometry of the lens is characterized by the diameter of the rings, their thickness and their pitch, other lengths are of minor importance.

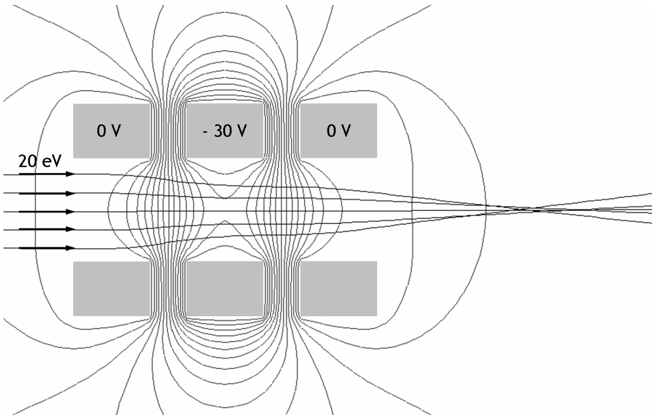

Figure 3.10 – A $20\,\mathrm{eV}$ parallel ion beam focused by an Einzel lens (cross section). Equipotential lines show that areas with a high potential gradient are in the gap between the lens rings. Due to lens errors, the two outer ions are focused more strongly.

Despite its apparent simplicity, the case in figure 3.10 is already so complex that an analytical treatment becomes unrealistic[117]. Nevertheless there also exists simplified analytical treatments that, although not giving reliable qualitative results, can be used to obtain general design paradigms.

Most importantly the focusing is independent of the mass-to-charge-ratio , but depends on the kinetic energy. All incoming ions from one direction with the same velocity are focused in the same point.

In general, the potential gradient created by the electrodes is responsible for the focusing. If it is high, the focus is moving closer to the lens, even inside the lens. As the key parameter of the lens, the potential gradient is a function of the applied voltages and scales with the geometry parameters pitch-to-ring-thickness and inner radius. The scaling of these parameters can be used to compensate for each other's effects. For instance if a bigger inner diameter is necessary, the pitch can be reduced or the voltage can be raised in order to reach the same focus length.

However, for the actual construction of an ion optical system quantitative considerations are inevitable. Numerical simulations are performed in order to optimize the lens performance for the application in the ion beam deposition source. Within this process, the mentioned design paradigms are helpful to reduce the number of iterations. In fact the results in figure 3.10 are obtained by means of numerical simulations as has been done for optimizing all the lenses of the ion beam deposition source.

Simulations with a large number of particles can be performed with *Simion 7*[121] in a rather short space of time. To get useful results it is crucial to find an initial ion distribution in phase space that reflects the real ion beam. If the initial phase space volume is chosen too large, it will be impossible to reach design goals such as a maximal focal spot size, a maximal inner diameter or maximal voltages. The other extreme, a perfectly collimated beam as starting package, will be focused nicely by almost any lens that will most probably not work with a real beam.

As discussed in section 2.1.3, page 17 for an electrospray ion beam source a mass range of $1 - 6000\,\mathrm{Th}$ and a kinetic energy in the range of $1 - 100\,\mathrm{eV}$ per charge is expected, which is used as starting parameters in the simulations. The transversal kinetic energy of the ion beam in the simulations is $1\,\mathrm{eV}$. This value is found both experimentally and in simulations to be the kinetic energy distribution after a thermalized beam is heated by the RF field in the mass selecting quadrupole. The cross section of the perfectly focused beam is set to $2\,\mathrm{mm}$ diameter. This size is given by the vacuum system requirements as size for the aperture (see section 3.1.3, page 39).

Further design parameters include the use of voltages lower than $100\,\mathrm{V}$, a device size in the range of centimeters and a focal spot below one millimeter. The focal length of the lens should be able to be shifted by the voltage settings in the range of $0 - 20\,\mathrm{cm}$. The final design, which shows to fulfill the required performance and is used for the ion beam source, is summarized in table 3.3.

3.3 SAMPLE PREPARATION and EXPERIMENTAL PROCEDURES

Throughout an ion beam deposition or mass spectrometry experiment many protocols are executed, several of them are repeated many times in almost

Geometry	
ring, inner diameter	$12\,\mathrm{mm}$
ring, length	$10\,\mathrm{mm}$
ring-steering plate, distance	$3\,\mathrm{mm}$
steering plate, length	$10\,\mathrm{mm}$
steering plate, inner diameter	$12\,\mathrm{mm}$
aperture, inner diameter	$12\,\mathrm{mm}$
aperture, hole diameter	$2\,\mathrm{mm}$
aperture, length	$8\,\mathrm{mm}$
ring-aperture, distance	$2\,\mathrm{mm}$
shield diameter,	$12\,\mathrm{mm}$
shield distance,	$2\,\mathrm{mm}$
Performance	
focal spot diameter $(1000\,\mathrm{Th},\ 20\,\mathrm{eV})$	$0.7\,\mathrm{mm}$
voltage needed	$60\,\mathrm{V},\ 20\,\mathrm{V}$
position of focal spot from lens shield	$0 - 120\,\mathrm{mm}$

Table 3.3 – Design parameters of the optimized electrostatic lens used in the ion beam deposition source.

every experiment. Often the success and reproducibility of the measurement depends on the accurate reproduction of various procedures.

These most important processes are collected in this section. The preparation of mass spectrometry samples (section 3.3.1, page 58) and solid substrates for deposition (section 3.3.2, page 59) needs to be done before the experiments. The first step after the start of the apparatus is the adjustment of the beam (section 3.3.3, page 60). After this, a mass spectrometry (section 3.3.4, page 61) or deposition experiment (section 3.3.5, page 63) takes place.

3.3.1 Solutions for Electrospray Ionization

In the preparation of samples for electrospray ionization there is not much difference between solutions for deposition or for mass spectrometry, besides the fact that mass spectrometry samples can be more diluted since a high current is not needed. The samples are prepared by dissolving or diluting a substance in a solvent.

Typical solvents used for electrospray are water, methanol (MeOH), ethanol (EtOH) and acetonitril (MeCN). Less typical are diethylether, dichlormethane (DCM), tricholormethane, acetone or tetrahydrofurane (THF).

Often samples are acidified in positive electrospray mode in order to raise the concentration of charge carriers in solution and thus the current. For acidification, formic acid (HCOOH) or acetic acid ($\mathrm{CH_3COOH}$) are used. Typically amounts of $0.1\,\%\mathrm{vol}$ up to $2.0\,\%\mathrm{vol}$ acid are added to the original solution.

Concentrations for mass spectrometry experiments range up to $1\,\frac{\mu\mathrm{mol}}{\mathrm{ml}}$, the lower limit being only set by the detection limit of the mass spectrometer. For deposition experiments higher concentrated solutions are used. Depending on the substance a concentration up to $0.1\,\frac{\mathrm{mmol}}{\mathrm{ml}}$ is used, whereas $10\,\frac{\mu\mathrm{mol}}{\mathrm{ml}}$ is the typical value.

Besides an increased current, very high concentrations have a few major disadvantages. Since a deposition experiment lasts several hours, the source gets heavily contaminated. Moreover, the risk of needle clogging is very high and a large amount of clusters can be formed (see section 4.1, page 68). Finally, substances are often very expensive so that the gain in current is heavily paid, since the current is only proportional to the square root of concentration and flow rate[67].

Liquid samples are prepared differently for the pneumatically assisted orthogonal source and for the nanospray source (see section 3.1.1, page 36). The amount of liquid needed for an hour of spray is $1 - 5\,\mathrm{ml}$ for the orthogonal source and $50 - 200\,\mu\mathrm{l}$ for the nanospray source. Due to the low amount of liquid the nanospray samples are very efficient but also very responsive to contamination, since already a small amount of material can result in a high concentration in solution. The orthogonal spray source on the other hand has advantages in the handling of the liquid sample and the stability of the spray. The large amount of prepared sample, milliliters are common, is dosed from a syringe. The larger volume-to-surface ratio of the milliliter sample also reduces eventual contaminations.

3.3.2 Deposition Substrates

Substrate holders as introduced in section 3.1.6, page 46 are used for the deposition in high vacuum. The dimensions of the samples that can be held are $12\,\mathrm{mm} \times 12\,\mathrm{mm} \times 3\,\mathrm{mm}$ for the single sample holder and $6\,\mathrm{mm} \times 6\,\mathrm{mm} \times 1\,\mathrm{mm}$ for the six-fold sample holder.

Generally, in order to avoid the buildup of charge at the surface of a substrate used in an ion beam deposition experiment, the material should be conductive. Otherwise Coulomb repulsion effect of the deposited charges with the incoming beam are the consequence. However, for currents in the range of $10\,\mathrm{pA}$, a voltage of only $0.1\,\mathrm{V}$ volts builds up for a resistance to ground of $\approx 10\,\mathrm{G\Omega}$. Such a resistance for instance is typical for a silicon sample with a native oxide, as widely used for ion beam depositions within this work. In general, the sample needs to show only very little conductivity.

Silicon with native oxide, silicon with a top layer of $200\,\mathrm{nm}$ silicon oxide ($\mathrm{SiO_x}$) and highly oriented pyrolytic graphite (HOPG) are used as substrates. Note that these are the abbreviations for the substrates used further throughout the text. Since the bulk material does not play a role in low hyperthermal ion-surface interactions, the silicon and silicon oxide samples are both referred to as $\mathrm{SiO_x}$ surfaces (section 2.3.3, page 31).

The silicon and silicon oxide samples are cut out of a wafer using tweezers and a diamond tip pen. HOPG was ordered from *Anfatec Instruments AG* (Oelsnitz, Germany) in the dimensions $5\,\mathrm{mm} \times 5\,\mathrm{mm} \times 1\,\mathrm{mm}$ which is suitable for both sample holders.

The samples are cleaned and glued to a stainless steel plate using conductive silver particle glue before they are mounted in the sample holder. The HOPG surface is cleaned by stripping the top layer with adhesive tape. The silicon samples are sonicated and rinsed in acetone, isopropanol and ultrapure water (*Millipore*) in this order, blown dry with nitrogen and dried for an hour in an oven at $100\,^{\circ}\mathrm{C}$. After the samples are mounted in the sample holder, the holder itself is placed in the loadlock and the pumps are started.

All three substrate types can be used for AFM analysis since they are all characterized by a flat surface (section 3.4.1, page 64). Additionally, HOPG exhibits a large number of very flat terraces with $0.2\,\mathrm{nm}$ high step edges which correspond to single carbon sheets. Si and $\mathrm{SiO_x}$ show flat surfaces with a roughness normally of under $0.5\,\mathrm{nm}$.

An especially non conductive surface is needed for the fluorescence spectrometry experiments in order to avoid the quenching of the luminescence. For this purpose the $200\,\mathrm{nm}$ $\mathrm{SiO_x}$ layers on silicon are used. For the secondary ion mass spectrometry analysis no special surfaces are needed. Their only requirement is that they are as clean as possible which makes the detection of small amounts of material especially in static SIMS mode much easier.

3.3.3 Beam Preparation

The *ESI-control* software can store the entire state of the ion beam source and of the TOF-MS. By recalling such a list of settings for another measurement, the ion beam conditions can be reproduced with good reliability. Normally, for a time-of-flight mass spectrometry or deposition experiment, only fine adjustments have to be done when a stored setting is used.

To define an ion beam ex-novo from a blank set of voltages becomes only necessary after a very long time to correct apparatus drifts, when major changes have been made on the apparatus or when a particular parameter is suspected to be far from optimal. In a parameter space of about 60 variables a global optimum is very hard to be identified.

Nevertheless, some parameters play a more important role than others, or have a specific function. For example the kinetic energy is defined by the potential gradient at the Q1Q2Ap aperture, thus the difference between the voltages Q1-DC, Q1Q2Ap and Q2-DC are the key parameters to act on, when the ion beam energy is set.

In general the ion beam is optimized towards properties that are primarily useful for ion beam deposition. Certainly a high current is helpful. The spread of the kinetic energy has to be narrow, while the absolute value of E_{kin} is of minor importance, because it can be set by the sample voltage. A beam with a low energy spread can be collimated nicely, which helps to achieve a high coverage. Generally such an ion beam is easier to handle than a very disperse beam. The composition of the beam needs to have a low amount of contamination and unwanted fragments. Finally, it has to be made sure that no solvent droplets are in the beam.

The algorithm for the optimization of the ion beam is an iteration of tuning subsequent ion optical elements downstream the optical axis of the deposition setup starting at the spray needle. During this procedure the current is always measured at the next possible electrode with respect to the ion optical element which is optimized.

First, the current is measured at the skimmer and the voltages of the capillary/entrace plate and of the fragmentor are optimized to reach a high but stable current for a duration of at least $15\,\mathrm{min}$. The next current measurement is done on the aperture between Q1 and Q2 (Q1Q2App). The parameters to be optimized are the voltage at the skimmer, the Q1-RF voltage and the Q1-DC voltage. To avoid that ions pass the aperture without being detected, the Q2-DC voltage is set to a high positive value during this optimization step. Later Q2-DC is set so to let pass as many ions as possible. The next current measurement point is the aperture of lens LB while Q2-RF, Q2-DC and the lens LA are optimized.

This procedure is further continued for the lenses and the sample holder in the HV-part, until a current of appropriate magnitude is measured at the desired deposition or mass spectrometry position. The whole optimization from the needle to the last lens can be repeated several times. After the current is optimized, a mass spectrum (section 3.3.4, page 61) is taken and the kinetic energy is measured (section 3.1.4, page 42).

Even though the parameter space of the ion beam source is very big and all parameters affect all ion beam properties, some components can be identified that have a major effect on a certain property. Obviously, the Q2 quadrupole can be used to set the mass range, the lenses can be used to adjust the focusing and the steering plates to move this focus perpendicular to the beam axis. The fragmentor voltage can be used to create fragments.

Finally it is noticed that the ion beam energy is defined at the point where the ions are extracted from the thermalization in Q1. Since the pressure changes non abruptly at the aperture Q1Q2Ap, the number of collisions is reduced throughout a certain flight length, which causes some energy loss. Therefore the potential gradient in this area is proportional, but not equal, to the kinetic energy of the ion beam. However, for energy dependent depositions, it is typically a better choice to adjust the kinetic energy at the sample holder, by applying a deceleration voltage.

3.3.4 Mass Spectrometry Experiments

Once an optimized beam has been obtained, mass spectrometry experiments can be performed. The mass spectrometer is moved into the beam axis. For a first alignment of beam and spectrometer the analyte solution is exchanged against a calibration solution, usually CsI (see section 4.1.2, page 71).

The first step is the alignment of the mass spectrometer. The steering plates of lens C (LC-S) are set to a volatge 0 V in both directions and the height of the MS is set, using the vertical manipulator, to the value that results in the highest net current at the mass spectrometer detector. Then the steering plate voltages and the focusing is varied in order to obtain an even higher current. These steps are repeated until variations in the height, the steering plate voltage or the focusing can not further raise the current in the TOF.

Additionally, it has to be made sure that the form of the peaks in the mass spectra is symmetric. An asymmetric peak shows that either the mass spectrometer is misaligned or the detector is saturated. These two cases can be easily distinguished from each other. When the beam enters the extraction volume non parallel to the push plate, the peaks of all mass-to-charge-ratio show a shoulder on one side.

On the other hand, a saturated detector is indicated by a strongly suppressed intensity for flight times just higher as the peak value. An intense peak in the mass spectrum is related to frequent detector events at this flight time. After an event a dynode detector in general is not capable to record another one for a certain dead time of 50 ns. For very intense ion beams each TOF detection cycle might generate even more than one event at a certain flight time, causing a dead time always at the same position in the mass spectrum, which results in the characteristic form of the saturated peak. The other less intense peaks typically appear symmetric.

In case of a misaligned spectrometer the height or the voltages have to be altered to improve the resolution. A saturated detector is in principle no problem for following measurements, as long as the affected peaks are not used for calibration.

After the alignment a calibration spectrum is taken, which is used for a preliminary calibration using only two identified peaks (see section 2.2.4, page 22). Thereafter, the actual measurements can be performed. After the measurements or if long measurements last for more than a one hour, it is necessary to repeat the calibration in order to correct a possible drift in the calibration constants. If necessary, the spectra can be calibrated more precisely by fitting all identified peaks, as described in section 4.1.2, page 69.

3.3.5 Deposition Procedure Details

In section 2.3.3 the basics of an ion beam deposition experiments at hyperthermal energies are outlined. Kinetic energy, charge state of the ion, mass of the ion, sample surface condition, ion current and beam temperature are the major parameters of the deposition experiment. Therefore these parameters need to be controlled or measured.

Section 3.3.3 describes how to provide a stable and focused beam of a certain energy and mass-to-charge-ratio range at the deposition target. The composition of this beam is determined by mass spectrometry (see section 3.3.4) before the actual deposition experiment. The desired incidence energy E_{col} is set by the sample voltage U_{sample} once the beam energy is known $E_{\text{col}} = E_{\text{kin}} - |zeU_{\text{sample}}|$), where z is the charge state of the ions in the beam. The geometry of the sample holder and of the retarding grid energy detector are designed in such a way that the spread of the kinetic energy distribution remains constant, when a sample voltage is applied[115].

Once the ion beam is focused and the energy is set, the steering plates are used to move the focal spot on the sample, which starts the deposition. The current I_S at the sample is monitored over time throughout the whole deposition experiment. From I_S and the ion beam properties (charge state z, particle area A_p) the coverage Θ can be derived as a function of the deposition time t.

The total number of deposited particles in a certain time $N = nt$ is calculated from the particle flux $n = \frac{I_S}{ze}$, which clearly depends on the charge state z. The final coverage $\Theta = N\frac{A_p}{A}$ depends on the geometry of the particle (particle area A_p) and on the geometry of the deposition setup (substrate area A):

$$\Theta(I_S, t) = \frac{I_s}{ze}\frac{A_p}{A}t \quad . \tag{3.7}$$

This way of computing the coverage is actually only a rough estimation. Several effects can induce strong deviations from the values obtained from equation (3.7), so that only their order of magnitude is reliable.

Over a deposition area of $10\,\text{mm}^2$ the ion beam can be inhomogeneous, which might result in a big range of different coverage across the sample. This effect can be reduced, if to the voltages applied at the the steering plates a low time dependent voltage offset is added, which for instance creates in a randomized motion of the focal spot across the target. This increases the homogeneity of the sample, but on the other hand increases deposition time (see section 5.3, page 127). Sometimes though, it can be quite convenient to have a gradient in coverage across the sample. This is particulary true for morphological studies with AFM, which can be performed on such a sample for a range of coverages. The single measurements for several coverages are all comparable without any constraint, since all are prepared under the exact same conditions (see section 5.1, page 112).

Further errors in the coverage estimation (equation (3.7)) originate from the fact that not all charges are detected via the electrometer connected to the sample. Charges can also stick to the particle at the surface or be emitted into vacuum, which reduces the measured current(see section 2.3.3, page 31).

3.4 ANALYTICAL TECHNIQUES

In this section those analytical techniques are briefly introduced that have been used besides the mass spectrometer in the ion beam deposition setup. Substrate surfaces which has been used for deposition have been characterized ex-situ concerning morphology, chemical composition and optical properties using atomic force microscopy (AFM), time-of-flight secondary ionization mass spectrometry (TOF-SIMS) and fluorescence microscopy coupled to a confocal microscope. Product ion mass spectrometry in which ions and their corresponding fragments are detected has been employed for detailed mass spectrometric investigations using a quadrupole instrument with a collision cell.

3.4.1 Atomic Force Microscopy (AFM)

Atomic force microscopy (AFM) is a scanning probe microscopy technique which is used to image the topography of a surface with a resolution in the nanometer range. The force between a sharp tip and the substrate is measured and used as input signal in a feedback loop which holds the distance between tip and sample constant and thus records the topography[122].

The AFM used in this study is a commercial ambient condition instrument (Nanoscope IV, Digital Instruments, Vecco), equipped with etched silicon tips. The instrument was used in intermittent contact mode (tapping mode) only. In this mode the cantilever, which holds the tip, is driven by a piezo actuator close to its resonance frequency. The force between tip and surface is measured by the change in oscillation amplitude resulting from a changed resonance frequency upon tip-surface interaction.

The resolution depends strongly on the quality of the tip and therefore varies for different tips. Typically, a lateral resolution in the range of $10 - 100\,\mathrm{nm}$ and a vertical resolution of $0.1 - 0.3\,\mathrm{nm}$ are reached in ambient conditions. This means that even small isolated objects can be detected easily by their height on a flat surface, while two small objects close to each other cannot be distinguished.

The AFM images are analyzed using the Nanoscope software and the WsxM software[123]. To achieve a better contrast, a second order fit is often used to flatten the images.

3.4.2 Confocal Microscopy and Fluorescence Spectroscopy

A confocal microscope (Leica) with a grid spectrometer and a micro-photoluminescence (μPL) spectrometer is used for fluorescence spectroscopy. Both setups illuminate the sample with a focused continuous Ar^+ laser beam at wavelengths of $488\,\mathrm{nm}$ and $514\,\mathrm{nm}$ respectively. The laser spot has a size of approximately $1\,\mu\mathrm{m}^2$.

The light emitted from the focal spot at the surface is transferred to the spectrometer where an appropriate notch filter is used to block the elastically scattered light. The spectrometer employs grids and a CCD camera to acquire the optical spectrum in a range from $480\,\mathrm{nm}$ to $800\,\mathrm{nm}$. The μPL setups are very sensitive to emission from the surface since they employ the confocal microscope geometry in which the light detected is only emitted from the focal spot.

3.4.3 Time-of-Flight Secondary Ion Mass Spectroscopy (TOF-SIMS)

Secondary ion mass spectrometry (SIMS) is a technique to analyze elemental composition of solid samples[124]. The sample surface is sputtered by a primary ion beam. The emitted secondary ions are detected with a mass spectrometer. In the case of TOF-SIMS a time-of-flight mass spectrometer is used, but also quadrupoles or even high energy accelerators with sector magnet mass separators are used as mass spectrometer for SIMS. Measurements are performed in high or ultra high vacuum typically at $10^{-8} - 10^{-10}\,\mathrm{mbar}$.

The TOF-SIMS data presented in this work are taken with a *TOF-SIMS 5* (IonTOF Corp. Muenster, Germany) (see sections 5.3.4 and 5.4.4). This device contains three different ion beam sources for gallium, oxygen and cesium. Oxygen and cesium ion beams of $250 - 2000\,\mathrm{eV}$ kinetic energy are used for sputtering in order to remove material for depth profile measurements. The analytical sputtering is done using the Ga^+ beam at an energy of $15\,\mathrm{keV}$ or $25\,\mathrm{keV}$.

The time-of-flight mass spectrometer can detect either positive or negative ions in a mass range between $0\,\mathrm{Th}$ and $5000\,\mathrm{Th}$. The dynamic range of the device, which is the contrast between the lowest and highest detectable signal, is 10^6 .

The TOF-SIMS can be used for imaging the composition in three dimensions with optimal resolution of $100\,\mathrm{nm}$. For other applications the resolution can be optimized for the mass analysis to a value of 5000 .

In static SIMS mode only the Ga^+ analysis beam of $15\,\mathrm{keV}$ is used to create secondary ions. Then almost no material is sputtered and only the very surface is analyzed. This mode is used to study the surfaces of samples after ion beam deposition. Only positively charged secondary ions are analyzed in order to detect the dye molecules or the chemical signature of the nanoparticles.

3.4.4 Product Ion Mass Spectroscopy (PIMS)

Product ion mass spectrometry (PIMS) is a mode of tandem mass spectrometry, employing two mass selecting devices and a collision cell[33]. From an ion beam a small mass range is selected with the first mass separator. Only the ions of this mass-to-charge-ratio are transmitted into the collision cell, where collision induced dissociation (CID, see section 2.3.2, page 24) is used to create fragment ions, which are analyzed in the second mass separator. For each selected mass-to-charge-ratio , a product ion mass spectrum is recorded for different CID settings like collision energy and collision cell pressure. Therefore, product ion mass spectra give information about the structure of the selected ions and also about their stability.

The tandem mass spectrometer used for the study of Cytochrome c (section 4.1.4, page 79) employs quadrupoles as mass filter and a collision cell (*QStar, Applied Biosystems, Proteomzentrum Tuebingen*). Ions in a mass-to-charge-ratio range up to $1800\,\mathrm{Th}$ can be studied at a resolution of $500 - 1000$ depending on the instrument's setting. The acceleration potential in the collision cell can be varied continuously, while the pressure can be chosen from 3 fixed values in the range of $(10^{-4} - 10^{-5}\,\mathrm{mbar})$.

4

RESULTS and DISCUSSION MASS SPECTROMETRY

Introduction

Successful ion beam deposition depends on the complete control of the properties of the ion beam. This involves the beam composition or in other words control over what is deposited. Several analytical techniques can be used to test the composition of an ion beam. The most direct way is mass spectrometry, from which ion beam deposition experiments derived in the first place[63]. This is also the reason why often it is called *preparative mass spectrometry*[66, 107, 106, 56, 110, 57].

The work presented in this chapter therefore explores how a certain particle can be ionized in the electrospray and transferred into high or ultrahigh vacuum. Therefore large molecular ions, their fragments and contaminations need to be identified. A special focus lies on the behavior of the ions upon collision event. Fragmentation that occurs as a consequence of ion gas interaction can give information about the stability of the used particle.

Under this agenda mass spectrometry experiments on different classes of substances are performed and the composition of the ion beams is studied under varying conditions. Organic and inorganic ionic compounds show to form small ionically bound clusters (section 4.1, page 68). Cluster size and charge state depend on ion gas interaction in the collision cell. Mass spectra of ionic compounds are useful for the calibration of the mass spectrometer. Clusters of multiply charged protein ions show similar properties as the salt clusters.

Different types of large organic molecules are ionized with electrospray ionization and mass spectra show that the molecule can be brought into gas phase (section 4.2, page 82). The molecules show a specific fragmentation pattern upon energetic ion gas collisions. The mass range ($500 - 6000\,\mathrm{u}$) of molecules studied illustrates the wide variety of molecules that can be used in a deposition experiment. Metallo-organic complexes and dye molecules are among the large organic molecules that are demonstrated to be ionizable. Besides, for the monitoring deposition experiments mass spectrometry is used to prove the presence of small amounts of complex organic molecules.

A different class of large organic molecules that are analyzed with mass spectrometry are polymers (section 4.2.3, page 101). The mass of a polymer is determined by the mass of the monomer unit times the length of the polymer. Since polymers are rarely evaporable they are very interesting candidates for ion beam deposition. Experiments show that polymers can be ionized over a wide range of lengths and their charge state can be manipulated with ion-gas collisions.

Proteins besides being natural molecules with a special functionality are inhomogeneous polymers with very high masses (section 4.3, page 105). Mass spectra show typical patterns related to the different charge states of a protein. It can be shown that these patterns also reflect the conformational state of the protein.

4.1 CLUSTERS

4.1.1 Introduction

Charged Clusters: Useful for Calibration, Candidates for Deposition and Probes for Very Low Energy Collision

High concentrations of solvated molecules or ions in solution lead to the formation of charged clusters in electrospray ionization (section 2.1.3, page 17. Small crystals of solvated salt ions are formed in the drying and supersaturated electrospray droplets are emitted as gas phase clusters.[72] Some are charged due to an electric field induced excess of one ion species at the capillary apex. Those cluster ions can be observed in the mass spectrum[125, 79, 78, 126, 80, 48].

Different types of charged clusters created by electrospray ionization are analyzed by TOF-MS (see section 3.1.5, page 44). Clusters of inorganic and organic salts as well as non-covalently bound protein clusters are investigated.

The structure of nanoscale clusters is a field of intense research[113], which makes gas phase salt cluster ions interesting candidates for vacuum deposition and study in an UHV-STM[127, 128, 129].

Moreover, clusters are useful for the calibration of the mass spectrometer since they lead to an easy to identify, periodic arrangement of peaks over a large mass-to-charge-ratio range[75, 76, 130]. Finally, information about physical and chemical properties of the cluster and its components are obtained using background gas collisions as probes with defined energy[131, 132, 133, 81, 134, 135, 136, 137].

Dependencies of the Cluster Abundance on Apparative Parameters

Depending on the experimental conditions, cluster ions can appear in an electrospray ion beam for all types of analyte particles. Many examples have been reported in literature: neutral solvent molecules with H^+ or Na^+ attached[76, 77], ionic bound salt clusters[125], protein clusters[138], acid-base clusters or organic ampholytes form cluster ions[130].

The size and the charge of the cluster depend on various parameters. The settings of the atmospheric interface, the solution used and the properties of the cluster forming substance play major roles.

In general, by acting on the available parameters so as to increase the supersaturation of the cluster forming substance within the sprayed droplets, the cluster abundance increases correspondingly[125]. According to this rule, an increased concentration, a more volatile solvent, a lower solubility, a higher curtain gas temperature or the use of a nanospray source will promote the cluster formation.

In addition, the parameters that control the ion-molecule collisions in the first and second pumping stage have an effect on the cluster abundance. In particular, the potential differences between the fragmentor and the skimmer electrode (declustering potential U_{dec}), skimmer and Q1, as well as that between Q1 and the aperture Q1Q2Ap determine the intensity of the ion gas collisions and therefore influence the final cluster distribution in the ion beam[78]. The possibility to quantify the collision energy of ion gas collisions as described in section 2.3.2, page 28, allows one to study the stability in clusters by the combination of mass spectrometry and CID.

4.1.2 Inorganic Cluster Ion Beams for Calibration

Sodium Chloride Clusters

Sodium chloride (NaCl) is one of the most common salts and of great importance in many areas of nature, science and technology. It consists of singly positively charged sodium ions ($100\,\%$ $^{23}\mathrm{Na}$) and singly negatively charged chloride ions ($75.77\,\%$ $^{35}\mathrm{Cl}$, $24.23\,\%$ $^{37}\mathrm{Cl}$) arranged in a face centered cubic crystal structure. NaCl dissolves very well in water but is also soluble in other solvents [139].

Sodium Chloride solutions can be used to create intense cluster ion beams from the electrospray ion beam source. Singly and doubly charged clusters of mass-to-charge-ratios between $200\,\mathrm{Th}$ and $2000\,\mathrm{Th}$ are usually observed.

For the mass spectrometry experiments solutions of $0.1\,\frac{\mathrm{mg}}{\mathrm{ml}}$ NaCl in a water/ethanol mixture are used, which corresponds to a concentration of $1.7\,\mathrm{mM}$. Electrospraying of these solutions results in mass spectra as displayed in figure 4.1. For the given settings of the ion optical system ($U_{\mathrm{frg}} = 50\,\mathrm{V}$, $V_{\mathrm{Q1}} = 100\,\mathrm{V}$, $V_{\mathrm{Q2}} = 400\,\mathrm{V}$) singly $\mathrm{Na}^+(\mathrm{NaCl})_{\mathrm{n}}$ and doubly $2\mathrm{Na}^{2+}(\mathrm{NaCl})_{\mathrm{n}}$ charged

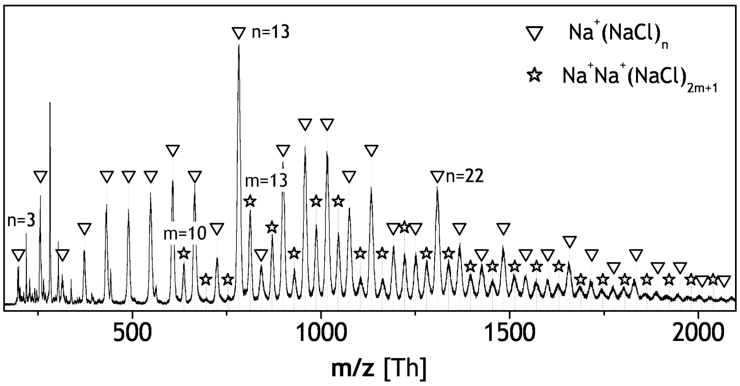

Figure 4.1 – Typical mass spectrum of an ion beam created from a NaCl solution in the nanospray interface. Singly (∇) and doubly ($\star$) charged clusters are abundant over a broad mass-to-charge-ratio range. The highest peak corresponds to the $\mathrm{Na_{14}Cl_{13}}$ ($n = 13$) cluster, which represents a cube of $27 = 3^3$ atoms.

clusters can be identified in the mass spectrum. Since the detected quantity is the mass-to-charge-ratio , the doubly charged clusters appear alone only for odd numbers of n. For an even amount of NaCl units the yield of doubly charged clusters adds to the peak of the half sized singly charged clusters. Therefore doubly charged clusters in the mass spectrum are indexed by the integer m, according to the chemical formula $\mathrm{Na^+Na^+(NaCl)_{2m+1}}$.

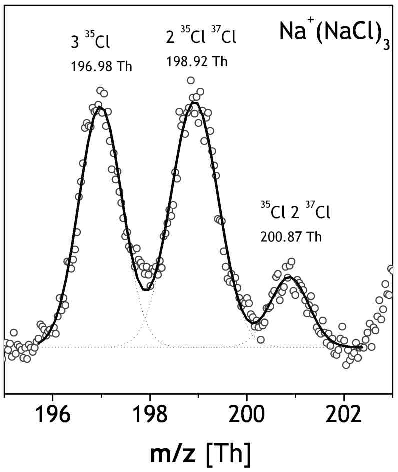

Cluster	**calc.** mass (u) (abund.)	**meas.** mass (u) (abund.)
$\mathrm{Na^+(Na_3\,{}^{35}Cl_3)}$	196.86 (0.435)	196.98 (0.419)
$\mathrm{Na^+(Na_3\,{}^{35}Cl_2\,{}^{37}Cl)}$	198.89 (0.417)	198.92 (0.471)
$\mathrm{Na^+(Na_3\,{}^{35}Cl\,{}^{37}Cl_2)}$	200.92 (0.133)	200.87 (0.110)
$\mathrm{Na^+(Na_3\,{}^{37}Cl_3)}$	202.95 (0.014)	n/a (n/a)

Figure 4.2 – Effect of isotopes in the $\mathrm{Na^+(NaCl)_3}$ cluster peak. The two stable chlorine isotopes $^{35}\mathrm{Cl}$ and $^{37}\mathrm{Cl}$ lead to clusters of four different masses. Three of them with high relative abundances can be identified in the mass spectrum of a NaCl solution. The measured values match with the calculates masses and abundances.

Both types of clusters are used in a calibration fit according to equation (2.10). The calibration procedure using mass spectra of charged clusters is explained in detail for CsI clusters on page 71.

The measured spacing between the singly charged clusters corresponds to the mass of NaCl which is $58.44\,\mathrm{u}$, the average over the different chlorine isotopes. For low masses the isotopic peaks are resolved as displayed in figure 4.2 for the $\mathrm{Na}^+(\mathrm{NaCl})_3$ peak. The calculated values for the cluster masses and abundances obtained from the isotopic distributions of Na and Cl match with the measured values as derived from the calibration fit (see table in figure 4.2).

Clusters of atoms, molecules or ions often show a particular high stability for given number of units. This is because at these particular numbers special geometric or electronic conditions are fulfilled, which result in high binding energy and thus in high stability of the cluster. The number of units is then called magic number[140, 80, 81, 77, 78].

The most abundant peak in the mass spectrum of NaCl clusters is the $n = 13$ peak, which corresponds to a cluster of 27 atoms. This cluster can be imagined as a 3×3 cube cut out of a NaCl crystal. The observation of other locally highly abundant clusters such as $n = 22$, $m = 10$ or $m = 13$ is in accordance with other experimental and theoretical results[78]. The $n = 22$ cluster for example corresponds to the $5 \times 3 \times 3$ cuboid.

Despite the precision, the NaCl calibration also bears some major disadvantages that forbid its use for everyday application. The Na^+ ion is very likely to contaminate following measurements and would make frequent extensive cleaning necessary. The Cl^- ion is chemically very aggressive since it is present as an ion or in nanocrystalline form. The two stable isotopes of chlorine result in isotopic distributions for each cluster. At the present resolution of our mass spectrometer the corresponding peaks overlap completely into a single wide peak for each cluster for $n > 5$, which limits the precision of the calibration. Another calibration solution without these disadvantages would therefore be most useful.

Cesium Iodide – The Standard Calibration

Better for calibration is Cesium Iodide (CsI). Like NaCl it is a salt composed of group I and VII elements and creates ionic clusters in an electrospray ion beam source. The components are less reactive than those of NaCl and have the advantage of only one stable isotope each, which are $^{133}\mathrm{Cs}$ ($132.905447\,\mathrm{u}$) and $^{127}\mathrm{I}$ ($126.90446\,\mathrm{u}$) respectively.

Positively charged CsI clusters, produced by electrospray ionization, are of the type $\mathrm{mCs}^+(\mathrm{CsI})_\mathrm{n}$. In order to avoid contamination of the apparatus, a low concentrated CsI solution is used for calibration ($0.1\,\frac{\mathrm{mg}}{\mathrm{ml}} \mathrel{\widehat{=}} 0.38\,\mathrm{mM}$). A mixture of water with methanol or ethanol is used as solvent. Usually, only singly charged clusters of CsI are observed in the ion beam, due the low concentration. Table 4.1 displays the reference mass-to-charge-ratios of the clusters most frequently used for calibration with CsI.

To find the calibration constants A and t_0 in equation (2.10) a minimum of two fixpoints is needed, which are tuples of the type $(t, M(t))$ with t the mea-

I^-	Cs^+	charge z	$\frac{m}{z}$ (Th)	I^-	Cs^+	charge z	$\frac{m}{z}$ (Th)
0	1	1	132.9054	9	10	1	2471.1540
1	2	1	392.7108	10	11	1	2730.9594
2	3	1	652.5162	11	12	1	2990.7648
3	4	1	912.3216	12	13	1	3250.5702
4	5	1	1172.1270				
5	6	1	1431.9324	doubly charged			
6	7	1	1691.7378	3	5	2	522.6135
7	8	1	1951.5432	5	7	2	782.4189
8	9	1	2211.3486	7	9	2	1042.2243

Table 4.1 – Mass-to-charge-ratio of singly and doubly charged clusters of CsI which are typically used for calibration (see figure 4.4)

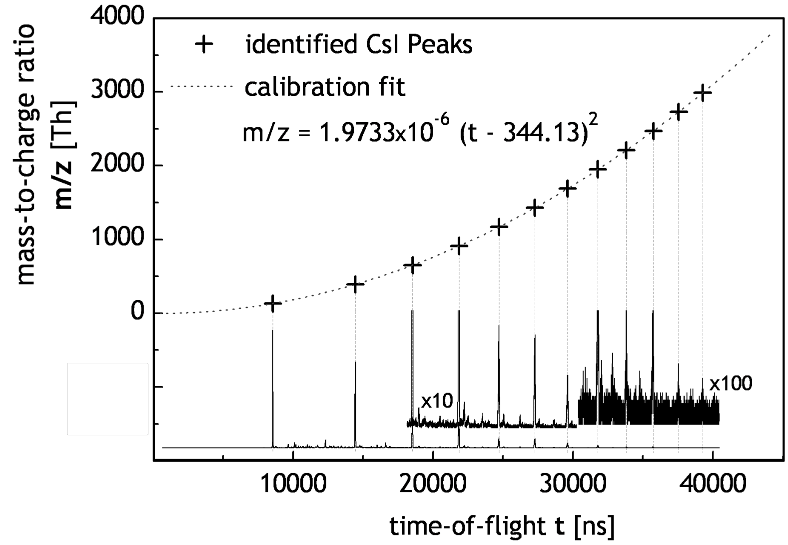

Figure 4.3 – Mass-to-charge-ratio as a function of time-of-flight and time-of-flight spectrum for a CsI cluster beam. Each cross (+) marks a fixed point in the time-of-flight spectrum which corresponds to an identified peak for which the mass can be calculated.

sured flight time and M the corresponding mass-to-charge-ratio . However the calibration is more precise if several fixpoints are taken into account.

In figure 4.3 the mass spectrum of CsI is displayed in the time-of-flight representation. The peaks are identified to be increasingly larger clusters of the type $\mathrm{Cs^+(CsI)_n}$, which results in the fixpoints marked with (+). The function (2.10) is then fitted to all these points with free calibration parameters A and t_0 to be determined. Such a fit is shown in figure 4.3 as a dotted line. The calibration constants found in this example are $A = (1.973 \pm 0.002) \times 10^{-6}\,\mathrm{Th\,ns^{-2}}$ and $t_0 = (344 \pm 15)\,\mathrm{ns}$.

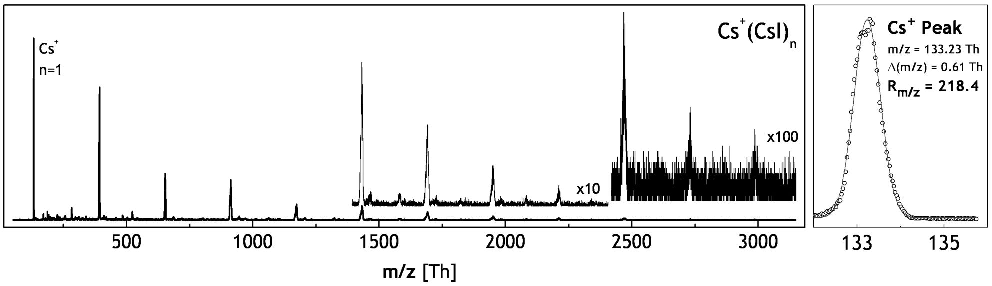

Figure 4.4 – **[left]** Calibrated CsI mass spectrum. Cluster peaks from $\mathrm{Cs^+}$ up to $\mathrm{Cs^+(CsI)_{11}}$ are displayed. (note the enlarged y-axis scale for higher masses). **[right]** The resolution is calculated for the $\mathrm{Cs^+}$ peak to be 218 .

To transform the measured time-of-flight spectra into actual mass spectra, the calibration function is applied to the measured data (see figure 4.4). The typical equidistant spacing of singly charged clusters can be observed. The mass resolution of the spectrometer can be determined as the ratio between the peak position and its width (equation (2.8) and equation (2.9)) and is found to be approximately 200 (see figure 4.4 [right]).

A resolution of 200 limits the distinction of neighboring peaks to $\frac{1}{200}$ of their position. This is not the only error in a mass-to-charge-ratio measurement, since a further resolution limitation is given by the errors in the calibration constants (see equation (2.14)). If equation (2.14) is evaluated with the above calibration constants for high and low flight times, $10000\,\mathrm{ns}$ and $30000\,\mathrm{ns}$ for example, the resolution limitations found are 250 and 500 respectively. This means that the calibration precision is good enough for the given instrumental resolution of 200 for our mass spectrometer.

The values found for resolution error and calibration error show that CsI cluster beams can be used for calibration of the mass spectrometer. Repeated calibration measurements show that in fact the constants shift with time and as a function of apparatus parameters, although only minor shift between subsequent measurements are observed.

Since a precise calibration using a fit over many fix points is very time consuming for each measurement, a rough calibration using two points is done and the CsI mass spectrum is recorded in case a more precise calibration is necessary.

4.1.3 Amphiphilic Metallo-Organic Salt Cluster Ions

Considering that physiological conditions are nothing else than aqueous solutions with a high concentration of solvated ions, it is clear that ionic organic compounds are also very important in biology. Actually a large group of organic and biological molecules are in the form of ionically bound salts. Among these molecules the class of ionic surfactants is one of the most prominent. They have great importance in biological systems and industrial applications due to their special behavior at interfaces (see section 5.2, page 119 for more detail)[141, 142]. It is therefore very interesting to study surfactants in gas phase in (ultra) high vacuum, where their interaction is not dominated by the presence of water any more.

In this section mass spectrometry is used to study sodium-alcyl sulfates in particular sodium dodecyl sulfate (**SDS**) and sodium octyl sulfate (**SOS**) which are ionic surfactants and examples for metallo-organic salts. As a first step here the formation of metallo-organic ionic clusters in the electrospray is investigated in order to fundamentally understand the formation of sodium alkyl sulfate gas phase ions.

For ion beam deposition experiments a very important question is whether an aggregate of **SDS** and a dispersed molecule or particle can be charged and transferred into gas phase. Related deposition experiments with carbon nanotubes and **SDS** are discussed in section 5.4.

Singly and Highly Charged Clusters

SDS and **SOS** in powder form that are dissolved in a mixture of methanol and water are used for mass spectrometry experiments. Typical concentrations are between $1\,\frac{\mathrm{mg}}{\mathrm{ml}}$ and $0.005\,\frac{\mathrm{mg}}{\mathrm{ml}}$.

In figure 4.5 typical mass spectra of **SDS** and **SOS** are displayed for $200\,\mathrm{V}$ fragmentor voltage. Both mass spectra show the equidistant spacing between the singly charged cluster peaks, typical for salt clusters. The composition of the clusters can be identified as $\mathrm{Na^+(NaSO_4(CH_2)_7CH_3)_n}$ for singly charged **SOS** clusters and $\mathrm{Na^+(NaSO_4(CH_2)_{11}CH_3)_n}$ for singly charged **SDS** clusters.

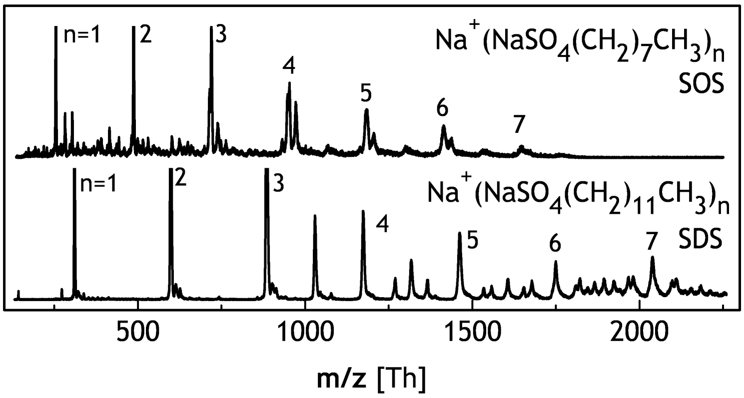

Figure 4.5 – Mass spectra of sodium dodecyl sulfate (**SDS**) and sodium octyl sulfate (**SOS**) at 200 V fragmentor voltage. Equidistant, indexed peaks correspond to the singly charged clusters. In between highly charged clusters are observed.

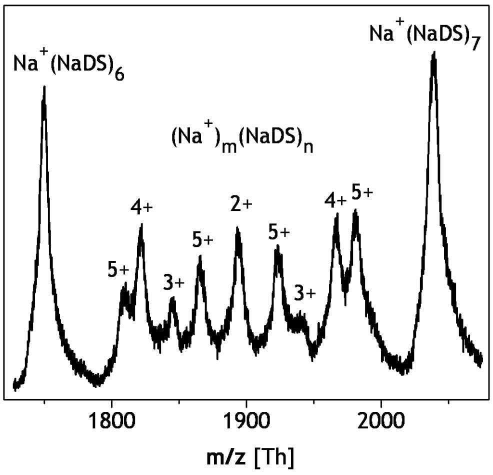

Figure 4.6 – Highly charged clusters, up to $+5$, of **SDS** between the $n = 6$ and $n = 7$ single charged peaks.

Although highly charged clusters can be observed in both mass spectra, they are much more clearly visible for **SDS** than for **SOS**. In general the peaks corresponding to more highly charged clusters show a higher periodicity than those of singly charges ones, since their separation m/z decreases for rising z. In figure 4.6 a mass spectrum from a different **SDS** experiment is shown, which contains highly charged **SDS** clusters. For 150 V fragmentor voltage, clusters with up to 5 charges can be identified.

The main difference between the inorganic and the organic salt clusters is represented by the observed charge states. For NaCl and CsI only singely and doubly charged clusters can be observed, which agrees with literature on the subject [78]. For **SDS** on the contrary, charges up to $+5$ are measured.

Comparable high charge states have been reported for organic ampholytes of comparable mass [125], but not for inorganic salts.

If different cluster ion beams are to be compared from the perspective of cluster ion abundance, two important aspects have to be considered. The stability of the cluster itself depends on criteria like supersaturation or temperature and material properties like surface- or binding energy. Whether or not a cluster can be created in first place depends on the cluster source and again on the material properties like solubility, because certain growth conditions like supersaturation need to be provided.

Firstly, the maximum charge $Q \propto \sqrt{\epsilon\gamma V}$ that a cluster can bear without being unstable, is defined by its Rayleigh limit ((equation (2.1)), section 2.1.2, page 14). This charge depends on the electric permittivity ϵ_0, the surface tension γ and the volume $V = nV_0$ for a cluster containing n units of volume V_0. The molar volume for **SDS** is much larger than the molar volume of CsI or NaCl. Considering that these substances have similar dielectric properties, it becomes obvious that **SDS** is much more likely to produce highly charged clusters than an inorganic salt of low molar volume.

This argumentation is only correct for macroscopic systems, since material parameters like surface tension and electric permittivity are not well defined for systems that only contain few molecules. However, the forces that are the reason for a certain behavior of a macroscopic material, like adhesion due to van-der-Waals interaction, are still present at the nanoscale. The rough macroscopic approximation thus gives trends for the stability of clusters that are valid also for very few molecules.

The second aspect to be taken into account is the unstable nature of an electrospray ionization cluster beam source. If the parameters of the ion source are set so that a high abundance of clusters is achieved, the spray typically becomes unstable due to an excess of salt deposited at the needle. Depending on the settings of the atmospheric interface, the lifespan of a stable beam can vary between some seconds and several hours. Therefore, an absolute optimal set of parameters for the creation of a high density cluster beam can never be found. However for a certain time span the source parameters can be set in a way that a stable cluster beam can be observed.

Clusters with charges higher than $+2$ are never observed for CsI and NaCl. On the other hand for **SDS** at similar conditions and after the same optimization procedure clusters of the charge $+5$ and higher are identified.

Since the mechanism of cluster formation in the electrospray source is the same for organic and inorganic salts and the external conditions are similar, the big difference in observed charges per cluster are related to a difference in stability, which depends on material parameters. For salts neither the permittivity nor the surface tension show a big difference, but the molar volume does. Large clusters of **SDS** thus can carry more charges than inorganic salt clusters. This result is also valid for gas phase protein ions, which are comparable in mass and volume to **SDS** clusters. Mass spectrometry experiments at proteins in section 4.3, page 105 show that they are highly charged as well.

Missing Magic Numbers

In contrast to NaCl **SDS** mass spectra do not show clusters that are distinctively more abundant than the others. Such pronounced peaks in cluster mass spectra are called *magic numbers* and they correspond to clusters that are especially stable (see section 4.1.2, page 69). In the case of NaCl the cluster containing $3^3 = 27$ atoms is very stable because it resembles a cube. In this configuration the surfaces are minimal versions of the [100], [010] and [001] surfaces and therefore minimize the surface energy necessary to create the cluster. They can be considered defect free.

The absence of such magic number clusters for all organic salt cluster ions thus indicates that small ordered structures like the NaCl clusters do not exist or if they exist have a very low surface energy and therefore do not play a major role for the stability of a certain cluster at the given temperature.

Fragmentation of Organic Salt Clusters

All ions undergo collisions with the background gas in the first and second differential pumping stage, before they enter the mass spectrometer in high vacuum. As already stated, besides the conditions of the solution and the atmospheric interface, these collisions play a key role in the formation of gas phase cluster ions. In fact, cluster fissions can occur upon energetic collisions with gas molecules (see section 2.3.2, page 24). The declustering potential in the first pumping stage at $1.3\,\mathrm{mbar}$ is the parameter that regulates the intensity of these collisions.

If the fragmentor voltage is increased, the amount of highly charged clusters in the ion beam is reduced. Figure 4.7 shows the mass spectra of **SDS** for several fragmentor voltages between $100\,\mathrm{V}$ and $500\,\mathrm{V}$. For rising fragmentor voltages the intensity of intermediate peaks that correspond to highly charged clusters decreases, while other peaks that correspond to singly charged clusters become visible at higher mass-to-charge-ratio .

The observed changes in the mass spectrum could be explained by two different effects introduced by collisions: Either the clusters are stripped off their charges or the clusters are fissioned.

The second explanation is the more probable one, even though there is no direct proof in the experiments with salt clusters that charge stripping can be completely excluded. Other experiments and simulations, for instance with polymers (see section 4.2.3) or tandem mass spectrometry on protein clusters (see section 4.1.4), show that a simple fission model is sufficient to explain the resulting mass spectra after background gas collisions. Additionally, for

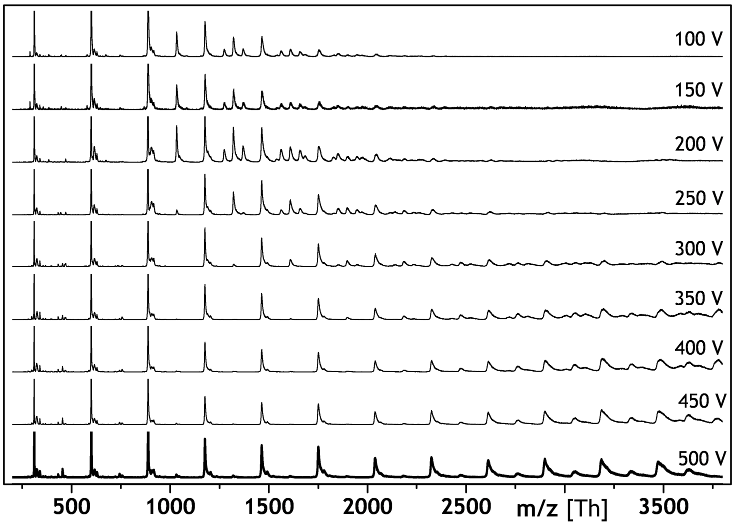

Figure 4.7 – Mass spectra of **SDS** for fragmentor voltages between $100\,\mathrm{V}$ and $500\,\mathrm{V}$. The abundance of highly charged clusters is reduced with rising voltage, while large singly charged clusters become more abundant.

protein clusters charge stripping could be excluded as an effect caused by ion gas collisions.

In order to resemble the observed mass spectra for the CID of **SDS** clusters, the only effect considered is the random splitting of a big ion into two parts. The mass and the net charge of the primary ion is distributed among the daughter particles which therefore can be ions or neutrals. As a consequence of the fission process, the mass-to-charge-ratio range where peaks appear in the mass spectrum gets larger, which seems counterintuitive. Ions from a mass range of $m_1 \dots m_2$ with charges between z_1 and z_2, where $m_1 < m_2$ and $z_1 < z_2$ will create peaks in the mass-to-charge-ratio range between $M_{\mathrm{hi}} = \frac{m_2}{z_1}$ and $M_{\mathrm{low}} = \frac{m_1}{z_2}$. After a fragmentation the upper limit for the mass m_2 and the charge z_2 remains the same while the lower limits m_1 and z_1 have become lower. This affects also the limits of the mass-to-charge-ratio . The upper limit M_{hi} has become larger, since z_1 decreased while the lower limit M_{low} decreased because m_2 got reduced.

The described mechanism resembles the effect observed for CID with highly charged clusters of **SDS**. In fact no information about the fissioned molecule is needed in the description. Therefore this model applies to all collision induced dissociations of highly charged ions. Additionally it can be concluded that the mass-to-charge-ratio range of singly charged particles can only decrease upon CID since the charge state is fixed to 1.

4.1.4 Non Covalently Bound Protein Clusters

In solution protein arrangements are of great importance due to their role in cell signaling[11]. Many biochemical processes including cell proliferation, immune reactions and metabolism are controlled by protein agglomerations.

Protein clusters can also be observed in gas phase[136]. Mass spectrometry and ion-gas-interactions are used to study the properties of these clusters in order to compare them to their solution properties. The properties of gas phase proteins and their solution counterparts differ substantially. Therefore it is one important question to what extent the protein reactions in solution are reflected by gas phase protein ions[143, 32, 144].

Finally, it is most interesting to use proteins for vacuum deposition as illustrated here (see section 5.1, page 112) or by other works[52, 53]. In this framework also the behavior of protein clusters on a surface is of great interest and will have to be compared to their properties in the gas phase.

One way to study gas phase cluster ions is to use controlled intense collisions with gas molecules and analyze the fragments, which gives information about the primary ions, like binding strength and charge site. Nozzle skimmer fragmentation like used for **SDS** (section 4.1.3, page 74), Rhodamines (section 4.2.1, page 82) or Catenenes (section 4.2.2, page 90) cannot be used for an ion beam containing more than one primary particle, since resulting mass spectra would contain product ions from all types of primary particles.

Therefore the study of protein agglomerations of Cytochrome c (**Cyc**) is done with product ion mass spectrometry on the triple quadrupole mass spectrometer at the *Proteomzentrum Tuebingen*(see section 3.4.4 for details on the experimental setup). This technique is used to determine the composition of the protein clusters, which can give information on whether these clusters are formed due to denaturing or due to binding under equilibrium condition solution reaction.

Clusters of proteins show some distinct differences to salt clusters. Both types of ionic clusters are composed of charged particles. The building unit of a salt cluster is the ion pair $\mathrm{A^+B^-}$. The net charge of the cluster results from an excess in one of the components, i.e. $\mathrm{A^+(A^+B^-)_n}$. Protein clusters only have one charge type depending on the configuration of the source. The proteins studied in this work are all multiply positively charged.

For the protein Cytochrome c, charge states between $+4$ and $+12$ are observed (see section 4.3.2). Figure 4.8 shows the mass spectrum of Cytochrome c that was used to create the product ion spectra, which are also displayed underneath. Highly charged clusters consisting of two ($\mathrm{2M}$) or three ($\mathrm{3M}$) proteins are observed in addition to the single particle ions.

Product ion mass spectra are obtained by mass selecting one peak in the first quadrupole (Q1), passing it through a collision cell (q2) ($p = 2 \times 10^{-4}\,\mathrm{mbar}$) and recording a mass spectrum with the third quadrupole (Q3). The clusters

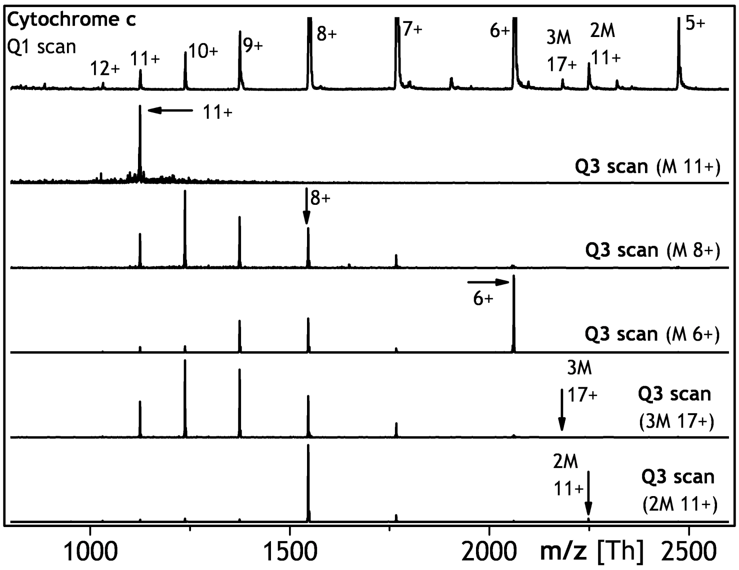

Figure 4.8 – Product ion mass spectra of Cytochrome c ions and clusters. The primary mass spectrum is displayed on top. Underneath the product ion mass spectra are shown. The mass selected ion from the primary spectrum is marked with an arrow in its product ion spectrum.

Ion or Cluster	Product Ions
M^{11+}	M^{11+}
M^{8+} $(2M^{16+})$	M^{10+}, M^{9+}, M^{11+}, M^{7+}
M^{6+} $(2M^{12+})$	M^{8+}, M^{9+}, M^{10+}, M^{11+},M^{7+}
$3M^{17+}$	M^{10+}, M^{9+}, M^{8+}, M^{12+}, M^{7+},
$2M^{11+}$	M^{6+}, M^{7+},

Table 4.2 – Product ions of Cytochrome c clusters ($\mathbf{Cyc}+nH^+$). The clusters are sorted by ascending mass-to-charge-ratio , the product ions by abundance.

M^{11+}, M^{8+}, M^{6+}, $3M^{17+}$ and $2M^{11+}$ are investigated. Their product ion spectra are displayed in figure 4.8 underneath the primary mass spectrum. All product ion mass spectra show only peaks that can be identified with charged Cytochrome c ions, no small fragments are observed.

In table 4.2 the found product ions are summarized. A trend is visible: For clusters with higher mass-to-charge-ratio also the product ions have a higher mass-to-charge-ratio , hence a lower charge. But some exceptions are also observable. Even though the $3M^{17+}$ and the $2M^{11+}$ clusters have almost the same mass-to-charge-ratio , their product ion spectra differ substantially. Finally it has to be noted that due to the mass range of the quadrupole spectrometer, $+5$ is the lowest charged Cytochrome c ion observable. The list of product ions is thus not complete.

The fragmentation into single protein ions in the product ion mass spectra is complete. This can be deduced from the complete disappearance of the $3\mathrm{M}^{17+}$ and $2\mathrm{M}^{11+}$ clusters which cannot contain single particle ions. Therefore the product ion peaks observed for M^{11+}, M^{8+} and M^{6+} correspond to the single particle ion.

The product ion mass spectrum of the M^{11+} ion does not contain any other ion than the primary itself. This is a very important result because it shows that stripping of charges upon gas collision does not occur. Otherwise lower charged ions would have been observed. Moreover the observation that M^{11+} does not contain any cluster ions in contrast to the lower charged clusters suggests that charge repulsion plays a role for the cluster stability.

In the fragmentation of the clusters, the most abundant product ion is not necessarily the ion with ±1 charge but rather with ±2 charges with respect to the mean cluster charge (charge per **Cyc**). Since charge stripping and therefore also charge transfer between the ions in the cluster can be excluded, only an asymmetric charge distribution in the cluster can give rise to these observations.

In general the abundance of clusters in a molecular beam can be expressed in terms of the energy gains during their growth[72]. The cluster has to form a surface which costs energy while it gains volume energy from the binding to other molecules.

The observation of Cytochrome c ion clusters in the gas phase illustrate that already an agglomeration of two clusters gains enough energy in order to overcome the charge repulsion between the two ions. This energy gain is related to the polar outer shell of a protein which is desolvated in the gas phase. Therefore it is favorable for proteins to be in contact with other proteins in the gas phase.

Moreover the observations show that it is energetically more favorable to distribute the net charge asymmetrically between the parts of the cluster. Considering the electrostatic force between two charges particles $F \propto z_1 z_2$ with z_i being the charge state, for a constant net charge $z = z_1 + z_2$ the largest force will be found for the most equal sharing of z between z_1 and z_2. This argument certainly does not describe the observations entirely, but it gives an idea why the charge distribution is asymmetric.

Finally the results found for the mechanisms under which the protein agglomerations are formed, indicate that the driving force is present either for highly or for lowly charged **Cyc** clusters. Mass spectrometry as well as other results indicate that highly charged protein clusters are often in an unfolded form, while lowly charged proteins are still correctly folded (see section 4.3.2, page 108 and [145, 144]). Therefore the attractive interaction between the **Cyc** proteins is not related to a specific protein interaction, but rather caused by the hydrophobic-hydrophilic effect between two large complex molecules.

4.2 ORGANIC MOLECULES

Today organic chemistry knows of 17 million compounds. Their size ranges from methane CH_4 ($m = 16\,\mathrm{u}$) to polymers of many million atomic masses. The number of elementary building units on the other hand is rather small. Besides the major atomic fraction of carbon and hydrogen, organic molecules typically contain oxygen, nitrogen, sulfur, phosphor and halogens as a minor part. This minor atomic fraction is arranged in functional groups, which define how organic molecules chemically behave.

With increasing complexity the functionality of organic molecules is increased. Thus many properties and applications can be found for organic molecules. Synthetic organic chemistry today can create tailor made molecules with very desirable functionalities[146, 147, 5, 148]. A big roadblock though is that large functional organic molecules rarely have a vapor pressure high enough for vaporization. Therefore, neither structuring nor analytical methods based on ultra high vacuum technology can be used with these molecules, due to the lack of a suitable deposition technique.

Electrospray ionization has been shown to be able to create gas phase ions in vacuum[35]. The electrospray ion beam deposition source developed during this thesis is aimed at bridging this gap of the missing deposition technique. By its use organic molecules can in fact now be deposited and explored in vacuum. As for the organic and inorganic salts (section 4.1, page 68), the basis of a successful deposition is the control over the beam composition. Therefore, mass spectrometry studies are performed to learn how to ionize molecules and learn how they behave in an ion beam, especially when encountering collisions with a background gas.

At the beginning of this chapter organic dye molecules are studied, because due to their fluorescence properties (section 4.2.1, page 82) they can be used as probes for a successful soft landing deposition (section 5.3, page 127). [2]-catenanes, topologically connected organic molecules able to form complex coordination bonds with metal ions, are further studied in section 4.2.2, page 90. Due to their different binding motives these molecules behave as interesting molecular switches. Finally polymers, the largest organic molecules, are studied by the example of poly-ethylene-imine. Their general behavior makes them an easy to handle model system for many organic macromolecules of higher complexity, such as proteins or DNA.

4.2.1 Rhodamine Dye Molecules

Rhodamine is a family of dye molecules that is characterized by a common fluorophore, phenyl-xanthene (see figure 4.9). Typically they are soluble in water or alcohols where they are present as ions stabilized by counter ions[149].

The key property of Rhodamines is their fluorescence (see table 4.3). They

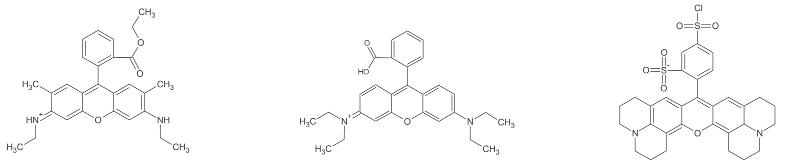

Rhodamine 6G
$C_{28}H_{31}N_2O_3$
443.56 Da

Rhodamine B
$C_{28}H_{31}N_2O_3$
443.56 Da

Sulforhodamine
$C_{31}H_{30}ClN_2O_6S_2$
626.16 Da

Figure 4.9 – Examples from the Rhodamine family of dye molecules: Rhodamine 6G, B, Sulforhodamine

Rhodamine Molecule	**Abbreviation**	**Excitation Wavelength** (nm)	**Emission Wavelength** (nm)	Color in Solution
Rhodamine 6G	**Rho6G**	480 – 555	520 – 680	orange
Rhodamine B	**RhoB**	500 – 565	530 – 655	violet
Sulforhodamine	**SRho**	510 – 600	560 – 670	red

Table 4.3 – Rhodamine dye molecules with excitation and emission wavelength used in this study[150].

are used as laser dyes and stains for fluorescent labeling[151, 152]. The emission spectrum depends on the sidegroups of the fluorophore and on the environment (solvent, pH value)[153, 154]. Rhodamine molecules are very effective dyes with quantum efficiencies up to almost 100%, which is the reason why they are used in single molecule spectroscopy experiments[155].

Rhodamines are also interesting probes for ion beam deposition experiments on solid substrates. Since only the intact molecule will generate the typical fluorescence spectrum, optical spectroscopy can be used to prove and quantify the soft landing process.

Soft landing experiments carried out with Rhodamine 6G (**Rho6G**) ion beams are described in detail in section 5.3, page 127. Here the behavior of gas phase Rhodamine ions is studied with mass spectrometry. The fragmentation of the molecules upon collisions with a high pressure background gas is analyzed in detail because of the expected parallels with collisions at solid surfaces.

The fragmentation experiments are done by nozzle skimmer fragmentation in the first pumping stage. As modeled in section 2.3.2, page 28 the fragmentor voltage can be used to control the collision energy. The resulting fragment ion spectra are recorded and fragments are identified in order to establish general rules for the fragmentation of this class of molecules.

Mass Spectra of Rhodamines

For mass spectrometry, Rhodamine 6G, B and Sulforhodamine are dissolved in a mixture of water and methanol at concentrations between $0.5\,\frac{\mathrm{mg}}{\mathrm{ml}}$ and $0.05\,\frac{\mathrm{mg}}{\mathrm{ml}}$. The solution is acidified by adding $0.1\,\%$ up to $1\,\%$ of formic acid.

Mass spectra for Rhodamine 6G are displayed in figure 4.10 for fragmentor voltages between $50\,\mathrm{V}$ and $550\,\mathrm{V}$. For low voltages ($50\,\mathrm{V}$ - $200\,\mathrm{V}$) the only intense peak observed is at $443\,\mathrm{Th}$ - a singly charged Rhodamine ion. A minor peak at $415\,\mathrm{Th}$ corresponds to a Rhodamine ion with a missing ethyl group (m =29 u).

Further fragmentation sets in at fragmentor voltages of $225\,\mathrm{V}$. With increasing fragmentor voltage the masses of the observed fragments decrease down to $100\,\mathrm{Th}$. Intense peaks are recorded at $400, 386, 358, 341, 327, 311, 298, 283,$ $269\,\mathrm{Th}$ and $257\,\mathrm{Th}$. The distance between neighboring peaks is always in the range between $12\,\mathrm{Th}$ and $16\,\mathrm{Th}$.

Like Rhodamine 6G the molecule Rhodamine B has a mass of $443\,\mathrm{Th}$. The two molecules are isomers, i.e. they have the same molecular formula and the same backbone fluorophore but the structure is only similar. This results in distinctly different optical properties (see table 4.3).

The fragmentation mass spectra of Rhodamine B (figure 4.11) are similar to those of Rhodamine 6G. Major fragment peaks appear for fragmentor voltages higher then $200\,\mathrm{V}$. The smallest fragments observed for the highest voltages have a mass-to-charge-ratio of about $100\,\mathrm{Th}$. Even though the general appearance of the fragmentation mass spectra is similar, the exact positions of the peaks and their abundances are different in many details, except for the peak at $443\,\mathrm{Th}$.

Sulforhodamine 101 Sulfonyl Chloride (**SRho**, *Sigma Aldrich S3388*) also known as *Texas Red* is a very popular stain for amino acids[151]. It binds covalently to proteins making them detectable in fluorescence microscopy while they are still folded. In contrast to Rhodamine B and Rhodamine 6G it can carry two different charges in solution, a positive charge at the amino group and a negative charge at the sulfate group.

A further difference of **SRho** in respect to the other Rhodamines is that only the sulfate (SO_3) and the chlorosulfate ($SClO_2$) groups are connected with a single bond to the phenyl-xanthene backbone of the molecule. The other sidegroups are connected with the fluorophore by at least two bonds.

For mass spectrometry **SRho** is dissolved in a mixture of water and ethanol at concentrations of approx. $0.1\,\frac{\mathrm{mg}}{\mathrm{ml}}$. The resulting mass spectra are displayed in figure 4.12 for a range of fragmentor voltages from $50\,\mathrm{V}$ to $650\,\mathrm{V}$. For low fragmentor voltages the base peak is found at $609\,\mathrm{Th}$, which can be attributed to an **SRho** ion in which an oxygen atom is missing. Fragment peaks appear at $400\,\mathrm{V}$ fragmentor voltage with mass-to-charge-ratios down to 200 .

Sulforhodamine is an example for a molecule that is charged by an electro-

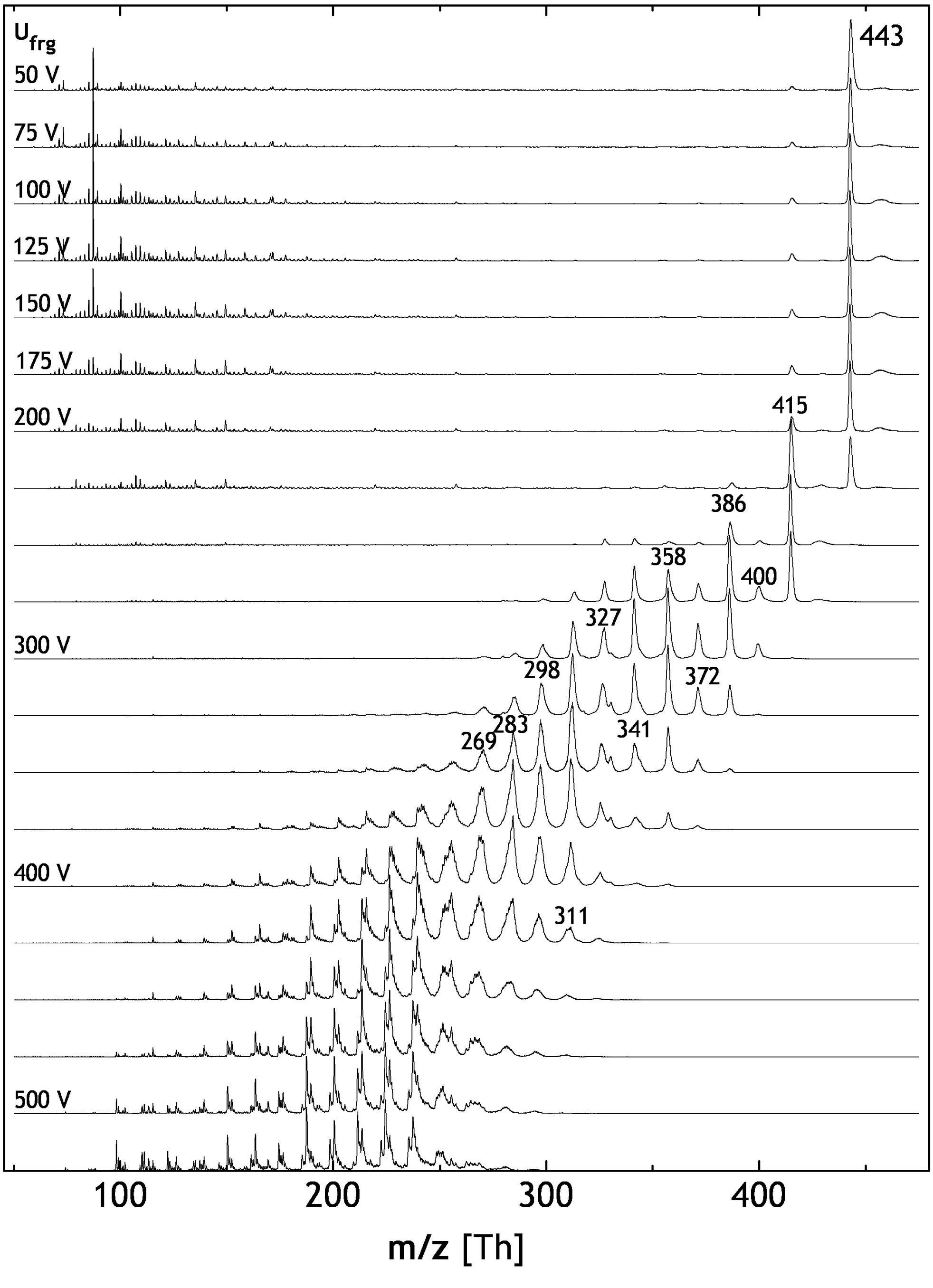

Figure 4.10 – Mass spectra of Rhodamine 6G, for fragmentor voltages between $50\,\mathrm{V}$ and $525\,\mathrm{V}$. For low voltages the base peak is found at $443\,\mathrm{Th}$, for voltages higher than $225\,\mathrm{V}$ peaks at lower mass-to-charge-ratio are the most intense.

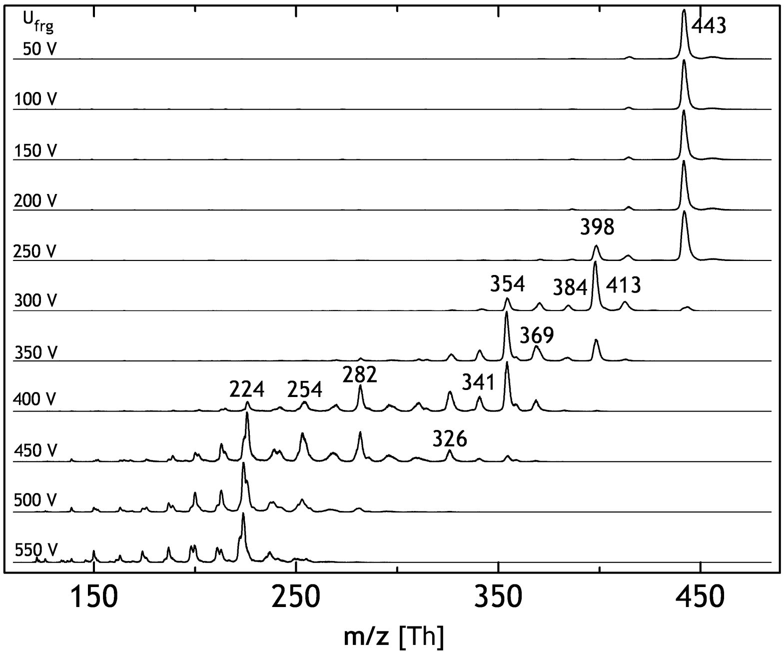

Figure 4.11 – Mass spectra of Rhodamine B, for fragmentor voltages between 50 V and 550 V. The pattern of fragment peaks appears to be similar to the fragmentation of **Rho6G**.

chemical reaction in electrospray ionization (see section 2, page 13). In contrast to **Rho6G** and **RhoB**, which are charged at the amino group and therefore are ions by themselves, the amino group in the sulforhodamine ternary, which is less likely to be protonated then primary or secondary amino groups[67]. The base peak at 609 Th is therefore related to the chemically modified molecule, while only a small peak is found at 626 Th for the intact **SRho**.

Fragmentation Mechanism of Dye Molecules

Since the Rhodamine molecules are all singly charged, the mass-to-charge-ratio of the fragments and their masses are identical and thus can be used to identify the fragments directly. The resolution of the mass spectrometer, which results in an error of $\pm 1.5\,\mathrm{u}$ for the mass range of the fragments, is only a minor limitation. In fact the mass spectra show that the typical fragments are hydrocarbon and thus are separated by $12 - 15\,\mathrm{u}$.

Fragments identified for **Rho6G**, **RhoB** and **SRho** are shown in figures 4.13, 4.14 and 4.15. In general it is observed that fragmentation occurs within a certain hierarchy as a function of the fragmentor voltage, because otherwise all possible fragments would appear at the same time, with the same abundance. Fragments that appear at low fragmentor voltages therefore are related to a weak bond within the molecule. On the contrary, the difference in abundance

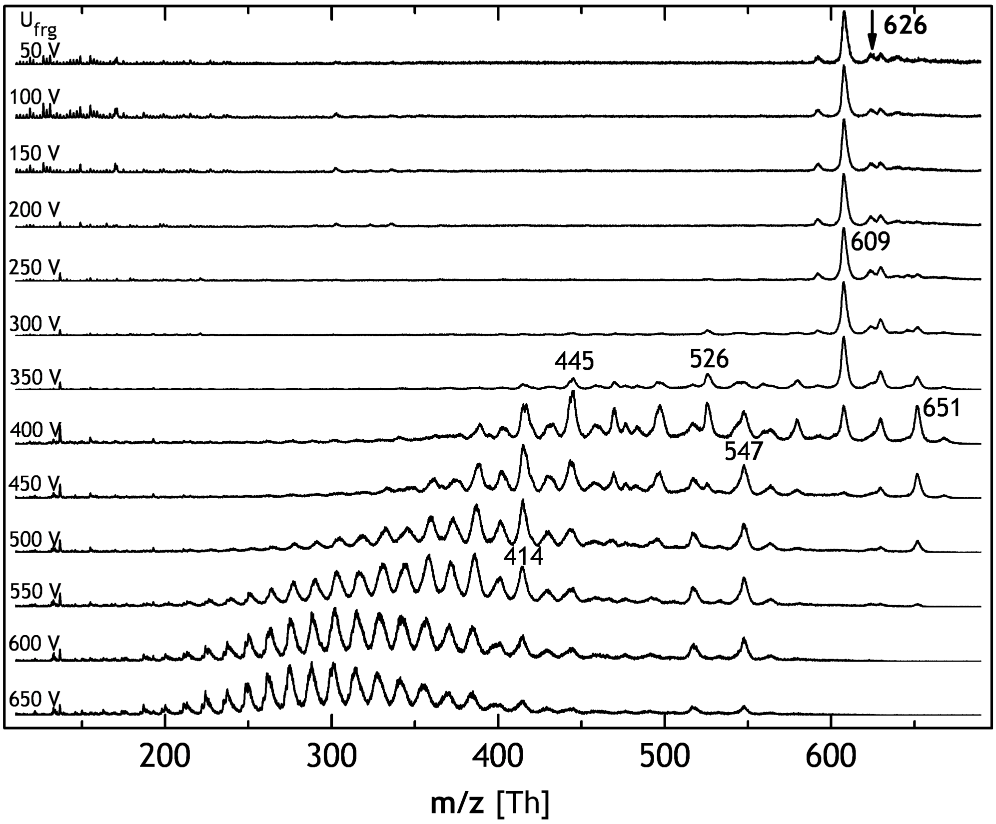

Figure 4.12 – Mass spectra of Sulforhodamine, for several declustering potentials. The major peak for low fragmentor voltages is not the molecule itself ($626\,\mathrm{Th}$) but a fragment with one oxygen atom missing ($609\,\mathrm{Th}$). Intense fragment peaks appear only for fragmentor voltages higher than $400\,\mathrm{V}$

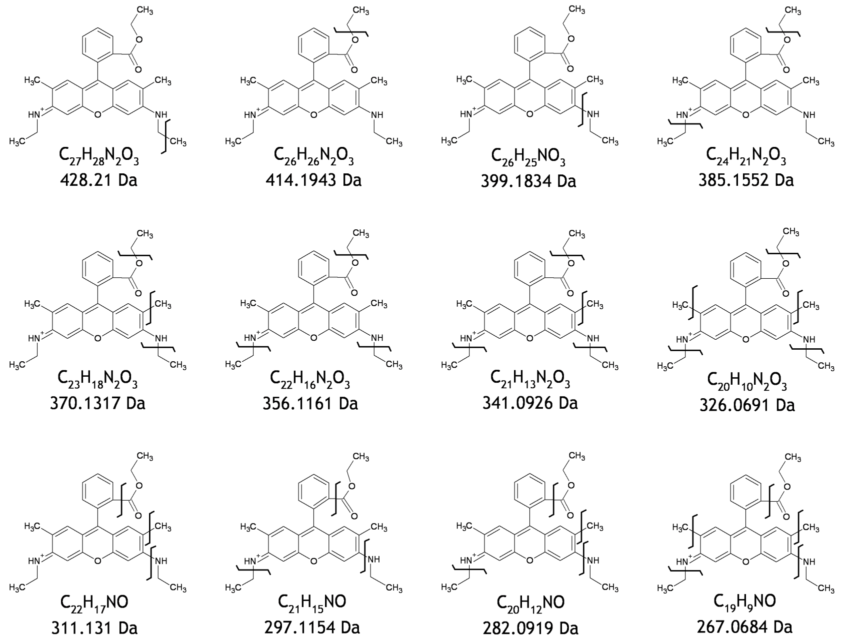

$C_{27}H_{28}N_2O_3$ 428.21 Da

$C_{26}H_{26}N_2O_3$ 414.1943 Da

$C_{26}H_{25}NO_3$ 399.1834 Da

$C_{24}H_{21}N_2O_3$ 385.1552 Da

$C_{23}H_{18}N_2O_3$ 370.1317 Da

$C_{22}H_{16}N_2O_3$ 356.1161 Da

$C_{21}H_{13}N_2O_3$ 341.0926 Da

$C_{20}H_{10}N_2O_3$ 326.0691 Da

$C_{22}H_{17}NO$ 311.131 Da

$C_{21}H_{15}NO$ 297.1154 Da

$C_{20}H_{12}NO$ 282.0919 Da

$C_{19}H_9NO$ 267.0684 Da

Figure 4.13 – Molecular structure of **Rho6G** fragments. The pattern of peaks down to $257\,\mathrm{Th}$ can be interpreted as the subsequent fragmentation of the sidegroups ($-\mathrm{CH}_{1,2,3}$, $-\mathrm{NH}_2$, $-\mathrm{OH}$, $=\mathrm{O}$, $-\mathrm{CH}_2-\mathrm{CH}_3$). The given structures represent only examples for fragments of the given mass, many other fragments are possible. Further smaller fragments result from the fragmentation of phenyl-xanthene itself.

of fragments that are detected at the same fragmentor voltage can be related to the cross section of the reaction, the collision energy distribution of the ion-collision or the multiplicity of fragments for the same mass-to-charge-ratio .

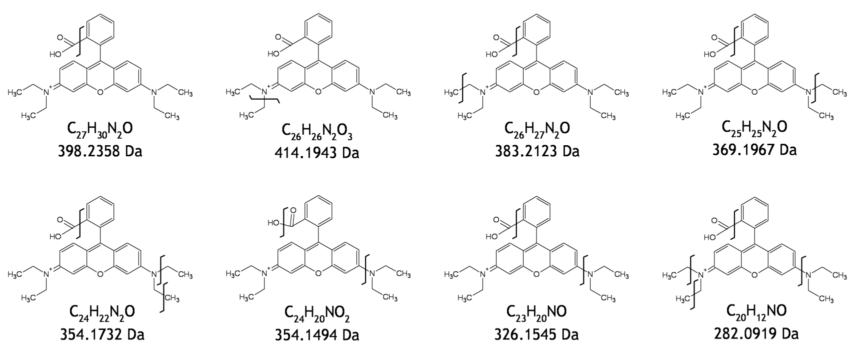
$C_{27}H_{30}N_2O$ 398.2358 Da
$C_{26}H_{26}N_2O_3$ 414.1943 Da
$C_{26}H_{27}N_2O$ 383.2123 Da
$C_{25}H_{25}N_2O$ 369.1967 Da
$C_{24}H_{22}N_2O$ 354.1732 Da
$C_{24}H_{20}NO_2$ 354.1494 Da
$C_{23}H_{20}NO$ 326.1545 Da
$C_{20}H_{12}NO$ 282.0919 Da

Figure 4.14 – Major fragments of Rhodamine B.

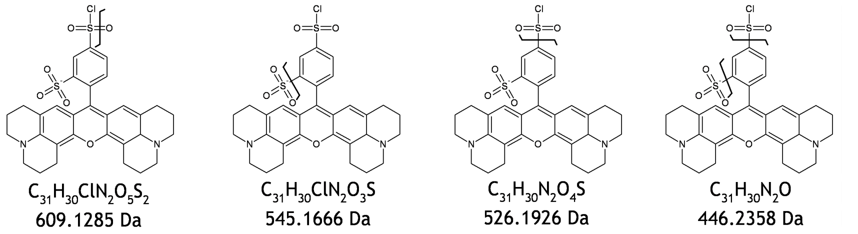
$C_{31}H_{30}ClN_2O_5S_2$ 609.1285 Da
$C_{31}H_{30}ClN_2O_3S$ 545.1666 Da
$C_{31}H_{30}N_2O_4S$ 526.1926 Da
$C_{31}H_{30}N_2O$ 446.2358 Da

Figure 4.15 – Typical fragments of Sulforhodamine as they appear in the mass spectrum.

The fragmentation of the Rhodamine molecules can be understood as a multiple collision process which results in subsequent fragmentation. In the first pumping stage, at a pressure of $1\,\mathrm{mbar}$, the molecular beam is driven towards the skimmer electrode by the supersonic expansion and by the applied declustering potential ($U_{\mathrm{dec}} = U_{\mathrm{frag}} - U_{\mathrm{skimmer}}$). On their way the molecular ions collide with the background gas molecules, which is mainly nitrogen.

While the number of collisions is only dependent on the pressure, a rising declustering potential results in an increased collision energy (see section 2.3.2, page 24). Above a certain threshold such intense collisions can lead to a molecule with a cracked bond, for instance a missing sidegroup or an opened benzene ring. At $200\,\mathrm{V}$ declustering potential (i.e. $U_{\mathrm{frag}} = 250\,\mathrm{V}$ and $U_{\mathrm{skimmmer}} = 50\,\mathrm{V}$) the collision energy for an ion of $500\,\mathrm{Th}$ in $1\,\mathrm{mbar}$ nitrogen is $\approx 1.2\,\mathrm{eV}$ (see figure 2.4), which is in the same order of magnitude as the typical energy of a chemical bond in organic molecules ($2 - 4\,\mathrm{eV}$).

If a molecule undergoes more than one collision, further sidegroups can be removed, if the collision energy is high enough or previous collisions excited the molecule before. Therefore, the subsequent appearance of fragments for increasing fragmentor voltages is related to their binding strength. The sidegroups which are first cleaved off are also the weakest bound.

For **Rho6G** the first three major fragments peaks at 425 Th, 386 Th and 358 Th correspond to the removal of the three ethyl groups[49]. For **RhoB**, in contrast, the first to be removed are not the ethyl sidegroups, but the carboxyl group, resulting in a fragment at 398 Th.

Finally for **SRho** the weakest bound sidegroup is the sulfate group itself, which carries the charge in most of the cases. Therefore almost no fragments appear for voltages up to 350 V, since the fragmentation of the sulfate group results in an uncharged remainder. Only if the molecule is charged at a different site, charged fragments can be observed, which are at 547 Th for the missing sulfate group and at 526 Th when the chlorosulfate is cleaved.

The smaller fragments for all three Rhodamine molecules are related to cleavage of further sidegroups and finally the destruction of the backbone, which occurs at the highest fragmentor voltages since many bonds have to be broken. The mass spectra show wide peaks for the small fragments, since many different fragments are possible and their peaks overlap, which cannot be resolved.

The Rhodamine fragmentation experiments show that large organic molecules are indeed very stable at low collision energies – at least when they collide with lighter molecules from the background gas. Rhodamine molecules lose their sidegroups before the inner structure of the molecule is destroyed. Finally, the details of the fragmentation mass spectra give a hint on the binding strength of sidegroups. All this information represents knowledge important for analyzing the deposition and collision events at a solid surface.

4.2.2 Catenanes – Metallo-Organic Coordination Compounds

[2]Catenanes are one class of molecules that are topologically bound[156, 157, 158, 159]. They consist of two macrocycle molecules which are interlocked with each other. [1] This additional binding motive on top of the covalent binding within each macrocycle makes them promising candidates for molecular machines, in which the structure is contained by the covalently bound organic molecule and a motion is induced by switching the coordination bond selectively.

In fact the interlocked parts can undergo conformational changes upon an external stimulus, while the covalent structure remains intact[160, 161, 162, 163]. Therefore the possibility to control catenanes and rotaxanes on the single molecular level is of great interest. Grafting of the molecules on solid surfaces is one route to access catenanes or rotaxanes with nanoscale imaging and manipula-

---

[1] Only the macrocycle and the catenane are organic molecules, while the copper catenate is a coordination compound. However due to the organic origin this section is listed under organic molecules.

tion techniques. This is an essential prerequisite to realize molecular motor or molecular switch concepts[164, 165, 166, 167].

To understand the behavior of [2]catenanes upon adsorption on solid surfaces, e.g. adsorption strength, conformation relaxation, mobility on the surfaces and, in particular, the freedom of mechanic switching, an UHV-STM study has recently been performed[168]. Within this work the question of intact deposition of complex organic molecules arises. Thermally evaporated and deposited [2]catenane molecules that are observed in STM (figure 4.16) do not necessarily have to be intact, since thermal treatment or chemical reaction with the metal surface might induce strong modifications.

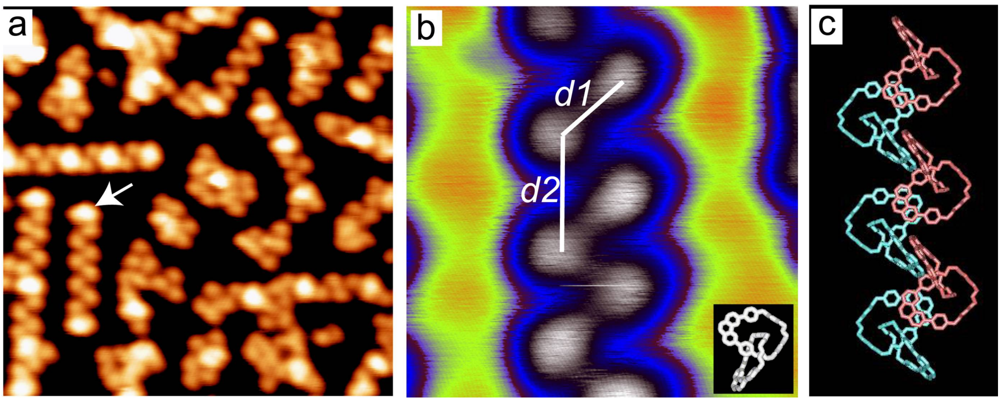

Figure 4.16 – STM topograph of dimer chain structures of **Cat30** on the Ag(111) surface. The arrow points to a molecule sitting on top of a chain. (b) High-resolution STM topograph showing the uniform circular or oval shape of observed **Cat30** molecules, the inset shows the molecular structure of **Cat30** at the same scale of the STM image. (c) A tentative model of the dimer chain structure derived from the STM data and the solid phase X-ray crystallography of **Cat30**, where the overlapping phenanthroline units of the neighboring molecules interact via π-stacking. Different colors are used for clarity (reproduced from [168].)

In order to interpret the molecular resolved STM images, mass spectrometric information of the deposited molecules is very helpful. Therefore, electrospray ionization mass spectrometry has been used to detect catenanes **Cat30**, its metal complexes **Cucat30** and **AgCat30**, the single rings (**M30**, **Mt33**) and the synthesis precursor **dap**.

The study involves not only the mass spectrometric evaluation of the molecule but also of their fragments. The molecules are in fact connected by a hierarchical design: **CuCat30** is obtained by complexation of **Cat30** with copper, **Cat30** is formed by interlocking two open **M30** macrocycle precursors, and the **M30** macrocylce is made by closing the **dap** half ring with ether chains. The observation of fragmentation patterns can thus lead to conclusions about the stability, the chemical reactivity and the charging of the studied molecules.

Figure 4.17 displays the molecules used in the mass spectrometry exper-

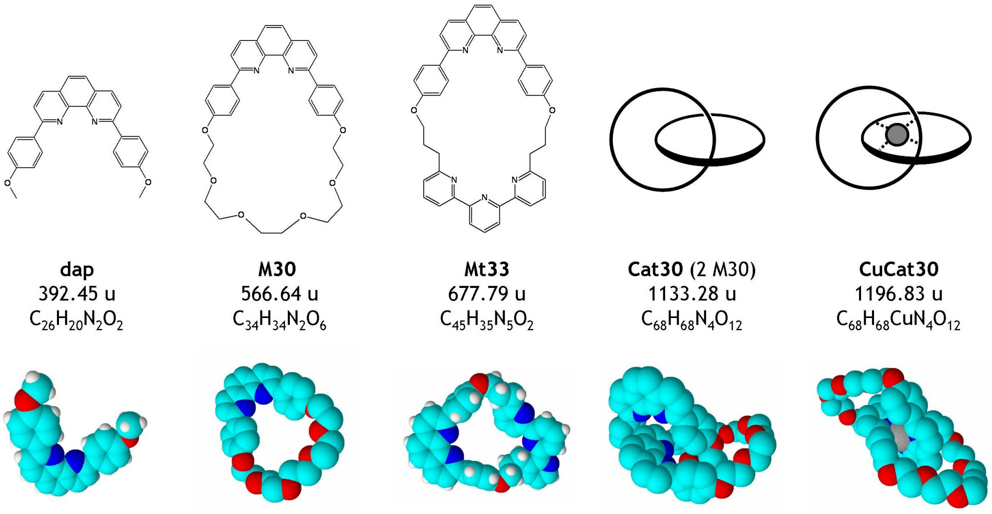

dap 392.45 u $C_{26}H_{20}N_2O_2$

M30 566.64 u $C_{34}H_{34}N_2O_6$

Mt33 677.79 u $C_{45}H_{35}N_5O_2$

Cat30 (2 M30) 1133.28 u $C_{68}H_{68}N_4O_{12}$

CuCat30 1196.83 u $C_{68}H_{68}CuN_4O_{12}$

Figure 4.17 – Catenanes and related molecules used in this study. **dap** is the precursor molecule for the rings **M30** and **Mt33**. The [2]catenane **Cat30** consists of two **M30** rings. The complex **CuCat30** is charged and stabilized in a crystal by BF_4^- counter ions.

iments. The molecules are synthesized by the group of J.-P. Sauvage (University Strassbourg, France)[169]. The molecular masses range from 392 u for the half ring (**dap**) to 1197 u for the copper catenate. All molecules contain basic nitrogen heterocycles like phenantrolines or terpyridines, since the precursor **dap** contains phenantroline ($C_{12}N_2H_{10}$) and functional groups of ether, which are used to close the ring[170]. At ambient conditions they dissolve in dichloromethane completely. Solutions for the use in mass spectrometry are further diluted and acidified (see section 3.3.1, page 58).

Samples for mass spectrometry are prepared by dissolving bulk material or rinsing evaporated molecules off the metal surfaces. In particular, the complexion of the solvated catenane with metals is tested by immersing bulk metal rods in a solution containing **Cat30** or **M30** for a few minutes.

Catenane Cat30 and Copper-Catenate CuCat30

Ion beams of all compounds shown in figure 4.17 are prepared as described in section 3.3.3, page 60. Mass spectra are taken as a function of the fragmentor voltage. Beyond a certain threshold all compounds show fragmentation.

The catenane **Cat30** is found in the mass spectrum as singly and doubly charged molecules at 1132 Th and 567 Th respectively (figure 4.18). Since the peak at 567 Th also corresponds to the single charged **M30**, the **Cat30** was tested for **M30** content by complexation with copper. After the reaction only a **CuCat30** peak (1197 Th) is found in the mass spectrum. Since in a reference experiments, the complexation of Cu and **M30** no peak at this mass-to-charge-ratio has been found, the ion at 567 Th in the mass spectrum of **Cat30** has to

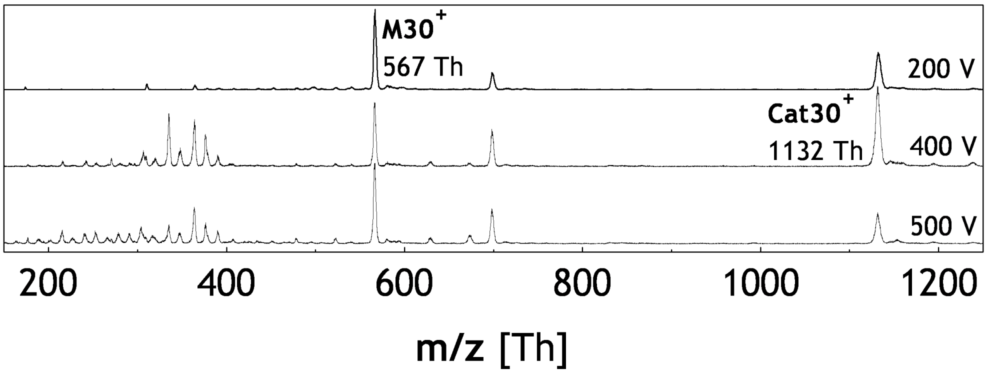

Figure 4.18 – Mass spectra of **Cat30** solution at fragmentor voltages between 200 V and 500 V. The fragmentation is similar to **M30**.

be identified as double charged catenane.

For increased fragmentor voltages the relative abundance between the 1132 Th peak and the 567 Th peak shifts towards the lighter ion. Intense fragment peaks of **M30** are only found for masses lower than 400 Th.

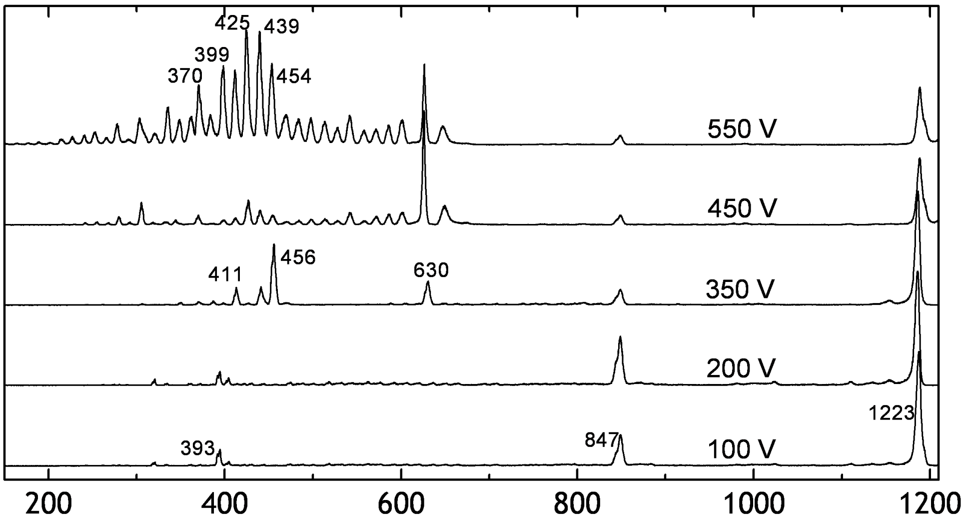

Figure 4.19 – Mass spectra of $\mathbf{CuCat30}^+\mathrm{BF}_4^-$ solution for fragmentor voltages between 100 V and 550 V. The intense peak at 630 Th can be attributed to $\mathrm{Cu}\mathbf{M30}^+$. Neither **Cat30** nor **M30** is present in the spectrum.

For the study of copper catenate a solution of its ionic form $\mathbf{CuCat30}^+\mathrm{BF}_4^-$ has been analyzed with the mass spectrometer (figure 4.19). The peak at 1223 Th can be allocated to **CuCat30**. For low fragmentor voltages also peaks at 847 Th and 393 Th are observed, which most likely correspond to contaminations or higher charged clusters. **CuCat30** shows fragments for high voltages.

Only light fragments with a mass-to-charge-ratio less than half the primary ion appear. The intense fragment at 630 Th belongs to the Cu**M30**$^+$ fragment. Other intense fragments appear only for lower mass-to-charge-ratios .

The fragmentation patterns of **Cat30** and **CuCat30** are distinctively different. Both have in common that a first important group to be split off is a **M30** molecule. The lighter fragments are different. Most importantly the copper ion is not split off the **CuCat30** since neither a **Cat30** nor an **M30** peak can be found.

Mass Spectra of the Macrocycles M30 and Mt33

In order to better understand the mass spectra of the catenane and of its copper complex, the catenate, the mass spectrum of **M30** is studied. The catenane **Cat30** consists of two macrocycles as only components, which is the reason that parallels in the mass spectra have to be expected. To learn what is specific for macrocycle rings, apart from **M30**, another macrocycle (**Mt33**) is used for comparison.

The mass spectrum of the ring molecule **M30** (567 u) is displayed in figure 4.20. High mass fragments, heavier than 390 Th, appear at fragmentor voltages of 250 V, low mass fragments for voltages higher than 300 V. The abundance of the heavy fragments is much lower than those of the light fragments.

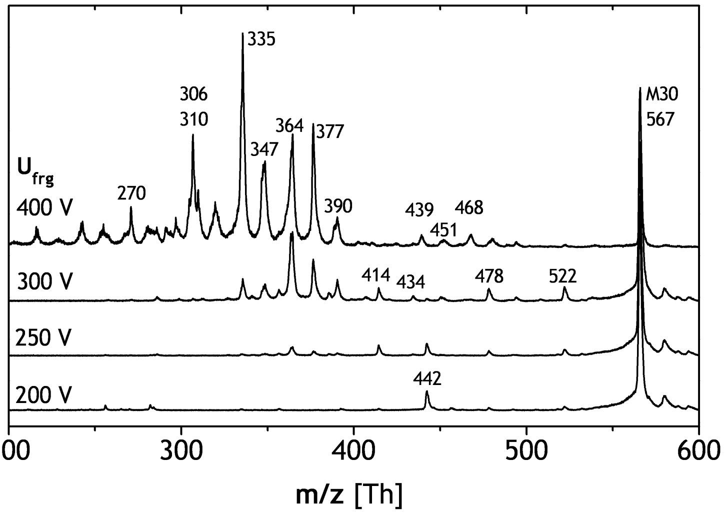

Figure 4.20 – Mass spectra of **M30** for fragmentor voltages between 200 V and 400 V. The peak at 567 Th corresponds to **M30**. Major fragments appear at 306, 310, 335, 347, 364, 377 and 390 Th.

For **Mt33** similar mass spectra like those for **M30** can be observed (figure 4.21). The molecule itself appears as a strong peak at 676 Th when singly charged and at 339 Th when doubly charged. Intense fragment peaks are only observable for masses lower than approximately half the molecule size.

Since the solution is highly concentrated, clusters of **MT33** can be observed at 1035 Th and 1352 Th, which corresponds to (3**Mt33** Na)$^{2+}$ and (2**Mt33**)$^{+}$ respectively.

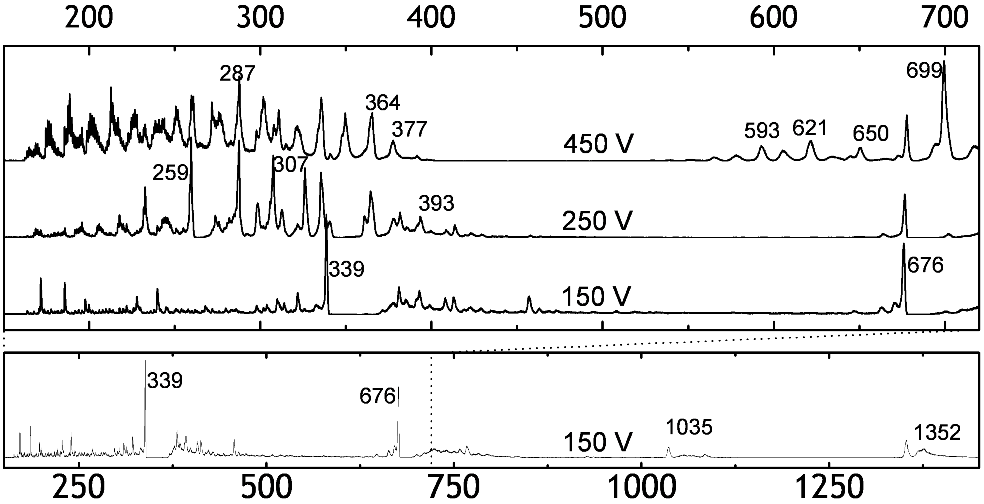

Figure 4.21 – **[top]** Mass spectra of **Mt33** for fragmentor voltages between 150 V and 450 V. The peaks at 656 Th and 339 Th correspond to singly and doubly charged **Mt33**. Major fragments appear at 364, 307, 287 and 259 Th. **[bottom]** Mass spectrum of **Mt33** larger range: Clusters at 1352 Th and 1035 Th are identified as (2**Mt33**)$^{+}$ and (3**Mt33** Na)$^{2+}$.

The two different ring molecule's correlations in the mass spectra are due to the partially common molecular structure and due to the fact that both are macrocycles. Both mass spectra have some major fragment peaks in common (335 Th, 364 Th, 377 Th and 390 Th). In comparison to other organic molecules of similar molecular structure and molecule mass, fragments are only observed for relatively high fragmentor voltage. Rhodamine 6G or Rhodamine B for instance show first intense fragment peaks at 225 V while for **M30** only 300 V seem to be a high enough voltage to induce fragmentation. Since **Mt33** can be doubly charged, its kinetic energy is higher and the fragmentation threshold is thus lower.

Mass spectra of the Precursor Molecule dap

The common fragment at 390 Th in the **M30** and **Mt33** spectra is the **dap** ion, which is used as a precursor in the synthesis of the macrocycles, or one of its isomers (see figure 4.17). The intact **dap** has actually a mass of 392.45 u but it appears as a fragment with a mass of 2 u less, due to two missing hydrogen atoms at the terminal carbon or oxigen atoms, depending at which atom the ether chain has broken. **dap** samples are also measured with MS for comparison with the fragmentation of **M30**, **Mt33**, **Cat30** and **CuCat30**.

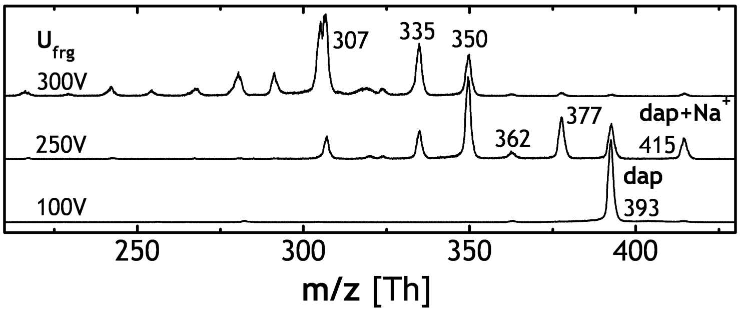

Figure 4.22 – Mass spectra of **dap** for fragmentor voltages of 100 V, 250 V and 300 V. Besides **dap** at 393 Th fragmentation creates peaks of lower masses which correspond to **dap** fragments. One peak of higher mass 414 Th can be identified as Na^+**dap**.

For 100 V fragmentor voltage the mass spectrum shows only one peak at 393 Th which corresponds to the mass of the intact **dap** molecule (figure 4.22). At higher voltages first heavy, then lighter fragments appear. Major fragments are identified to be 377, 362, 350, 334, 307 Th. The peak at 414 Th can be assigned to the Na^+**dap** ion, which is present in low concentration due to contamination. It is only detected at high fragmentor voltages, since it is more stable than the H^+**dap** ion (see section 2.1.3, page 17).

Fragmentation of Catenanes

The charge states and fragment masses observed for the different molecules can be used to determine the location of the charge, the structure of the fragments and to estimate of the stability of the molecular bonds.

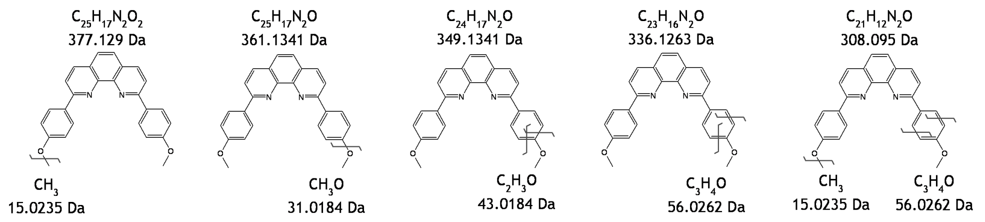

Figure 4.23 – Fragmentation of **dap**. The major fragments can be allocated to molecules with cleaved end groups.

For the **dap** molecule the structure of the principle fragments can be determined by the subsequent removal of sidegroups (figure 4.23). For example the largest intense fragment peak of **dap** with a mass of 377 u can be explained with the loss of a CH_3 group ($m(CH_3) = 15\,u$) at one end of the molecule.

Figure 4.24 shows that independently of the primary ion **Mt33**, **M30** or **Cat30** the lower mass fragment peaks are almost identical to those in the mass spectrum of **dap** at 377, 362, 350, 334 and 307 Th. This is particulary true for **M30** whose fragments smaller than 390 Th, which can be explained by the same pattern proposed for **dap**.

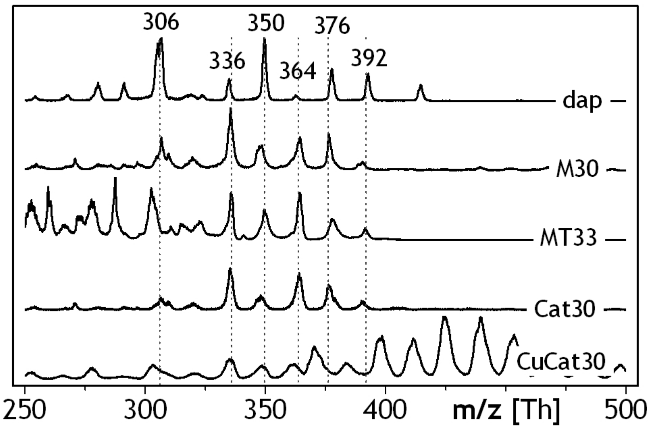

Figure 4.24 – Comparison of the fragmentation of **dap**, **M30**, **Mt33**, **Cat30** and **CuCat30**. Major fragment peaks of **dap** are indicated and found in all mass spectra except **CuCat30**. The similarity can be explained with identical fragmentation patterns in the low mass range.

In order to observe a fragment of a macrocycle molecule, bonds have to break at two points of the ring. The first rupture converts it into a chain, the second creates a fragment. The mass of a ring that has been broken at a single position (open macrocylce) is identical to that of the closed macrocycle and therefore cannot be distinguished in mass spectrometry. Peaks with masses lower than the ring molecule can therefore only be observed after at least two effective collisions have taken place (see section 2.3.2, page 24). The necessity of two collision that create fragments requires high collision energies and thus a high fragmentor voltage.

For all molecules except **CuCat30** light fragments with a patterns similar to **dap** fragments appear. Even lighter fragment ions are created by subsequent fission of a side- or endgroup. All fragment ions contain the phenantroline group, which is known to be protonated by electrospray[25]. This functional group is thus the charge carrier site in the molecules **dap, M30, Mt33** and **Cat30**.

This conclusion is supported by the fact that all molecules are found in the singly charged, except **Cat30** which can be both singly and doubly charged. The catenane, in its non coordinated form, can be treated as two (almost) independent **M30**, both of which can be charged. Moreover no doubly charged fragments of **Cat30**$^{2+}$ ion are detected, what further supports the idea that each ring can carry only one charge at the phenanthroline site.

In contrast, the copper complex form **CuCat30** is only found singly charged and its fragmentation pattern differs significantly from that of **Cat30** (figure

4.24). This implies that copper is coordinatively bound to the phenantroline site that acts as a charge carrier in the uncoordinated molecule. [171]. Since in this case the two macrocycles cannot be charged independently any more, the charge carrier must either be the copper ion itself or the molecule is charged at another position. The fragmentation pathway is therefore significantly different and the molecule can only be singly charged (see figure 4.24). This result confirms previous findings, which state that the complex binding site is in the **dap** part of the molecule[171].

The fact that the subunits **Cat30** or **M30** of copper-catenate are not observed in the mass spectra shows the high stability of the copper complex. Obviously the bonds of the macrocycles break before the copper ion is removed from the molecule. Also no copper ions were observed, which excludes the possibility of undetected neutral **M30** or **Cat30** fragments of the copper catenate.

Metal Coordination of Cat30

Complex coordination plays a crucial role in the synthesis of **M30** type [2]catenanes. Initially two **dap** precursor molecules are bound via a copper atom in solution. In a next step a chemical reaction closes the rings and forms the copper-catenate[170].

The coordination ability of **Cat30**, which is inherited from the **dap** precursor is a reversible reaction in solution. Moreover, this reaction switches the conformation of the molecule[171]. This generates the idea to study the possibility of a similar reversible switching process in vacuum and monitor and control it on the molecular level in order to find out how to stimulate a molecular device. The recent UHV-STM study of **Cat30** type molecules on silver surfaces showed a complexiation reaction that can be used to switch the structure of adsorbed **Cat30** in vacuum, which, however, is not reversible so far[168].

Coordination binding of molecules can be monitored with ESI-MS through the mass change upon addition of a metal atom. In the experiments presented here, the complexion of **Cat30** with metals is obtained by simply immersing the bulk metal in the solution or by the addition of a salt containing the desired metal ion[171]. Dichloromethane/ethanol solutions containing **M30** and **Cat30** are brought in contact with copper, silver and gold for approximately $30min$. Before, the metals are cleaned in $2M$ citric acid and rinsed in water and ethanol. The solutions are then analyzed with the mass spectrometer.

Figure 4.25 displays the mass spectra for the **M30** and **Cat30** solution after having been in contact with copper and silver. Solutions in contact with gold does not show a changed mass spectrum and are therefore not displayed. Both **M30** and **Cat30** react with silver and copper. The mass spectra show the related peaks: **CuM30** at $632\,\mathrm{Th}$, **AgM30** at $675\,\mathrm{Th}$, **CuCat30** at $1195\,\mathrm{Th}$ and

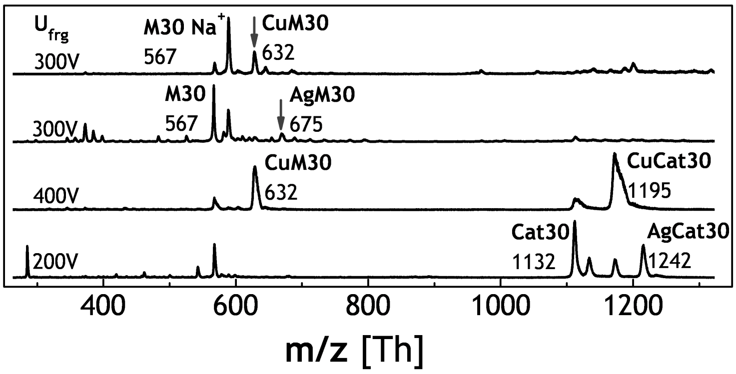

Figure 4.25 – Mass spectra **M30** and **Cat30** solutions brought in contact with silver and copper. **[top]** Cu + **M30**, **[upper]** Ag + **M30**, **[lower]** Cu + **Cat30**, **[bottom]** Ag + **Cat30**

AgCat30 at 1242 Th.

The relative abundances are significantly different, which often also depends on the concentration of the sample. Nevertheless it is clear that the reaction of **Cat30** with copper is the most favorable among the coordination reactions tested. Not only did almost all of the **Cat30** present in solution react to **CuCat30** but also small contaminations of copper present in the bulk silver resulted in a **CuCat30** contamination peak in the **AgCat30** spectrum with a significant abundance.

On the other hand, the **CuM30** and **AgM30** peaks are much less pronounced than their uncoordinated counterparts. Thus it can be concluded that the complexes of a single **M30** molecule are much less likely formed than those with **Cat30**, which offers two instead of one possible binding sites for the metal ions.

Detection of Small Amounts of Evaporated Cat30

In the aforementioned recent UHV-STM study[168] **M30**, **MT33**, **Cat30** and **CuCat30** are brought onto a silver surface in ultra high vacuum via thermal evaporation. Temperatures of 600 – 630 K were used, which might a priori lead to the decomposition of the organic molecules. In order to clarify whether the molecules observed on the surface really represent the intact compounds, ESI-MS is employed.

The molecules in question are evaporated and deposited on a gold surface, rinsed off and analyzed by mass spectrometry. Since the ionization technique is known the be non-destructive, the ions found in the mass spectrum represent the ions that have been deposited on the surface before (see section 2.1, page 13). Thus finding intact molecules proves that the compound in question in fact survives evaporation.

The molecules have been evaporated in high vacuum 1×10^{-6} mbar onto a gold on mica surface. A $10\,\mu$l droplet of DCM is applicated to the surface, dissolved the deposited molecules, and picked up by a microliter pipet again. The drop is then further diluted with ethanol containing approximately $0.1\,\%$ formic acid. The linear time-of-flight mass spectrometer finally analyzes this solution.

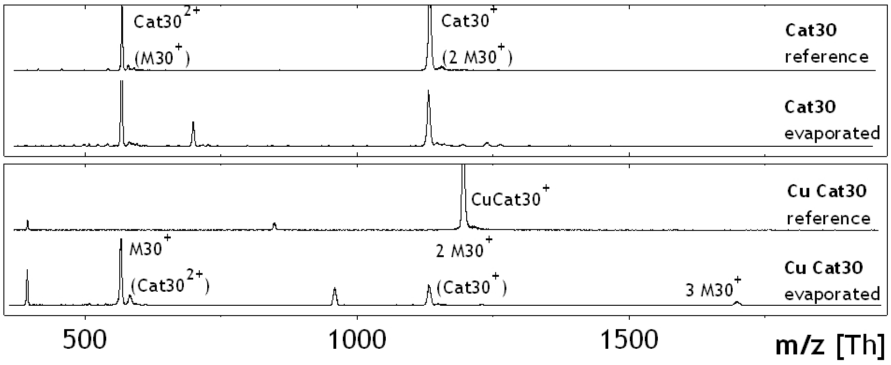

Figure 4.26 – **[top]** Mass spectra of evaporated **Cat30** with reference solution. Relative abundances and a complexion test with copper prove the absence of **M30** in the sample. **[bottom]** Mass spectrum of evaporated **CuCat30**. The sample contains mostly **M30**. No copper catenate is found.

The experiments are performed with **M30**, **Mt33**, **Cat30** and **CuCat30** $\cdot$ BF_4^-. While the first three compounds were found intact in ESI-MS indicating that they survived sublimation and adsorption on the surface, this is not the case for **CuCat30** $\cdot$ BF_4^-. Figure 4.26 shows the results for **Cat30** and **CuCat30** together with a reference mass spectrum. The latter is obtained by ESI-MS of the dissolved molecules.

The mass spectrum of **Cat30** is almost identical with the reference. The only difference is a peak at 700 Th that can be attributed to a contamination in the formic acid used. The relative abundance of the peaks at 567 Th and 1132 Th is characteristic for the singly and doubly charged **Cat30**. This mass spectrum indicates that in fact no **M30** but only double charged **Cat30** gives rise to the peak at 567 Th. The complexion reaction described above shows that **Cat30** survived the evaporation as a catenane.

The evaporated **CuCat30** $\cdot$ BF_4^- sample shows a completely different mass spectrum in respect to its reference. This already demonstrates that the molecule is not present as an intact unit at the surface. Mass spectrometry with remaining material from the crucible of the evaporator was found to contain intact **CuCat30**, indicating decomposition of the copper catenate instead of its sublimation. The fact that mostly **M30** can be identified by its typical peak pattern further confirms the latter finding.

Control experiments demonstrated that **M30** can be evaporated and deposited intact. **CuCat30** deposited on gold from a solution did not show any decomposition. Thus the **CuCat30** molecule decomposed upon heating and **M30** either as macrocycle or opened is emitted and deposited on the gold sample.

4.2.3 Polymers: Polyethylenimine (PEI)

Polymers are a class of organic macromolecules characterized by being a one dimensional, molecular chain structure obtained by the periodic repetition of a basic organic unit. In contrast to organic molecules, additional properties derive from this periodic structure, for instance viscoelastic mechanical properties that depend on the chain length. Polymers find many applications ranging from industrial to biological due to the possibility to assemble them from a relatively simple building block.

The high molecular mass of the polymer strands hinders their evaporation since polymers typically decompose when heated. Therefore the electrospraying of polymers becomes an attractive possibility to transfer them into an ultra high vacuum environment.

Due to the scalability of their size it is also interesting to monitor the general properties of molecular ions, for instance the mass-to-charge-ratio or the absolute charge state. The periodicity of the molecular structure enables the correlation of observed effects to the size of the particle, for instance the electronic structure observed in STM.

Polyethylenimine (**PEI**) is used as a typical example for polymer ion beams. PEI is a branched polymer with ethylenimine ($-(\mathrm{CH_2} - \mathrm{CH_2} - \mathrm{NH})_\mathrm{n}-$) as monomer unit (figure 4.27) whose molecular mass is $43.0678\,\mathrm{u}$. This polymer is commercially available in sizes ranging from $1000\,\mathrm{g/mol}$ to $\times 10^6\,\mathrm{g/mol}$, which corresponds to approximately 20 to 20000 monomer units in the polymer.

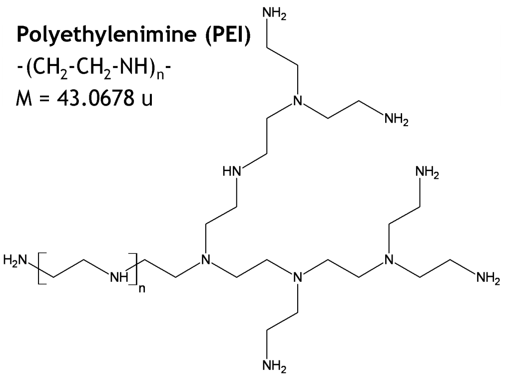

Figure 4.27 – Molecular structure of branched polyethylenimine (**PEI**). The monomer unit $-(\mathrm{CH_2} - \mathrm{CH_2} - \mathrm{NH})_\mathrm{n}-$ has a molecular mass of $43.0678\,\mathrm{u}$. The polymer is branched and amino terminated.

Due to the amine (−NH2, −NH) functional groups the polymer is strongly positively charged in solution when these groups are protonated[67]. The extreme hydrophility is also the result of the same functional groups.

Among many applications the use of **PEI** in biology and biochemistry is the most significant. Due to the its strong charging, **PEI** binds to other charged biomolecules leading to the precipitation of DNA or charged proteins. Todays most prominent application is the use of **PEI** as a RNA vector[172]. Finally **PEI** can also be used as backbone for synthetic DNA[173].

Observation of Different Terminations in MS

PEI solutions are created by the dilution of the commercially available stock solution (*Sigma P3143*) by the ration of $1:100$. In the mass spectrum, **PEI** is easily identified due to the repeated peaks every $43\,\mathrm{Th}$. As indicated in figure 4.28 by the letters (A),(B) and (C) there are at least three periodic series of peaks with this distance, which differs by a constant offset in mass-to-charge-ratio . This observation is made for a variety of parameters across the whole mass range.

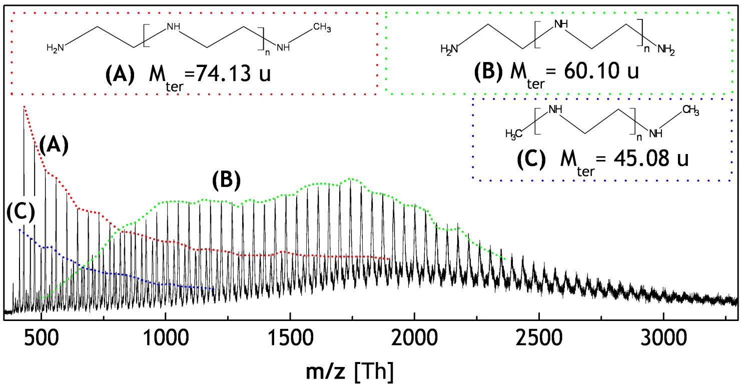

Figure 4.28 – Polyethylimine ions can have different terminations. Ions with the same termination are identified as groups of equidistant ($43\,\mathrm{Th}$) peaks in the mass spectrum (connected with lines).

The series of periodic peaks can be explained with the possible terminations of the polymer. The mass-to-charge-ratio of a singly charged **PEI** with n monomers and a termination with mass M_{ter} is $M_{\mathrm{PEI}} = n \cdot 43\,\mathrm{Th} + M_{\mathrm{ter}}$. Some examples for an unbranched polymer are given in figure 4.28. These terminations resemble the observed peak structure very well, even though the polymer is known to be branched.

The branching actually does not change the mass of the polymer. For each branch point introduced, an additional terminal is created. Thus the loss of a proton at the branch (−NH− becomes $-\mathrm{N}\overline{}$) is compensated with an additional proton at the terminal (NH_2 instead NH). Therefore many terminations of the branched polymer are equivalent to a linear polymer, at least for a mass spectrometric analysis.

Fragmentation and Charging

Upon a change in the fragmentor voltage, the composition of the **PEI** ion beams change dramatically (see figure 4.29). At 100 V a dense series of peaks can be observed between 100 Th and 1000 Th. The density of peaks gets lower for higher fragmentor voltages until the typical distance of 43 Th can be observed above 300 V fragmentor voltage. Moreover, for even higher fragmentor voltages, intense peaks are observed up to 3000 Th.

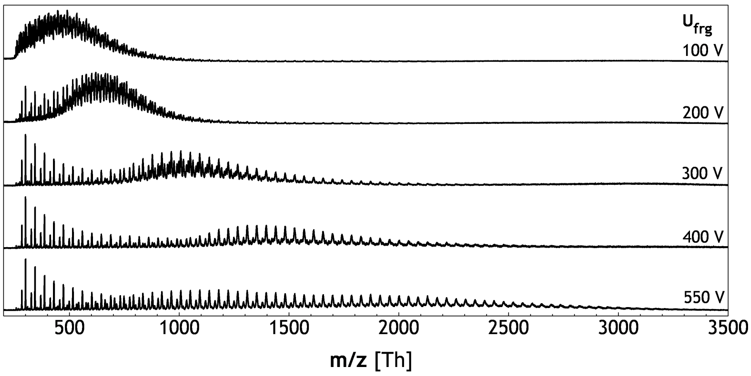

Figure 4.29 – Mass spectra of polyethylenimine for different fragmentor voltages. For low collision energies a highly charged polymer is observed. High declustering potentials result in singly charged oligomers of 2 to 80 monomer units.

The way **PEI** is charged is similar to the charging of a protein: $-NH_2$ terminals are protonated and become $-NH_3^+$ [67]. As a consequence each molecule of **PEI** can be at least doubly charged. Due to the branching the charge number can be even higher.

A first explanation of the observed mass spectra and of their dependence on the fragmentor voltage could be given by a transition to lowly charged molecules of the same size due to charge stripping. However, there are several strong arguments against this interpretation. Experiments with Cytochrome c clusters show that stripping of charges does not happen upon buffer gas collision (see section 4.1.4). Other experiments with organic molecules (Rhodamines see section 4.2.1, page 82, Catenanes see section 4.2.2, page 90) show that for fragmentor voltages of 150 V or higher, fragmentation is generally observed. Therefore, it can safely be assumed that also for **PEI** the rise in the mass-to-charge-ratio and the contemporary disappearance of peaks in the low mass-to-charge-ratio region is the result of fragmentation.

A simple model to test this hypothesis is implemented by means of a computer simulation. Unbranched polymers are represented by a linear chain of connected CH_2 and NH groups with the appropriate terminals. A number of charges is distributed randomly along the chain at the amino groups. The point at which the fragmentation occurs is randomized as well. Mass spectra averaged on many runs (typically 10^5) are recorded for up to three fragmentation events.

The results of the simulation qualitatively resemble the observed mass spectra of **PEI** to a great extent. Figure 4.30 shows an example for one polymer ion with a mass-to-charge-ratio of 358.4 Th which corresponds to a polymer of 167 monomer units with 20 charges. After three effective collisions a mass spectrum with the typical periodic peak pattern seperated by 43 Th can be observed.

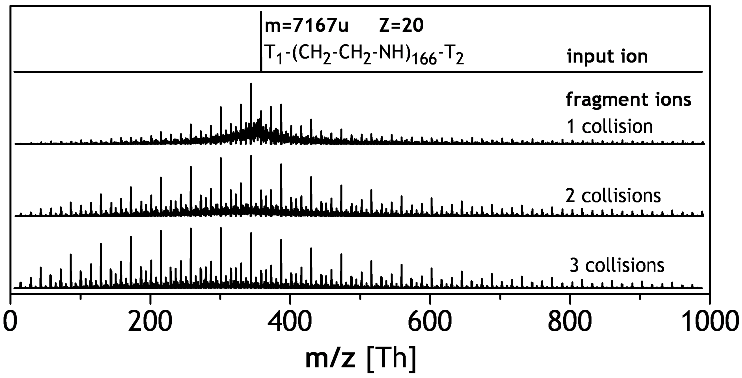

Figure 4.30 – Simulation of the fragmentation of an **PEI** ion of 167 monomer units with 20 charges. The simple fragmentation model is based on subsequently splitting of linear polymers with randomly distributed charges. This result shows that the polymers from the electrospray source are initially highly charged and get fragmented several times.

By using a starting configuration similar to the experimental one (upper spectrum in figure 4.29), the final result is very similar to the mass spectrum for 500 V, but the transition, reflected by mass spectra for intermediate fragmentor voltages, is different. In the mass spectra displayed in figure 4.29 for a fragmentor voltage of 300 V only singly charged polymer ions are observed at low mass-to-charge-ratio . In the higher mass-to-charge-ratio range still closely spaced peaks are observed which indicates that the heavier ions are still multiply charged.

The model is only able to reproduce the results of the fragmentation accurately when all molecule are fragmented the same number of times independent of their charge state. In the real experiment, however, this is not the case. Depending on the charge state, effective collisions occur more or less often. Since the kinetic energy of a charged particle in an electric field depends on the charge state, the higher charged particles overcome the fragmentation threshold in kinetic energy more often. The model in section 2.3.2, page 28 describes this process in detail.

As a result, among particles of the same mass, the more highly charged ones get already fissioned at lower fragmentor voltages. This effect is observed even more obvious for the many charge states of **BSA** in section 4.3.3.

4.3 PROTEINS

The most complex molecules that are dealt with throughout this work are proteins. Proteins are one of the most important classes of biomolecules. From the structural point of view a protein is a chain molecule composed of different amino acids and weighs between 10^3 u and 10^6 u. On top of this level of structural complexity, proteins interact with themselves to take on a specific functional form that is energetically most favorable[174, 175]. Therefore proteins can reach their functional form by self assembly when they are solvated in an aqueous solution at physiological conditions, which means near neutral pH-value, temperatures around 300 K and the presence of a variety of ions.

Due to its complexity, a protein has to be described on many levels. Often three different structures, primary, secondary and ternary, are differentiated. Primarily a protein is an inhomogeneous polymer bound by peptide bonds, composed of 22 different amino acids. This chain folds into structure elements, namely α-helix, β-sheet and different loops and turns, which are called the secondary structure. These structural domains then form the ternary structure which is the functional protein.

The unique structure of each protein after folding is thus a result of the interaction of the many different parts of the chain with the solvent, with itself and in some cases with other proteins that assist the folding[175].

The interaction with the solvent can be described in a simplified way in terms of hydrophobic and hydrophilic interactions. The hydrophobic parts of a protein chain are typically found in the center of the protein and thus are not in contact with the solvent, while the hydrophilic parts are on the outside. These hydrophilic groups can be charged depending on the pH value of the solvent.

Since proteins are nanoscale objects, for their detection and characterization elaborate techniques are necessary. Most microscopic techniques only resolve them as objects of a near round shape containing mostly carbon. The techniques to analyze protein ternary structures are X-ray diffraction (XRD) and nuclear magnetic resonance (NMR) spectroscopy, which both require a large amount of sample material and are thus very extensive. Biochemical reactions such as the binding of an antibody to a protein can be used for specific identification. This group of methods is used in many special cases where the detection of the special reaction is of interest, rather than the detection of the protein.

The invention and development of electrospray ionization enabled the introduction of mass spectrometry into the field of biochemistry, since large fragile ions like proteins can be ionized and thus detected. Today protein analysis with a high throughput and a high resolution is available. The most common method is high pressure liquid chromatography coupled to a tandem mass spectrometer. It is capable of identifying proteins from biological samples by comparing them to huge databases. Modern techniques are capable to screen for modifications like phosphorylation on specific sites of a protein[33].

For preparative mass spectrometry the goal is set differently. In order to bring a large current under controlled conditions onto a surface for soft landing, the composition has to be monitored. The starting point of a deposition experiment is always a solution with known ingredients. The task is to optimize the settings of the apparatus for the deposition of an ion beam with the desired properties (ion type, charge state, energy, etc.).

Furthermore, as mentioned before in the sections about electrospray ion beam mass spectrometry (section 2.3, page 24), from the interaction of ions and background gas, information related to the stability upon collision can be gained. For proteins as for any other molecule to be deposited, these insights are valuable when the behavior of the molecule in a soft landing experiment is investigated.

Mass spectrometry experiments are performed on bovine serum albumin (**BSA**, *Sigma A4919*) and Cytochrome c (**Cyc**, *Fluka 30398*). The two proteins differ greatly in mass (66560 u and 12300 u) and also in their inner structure. **BSA** is stabilized by 15 disulfide bonds, while no disulfide bonds are present in Cytochrome c. The goal of the mass spectrometrical studies of these two proteins is to establish the techniques that are necessary in order to generate a protein ion beam with properties required for ion beam deposition. The focus of the experiments is directed on the ion-gas-interactions, due to the fact that the insights on the behavior upon collisions gained from these might as well be applied to ion surface interaction (section 2.3.3, page 31).

4.3.1 BSA as Highly Charged Gas Phase Ion

Bovine serum albumin **BSA** is the main protein in the blood serum of cattle. Serum albumin in general has a good binding capacity for water, some types of ions, fatty acids, hormones, bilirubin[2] and drugs[176]. Its main functions are the regulation of the colloidal osmotic pressure of blood and the transport of substances relevant for the metabolism. Moreover it is used widely in biochemistry since it shows almost no effect on other proteins and can therefore be used to create artificial environments that can mimic physiological conditions[177].

---

[2] Bilirubin is an important Heme precursor.

The molecular mass of **BSA** is 66430 u. Figure 4.31 shows a mass spectrum of the protein. The solution for mass spectrometry are prepared as described in section 5.1.1, page 113 and section 3.3.1, page 58. The peaks that belong to the protein are marked (△). The spacing between the peaks becomes larger for higher mass-to-charge-ratio , which is characteristic for multiply charged particles that are present in the ion beam at different charge states.

The observed peaks for the different charge states of **BSA** can be used to determine its precise mass. In figure 4.31 [left]the mass-to-charge-ratio M of the peaks is displayed as a function of the peak number X (from left to right in the mass spectrum). The resulting curve can be fitted with the function $M(X) = \frac{m}{Z_0 - X + 1}$, where m is the mass of the protein and Z_0 is the charge state of the peak with the lowest mass-to-charge-ratio and X is the peak number. The fit results are given in charge states z and lie between 64 and 24. The mass of the protein is found to be 66454 ± 22 u. Since many peaks were used to calculate the mass, the precision exceeds the limitation of the instrumental resolution by a factor of 10.

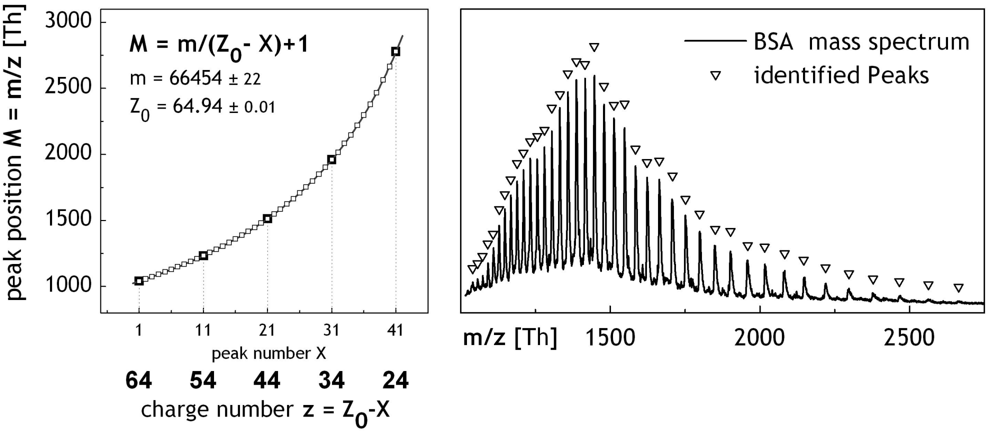

Figure 4.31 – Mass spectrum of BSA **[right]** and calculation of molecule mass and charge states **[left]** with fitting function and found parameters.

BSA is a heavy protein compared to others. The measured mass is in good accordance with literature values[176], the deviation can be attributed to adducts and the low instrumental resolution. Besides pure mass measurements, electrospray ionization mass spectrometry can give additional information about a protein. As mentioned in section 4.3 proteins can be described by different substructures. Transitions between these, especially folding and unfolding, results in major changes in the properties of the protein. In particular the biological function of the protein is lost upon unfolding. Such transitions can be expressed by changes in the mass spectrum, since they affect the structure of the molecule.

The charge state distribution for instance is an important indicator for the state of a protein. The number of charging sites available depend on the folding status of the protein[174]. Typically an unfolded protein can be charged more highly than its folded counterpart.

For **BSA** it is known that the breaking of the disulfide bonds leads to an increase in charge by 10 charges. Typically, molecules with a thiol group like dithiolether or mercaptoethanol irreversibly bind to an opened disulfide bond, which hinders the folding. According to literature[178], the present charge states of **BSA** in the mass spectrum in figure 4.31 thus indicates that the disulfide bonds in the studied **BSA** solution are still intact, hence the protein is folded or at least not completely unfolded. Therefore the ion beam created in this experiment can be used in order to deposit folded proteins onto a surface in vacuum.

4.3.2 Charge State Distribution of Cytochrome c

Cytochrome c (**Cyc**) is a very important protein from the mitochondria involved in many cell functions such as electron transfer in the citric acid cycle and apoptosis[179]. Cytochrome c shows some distinct differences to **BSA**. It is smaller, has less charging sites and no disulfide bonds. The latter fact makes Cytochrome c more responsive to harsh environmental conditions. Nevertheless both molecules are proteins and thus should provide similar results in an electrospray mass spectrometry experiment.

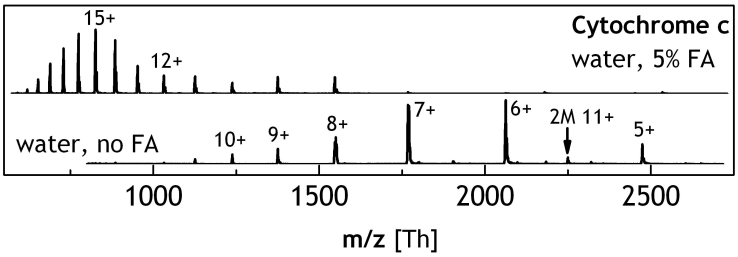

Figure 4.32 – Mass spectra of Cytochrome c. **[top]** 5 % formic acid (FA) is added to the same solution, that before produced the **[bottom]** mass spectrum.

Figure 4.32 shows the mass spectra of two Cytochrome c samples. One spectrum, (figure 4.32[bottom]) where no formic acid is added to the protein solution, and the other with 5 % formic acid. Both spectra show peak groups that can be identified as Cytochrome c in different charge states, calculated by the same method as for **BSA** section 4.3.1, page 106. The acidified **Cyc** shows charges between $+8$ and $+20$, while the non acidified protein shows charges between $+5$ and $+11$. The amount of charges per protein almost doubles upon acidification.

There are two possible mechanisms that could result in a higher charged protein when the solution is acidified. First, a lower pH value simply shifts the equilibrium towards higher charged proteins in solution since the concentration of H^+ is increased. Second, as an effect of the addition of acid, the protein is denatured. An unfolded protein exhibits more potential charge sites and thus is expected be higher charged.

The acidification also goes along with a change in color. The slightly red **Cyc** solution becomes colorless. The same transition, color change and high charges in the mass spectrum, is observed after heating or long ultrasonication of a **Cyc** sample.

Heat or rough mechanical treatment is known to denature proteins. This indicates that indeed the unfolding of the protein is responsible for the high charge states observed. The experimental results and conclusions confirm results published for Cytochrome c[145, 144]. Nevertheless these experiments demonstrate that it is indeed possible to transfer solvated protein molecules into the gas phase in their native configuration. This is an important characteristic of a protein ion beam in general which is to be used in deposition experiments (see section 5.1).

4.3.3 Fragmentation of BSA

Fragmentation is used as identification method for proteins. The product ion mass spectrum is characteristic like a fingerprint for a specific protein. Even mixtures of proteins can identified: the comparison with a database and the known mass of the selected primary ion is typically enough. The typical fragments of a protein are only of secondary importance for a soft landing experiment. More interesting is the question at which energy the threshold for fragmentation is, as already discussed for various organic molecules (section 4.2, page 82), polymers (section 4.2.3, page 101) and clusters (section 4.1.3, page 74 and section 4.1.4, page 79).

In figure 4.33 three mass spectra of **BSA** at 150 V, 250 V and 300 V fragmentor voltage are displayed. At the lowest voltage the typical pattern for a highly charged protein is observed. For 250 V the highly charged **BSA** peaks cannot be distinguished anymore and many intense peaks at a low mass-to-charge-ratio have appeared. At high mass-to-charge-ratio the lowly charged **BSA** peaks can still be separated from the background, while in the low mass-to-charge-ratio the highly charged **BSA** peaks are no longer visible. Finally at the highest voltage there is almost no signal from **BSA** molecules left, while the low mass-to-charge-ratio peaks are still present and more abundant for lower mass-to-charge-ratio .

The nozzle skimmer fragmentation (see section 2.3.2, page 28) takes place at a pressure of 2.3 mbar which results in a very high number of collisions. In this case the collision energy only depends on the energy gained between two events (equation (2.21)), which is proportional to the dragging electric field, the mean free path, and the charge of the particle.

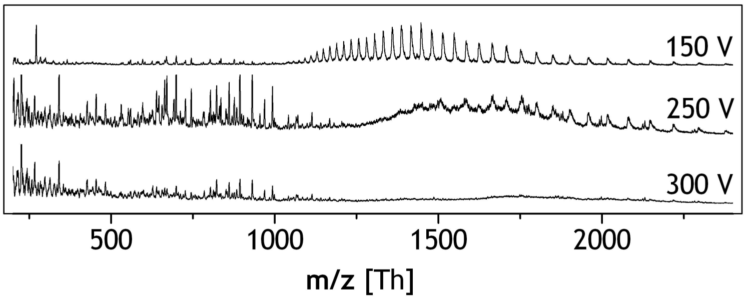

Figure 4.33 – Mass spectra of **BSA** for several fragmentor voltages and pressures.

For a certain threshold value of collision energy the protein will be fragmented, either by a single intense collision or due to the buildup of internal energy caused by many collisions. The linear dependence of the collision energy on the charge state means that the highly charged proteins collide with a higher energy than the proteins with a lower charge.

The mass spectrum for $250\,\mathrm{V}$ fragmentor voltage ($U_{\mathrm{dec}} = 200\,\mathrm{V}$) allows the estimation of the threshold energy since the proteins with charge states above $45+$ are already fragmented. For such large particles the mean free path is rather short which leads to low collision energies. From equation (2.26) a value of $0.25\,\mathrm{eV}$ can be calculated for **BSA**. The threshold value for the collision energy of $0.25\,\mathrm{eV}$ is in a range which can affect the ternary structure of the protein, but not the covalent bonds in its backbone. However, the distribution in kinetic energy of the background gas and the ion beam and free flight length lead to a broadening of the collision energy distribution. Thus, when the collisions are numerous and the collision energy distribution is broad, the probability of one high energy collision which is above the fragmentation threshold is high. Furthermore the high number of collisions promote the fragmentation due to the buildup of internal energy.

The strong underground signal in the mass-to-charge-ratio region of the protein is due to protein fragments. Similar to the fragmentation of the polymer (see section 4.2.3) the fragments of a highly charged large molecular ion are in the same mass-to-charge-ratio region as the ion itself.

5

RESULTS and DISCUSSION ION BEAM DEPOSITION

The sole purpose of the electrospray ion beam deposition apparatus is the controlled vacuum deposition of particles that otherwise cannot be brought into the gas phase. In chapter 4 the creation and mass spectrometric analysis of ion beams from a variety of materials is discussed. It is shown that ion beams of ionic and non-covalently bound clusters, large organic molecules, polymers and even proteins can be created.

In the chapters 2 and 3 the function of the deposition apparatus and the involved phenomena are discussed. The ions are created by electrospray ionization (section 2.1, page 13) and the ion beam is formed by ion-gas-interactions (section 2.3.2, page 24). An ion beam can be mass selected (section 3.2.1, page 52), mass-analyzed (section 2.2, page 20 and section 3.1.5, page 44) and its energy (section 3.1.4, page 42) and focusing can be defined (section 3.1.2, page 38 and section 3.2.2, page 56). Finally the deposition can take place in high- or ultra high vacuum on sample holders which allow to adjust the collision energy in order to achieve soft landing and to control the coverage by measurement of the current (section 3.1.6, page 46).

In this chapter experiments on ion beam vacuum deposition of molecules and clusters are presented. These experiments show the capabilities of the developed ion beam apparatus. The deposition of the protein **BSA** shows that soft landing even of the largest biological molecules is possible and the structures formed by this protein on the surface is shown. The surfactant sodium dodecyl-sulfate (**SDS**) is used to show that functionalities of organic molecules are related to the structures they form in vacuum. Rhodamine, a dye molecule, is used as a soft landing probe due to its fluorescence. With this molecule it is shown that the soft landing ratio can be determined quantitatively. Finally it is demonstrated that very large nanoparticles can be ionized highly in electrospray and deposited.

5.1 PROTEIN DEPOSITION – BSA

Introduction

As outlined in section 4.3, page 105 proteins are very versatile molecules with many interesting aspects to study and many applications, not to mention their natural functions in all living beings, which cannot be matched by anything manmade. One of the main reasons for the popularity of electrospray ionization is the fact that it is capable of ionizing proteins without destroying them.

In section 4.3, page 105 the properties of protein ion beams created by an electrospray source are studied by means of time-of-flight mass spectrometry. **BSA** and Cytochrome c are found both to be highly positively charged. Especially the collision induced dissociation of these protein ions is studied and it is shown that fragmentation occurs as a result of ion gas collisions when a certain threshold value for the collision energy is exceeded.

The interest in studying proteins in the gas phase is mainly caused by the prospect of further advancing the analytical techniques related mass spectrometry for biological systems. Nevertheless, proteins at surfaces offer the possibility to use their specific functions in applications like sensors[11] and chemical reactors or to study proteins with the available surface sensitive techniques, that otherwise cannot be applied to proteins in solution.

The typical approach to deposit proteins on surfaces is solution chemistry. Proteins are bound in some way to a solid or a soft matter surface, which is immersed in an aqueous solution. The environment created by the liquid keeps the proteins in their native state. This approach has the advantage of being gentle with respect to the protein. The disadvantage is that such samples are not suitable for vacuum based analytical and preparative techniques, which often can deliver information that otherwise cannot be obtained.

Preparative mass spectrometry with soft landing is one possible approach to bring proteins to a surface in vacuum. There exist only few examples where proteins have successfully deposited[54, 53, 56]. All these examples show that the soft landing technique contains a number of inherent difficulties: the soft electrospray ionization technique with mass selection and differential pumping for high vacuum is barely able to produce enough ions for deposition, the protein ions might be intact but denatured and the biggest issue of all is the soft landing of the protein ion beam on a substrate[66].

The goal of this section is to study the protein deposition from the viewpoint of morphology of the protein, since its functionality is strictly coupled to its structure. For this purpose BSA ion beams (as introduced in section 4.3.1, page 106) are used as a model system for a complex functional biological material. For the deposition experiments and morphology studies they have the advantage of being big enough to be observed in AFM, which can be discerned from figure 5.1.

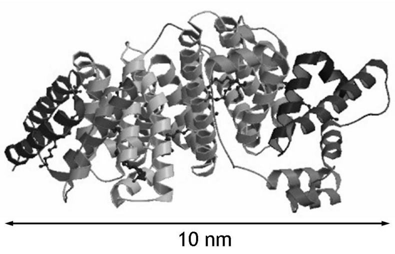

Figure 5.1 – BSA ribbon model. The globular protein has a size of approximately $2.5 \times 3.0 \times 10\,\mathrm{nm}$ sized when folded.

The effect of the ion surface interaction on the morphology of **BSA** is studied as a function of several parameters, such as kinetic energy, ion beam composition and substrate surface.

5.1.1 BSA Deposition - Morphology

BSA is a common large globular protein of mass $66500\,\mathrm{u}$ as introduced in section 4.3.1, page 106. Ion beams of **BSA** are prepared from acidified solutions of the molecule in methanol and water at a concentration of $1.5\,\mathrm{M}$ (section 3.3.3, page 60). The beams of **BSA** are typically very intense, up to $100\,\mathrm{pA}$ have been detected in the TOF chamber for an ion beam of many different charge states. Their kinetic energy can be tuned between $10\,\mathrm{eV}$ and $20\,\mathrm{eV}$ per charge (see section 3.3.3, page 60) and an additional deceleration voltage can be applied at the deposition target in order to set the collision energy to a value well below $5\,\mathrm{eV}$ per charge in order to achieve soft landing.

Time-of-flight mass spectrometry is used before the deposition to investigate the beam composition. Depending on the pH-value, **BSA** ions as prepared by the ion beam deposition setup have around $25 - 65$ charges per molecule, which corresponds to a mass-to-charge-ratio of about $1000 - 2500\,\mathrm{Th}$ (see section 4.3.1, page 106). The RF-voltage at the low pressure quadrupole Q2 is set to $V_{\mathrm{RF-Q2}} = 250\,\mathrm{V}$ in order to transmit **BSA** ions only and avoid the transmission of fragments of lower mass-to-charge-ratios .

On the sample which is located in the 4th pumping stage at high vacuum a current between $1\,\mathrm{pA}$ and $50\,\mathrm{pA}$ depending on the beam energy is measured. For a deposition spot of $12.5\,\mathrm{mm}^2$ (see section 3.1.6, page 46) this corresponds to a particle flux between $6 \times 10^6\,\mathrm{s}^{-1}$ and $3 \times 10^8\,\mathrm{s}^{-1}$. In the case of proteins, which are $1 - 20\,\mathrm{nm}$ in diameter, such currents result in a duration in the order of $1 - 10\,\mathrm{h}$ for the deposition of a full monolayer.

Silicon samples with native $\mathrm{SiO_x}$ surfaces and freshly cleaved HOPG is used as deposition target (section 3.3.2, page 59). After deposition the samples are analyzed with AFM.

BSA on Graphite: Diffusion Limited Fractal Growth

Figure 5.2 shows AFM images of a highly oriented pyrolytic graphite (HOPG) surface after deposition of BSA at low kinetic energy. On the HOPG surface two dimensional fractal islands are observed. Globular objects of approximately $2\,\mathrm{nm}$ height and up to $30\,\mathrm{nm}$ diameter can be identified as single building units in the images with lowest magnification (figure 5.2[left]). The size of the building units is compatible with that of a single BSA molecule in aqueous solution ($116\,\text{Å} \times 27\,\text{Å}$)[92, 93].

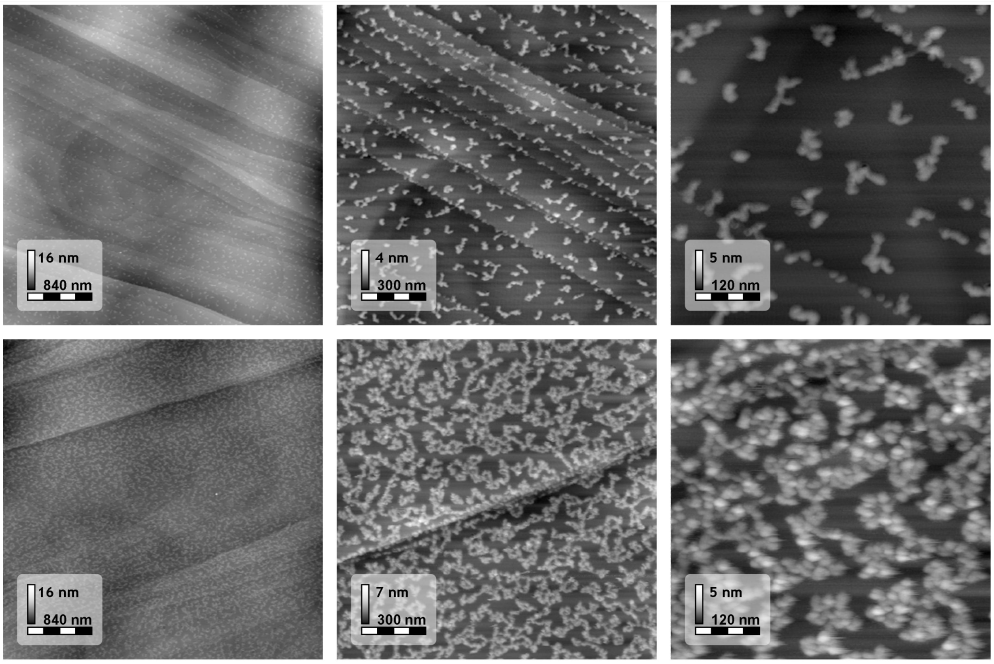

Figure 5.2 – AFM images of **BSA** deposited on HOPG for different coverages and magnifications. Single **BSA** units (bright spots) form fractal agglomerations. A second layer is formed at high coverage before the first layer is closed, which can be observed at high magnification for high coverage.

On HOPG, the BSA molecules decorate primarily the step edges at low coverage. 2-dimensional fractal clusters are not only formed at step edges but also on terraces. Upon further growth, preferably the terraces are covered with a 2D fractal networks, but also a beginning second layer is observed even though the first monolayer is not finished. The brighter spots in figure 5.2 can be attributed to the growth of a second layer of BSA. In the cross sections shown in figure 5.4[left]the line scan for the high coverage sample shows structures of $4\,\mathrm{nm}$ height while the graph for low coverage is limited to $2\,\mathrm{nm}$.

The observed structure suggests a diffusion limited growth mode for the system **BSA** on HOPG[180, 129]. Step edge decoration and fractal agglomeration show that one **BSA** particle is mobile on the graphite surface. However, the mobility of an agglomeration is limited, just like the mobility of **BSA**, once it is bound to a step edge. The observation of the second layer before the first monolayer is completely closed can also be explained by the strong interaction between the particles in contrast to a rather weak interaction between the molecule and the HOPG surface.

In most cases, proteins taken from their natural environment will change their structure. In solution, **BSA** is known to undergo structural changes as a function of the pH-value. In particular for low pH, as used for the spray solution in the present experiments, **BSA** unfolds partially to a string-like molecule with four bulky centers along the string[181]. Further environmental stress can cause an even stronger unfolding and the protein then arranges into a random coil.

The charge states of the **BSA** molecules between 25 and 65 elementary charges per molecule observed with time-of-flight mass spectrometry suggests that the ion beam consists of folded or partially folded protein ions (see figure 4.31, [182, 183]). Nevertheless the collision with the surface induces further stress on the molecule, which can lead to partially or complete unfolding of the molecule.

In whatever form the **BSA** molecule is present at the surface does not play a mayor role on the interaction of the molecule with each other or with the substrate. In solution **BSA** is known to be a very passive molecule, because it does not react with other proteins .

Taken out of solution the behavior can be assumed to be different. The formerly solvated hydrophobic shell of the protein is in an energetically unfavorable state in vacuum. The same is true for a partially or completely unfolded **BSA**. This is causing a substantial interaction with other **BSA** molecules and with the substrate surface. This interaction is not strong enough to prevent the monomer from being mobile at all, but it inhibits the motion at least of bigger agglomerations. These nucleation conditions are very similar to those defining the diffusion-limited-aggregation growth[180]. In fact, the fractal shape of the BSA-clusters appears to be similar to aggregates formed under these conditions in various surface-supported atomic and molecular systems[129, 111].

Since it is not very likely for a protein to fold back to its native structure in presence of an inorganic surface and obviously impossible for a fragment, it is reasonable to expect that both unfolded and intact **BSA** molecules are present on the surface as random coils. Since **BSA** does not show any specific chemical binding site with each other, its binding properties with other **BSA**, the surface or a random coil are not dependent on its folding state. The observed structures therefore can originate from both folded or unfolded **BSA** or even from a mixture of them. This conclusion accords very well with the observation that, independently of their size, the building units in the fractal agglomerations appear non-uniform.

BSA on Silicon: Random Growth

The results of the deposition of $\mathbf{BSA}$ ions at low energy on $\mathrm{SiO_x}$ substrates is distinctly different from the result for HOPG. No ordering whatsoever is observed. The roughness of the surface has increased from $0.5\,\mathrm{nm}$ typical for a native silicon surface to a value of $2.5\,\mathrm{nm}$. This indicates sub monolayer coverage of the $\mathrm{SiO_x}$ with $\mathbf{BSA}$ molecules. The roughness results from a random distribution of the particles of the same size as already found on graphite. Since no ordering of the $\mathbf{BSA}$ molecules occurs, the single particle is not clearly distinguishable in AFM.

Some single $\mathbf{BSA}$ particles are identified as isolated bright spots, best seen in figure 5.3[right]for the highest magnification. Their size is similar to the building units of the fractal agglomerations found in the HOPG experiments. This supports the conclusion that the same $\mathbf{BSA}$ particles are present on both $\mathrm{SiO_x}$ and HPOPG substrates after ion beam deposition. Assuming that same size means same folding state and same mass, that observation also suggests soft landing deposition.

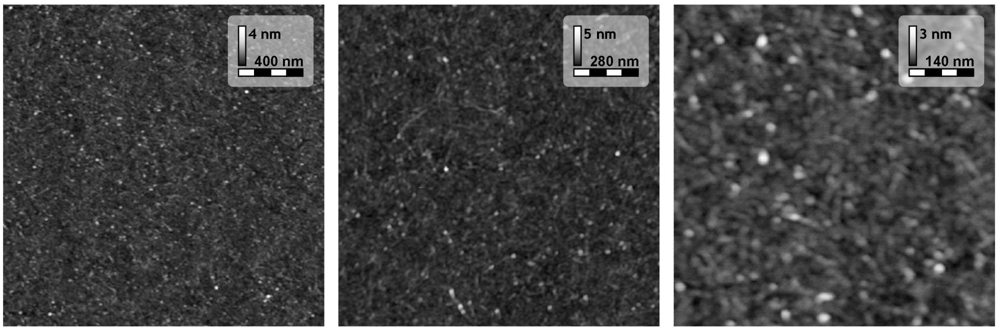

Figure 5.3 – AFM images of a silicon surface after ion beam deposition with $\mathbf{BSA}$ ions at $5\,\mathrm{eV}$. The single bright spots correspond to $\mathbf{BSA}$ particles.

No larger agglomerations of particles are found on the silicon surface in contrast to HOPG. The reason for this is the different nature of the surface. The chemically more active silicon surface offers many pinning sites in form of defects, but also simply due to its amorphous nature [112, 184]. Moreover the polar surface interacts strongly with the $\mathbf{BSA}$ molecules, which lead to less diffusion in contrast to $\mathbf{BSA}$.

5.1.2 Soft and Hard Landing of Large Protein Ions

Introduction and Experimental Details

The morphologies found for the low energy deposition of $\mathbf{BSA}$ on $\mathrm{SiO_x}$ and graphite might suggest that the spherical particles found are in fact intact $\mathbf{BSA}$ proteins, yet they do not prove it. The deposition of proteins, when done in order to employ their unique functionality only makes sense, when soft landing can be ensured.

To address the question whether the $\mathbf{BSA}$ deposition process can be considered as soft landing, further experiments are performed in order to gain more information of the dependence of the morphology on the deposition energy (see section 2.3.3, page 31). In particular, deposition experiments on HOPG surfaces are carried out as a function of the beam energy in the range of $0.5 - 65\,\mathrm{eV}$ per charge. At the highest collision energies the fragmentation of the protein ions due to surface induced dissociation has to be expected. For comparison a $\mathbf{BSA}$ fragment beam is intentionally created by collision induced dissociation and deposited at soft landing energies.

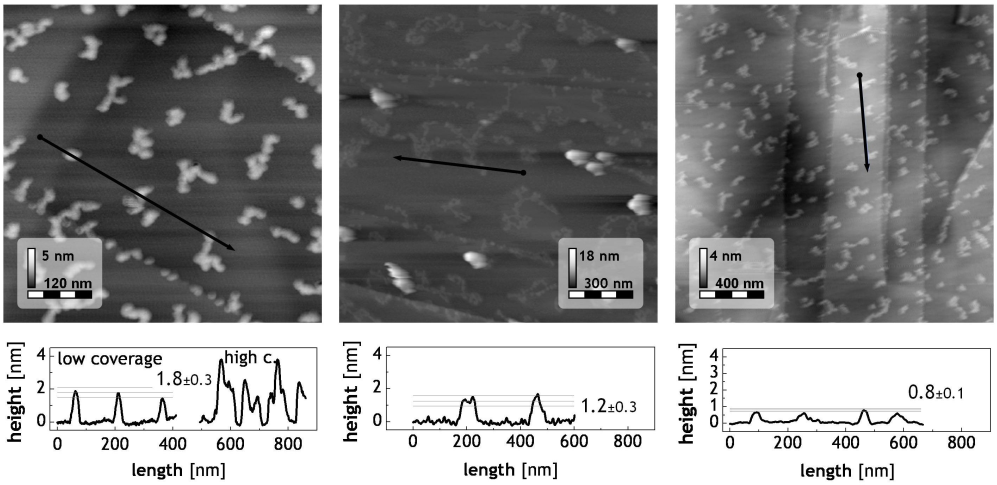

Figure 5.4 – AFM images and cross sections of HOPG surfaces after $\mathbf{BSA}$ deposition. **[left]** low energy $\mathbf{BSA}$ **[middle]** deposition at high energies **[right]** fragment deposition at low energies. In all cases fractal growth is observed. The building units of the high energy deposition and the fragment deposition are distinctly smaller than the soft landed BSA particles.

The beams at different ion energies are prepared under conditions identical to those in section 5.1.1, page 113. At the highest energies, because of the better collimation, deposition currents as high as $60\,\mathrm{pA}$ are measured. The fragment beam is prepared by applying $350\,\mathrm{V}$ to the fragmentor electrode and by mass selecting the resulting beam in the low pressure quadrupole Q2. Only the ions between $0\,\mathrm{Th}$ and $1000\,\mathrm{Th}$, which correspond to $\mathbf{BSA}$ fragments, pass the quadrupole. Due to the mass selection, the current at the sample is reduced to $8\,\mathrm{pA}$ and accordingly longer deposition times (up to $3\,\mathrm{h}$) are employed.

Results and Discussion

The results obtained for the intact ion beams with energies lower than $15\,\mathrm{eV}$ are identical to those shown in section 5.1.1, page 113. The situation is different for the high energy (65 eV) and the fragment ions. The corresponding surface morphologies are depicted in figure 5.4 middle and right, respectively, the low energy case is displayed on the left. At a first sight, the AFM images show the same fractal agglomerations of BSA on HOPG at low energies. The only evident difference are the additional structures with diameters up to 100 nm for the high energy deposition.

Nevertheless, a detailed quantitative analysis shows that the fractal islands in figure 5.4[middle][right]actually differ in height from the soft landed **BSA**. The building units of the structures shown in figure 5.4[left]have a height of $1.8{\pm}0.3$ nm, while those obtained from the fragment beam are only $0.8{\pm}0.1$ nm high.

This smaller size is clearly due to the reduced mass of the fragments in respect to the intact BSA proteins. As a consequence, the height of 1.2 ± 0.3 nm measured for the structures formed by depositing 65 eV ions becomes an indication that energetic particle-surface collisions induce partial fragmentation of BSA. The observation that for lower deposition energies no fragmentation is taking place agrees well with similar results reported in literature[53, 54].

The collision energies at the onset of fragmentation in ion-gas and ion-surface-collisions though can only compared by magnitude of order at best, since it is not know, which fraction of the collision energy is taken up by the surface, and which by the molecules (section 2.3.3, page 31). Especially large molecules like proteins with many degrees of freedom can store a large amount of internal energy before a bond is broken.

The observation of a common fractal growth mechanism is observed in the deposition experiments that produce building units of different sizes (low energy, high energy and fragment beam), implies that the particle-particle and the particle-substrate interactions are weakly dependent on the particle size. This could happen if the **BSA** proteins and their fragments are denatured and assume a random coil conformation.

In summary the protein **BSA** has been deposited successfully from low energy ion beams on solid surfaces in vacuum. Depending on the substrate the protein is found to have a limited or no mobility on the surface, which results in diffusion limited aggregation on HOPG and random thin films on proteins on SiO_x substrates.

Soft landing of the protein is achieved for kinetic energies of up to 15 eV per charge. This evidence is found in the size of the single building unit of the fractal agglomeration of **BSA** on graphite. For high collision energies and for fragment deposition small particles are found in contrast to big particles for the low energy deposition. The values found for the soft landing energy fit with the values published for similar protein deposition experiments.

5.2 DEPOSITION OF AMPHOPHILIC SALTS

Introduction

The name surfactant is derived from the term surface active agent and is used for a group of molecules that show strong effects on wetting and surface tension. Such molecules consist of two parts. The hydrophilic part likes to be in contact with water, while the hydrophobic or lipophilic part does not. It is this double functionality named amphophilic that lead to the characteristic behavior. Surfactants have a low surface energy which is why they form large interfaces. Due to hydrophobic-hydrophilic interaction they also tend to populate interfaces.

The interaction of amphophilic molecules and water results in a variety of complex structures. At a certain concentration micelles are formed in which few surfactant molecules are arranged in a spheres with the hydrophobic part inside the sphere preventing the hydrophobic part from being solvated by water. With growing concentration the structures get more complex: double layers are formed at interfaces, vesicles can be formed in solution, finally stacks of surfactant double layer tubular and other structures with a huge interface area can be observed[185, 186], which underlines how big the effect can be that is merely caused by a double functionality in a molecule.

The Hydrophobic-Hydrophilic Effect

The hydrophobic-hydrophilic effect is driven by the gain in entropy for the water molecules, due to the fact that the hydrophobic tails of sodium dodecyl sulfate **SDS** molecules do not need to be solvated, when they are in contact with a surface or incorporated in a micelle or a double layer[187]. The reason is that the solvation energy of the hydrophobic tail of an amphophilic molecule in water would not compensate the energy loss through the increased entropy of the water. Therefore the ordering of surfactant molecules at an interface is attributed to what appears like a repulsive force between the hydrophobic part of the surfactant molecule and the water. This force is not due to any electromagnetic interaction but purely present due to gain in entropy in the water since it has especially strong intermolecular bonds.

A great number of other molecules ranging from small ones like **SDS** to big proteins like the Hydrophobin protein show properties related to the hydrophobic-hydrophilic effect[188]. This interface effect has an enormous importance especially in many biological processes including formation of biological membranes from lipids and the folding of proteins[142].

Properties and Applications of SDS

Ionic surfactants such as sodium dodecyl sulfate (**SDS**, $C_{12}H_{25}SO_4Na$, 288.38 u, Sigma Aldrich L4390) have a wide range of important applications in science and technology, for example for cleaning, as emulgators, as wetting agents, for surface passivation or as lubricants.

In particular **SDS** is very important in biochemistry due to its application in the SDS-PAGE (**P**oly**A**crylamide **G**el **E**lectrophoresis) separation technique. Here **SDS** is used to solvate especially insoluble proteins and to stabilize all types of proteins in their denatured form, which makes the separation independent from the specific protein properties but only dependent on their size. Another popular application of **SDS** is the dispersion of otherwise insoluble nanoparticles like carbon nanotubes in aqueous solutions[186]. Both applications make use of the hydrophobic-hydrophilic interactions.

Due to its wide range of applications, **SDS** is useful as a model system for amphophilic molecules in order to study the film growth of surfactants on different substrates under high vacuum conditions and compare it to the film growth observed in solution. It is shown in section 4.1.3, page 74, that a **SDS** cluster ion beam can be created using electrospray ionization.

In order to study the film growth of a surfactant in vacuum, an **SDS** ion beam is landed on HOPG and SiO_x substrates, which are analyzed by ex-situ AFM measurements under ambient conditions (section 3.4.1, page 64). The results are compared to samples created by solution casting of **SDS** on equivalent surfaces. The difference from the solution cast samples is, that the growth process of the **SDS** thin films in vacuum takes place without water, which plays a crucial role in the formation of surfactant structures due to its role in hydrophobic-hydrophilic interactions. Therefore it is expected that the morphology of the **SDS** films reacts to this change of environment.

In addition, the role of the surface on the growth of **SDS** in vacuum is investigated by introducing two different substrates with distinctly different properties. SiO_x is known to be moderately hydrophilic, while HOPG has a very hydrophobic surface.

5.2.1 Ion Beam Deposition of SDS

Solutions of **SDS** are prepared of $50\,\%$ water and $50\,\%$ methanol at a concentration of $1\,\mathrm{mg/ml}$. The ion beam is generated either using the pneumatically assisted orthogonal spray at flow rates of $2\,\mathrm{ml/h}$ or the off line nanospray interface operating at approximately $10\,\mathrm{ul/h}$. A typical mass spectra obtained is shown and discussed in section 4.1.3, page 74. The ion beam consists of clusters of many **SDS** molecules with one or two excess Na^+ as charge carriers per cluster. For the deposition experiments the ion beam is limited to single charged clusters by applying high fragmentor voltages.

The mass-to-charge-ratio range for deposition is set using the quadrupole Q2. The large clusters of **SDS** require transmission only above $311\,\mathrm{Th}$ which is the mass-to-charge-ratio of the smallest **SDS** ion. The mass range for deposition is therefore set from $250\,\mathrm{Th}$ to $4000\,\mathrm{Th}$, which helps to avoid the contamination with small ions. This mass range can be selected using the RF-only mode. At $2\,\mathrm{MHz}$ the applied RF-voltage is $350\,\mathrm{V}$. The adjustment of the mass range is monitored in the time-of-flight mass spectrometer prior to deposition.

The ion beam is adjusted according to the deposition procedure described in section 3.3.5, page 63. The kinetic energy of the **SDS** beam is typically in the range of $20 \pm 2.5\,\mathrm{eV}$ per charge. In order to achieve soft landing conditions a deceleration voltage of $+15\,\mathrm{V}$ is applied to the sample, which limits the collision energy to $5.0 \pm 2.5\,\mathrm{eV}$ per charge. The sample is placed slightly off-axis to avoid the contamination of the sample by neutral particles or droplets in the beam. The steering plates are used to bend the beam onto the sample (section 3.3.5, page 63).

SDS is deposited on HOPG and $\mathrm{SiO_x}$ surfaces. The samples are prepared for deposition as described in section 3.3.2, page 59. Currents of $10 - 20\,\mathrm{pA}$ are measured on the sample during deposition. A charge of $40\,\mathrm{pAh}$ is accumulated, which leads to deposition durations between 4 and 2 hours depending on the current. In order to ensure that the conditions have been stable through the experiment, the ion beam composition is remeasured with mass spectrometry after the deposition. Finally the sample is transferred in the loadlock and taken out of the vacuum chamber for further analysis.

The morphology of the surface after deposition is analyzed by ex-situ AFM under ambient conditions (see section 3.4.1, page 64). To ensure that no droplets have been deposited, the surface is additionally analyzed by optical microscopy as described in section 3.3.5, page 63. In order to test the stability of the **SDS** film deposited by the ion beam, the samples are remeasured with the AFM after a few days left in air.

Reference samples are prepared by immersing $\mathrm{SiO_x}$ substrates in a concentrated **SDS** solution for a short time and subsequently blow dried. For the comparison with the samples prepared by ion beam deposition, AFM images are taken.

5.2.2 Morphology of SDS Islands Fabricated by Ion Beam Deposition

SDS on Native Silicon Oxide ($\mathrm{SiO_x}$)

The deposition of $40\,\mathrm{pAh}$ singly charged **SDS** clusters of $250 - 4000\,\mathrm{u}$ mass onto a substrate area $10\,\mathrm{mm}^2$ results in submonolayer coverage of $10 - 25\,\%$, as observed by AFM (figure 5.5). This experimental value for the coverage complies with the estimation calculated from the deposited charge using equation

(3.7) (section 3.7, page 63) and assuming a rough average of 5 molecules per cluster which corresponds to the average cluster size in the mass spectra.

Flat islands of nearly round shape and uniform height are found to cover the surface. Their diameter is in the range of $50 - 150\,\mathrm{nm}$ and they are distributed homogenously across the surface. The distance between islands varies between $20\,\mathrm{nm}$ and $100\,\mathrm{nm}$. A cross section through one of the islands is shown in figure 5.5 [middle]. Its height is $2.0 \pm 0.4\,\mathrm{nm}$. This agrees well with the value found for averaging over many islands.

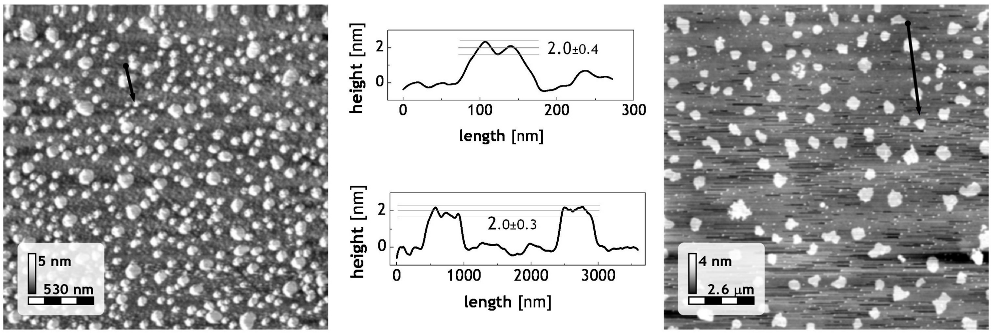

Figure 5.5 – Islands of a submonolayer of **SDS** on a $\mathrm{SiO_x}$ surface. **[left]** As deposited. **[right]** 2 days after deposition. **[middle]** The upper cross section belongs to the sample as deposited, the lower to the same sample stored in air for 2 days.The island height is constant, but the size of the islands has increased. Note the different scalebar in the two AFM images.

The aged sample in figure 5.5[right]is covered with a submonolayer of material. The islands still have the height and coverage, but their morphology has changed. The size of the islands has grown to a diameter of $1\,\mu\mathrm{m}$ and the distance and density of the islands have both decreased accordingly. Few small islands are still observed but with increased distance to each other.

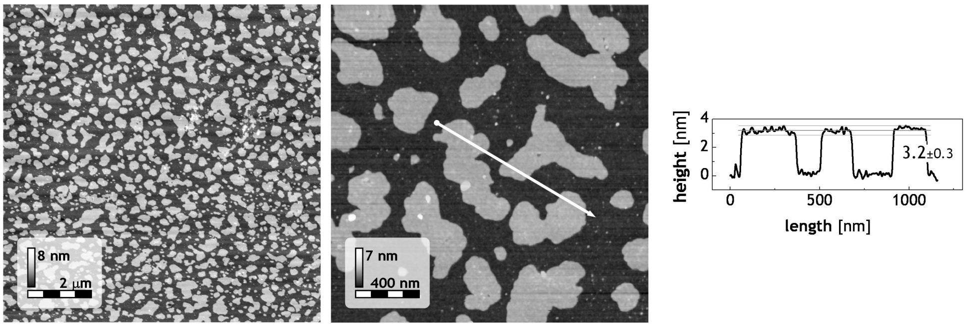

Figure 5.6 – AFM images (two magnifications) **SDS** on a $\mathrm{SiO_x}$ substrate prepared by the solution cast method. Flat islands of $3.2 \pm 0.3\,\mathrm{nm}$ height are found.

The reference samples **SDS** on $\mathrm{SiO_x}$ prepared by solution casting show a similar morphology of the submonolayer surfactant film (see figure 5.6). An island height of $3.2 \pm 0.3\,\mathrm{nm}$ is found in average, which is about $1\,\mathrm{nm}$ higher than for the ion beam coated samples. In general the height, coverage and island shape of samples created by liquid deposition differs depending on parameters like solvent mixture, immersion time or temperature. However, heights of two nanometers as in the samples prepared in vacuum are not observed for films casted from solution.

The deposition of **SDS** on $\mathrm{SiO_x}$ results in two dimensional (2D) film growth for the first monolayer, both in the case of ion beam deposition and solution casting.

The film deposited by the ion beam has a thickness of $2.0 \pm 0.4\,\mathrm{nm}$ either before or after ageing. This height corresponds to the length of the **SDS** molecule which is $1.8 \pm 0.3\,\mathrm{nm}$ in a ball-stick model. In AFM flat islands with steep edges can be observed. This indicates that the molecules are ordered perpendicular to the surface and thus form a monolayer. In contrast, if the molecules were ordered in parallel to the substrate surface, the islands would not be expected to be flat and would not have steep edges.

The reference samples made from solution show thicker islands. Films of surfactants prepared from solution are known to be double layers[187, 142]. Due to the hydrophilic-hydrophobic interaction the surfactant molecules tend to organize in a way that their hydrophobic part is inside the double layer while the hydrophilic head forms the interface with the water[189]. In general the thickness of these films is not twice the length of the molecules they are made of. Bent, tilted or interlocked arrangements can lead to thinner films.

Due to change in the strength of the intramolecular interactions at a phase boundary also monomolecular films can be formed by surfactants. For example at the air-water interface surfactant molecules arrange with the hydrophobic part in air and the hydrophilic part in the water and thus form a single molecular layer[189]. In order to further clarify the influence of the solvent and the surface used for the film growth of surfactants in vacuum, more experimental data is needed, for instance the variation of the surface on which the molecules are deposited.

SDS on Graphite

Figure 5.7 shows the results of the ion beam deposition of **SDS** on a HOPG surface. The height of the **SDS** islands on HOPG is found to be between $4.0 \pm 0.1\,\mathrm{nm}$ which corresponds to twice the length of the **SDS** molecule. The surface area occupied by each island agrees with **SDS** deposited on $\mathrm{SiO_x}$, the shape in contrast is elongated with straight edges, some of which are parallel.

For many neighboring islands a common preferential orientation of $60\,^\circ$ or $120\,^\circ$ between their straight edges can be found. Such an arrangement corresponds to six fold symmetry. The elongated shape of the islands and the frequent observation of the angles $60\,^{\circ}$ and $120\,^{\circ}$ between edges indicates that the morphology of **SDS** on a graphite surface is influenced by the crystallinity of the substrate.

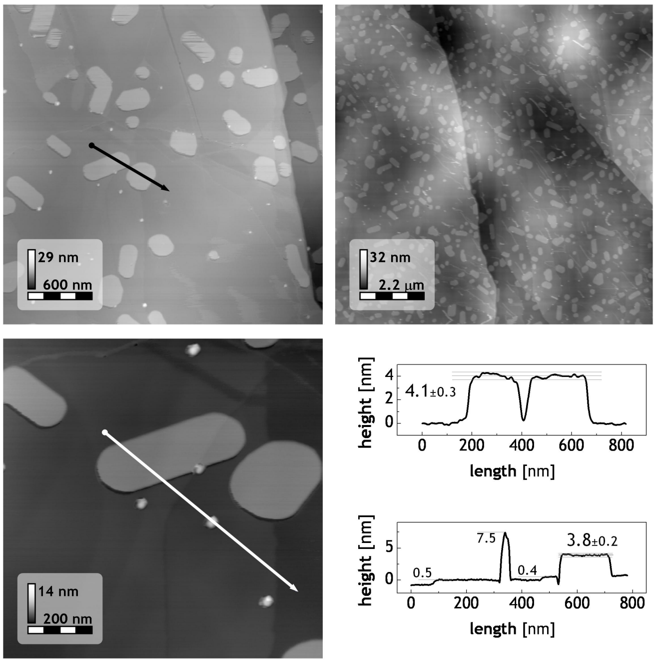

Figure 5.7 – **SDS** ion beam deposited on HOPG. Islands of $4\,\mathrm{nm}$ height are found besides smaller, but higher features. Most of the islands are frequently observed, often have parallel edges and the angles of $60\,^{\circ}$ and $120\,^{\circ}$ are observed between their edges.

Besides the large flat islands also a second type is found which appears round and is much larger in height ($7.5\,\mathrm{nm}$). These islands have a diameter of ($\approx 50\,\mathrm{nm}$), but due to tip convolution in AFM it is possible that they are in fact much smaller.

5.2.3 Growth Mechanism of SDS in Vacuum

The respective height of the **SDS** films measured on $\mathrm{SiO_x}$ and HOPG after ion beam or solution deposition are summarized in figure 5.8 together with models that propose a molecular arrangement which resembles the measured heights.

For ion beam as well as liquid deposition compact islands are observed independent from the substrate. Therefore it can be assumed that the **SDS** molecules are highly mobile on the surface in vacuum, in air and in the solution at room temperature. Even though the molecules are mobile on the surface, agglomerations of **SDS** are formed due to interactions of mobile particles among each other and with the substrate.

Mobile particles are crucial for the formation of agglomerations. In contrast to **SDS**, the large **BSA** molecules, which have similar properties, due to their high mass, only show limited mobility on HOPG and no mobility on SiO_x and thus form ramified islands on HOPG and no ordered arrangements on SiO_x (section 5.1, page 112).

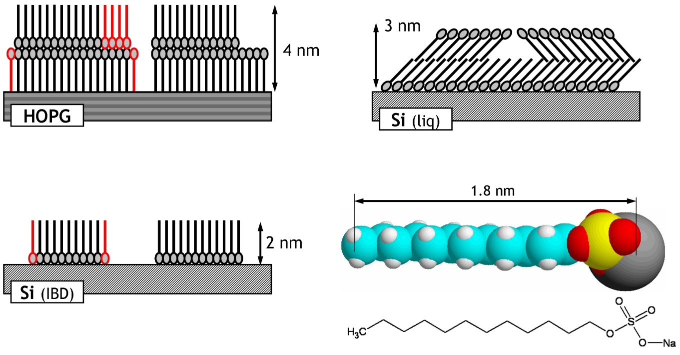

Figure 5.8 – Molecular models for the **SDS** films on SiO_x and on HOPG grown by ion beam deposition (IBD) on SiO_x and HOPG. **[top right]** Model of **SDS** on SiO_x grown by liquid deposition. **[bottom right]** Space filling model of the **SDS** molecule.

A layered arrangement is an energy minimum for amphophilic molecules like **SDS** in an aqueous environment at a hydrophilic surface.

The sodium sulfate groups, being the hydrophilic part of the molecule, like to be solvated by water or bound to a polar surface, such as SiO_x. On the other hand the solvation of the hydrophobic tails is energetically more unfavorable than an arrangement in which the alkyl chains are directed away from both, the hydrophilic substrate as well as the hydrophilic solvent. Such an arrangement is given for example if the alkyl chains of the **SDS** molecules are embedded inside a molecular double layer[189].

In vacuum the solvent which leads to the formation of a bilayer of the **SDS** molecules on the SiO_x is missing. Here layered islands of a smaller thickness are observed.

Due to the absence of water, the hydrophobic-hydrophilic interaction is not present. The hydrophobic tails of **SDS** do not need to be solvated, which means that there is no virtual force due to the entropy of water. Two alkyl chains thus can only interact steric and by van-der-Waals forces[148], which are weak compared with the other forces involved. The formation of the agglomerations has to be explained by ionic interactions between the sodium sulfate heads with each other and the substrate. These two interactions together bind the molecules within an agglomeration and thus lower the diffusion rate of the molecules.

The position and orientation that a **SDS** molecule would take within an agglomeration at a surface can be estimated by the comparison of the available sites in terms of attractiveness to the molecule. Since the sodium sulfate group is ionically bound, it is favorable for two **SDS** molecules if they can bring these groups close to each other. It is also favorable if the ionic head can be close to a polar surface (SiO_x), while its position relative to a non polar surface as for example HOPG is not important.

When these rules are applied to the growth of **SDS** in vacuum, the 2D growth on a surface can be reconstructed. A single **SDS** molecule on a SiO_x surface will bind with the sodium sulfate group to the polar silicon surface, while on graphite the orientation of the molecule will be random, because the molecule-surface-interaction is much weaker. If more molecules arrive they will find favorable sites on both surfaces close to other **SDS** molecules due to the strong ionic interaction between the sodium sulfate groups, which is the reason why agglomerations of SDS molecules are formed. Favorable positions for incoming molecules at an existing island are marked in the schemes in figure 5.8 .

During the growth of the first monolayer of **SDS** on silicon all molecules interact strongly with the SiO_x surface. This force is strongly attractive so that all molecules will stick with the sodium sulfate group to the surface. With growing size the alkyl chains will have to align due to the steric hindering with neighboring molecules and due to van-der-Waals forces.

On HOPG the attraction between the molecule and the surface is much weaker. Here, the agglomeration of the molecules is driven by the ionic attraction between the sodium-sulfate groups, which is stronger than the interaction between the molecules and the HOPG. The sodium sulfate groups can thus overcome the sticking to the HOPG surface in order to offer more binding sites for other **SDS** molecules. This leads to the growth of globular clusters such as the ones shown in figure 5.7. Moreover the formation of small clusters on graphite that initiates further growth might not be necessary, since **SDS** clusters and not single molecules are deposited by the ion beam.

Upon further growth of such clusters it is more favorable to form two dimensional agglomerations. This is an instability driven process. Once a larger cluster is deformed, it will relax into 1D and finally 2D double layer arrangements in order to incorporate more molecules. The layered structures of $4\,\mathrm{nm}$ thickness on graphite can be associated with the double layers, while the observed structures of $7.5\,\mathrm{nm}$ height correspond to globular **SDS** clusters at the surface.

These clusters are excited upon incident at the surface with collision energies in the hyperthermic range, which might lead to their destruction but also to enhanced rearrangement. In general, the hyperthermic kinetic energies are high enough to be considered as equivalent to a thermal treatment of the sample when released upon collision[190]. On the other hand the changes in morphology of the aged samples shows that the diffusion of **SDS** at room temperature is high enough to lead to the rearrangement of the islands, which is why the influence of hyperthermic energies cannot be proven.

The effect that even though no solvent is present, surfactant films can be formed in vacuum is explained by the growth model presented. It only assumes ionic interaction of the sodium sulfate groups, steric interaction and weak van-der-Waals attraction of the alkyl chains and attractive interaction of molecules and substrate. In contrast the film growth of **SDS** in water is totally determined by the hydrophobic-hydrophilic interaction.

The difference from the growth of **BSA** is in fact only given by the diffusion limitation of the large particle in contrast to the fast diffusion of the small molecules. Even since the results show that the layer formation of a surfactant is not dependent on the presence of a solvent, the direct proof of the growth mechanism in vacuum is missing, which could be provided by temperature dependent measurements in order to investigate the evolution of the islands during growth.

5.3 DYE MOLECULE DEPOSITION – RHODAMINE

5.3.1 Introduction

A material that emits light after it is excited is called luminescent, if the excitation is done by a photon it is called photoluminescent and if the time constant is high it is fluorescent [154]. Fluorescence is found in many materials from single atoms [191, 153] to proteins [192]. Particularly dyes, a class of organic molecules, are widely used as probes due to their characteristic fluorescence [150]. Fluorescence microscopy for instance enables to investigate sensitive biological systems non invasively by light. Fluorescently marked molecules can be identified by their emission wavelength[150].

Highly sensitive methods that employ fluorescence are able to identify a single fluorescent molecule by its specific spectrum[193]. Such methods are especially sensitive to chemical changes and to the environment of the molecules. The identification capability of fluorescence spectroscopy here depends on the width of the spectral features, which is mainly limited by thermal broadening. At room temperature fluorescence emission is characterized by relatively broad spectral features limiting the resolving capability. Nevertheless, dyes of different colors can be distinguished and transitions due to chemical reactions can be observed.

Organic dye molecules exist in many different sizes with many different excitation and emission bands. Their special properties like sensitivity to chemical changes and detectability in small concentrations make them interesting probes to investigate the effect of molecular ion beam soft landing.

Soft landing of molecules on solid surfaces in vacuum is reported for a few systems mostly related to preparational mass spectrometry[105]. In order to produce arrays of biologically active substances mass selected enzymes and peptides are deposited at energies of $5 - 15\,\mathrm{eV}$ on liquid surfaces in vacuum[54, 53, 62, 56]. Smaller molecules have been proven to be soft landed by mass spectrometric techniques on self assembled monolayers[107, 58] or on bare metal surfaces[61, 106, 52, 194].

One study by Turecek et.al[110] investigates is the soft landing of fluorescently labeled peptides from intense electrospray ion beams deposited at $10^{-3}\,\mathrm{mbar}$ on plasma treated stainless steel surface at an energy of $5\,\mathrm{eV}$ per charge. The substrates are rinsed after deposition and the molecules or at least the fluorescent labels are detected in solution by fluorescent spectroscopy, which indicates soft landing .

The study presented here for the first time investigates soft landing of molecular ion beams in high vacuum directly on the deposition substrate employing fluorescent molecules. This is done using Rhodamine 6G (**Rho6G**) dye molecules as probes for soft landing of ion molecular beams on solid surfaces. Rhodamine has a very high quantum efficiency and can be identified by its fluorescent spectrum and its typical decay of intensity due to bleaching.[150, 195] The question whether the molecules are intact after a collision with a surface at hyperthermic energies can be answered by fluorescence spectroscopy. Soft landing has occurred, when the characteristic emission and bleaching of Rhodamine molecules is detected on the $\mathrm{Si/SiO_x}$ substrates on which the molecular ion beam has been deposited.

The soft landing ratio is directly coupled to the fluorescence intensity. The amount of inelastically scattered light is proportional to the number of excited molecules and thus to the coverage, if thin films are considered. Since minor chemical modifications like the cleavage of a sidegroup result in a change in the emission spectrum or in the loss of the fluorescence property, the net intensity reflects only the coverage of intact molecules.

The use of a confocal microscope coupled to the optical spectrometer enables the spatially resolved analysis of the deposition spot. The distribution of the fluorescence signal can give insight in the homogeneity of the coverage achieved by the deposition, since the intensity is proportional to the amount of soft landed material.

In order to confirm the deposition of Rhodamine by ion beam soft landing besides the optical methods time-of-flight secondary ion mass spectrometry (TOF-SIMS) is employed. This method is an extremely sensitive way to detect the chemical composition at a surface and has been proven to be able to detect whole molecules (see section 3.4.3, page 65).

5.3.2 Deposition of Rhodamine Ions Beams

The deposition experiment with Rhodamine 6G is done in the fourth pumping stage at $10^{-7}\,\mathrm{mbar}$ using the single and the 6-fold sample holder (see section 3.1.6, page 46). The preparation of ion beams of intact Rhodamine molecules for deposition is done equivalent to section 4.2.1, page 82. Beams of intact $\mathbf{Rho6G^+}$ are characterized by a single peak at $443\,\mathrm{Th}$ in the mass spectrum.

All deposition experiments are done on thin films of $200\,\mathrm{nm}$ $\mathrm{SiO_x}$ on Si substrates in order to avoid quenching of the fluorescence at a conductive surface (see section 3.3.2, page 59 for details). The deposition follows the procedure described in section 3.3.5, page 63, with ion beams optimized as described in section 3.3.3, page 60. For the deposition of Rhodamine kinetic energies of $10-20\,\mathrm{eV}$ are used. The sample holder is positioned slightly off-axis in order to avoid the contamination with neutral particles or droplets. The ion beam is adjusted every $10-20\,\mathrm{min}$ in order to maintain a high deposition current.

After deposition the samples are removed from the vacuum chamber for further analysis by optical microscopy, AFM (section 3.4.1, page 64), fluorescence spectroscopy (section 3.4.2, page 65) and TOF-SIMS. The performed deposition experiments are summarized in table 5.1 and the deposition parameter are given. All samples are measured shortly after deposition and again after a few months. In the fluorescence spectra measured at different times no difference is found.

Before fluorescence spectroscopy and SIMS measurements are performed, all samples are controlled by optical microscopy and AFM measurements in order to exclude droplet deposition of ill defined ion beams. If droplets have been deposited, ring structures with diameters of $100\,\mathrm{nm}$ to $10\,\mu\mathrm{m}$ and heights of several $10\,\mathrm{nm}$ are observed. These rings are attributed to the dried remainders of droplets. In contrast a $\mathrm{SiO_x}$ surface on which only gas phase ions have been deposited shows increased roughness or structures on nanometer length scale, depending on the size of the deposited objects.

5.3.3 Fluorescence Spectroscopy

The fluorescence spectroscopy is done using a confocal microscope to position a laser beam on the sample and a grid spectrometer to detect the light emitted from this point (see section 3.4.2, page 65). Figure 5.9 shows the results typical for a $\mathrm{SiO_x/Si}$ substrate on which a Rhodamine 6G ion beam has been deposited. The left panel displays the optical spectra as they are measured. Several spectra measured subsequently for $100\,\mathrm{ms}$ with intervals of $5\,\mathrm{s}$ show the decrease in intensity of the fluorescence signal due to bleaching, while the elastically scattered light is detected with constant intensity.

A notch filter before the spectrometer diminishes the intensity in a narrow spectral band around the excitation wavelength. The central peak at $488\,\mathrm{nm}$

appears reduced by several orders of magnitude. As the effective spectral width of the notch filter is less than the width of the Rayleigh component, secondary maxima in the spectral intensity appear in the flanks of it, where the notch filer's transmission approaches unity.

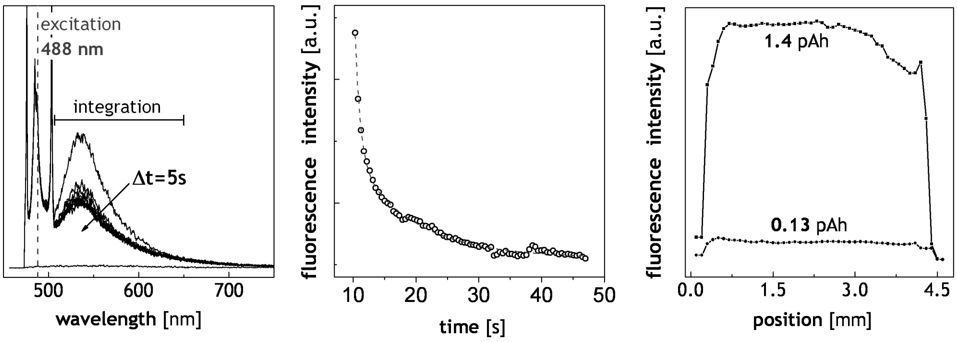

Figure 5.9 – Fluorescence spectroscopy measurements of Rhodamine 6G on $\mathrm{Si/SiO_x}$ deposited by ion beams. **[left]** The fluorescent spectra contain supressed peaks due to Rayleigh scattering ($488\,\mathrm{nm}$) and the broad fluorescent peak around $540\,\mathrm{nm}$. **[middle]** The integrated intensity shows that the fluorescent yield is reduced with time due to bleaching. **[right]** The fluorescent intensity across two different samples with high and low coverage is homogenous.

Towards lower photon energies, the characteristic broad signature of the fluorescence emission from **Rho6G** is detected between $500\,\mathrm{nm}$ and $700\,\mathrm{nm}$. As described in literature and confirmed by solution cast reference samples, it consists of a single, asymmetric peak with a maximum intensity near $540\,\mathrm{nm}$. In contrast to the laser peak, whose intensity remains stable for successively recorded spectra, the fluorescence intensity decreases due to bleaching.

The middle graph in figure 5.9 displays the time dependence of the intensity integrated over the spectral region indicated in the left panel. The bleaching curves can be fitted with an exponential decay and a time constant is derived. For similarly prepared samples these time constants should be reproducible and indeed half-life periods of $5 \pm 1\,\mathrm{s}$ are found for all samples. The same times are measured for reference samples made by solution casting and for aged ion beam deposited samples.

A movable sample stage is employed to study the uniformity of the deposition spot in the confocal microscope. The sample is scanned at a stepwidth of $0.1\,\mathrm{mm}$ per point. The intensity for each spot of $1\,\mu\mathrm{m}^2$ is calculated by integration of a spectrum which is acquired for $5\,\mathrm{s}$. The result of such scans is displayed in figure 5.9 [right]for two different coverages.

The diameter of the deposition spot used in this experiment was defined by an aperture of $3.5\,\mathrm{mm}$ diameter. The scan across the sample reveals a fluorescent spot of approximately $4\,\mathrm{mm}$ diameter for all samples. Within this area a homogenous plateau of $(0.7 - 4.0\,\mathrm{mm})$ is observed. It is delimited by steep

Energy (eV)	**Current** (pA)	**Duration** (min)	**Charge** (pAh)	**rel. Fluor. int.**	**rel. Charge**
12	$0.5 - 2.0$	84	1.3	0.87	0.89
12	$1.0 - 1.7$	70	1.2	0.8	0.63
12	$6.0 - 2.2$	20	1.5	1.00	1.00
12	0.8	10	0.13	0.09	0.08
18	$12 - 9$	60	10		
10	$2 - 3$	270	11.3		

Table 5.1 – Summarized deposition experiments with Rhodamine 6G. The amount of deposited material is given by the charge and can be compared to the fluorescent intensity.

edges ($0.3 - 0.7\,\mathrm{mm}$ and $4.0 - 4.4\,\mathrm{mm}$). For lower coverages essentially the same features are found, only scaled down in intensity (e.g. by a factor of 10 in figure 5.9 [right]).

As a consequence of the homogeneity in intensity across the deposition spot, samples measured under the same conditions (laser power, focal spot size, etc.) can be compared in terms of fluorescence intensity quantitatively. Table 5.1 displays the relative fluorescence intensity for four samples measured under the same conditions in relation to the amount of material deposited by the ion beam. Charges between $1.5\,\mathrm{pAh}$ and $0.13\,\mathrm{pAh}$ have been deposited. The fluorescence intensity for all samples is homogenous across the deposition area. The relative fluorescent intensities compared with the amount of deposited dye molecules shows the proportionality of intensity and coverage for soft landing deposition, which confirms the quantitative nature of the fluorescence spectroscopy method.

5.3.4 TOF-SIMS Detection of Intact Molecules

In order to prove the presence of the intact molecule besides fluorescence, secondary ion mass spectrometry with a time-of-flight mass spectrometer (TOF-SIMS) is employed. SIMS has been proven to be capable to ionize organic molecules of mass $200\,\mathrm{u}$ at a surface using a $15\,\mathrm{keV}$ Ga^+ beam[52, 58]. Besides fragments also the intact molecule has been detected in those experiments.

The experiments presented here are performed on the $\mathrm{SiO_x/Si}$ samples that were irradiated with $4.5\,\mathrm{pAh}$ **Rho6G** ions at $18\,\mathrm{eV}$. The static TOF-SIMS measurements are done according to the details given in section 3.4.3, page 65. A Ga^+ beam at $15\,\mathrm{keV}$ is used as only primary ion beam in the static mode. Spectra are collected for $500\,\mathrm{s}$.

Figure 5.10 shows a mass spectrum obtained by the SIMS measurements. In the low mass-to-charge-ratio range peaks related to the substrate (Si: $28\,\mathrm{Th}$) and to contaminations ($\mathrm{CH_3}$: $15\,\mathrm{Th}$, SiO: $45\,\mathrm{Th}$) are detected. The peaks at $443\,\mathrm{Th}$, $415\,\mathrm{Th}$ and $387\,\mathrm{Th}$ can be attributed to the Rhodamine molecules ionized by the Ga^+ bombardment. The same peaks are observed in the ESI-TOF of

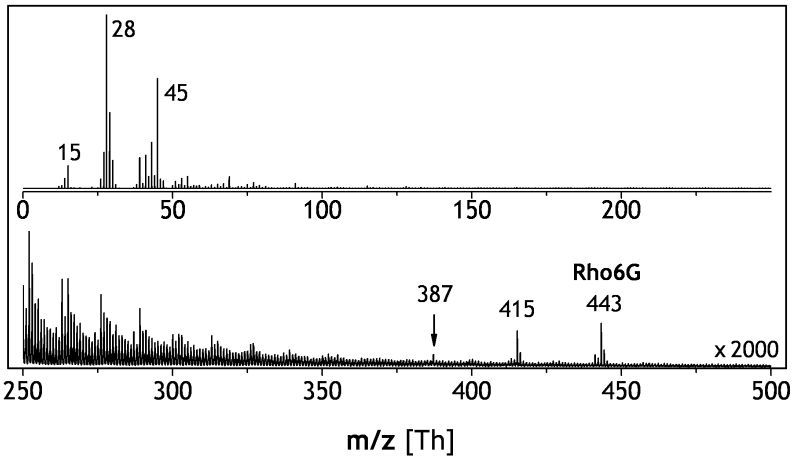

Figure 5.10 – Static TOF-SIMS mass spectrum of a Rhodamine 6G deposited on SiO_2 with an energy of 18 eV. The peaks at 443 Th,415 Th and 387 Th can be attributed to **Rho6G** and the fragments with one and two missing ethyl groups.

the ion beam deposition setup (see section 4.2.1, page 82). The peak at 443 Th belongs to the $\mathbf{Rho}^+$ ion. At 415 Th and 387 Th Rhodamine fragments are observed in TOF-SIMS, identical to the first two intense fragments created by nozzle skimmer fragmentation observed in the ESI-TOF-MS .

Additional intense Rhodamine fragment peaks are not detected. Instead starting from 370 Th towards lower mass-to-charge-ratio a rising background of organic fragments is observed, which is typical for secondary ions of organic molecules[106]. This background can be resolved into peaks, at least one for each integer mass-to-charge-ratio , where maxima are identified with a periodicity of $14 - 16$ Th typical for organic fragments. The intensity of the background peaks in between is $30 - 80\,\%$ of the adjacent maxima.

In contrast to the background Rhodamine and its fragments at 443, 415 and 387 Th stand out from the background fragments that are detected between them. Moreover the periodicity of 15 Th is less evident.

The presence of the three intense peaks at 443 Th, 415 Th and 387 Th suggests that they originate from a different fragmentation mechanism than the background peaks for the mass-to-charge-ratios lower than 370 Th. Therefore they are related to particles that are present at the surface and ionized intact, while the fragments of mass-to-charge-ratio lower than 370 Th relate to fragments created by the bombardment with the Ga^+ ions. The TOF-SIMS mass spectrometric measurements for the Rhodamine deposited at 18 eV thus indicate that part of the Rhodamine ion beam is soft landed, while another part fragments due to surface induced dissociation, and is not deposited as fragment or 415 Th of 387 Th.

Since the SIMS ionization by high energy ions is very intense and strongly dependent on the secondary particles chemistry, the abundance of the molecules found in the mass spectrum does not reflect the actual amount present on the surface precisely. Especially for molecules fragmentation occurs, therefore the abundance of the peaks at $415\,\mathrm{Th}$ and $387\,\mathrm{Th}$ is partially created by Ga^+ bombardment.

Nevertheless, compared with the background that is certainly related to fragmentation induced by the Ga^+ irradiation, the height of the fragment peaks at $415\,\mathrm{Th}$ and $387\,\mathrm{Th}$ is to big. Thus the major part of the intensity of these peaks has to be related to the Rhodamine and its fragments deposited from the electrospray ion beam.

The abundance ratio of $415\,\mathrm{Th}$ to $443\,\mathrm{Th}$ in a $\mathbf{Rho6G}^+$ deposition beam at $200\,\mathrm{V}$ fragmentor voltage is approximately $1 : 100$. Thus also the contamination by fragments in the deposition beam is excluded as source for the fragments at $415\,\mathrm{Th}$ and $387\,\mathrm{Th}$ found in TOF-SIMS. Therefore it is concluded that the ratio between the $\mathbf{Rho6G}$ peak and the fragment peaks at $415\,\mathrm{Th}$ and $387\,\mathrm{Th}$ in fact reflects ratio of surface induced dissociation of Rhodamine on $\mathrm{SiO_x}$ at $18\,\mathrm{eV}$ incidence energy. Taking into account the many error sources of the measurements, this means the soft landing ratio is approximately $50\,\%$.

5.3.5 Conclusions

The characteristic fluorescence signal which is emitted from the sample surface after the deposition of Rhodamine 6G proves that a substantial amount of the molecules is intact and present at the surface. It is shown that soft landing of Rhodamine is possible for energies up to $20\,\mathrm{eV}$.

From the abundances of the Rhodamine and its fragments in TOF-SIMS mass spectra, a soft landing ratio of approximately 0.5 is derived, which suggests that also for energies higher than $20\,\mathrm{eV}$ soft landing could be observed. Compared with the energy of a chemical bond in an organic molecule of $1 - 3\,\mathrm{eV}$ this result shows that the energy of the collision is distributed between Rhodamine and the surface in a way which avoids chemical alteration of the molecules in $50\,\%$ of the cases.

Additionally for deposition energies of $10 - 20\,\mathrm{eV}$ the half life time of the bleaching is found to be the same for the reference and for the ion beam deposited samples. This confirms that the molecules are not chemically modified or in an excited or unstable state after they have been deposited from the ion beam. The reproducibility of the fluorescence detection even after several months further supports this conclusion.

Spacial homogenous deposition over a spot size of $10\,\mathrm{mm}^2$ is confirmed by scanning measurements with the fluorescence spectrometer. This homogeneity shows that the used ion optics are capable to provide a beam with a homogenous flux and that furthermore the ion beam is free of contaminations in form of neutrals and droplets. The realignment of the beam during the deposition causes an averaging, that further enhances the homogeneity. The observation of differently steep edges in the intensity cross sections can be explained by imperfections in the electrostatic lenses and steering plates.

The quantitative measurements that are enabled by the combination of fluorescent spectroscopy and TOF-SIMS allow the estimation of the soft landing ratio as a function of experimental parameters like kinetic energy and used substrate. With these techniques the chemical modification of surfaces and deposited molecules can be studied under controlled high vacuum conditions.

Finally the well developed field of fluorescence spectroscopy and microscopy offers many prospects for sample analysis, including single molecule investigation or the uses of fluorescent protein probes likes GFP[192].

5.4 DEPOSITION of NANOSCALE OBJECTS

5.4.1 Introduction – Is it Possible to Ionize and Deposit Heavy Nanoscale Objects?

The unique features of nanoparticles[1] caused by the high surface to mass ratio makes them interesting for research and applications. Important examples for these applications are catalysis[196], light emitting devices , sensors or nanoscale electronics . Research from which these applications benefit is very intense for example in the field of nanoparticle growth[44, 128] and in researching their chemical and physical properties.

In the field of nanoparticle growth big advances have recently been made in the chemical processing of particles in solution. Particles with very well controlled sizes and shapes can be produced . The surface of nanoparticles can be modified chemically in order to tailor their properties .

In summary, the recent developments have lead to the possibility to make nanoscale objects for a specific application. These particles are composed of a material with the desired properties, have a tailored shape and many different surface modification available. But like for many other large molecular objects there is a significant drawback for nanoparticles, since they do not have vapor pressure, which hinders the deposition of these interesting objects in vacuum.

In fact atomic clusters on surfaces in vacuum show interesting properties . A number of studies have shown that the deposition of nanoparticles from cluster sources is indeed possible[129]. In these studies research has been dedicated to the soft landing of cluster ions. The threshold energy for a crash landing was found to rise with the size of the cluster. An energy of $1\,\mathrm{eV}$ per cluster atom is found to ensure soft landing of the cluster on the surface.

---

[1] The definition of nanoparticles used in this includes many shapes such as spherical particles, nanowires and nanorods.

Particle	**Diameter** (nm)	**Length** (nm)	**Mass**
CNT	1	100 – 1000	10^3 u/nm
Au colloids	5		10^6 u
CdS nanorods	20 – 30	200 – 500	2×10^6 u/nm
V_2O_5 nanowires	5 – 10	100 – 2000	5×10^4 u/nm

Table 5.2 – Overview of important parameters of the nanoparticles used for ion beam deposition: CNT, V_2O_5, CdS, Au-colloids.

Only a few experiments successfully showed that it is possible to ionize nanoparticles by the electrospray method[60, 51]. One of the most interesting experimental works is the soft landing deposition of whole viruses, which are still active after their soft landing on a surface[60, 51]. These experiments continue what has begun as deposition of proteins, which can be accounted as small nanoparticles[53, 62] (see section 5.1, page 112). The viruses composed from many proteins have masses up to 10^6 u and are highly charged. At present this is the only experiment in which mass and charge of large nanoparticles in the gas phase are measured.

Many experiments are reported which use electrospray ionization to disperse a solution that contains nanoparticles in order to distribute the spray droplets homogenously on a sample located in air or in vacuum [39, 44, 43, 42]. This technique is refereed to as ESI deposition which is not to be confused with ion beam deposition, since instead of gas phase ions, charged droplets of a liquid are deposited.

Within this group of experiments some effort has been made to ionize and deposit carbon nanotubes (CNT). In one of the examples in literature a simple two pumping stage setup is used in order to disperse a solution containing carbon nanotubes inside a vacuum chamber in order to recollect the ionized droplets in the next vacuum chamber at lower pressure[20, 21]. With this technique CNT are deposited in vacuum successfully. However the solvent is not removed completely and the deposition process is not controllable in terms of mass selection, current measurement or collision energy, mostly because droplets of unknown size and velocity are deposited. Nevertheless it is quite successfully demonstrated, that nanoparticles in solution or dispersion can be sprayed and are most probably charged.

The following section presents the efforts and results of nanoparticle ion deposition experiments conducted on the ion beam deposition setup. In contrast to the work presented above, in the ion beam deposition experiments the solvent is completely evaporated, which results in a charged gas phase nanoparticle ion beam. To successfully deposit nonvolatile nanoparticles in vacuum, they have to be ionized, collimated in a beam, eventually mass selected, detected in time-of-flight mass spectrometry or by current measurement and finally soft landed.

Table 5.2 shows the particles that are used with the electrospray ion beam deposition setup. The nanoparticles chosen represent a wide range in size, aspect ratio, and properties in order to demonstrate the various possibilities of the deposition technique.

In a first step ion beams of these nanoparticles are created and their deposition in demonstrated. The presence of the nanoparticles is proven morphologically and chemically. AFM (atomic force microscopy, see section 3.4.1, page 64) measurements show the modified topography and when necessary, due to unclear AFM results, a chemical analysis with SIMS (secondary ion mass spectrometry, see section 3.4.3, page 65) identifies the nanoparticles by their chemical composition.

The mass-to-charge-ratio of the ion beam is analyzed and the charge state of the nanoparticles is determined by two different methods. The size measured in AFM and the mass spectra from the linear TOF in the deposition apparatus can be used to calculate the charge state. Alternatively, the deposited charge and the number of particles found in AFM allow the calculation of an average charge state and thus the estimation of the mass-to-charge-ratio . This information is important in order to determine the soft landing conditions, which mainly depend on the kinetic energy and thus on mass and charge state of the nanoparticles.

5.4.2 Nanoparticle Ion Beam Deposition and MS Characterization

Stock solutions of the nanoparticles are either prepared in our laboratory (CdS nanorods[197], V_2O_5 nanowires[198], CNTs[199]) or purchased (Gold colloids $5\,\mathrm{nm}$, Fluka 54394). The nanoparticle solutions for the electrospray source are prepared by the dilution of a stock solution with ethanol and subsequent acidification (section 3.3.1, page 58)[198, 200, 197]. Since the concentrations of the stock solutions are unknown, the grade of dilution is modified in a first test spray until the solution provides a stable high current spray (see section 3.3.3, page 60 for details).

Ion beams of nanoparticle dispersions are prepared according to section 3.3.3, page 60. In order to transmit the heavy ions, the quadrupoles are driven at $500\,\mathrm{kHz}$ (see section 3.2.1, page 52). Typical parameters for achieving a good nanoparticle ion beam are high fragmentor voltages of approximately $400\,\mathrm{V}$ and moderate voltages at the quadrupoles ($100 - 200\,\mathrm{V}$).

Mass spectra of the nanoparticle ion beam are taken despite the fact that the linear TOF with a resolution of 300 is not capable to resolve the high mass particles. Distinct peaks in the mass spectrum thus indicate the formation of solvent clusters or relate to contamination for instance by salt clusters. These mass spectra can give information about the mass-to-charge-ratio range of the transmitted ions. The quadrupole Q2 is set in such a way that ions with mass-to-charge-ratio lower than 1200 Th are not transmitted. A mass-to-charge-ratio range of lower than 1200 Th typically contains solvent clusters and contaminations.

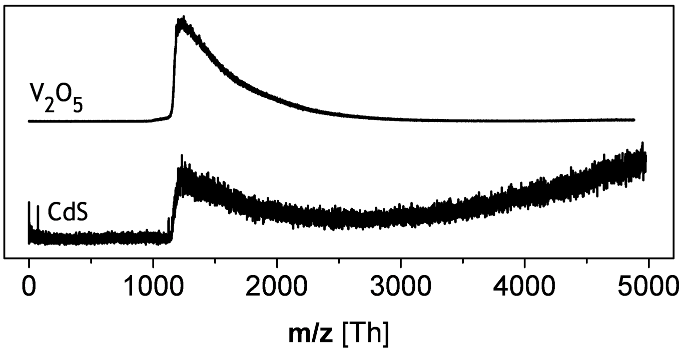

Figure 5.11 – Mass spectra of CdS and V_2O_5 nanoparticle beams for 150 V fragmentor voltage. The Q2 quadrupole is used to cut off the lower mass region.

As an example of a mass spectrum of nanoparticles, figure 5.11 shows the data measured for a CdS and for a V_2O_5 nanoparticle ion beam. Beginning at an onset around 1000 Th, defined by the transmission of Q2, a continuous signal up to high mass-to-charge-ratio is observed. The ion beams of all used nanomaterials show similar mass spectra.

The fact that single peaks cannot be identified, indicates that the nanoparticles are highly charged. For example, singly charged cadmium sulfide cluster peaks are separated by 145 Th, the mass of one CdS unit, which could be easily resolved in the mass spectrometer.

The single sample holder is used for deposition (see section 3.1.6, page 46). The retarding grid energy detector integrated in the sample holder is used to measure the ion beam energy. The sample voltage is set to achieve incidence energies lower than 10 eV per charge (see section 3.3.3, page 60). Typically currents of $1 - 5$ pA are achieved on the sample holder. The deposition is performed for several hours with the result that a charge of $3 - 5$ pAh is collected on the sample.

The samples are taken out of the vacuum for further analysis. The morphology is analyzed with AFM. For the cadmium sulfide particles and the vanadium oxide nanowires a static TOF-SIMS analysis is performed to ensure that the found structures can be related to the particles out of the electrosprayed solutions.

5.4.3 Morphology of Nanoparticles on Surfaces

Gold Nanoparticles

Gold nanoparticles of $5\,\mathrm{nm}$ nominal diameter are deposited on HOPG and silicon at energies of $5 \pm 1\,\mathrm{eV}$. Figure 5.12 displays AFM images for graphite in the top row and for silicon in the lower row for several magnifications (note that the color scale is inverted, dark for high and light for low areas). The cross sections marked in the images are displayed in the bottom row.

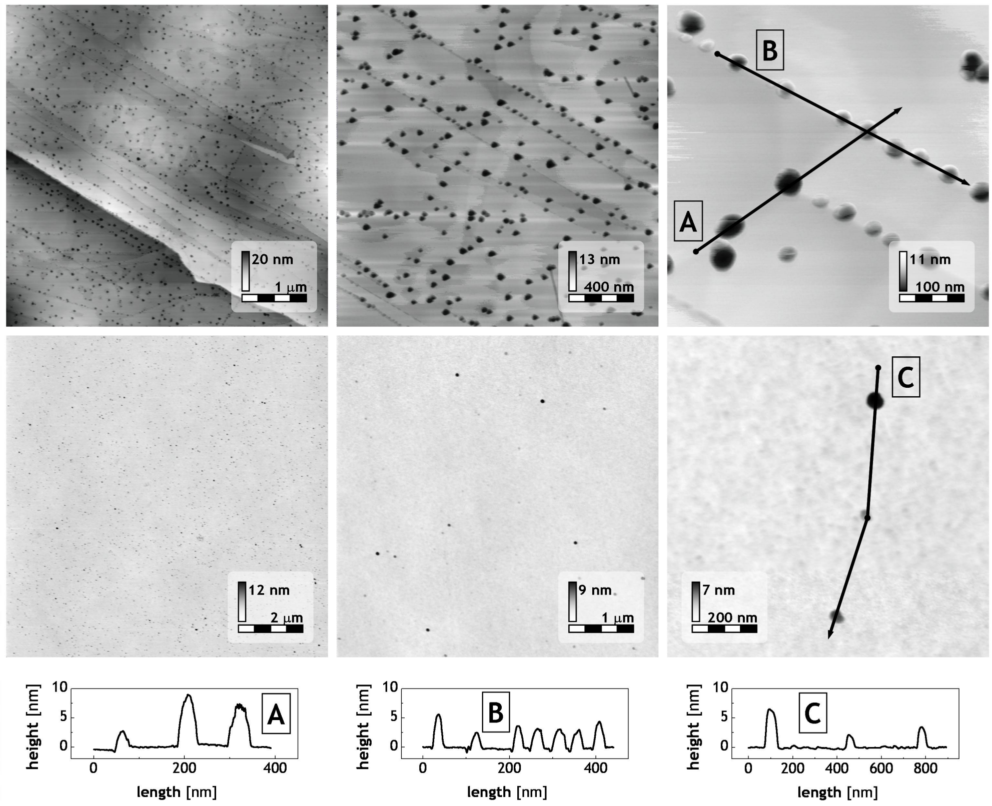

Figure 5.12 – AFM images of $5\,\mathrm{nm}$ gold nanoparticles on a **[top]** graphite surface and **[middle]** native $\mathrm{SiO_x}$ surface of a silicon crystal. On HOPG the gold particles are found at step edges preferably, indicating surface diffusion. **[bottom]** Cross sections indicated in the AFM images.

The lowest magnification shows a uniform coverage of particles on the surface. For both substrates the particle size measured lies between $3\,\mathrm{nm}$ and $7\,\mathrm{nm}$ in height, while the lateral dimensions in the range of $50 - 100\,\mathrm{nm}$ are found. The measured heights correspond to the size distribution of the gold colloids in dispersion. This observation suggests, that the particles have been softly landed at the conditions used in this experiments, which means that they have not been deformed upon collision. Moreover, their unchanged shape indicates that during the whole ion beam deposition process the gold particles have not been affected by the droplet fission, supersonic expansion or ion-gas collisions in the first or second pumping stage.

The mass-to-charge-ratio of the nanoparticle beam of more than $1000\,\mathrm{Th}$ is equivalent to one charge for every 5 gold atoms ($m(\mathrm{Au}_5) = 985\,\mathrm{u}$) in the cluster. This maximum charge results in a kinetic energy of up to $1\,\mathrm{eV}$ per atom. This energy is the soft landing limit for small clusters and thus further supports the finding that the gold colloids are deposited by soft landing.

On graphite the gold clusters decorate the step edges, while on silicon their distribution is completely uniform but random. As observed for **BSA** and **SDS** the diffusion on HOPG is very easy (section 5.2, page 119 and section 5.1, page 112). Typically the step edges are pinning sites for the nanoparticles, which is also the case for **BSA**.

Cross sections on HOPG show that the particles at the step edges are usually smaller than those on the terraces (figure 5.12 [top-right] A and B). This is a result of the faster diffusion of the smaller gold particles on the surface, which enables them to move across larger distances. For longer diffusion paths the probability to get trapped at a step edge rises, which is the reason for the smaller gold particle to be found preferably at the step edges[201].

Carbon Nanotubes

Carbon nanotubes (CNTs) are nanoscale objects that are elongated in one dimension. They can be identified on the silicon surface by their typically elongated shape and the typical diameter of approximately $1\,\mathrm{nm}$ measured in AFM as height (see figure 5.13). The deposition of $0.5\,\mathrm{pAh}$ results in a coverage of $1-10$ objects per $1\,\mu\mathrm{m}^2$ that are identified as CNT. The length of the nanotubes found on the surface is in the range of $200\,\mathrm{nm}$ and $1\,\mu\mathrm{m}$.

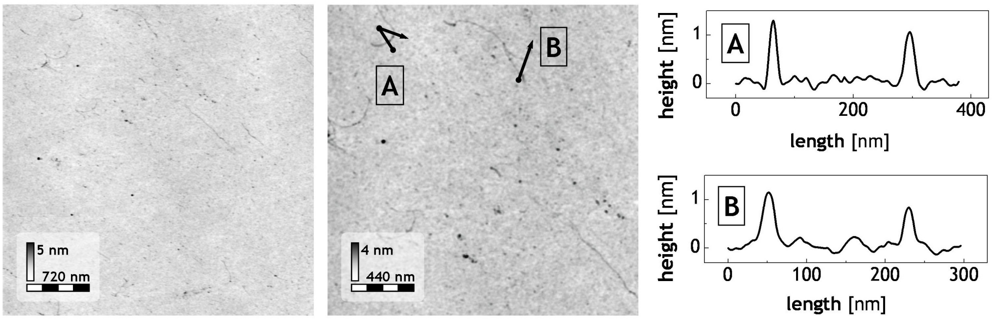

Figure 5.13 – AFM images of ion beam deposited CNT on the native oxide ($\mathrm{SiO_x}$) of a silicon surface. **[right]** Cross sections show that the diameter of the tubes is about $1\,\mathrm{nm}$.

Spherical objects of sizes larger than $2\,\mathrm{nm}$ are found besides the CNTs. In the AFM images in figure 5.13 the dark black spots correspond to these particles.

They originate from the CNT production process which is high pressure carbon monoxide conversion (HIPCO)[202]. This manufacturing process results in residual particles of either amorphous carbon or catalyst metal of a wide variety in size. Before the electrospraying, the solution is centrifuged, which removed the larger ones of these particles. Those, which have the same weight as the CNT could have been ionized and deposited.

Cadmium Sulfide Nanorods

The CdS nanorods in the dispersion used for the electrospray are $20 - 30\,\mathrm{nm}$ in diameter and have length of $200 - 500\,\mathrm{nm}$[197, 200]. These rods, although present in solution, are not found on the surface after deposition. Instead smaller particles are uniformly distributed on the surface (see figure 5.14). In the AFM images round disks with diameters between $50\,\mathrm{nm}$ and $150\,\mathrm{nm}$ appear with heights between $2\,\mathrm{nm}$ and $30\,\mathrm{nm}$. The maximal height corresponds to the diameter of the nanorods in solution. The compositional agreement between the found particle and the electrosprayed nanorods is confirmed by the chemical signature of cadmium found in TOF-SIMS measurements (see section 5.4.4, page 142).

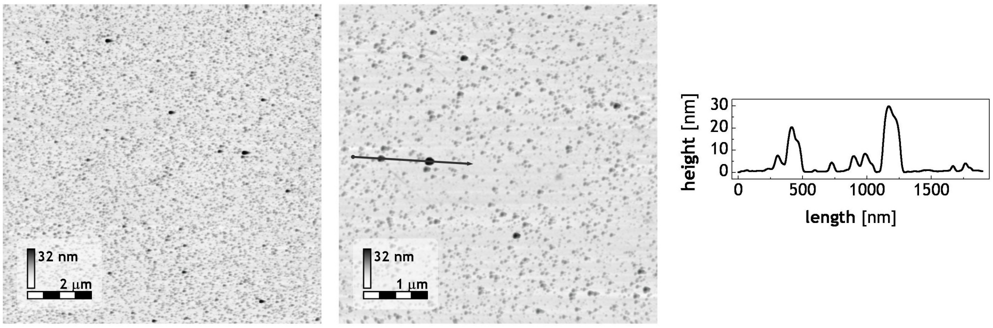

Figure 5.14 – AFM images of cadmium sulfide nanoparticles on a silicon surface. The largest particles are $30\,\mathrm{nm}$ in height.

There are several possible reasons for the deposition of only small particles. The destruction of the nanorods in the ultrasonic bath, which is used to stir up the dispersion, is excluded by reference measurements. After sonication solution cast samples show mostly intact nanorods in AFM. However some smaller fragments such as shown in figure 5.14 are observed as well.

The modification of the particles due to intense ion gas collisions in the first or second pumping stage is not likely since the collision energies here are not large enough to destroy for example gold clusters. The ion gas interactions therefore do not affect large particles, at least at the declustering potentials that are used for nanoparticle deposition.

A crash landing can also be ruled out since the kinetic energy of a 1000 times charged full sized nanorod is much lower than the decomposition threshold of 1 eV per atom, well known for clusters[129]. A typical nanorod ($30 \times 30 \times 300\,\mathrm{nm}$) of CdS contains $2{\times}10^8$ atoms. The kinetic energy in an ion beam of 5 eV per charge is 5000 eV per cluster would be within the soft landing limit. Even if the 1 eV per charge rule would not apply in this mass range, larger fragments than those that are found in AFM should be present at the surface.

From this estimation it is concluded that the particles found on the surface are soft landed. The particles therefore are already present in the ion beam when it is created in the atmospheric interface. The absence of the large nanorods on the deposited substrates can only be explained if one assumes that the original nanorods of a length larger than 30 nm have a charge state that is too low to be transmitted in the ion beam, especially not in the low pressure quadrupole Q2. The particles that are finally deposited are only the small, highly charged fragments.

Vanadium Oxide Nanowires

The dispersion of nanowires of vanadium oxide V_2O_5 contains mostly long wires. A solution casted reference sample shows their huge length of up to $10\,\mu$m.The wires are only 10 nm to 20 nm thick. If these wires are deposited with the ion beam vacuum deposition technique only small particles are found on the substrate surface (figure 5.15). The lateral size is found in the range of $50-100\,\mathrm{nm}$, heights are measured between 2 nm and 20 nm. The identity of the particles are confirmed by TOF-SIMS measurements (section 5.4.4, page 142).

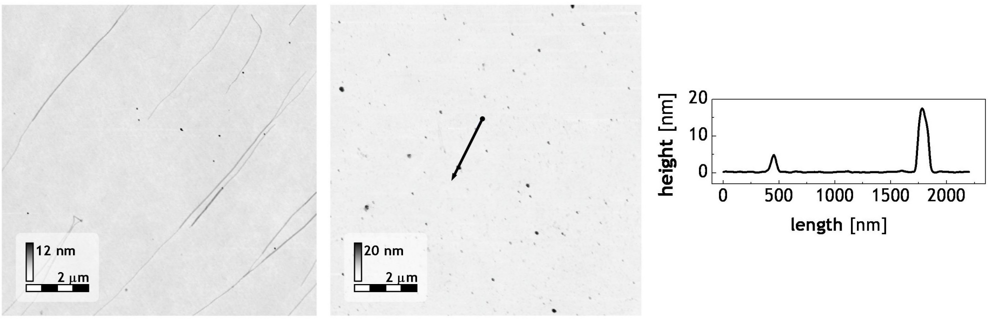

Figure 5.15 – Vanadium oxide (V_2O_5) nanoparticles deposited on silicon: **[left]** deposition from dispersion, long nanowires **[right]** ion beam vacuum deposition, only small particles.

This experimental result is very similar to that of the deposition of the CdS nanorods. Also in this case the possibilities of a crash landing and of the destruction of the particles in the ultrasonic bath can be ruled out by the same arguments as for CdS. Also here the explanation of the experimental observation is that the heavy particles can not be transmitted due to their too low charge state.

5.4.4 Chemical Identification of Nanoparticles on a Surface by TOF-SIMS

In order to study the chemical composition of a solid sample layer by layer, time-of-flight secondary ion mass spectrometry (TOF-SIMS) is a powerful tool (section 3.4.3, page 65). With this technique sputtered secondary ions are detected with mass spectrometry, which leads to a high sensitivity to very small amounts of material.

TOF-SIMS is used to confirm the chemical nature of the structures found after the ion beam deposition of CdS nanorods and V_2O_5 nanowires, since the morphology of the objects found on the surface after the ion beam deposition did not correspond to the original particles in the dispersion.

Both samples are studied in static SIMS mode, which means that no sputtering is used since the depth profile is not of interest. The primary ion beam is gallium $^{69}\mathrm{Ga}^+$ with an energy of $15\,\mathrm{keV}$. A short pulse ($1\,\mathrm{s}$, O_2^+ ions, $250\,\mathrm{eV}$) from the oxygen sputter gun is used to activate the surface chemically, which typically results in higher secondary ion yields.

Vanadium Oxide on Silicon

A typical static TOF-SIMS spectrum observed for V_2O_5 is shown in figure 5.16. In the linear representation only the strongest peaks are visible. Most of them correspond to common contaminations found with TOF-SIMS on every surface that has been exposed to ambient conditions. The signal at $23\,\mathrm{Th}$ corresponds to sodium.

The strongest peak at $28\,\mathrm{Th}$ relates to the substrate which is silicon, its neigboring peaks at $29\,\mathrm{Th}$ and $30\,\mathrm{Th}$ to the silicon isotopes $^{29}\mathrm{Si}$ and $^{30}\mathrm{Si}$. The peak found at $132.90\,\mathrm{Th}$ is the Cs^+ ion. This contamination originates from the ion beam deposition source. The linear TOF mass spectrometer in the source is calibrated with CsI clusters before the deposition experiments.

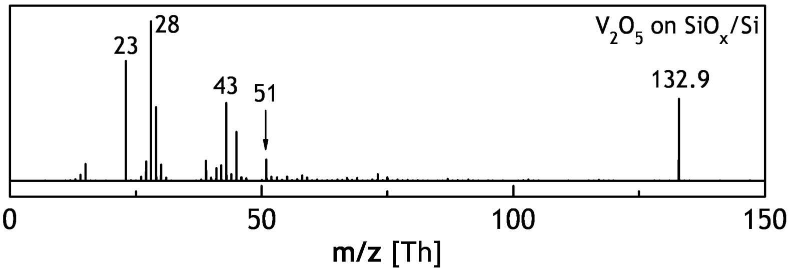

Figure 5.16 – Static TOF-SIMS mass spectrum of V_2O_5 nanoparticles on Si. The peak at $51\,\mathrm{Th}$ corresponds to the major vanadium isotope $^{51}\mathrm{V}$.

The presence of vanadium oxide is confirmed by the intense peak of the ^{51}V single charged ion at 50.9429 Th. Moreover minor peaks of VH$^+$ (51.9518 Th), VO$^+$ (66.9380 Th), V_2O^+ (117.9053 Th),VO_2H^+ (93.9414 Th) and VOH$^+$ (67.9467 Th) are found. The deviation of these peaks to their expected position is always smaller than 50 ppm.

Cadmium Sulfide on Silicon

It is more difficult to prove the presence of CdS on a surface with secondary ion mass spectrometry than for V_2O_5 due to the fact that both cadmium and sulfur have poor sputter yields in both the positive or the negative secondary ion mode[203]. Figure 5.17 [top]shows the static SIMS mass spectrum of a silicon substrate onto which CdS nanoparticles have been deposited. Na$^+$, the three silicon isotopes and SiO$^+$ at 44 Th can be observed in the linear representation.

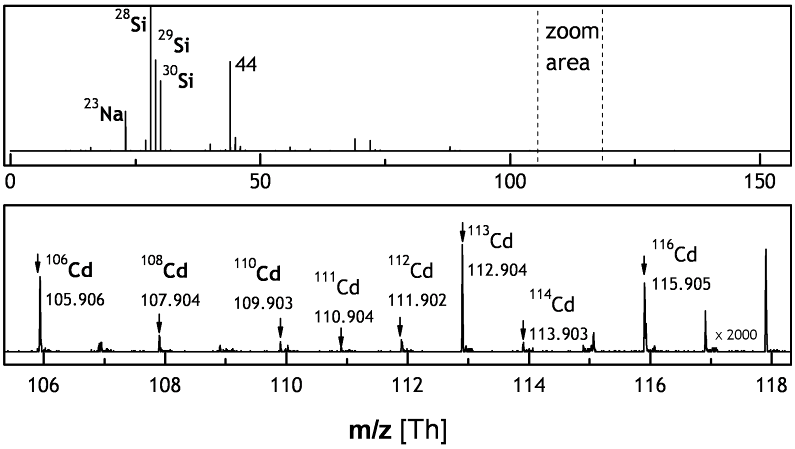

Figure 5.17 – SIMS mass spectra of CdS nanoparticles on silicon. **[top]** The overview spectrum shows sodium, silicon and carbon contamination. **[bottom]** In the range of $106 - 116$ Th eight different cadmium isotopes are identified and their position is given.

Due to contamination many low abundance peaks, basically at least one near every integer mass-to-charge-ratio value, are detected. Most correspond to carbon/silicon clusters. An especially precise calibration using many fix-points enables to separate these contamination peaks from the low abundant peaks of the cadmium present on the sample.

Due to its many stable isotopes (106, 108, 110, 111, 112, 113, 114, 116 u) the presence of cadmium is proven by the mass spectrum, since all these peaks are found at the expected positions with a deviation lower than 50 ppm. The distribution of intensities of the cadmium isotope peaks is not as expected for the ratio at which the different isotopes occur in nature. This discrepancy is explained by the presence of the Si_4^+ clusters at masses of 112 Th and higher. At a mass resolution of 5000 the peak width is 0.022 Th at a mass-to-charge-ratio of $112\,\mathrm{Th}$. Thus for instance the $^{112}\mathrm{Cd}$ peak at $111.903\,\mathrm{Th}$ can not be distinguished from the $4^{28}\mathrm{Si}$ peak at $111.908\,\mathrm{Th}$. On the other hand, the observed signals below $112\,\mathrm{Th}$ certainly correspond to cadmium ions emitted from the surface.

5.4.5 Results and Discussion: Charge State of Nanoparticles in Electrospray Ion Beams

The charging of nanoparticles in an electrospray ion source is not much discussed in literature, most probably due to the fact that nanoparticles are not interesting for mass spectrometry. Mass spectrometry measurements of very large, very highly charged particles are in fact most complicated, if not impossible. A nanoparticle of N_{atom} atoms and many charge states can compose a very high number of different mass-to-charge-ratios. The number of ions with different mass-to-charge-ratio is proportional to both the size of the atom number range of the cluster ΔN_{atom} and the number of possible charge states Δz. A rough approximation gives $\frac{1}{2}(\Delta N_{\mathrm{atom}}\Delta z)$.

For instance a gold nanoparticle of size $5 \pm 1\,\mathrm{nm}$ thus can contain between $1500 - 5000$ atoms. At charge states between $60 - 500$, estimated from mass spectra, this results in almost 10^6 different ions in the typical ESI mass-to-charge-ratio range of $500 - 5000\,\mathrm{Th}$. Most peaks will show up in high mass ranges, which makes resolutions of over 10^6 necessary to distinguish peaks from each other. Finally since the net current is now divided up in many channels, an extremely low signal to noise ratio is crucial as well.

Due to the limited resolution of the linear TOF, mass spectrometric measurements like those shown for $\mathrm{V_2O_5}$ and CdS particles can only give the mass-to-charge-ratio information. For an ion beam deposition experiment it would be indeed very important to know the charge state of the deposited particles, since it determines the kinetic energy and thus strongly influences whether soft or crash landing takes place. Such an indirect measurement of mass and charge state has been done for large viruses[60].

Determination of the Charge State from AFM Images and TOF-MS

Since mass spectrometric measurements with the linear TOF-MS will not result in resolved spectra, the mass information can be gained indirectly by analyzing the geometry of the particles found on the surface after deposition. Standard techniques like transmission electron microscopy (TEM), scanning electron microscopy (SEM) or AFM can be used for imaging.

For molecules the charge states can easily be determined from mass spectra. Their kinetic energy is then determined by the measurements in the retarding grid detector, which gives the kinetic energy per charge. This value multiplied by the charge number z is the kinetic energy of the ions in the beam.

The mass spectra of the nanoparticle ion beams shown in figure 5.11 do not show any resolved peaks which can be identified as a certain cluster ion with a charge state. Therefore only a mass-to-charge-ratio range can be measured (see table 5.3) and the particle charge can be calculated, if the mass of the particle is known.

The mass of the particles deposited by the ion beam can be estimated from their size which is derived from the AFM images. This information, combined with the mass-to-charge-ratio range from the mass spectra, is used to calculate the charge state of the particles, which is summarized in table 5.3.

In the mass spectra of the nanoparticles, ions with a mass-to-charge-ratio between $1000\,\mathrm{Th}$ and $5000\,\mathrm{Th}$ are observed. Since the spectra do not resolve single peaks, this only indicates the mass-to-charge-ratio range of the ions. For particle masses of $10^5 - 10^6\,\mathrm{u}$ this roughly corresponds to charge numbers of 100 per particle estimated from the mass spectra.

Indirect Mass Spectrometry using AFM and Deposition Current

Another way to calculate the charge state z of the particles uses the knowledge of the net charge and the amount of material deposited (see also section 3.3.5, page 63 for experimental details). The net charge deposited on the sample is the product of deposition time t and measured current I_{sample}. The amount of material deposited is estimated from the AFM images. The particles can be automatically counted by size using the scanning probe image analysis software *WsXM*[123], resulting in a histogram N_d of particles with diameter d for the AFM image area A_{AFM}. Alternatively this can be expressed by the net amount of particles $N_\Sigma = \sum_d N_d$.

Assuming that the coverage is approximately homogenous across the full deposition spot (diam. $3.5\,\mathrm{mm}$) with area A_{depo} , these numbers can be scaled up by the factor $\gamma = A_{\mathrm{depo}}/A_{\mathrm{AFM}}$. The relation between the measured current, particle number and charge state follows accordingly.

$$\begin{aligned} tI_{\mathrm{sample}} &= \gamma\, N_\Sigma\, \bar{z} && (5.1)\\ &= \gamma \sum_d N_d\, z(d) && (5.2)\end{aligned}$$

From equation (5.1) the average charge number per particle $\bar{z}$ is calculated. The results are displayed in table 5.3. This calculation is especially viable in the case of gold nanoparticles, which have a narrow size distribution around $5\,\mathrm{nm}$.

A more precise assumption is a uniform area charge density on the surface of the nanoparticles and is reflected by equation (5.2) in which $\bar{z}$ is replaced by the function $z(d) \propto d^2$. The AFM images for CdS and V_2O_5 are evaluated under this premiss. The deposited net charge tI_{sample} is then distributed proportional to the surface area of each fraction onto the histogram of the height

Particle	**Observed Size** (nm) (diam./length)	**Mass** (u)	**Charge State (AFM)** z	m/z (Th)	**Number of Atoms in Particle**	**Kinetic Energy at** $5\,\mathrm{eV/z}$	**per Atom**
CNT	224	1.3×10^5	590	219	13440	2950	0.22
Au	5	5.8×10^5	200	2900	2966	1000	0.34
CdS	3	1.2×10^5	41	2900	13720	205	0.015
V_2O_5	7	1.1×10^6	356	3200	346700	1780	0.005

Table 5.3 – Properties of charged nanoparticles used in ion beam deposition experiments. The charge state is derived from the deposition current and the achieved coverage on a sample.

of particles on the surface N_d. The results expressed in mass-to-charge-ratio are displayed in figure 5.18 for samples of V_2O_5 and CdS.

Results and Discussion

The estimation using the deposition current and the number and size of the particles found on the surface leads to similar results for the charge state as the calculations from the measured mass-to-charge-ratio and number of deposited particles. The charge state value ranges between 41 for CdS particles and 590 charges for a 200 nm long carbon nanotube. This results in mass-to-charge-ratio ranges of around 3000 Th for spherical particles and 219 Th for the carbon nanotubes.

The results of the more detailed calculations are displayed in figure 5.18 for three examples. The range in mass-to-charge-ratio calculated for the particle sizes found results in a distribution over an order in magnitude in mass-to-charge-ratio assuming a constant charge per particle surface area. Especially the comparison of two coverages found for CdS on the same sample show how precise the resulting values are. The charge states found in the two deposition experiments differ only by a value of three.

Two different methods have been used to estimate the charge of gas phase nanoparticle ions: mass spectrometry and AFM/current measurement. Both methods prove that nanoparticles in an electrospray get multiply charged. This is shown for particles representing a wide range of properties, masses and shapes. The typical mass-to-charge-ratio range of ions created in ESI of up to 6000 Th is also valid for these very heavy particles (section 2.1.3, page 17).

The value found for the charge state of carbon nanotubes might appear too high. Considering the fact that those are one dimensional particles, a high value has to be expected, since an elongated object can carry more charges compared to a globular one with the same volume. On the other hand the extreme deviation could be explained by a too large current measurement due to the contamination of the sample with other nanoparticles that are not identified in the AFM images.

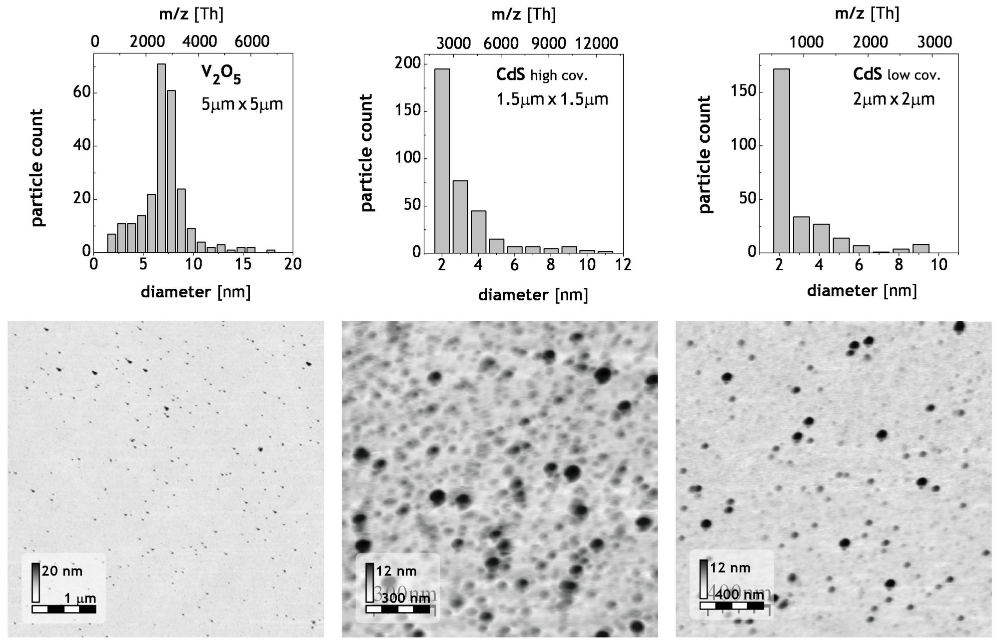

Figure 5.18 – Estimation of nanoparticle charge states from deposition current and AFM images. **[top]** Histograms of the particles size distribution which can be expressed in terms of mass-to-charge-ratio according to relation equation (5.2). **[bottom]** The AFM images of CdS and V_2O_5 used to create the histograms.

Generally speaking, deviations from the charge state given for the nanoparticles arise from many error sources. On the other hand these errors cancel each other out. For instance a higher charge state is calculated when the number of particles counted is too low, which is likely since very small particles are hard to identify so that several might have been missed. On the other hand charges can remain on the deposited particle instead of flowing through the sample[194]. The measured current is then lower than the real current that is deposited, which leads to a lower calculated charge state. Finally the estimation of the particle volume is a source of errors. Particles close to each other or of elongated shape can not be resolved in AFM measurements. This results in a mass measurement that is lower than the actual mass. Again the mass-to-charge-ratio is measured too high.

The estimation of the charge state from AFM images and measured current thus can only give a range for the charging of the nanoparticles. The values found nevertheless reflect the state of the beam, which contains multiply charged nanoparticles.

An interesting parallel is found if ions of nanoparticles are compared with proteins in the gas phase. The latter can be regarded as organic nanoparticles and are also highly charged (see section 4.3, page 105). In particular cytochrome c shows an analogy to the extremely highly charged carbon nanotubes. It is shown that the unfolded protein, which then is a one dimensional strand, can be higher charged than the folded, globular protein (see section 4.3.2, page 108)[145]. The difference in aspect ratio of folded and unfolded **Cyc** can be compared to the difference in shape between CNTs and for example the CdS nanoparticles, which is reflected in the different charge mass-to-charge-ratios .

In conclusion, the charge states found for the nanoparticles show, that like for small molecular ions, for large objects the typical mass-to-charge-ratio range of an ESI source is found. Moreover it is ensured, that nanoparticles in general can be deposited from a low energy ion beam, firstly because they can be ionized and secondly because soft landing is possible, since the kinetic energy can be reduced to a value below $1\,\mathrm{eV}$ per atom.

6 CONCLUSION and OUTLOOK

Electrospray mass spectrometry has been used for almost two decades as an extremely powerful tool to analyze non volatile particles. Within this thesis a general ion beam deposition method for nonvolatile particles based on electrospray ionization has been developed and demonstrated. The deposition source has been constructed in such a way that the ion soft landing can be controlled by a variety of parameters, such as kinetic energy, charge state or mass-to-charge-ratio .

The ion beam deposition apparatus used for the presented experiments employs differential pumping across six chambers to bridge the vacuum gap of 13 orders of magnitude between the atmospheric pressure ionization and the deposition in high vacuum. A variety of ion optical elements have been developed in order to guide a beam with a sufficiently high flux for deposition to a sample in UHV. A time-of-flight mass spectrometer and a retarding grid ion energy detector have been implemented to monitor the beam properties in order to achieve a controlled deposition.

Basic experiments show that control over the ion beam parameters can be achieved with the developed experimental setup. The kinetic energy and spacial distribution can be measured and adjusted. The ion beam composition can be monitored with the linear TOF at a resolution which is high enough to identify molecules and distinguish them from fragments. Finally, the sample holders in high and ultrahigh vacuum can be used to deposit intact ions at solid substrates with energies at the low end of the hyperthermic range.

Extensive mass spectrometric studies have been performed using the linear time-of-flight mass spectrometer of the ion beam source in order to learn how to prepare ion beams suitable for deposition. Since most molecules can be brought into the gas phase by electrospray ionization many different types of ion beams, for instance molecular and cluster ion beams, are available for deposition. Additionally the composition of the beam can be influenced by ion-gas-interactions.

Apart from controlling the properties of the ion beam, mass spectrometry has also been used to perform more advanced analysis, like for example determining the position of the charge site in a molecule, exploring the fragmentation pathway of complex molecules or the determination of the binding strength of molecular sidegroups or cluster components. Thus it has been shown that mass spectrometry gives valuable information on the ions in the gas phase which, coupled with the information obtained after surface deposition, will allow a very detailed description and control of functional surface nanostructures, which are the final aim of the deposition experiments.

Ion beam deposition at very low kinetic energies has been proven to be a technique that can be generally applied to a variety of molecules and clusters starting from small organic molecules up to very large nanoparticle ions.

By various means it has been shown that soft landing, i.e. destruction free deposition, is possible for all of these particles, if the kinetic energy is low enough. At deposition currents between $1\,\mathrm{pA}$ up to $50\,\mathrm{pA}$ it has been demonstrated, that on a sample surface of $10\,\mathrm{mm}^2$ a monolayer coverage can be achieved within a deposition time in the order of hours. These deposition durations make the technique applicable for research and also for specialized applications.

A wide variety of molecular nanostructures was shown to result from the ion beam deposition on surfaces in high vacuum. For example, **BSA** proteins are found to form fractal arrangements on graphite, while molecular surfactants were shown to form single or double layers depending on the surface. Apart from the specific details characteristic of each individual system, these experiments indicate that the mechanisms responsible for the wide variety of micro and nanostructures obtained by standard organic molecular beam epitaxy are also valid for ion beam deposition.

In particular, the deposition under UHV conditions will enable to analyze the fabricated samples in-situ. For that purpose an UHV scanning tunneling and force microscope has been recently connected with the ion beam deposition apparatus for in-situ transfer and analysis. Through a transfer with a vacuum suitcase, which has already been implemented as well, also other UHV analytical techniques become accessible, such as X-ray photoelectron spectroscopy (XPS) to analyze the chemical composition or very low temperature STMs for local electronic, vibrational and optic spectroscopic measurements.

Therefore, by means of electrospray ion beam deposition, it will in future be possible to exploit the endless catalog of organic and inorganic chemistry in order to create complex molecular structures at surfaces and to study and control their organization into functional compounds that could not be otherwise accessed so far. Examples for these compounds are natural molecules like peptides, sugars, DNA or lipids but also complex organic molecules designed and synthesized ad hoc for a certain function.

In fact it has been demonstrated that molecules which are synthesized according to a plan, can be ionized and detected in the ion beam. In figure 6.1 the mass spectra of the **P4P** fully conjugated ring precursor molecule (1/8 sector)[5] and the **3SEt5Fe**[146, 147, 4, 3] molecular motor molecules are displayed along with their structure.

The isolated deposition and analysis of the molecular motor molecule **3Set5Fe** under controlled conditions in an UHV-STM is most desirable in order to study the concept of the molecular machine. The fully conjugated ring, which

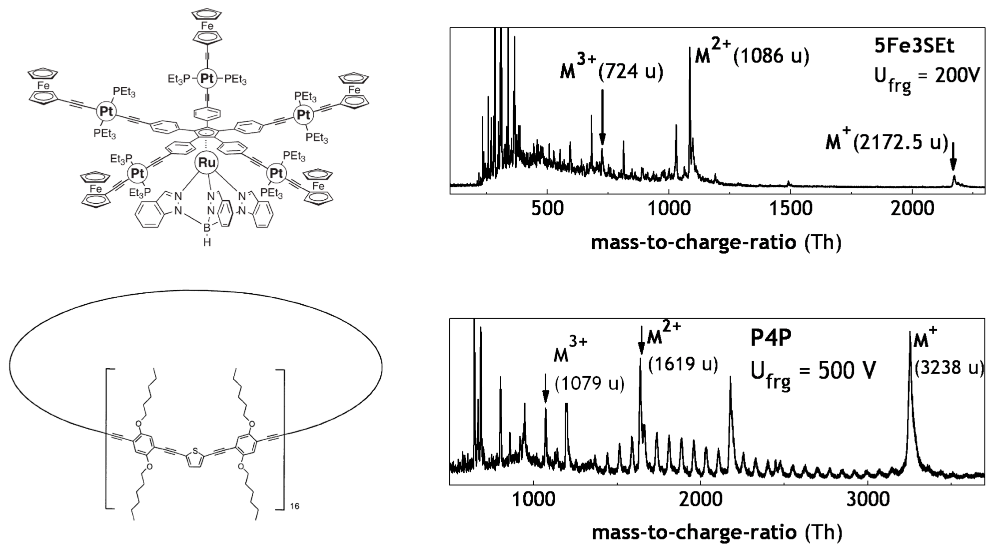

Figure 6.1 – Molecular structure and ESI mass spectrum of the **[top]** motor molecule **3SEt5Fe** and **[bottom]** fully conjugated ring **P4P**.

is made of eight **P4P** molecules, is interesting because of its special electronic properties. The goal of the design is to obtain a molecular system in which persistent currents can be investigated. Therefore structures need to be prepared in which such an observation is possible, which requires the ring to be opened and under controlled conditions, like in an UHV-STM.

The results of the preliminary experiments with these molecules and the state of the ion beam deposition technique as described within this work show that these and other proposed experiments are now possible. The electrospray ion beam deposition setup is able to get the particle in the gas phase, where they can be detected and afterwards deposit them controlled on a solid surface.

Bibliography

[1] G. E. Moore. Cramming more components onto integrated circuits. *Electronics*, 38(8), 1965.

[2] A. Gourdon. Synthesis of molecular landers. *European Journal of Organic Chemistry*, 12:2797–2801, 1998.

[3] Guillaume Vives, Alexandre Gonzalez, Joo Jaud, Jean-Pierre Launay, and Gwenael Rapenne. Synthesis of molecular motors incorporating para-phenylene-conjugated or bicyclo[2.2.2]octane-lasulated electroactive groups. *Chemistry-A European Journal*, 13(19):5622–5631, 2007.

[4] Guillaume Vives and Gwenael Rapenne. Breaking the symmetry in the molecular motor family: Synthesis of a dissymmetrized pentaphenyl cyclopentadienyl ligand and it's ruthenium tris(indazolyl)borate complex. *Tetrahedron Letters*, 47(49):8741–8744, 2006.

[5] M. Mayor and C. Didschies. A giant conjugated molecular ring. *Angewandte Chemie-International Edition*, 42(27):3176–3179, 2003.

[6] C. P. Collier, G. Mattersteig, E. W. Wong, Y. Luo, K. Beverly, J. Sampaio, F. M. Raymo, J. F. Stoddart, and J. R. Heath. A [2]catenane-based solid state electronically reconfigurable switch. *Science*, 289(5482):1172–1175, 2000. 16.

[7] P. L. Anelli, P. R. Ashton, R. Ballardini, V. Balzani, M. Delgado, M. T. Gandolfi, T. T. Goodnow, A. E. Kaifer, D. Philp, M. Pietraszkiewicz, L. Prodi, M. V. Reddington, A. M. Z. Slawin, N. Spencer, J. F. Stoddart, C. Vicent, and D. J. Williams. Molecular meccano .1. [2]rotaxanes and a [2]catenane made to order. *Journal of the American Chemical Society*, 114(1):193–218, 1992. 311.

[8] G. Rapenne. Synthesis of technomimetic molecules: towards rotation control in single-molecular machines and motors. *Org. Biomol. Chem.*, 3:1165, 2005.

[9] Y. Shirai, A. J. Osgood, Y. Zhao, K. F. Kelly, and J. M. Tour. Directional control in thermally driven single-molecule nanocars. *Nano Lett.*, 5(11):2330 –2334, 2005.

[10] J. H. Chen and N. C. Seeman. Synthesis from dna of a molecule with the connectivity of a cube. *Nature*, 350:631–633, 1991.

[11] S. D. Patterson and R. H. Aebersold. Proteomics: the first decade and beyond. *Nature Genetics*, 33:311–323, 2003. 198 Suppl. S.

[12] F. J. Giessibl. Atomic resolution on Si(111)-(7x7) by noncontact atomic force microscopy with a force sensor based on a quartz tuning fork. *Applied Physics Letters*, 76(11):14701472, 2000.

[13] L. Grill, K. H. Rieder, F. Moresco, G. Rapenne, S. Stojkovic, X. Bouju, and C. Joachim. Rolling a single molecular wheel at the atomic scale. *Nature Nanotechnology*, 2(2):95–98, 2007.

[14] T. Yamada, H. Suzuki, H. Miki, G. Maofa, and S. Mashiko. High-resolution scanning tunneling microscopy images of molecular overlayers prepared by a new molecular beam deposition apparatus with spray-jet technique. *J. Phys. Chem. B*, 109:3183 – 3188, 2005.

[15] Y. Okabayashi, K. Kanai, Y. Ouchi, and K. Seki. Apparatus for solution jet beam deposition of organic thin films and in situ ultraviolet photoelectron spectroscopy. *Rev. Sci. Instr.*, 77:033905, 2006.

[16] R. J. Beuhler, E. Flanigan, L. J. Greene, and L. Friedman. Proton transfer mass spectrometry of peptides. rapid heating technique for underivatized peptides containing arginine. *J. Am. Chem. Soc*, 96:3990, 1973.

[17] J. B. Fenn, M. Mann, C. K. Meng, S. F. Wong, and C. M. Whitehouse. Electrospray ionization for mass-spectrometry of large biomolecules. *Science*, 246(4926):64–71, 1989. 41.

[18] M. Karas, D. Bachmann, U. Bahr, and Hillenkamp F. Matrix-assisted ultraviolet-laser desorption of nonvolatile compounds. *International Journal Of Mass Spectrometry And Ion Processes*, 78:53–68, 1987.

[19] H. J. Rader, A. Rouhanipour, A. M. Talarico, V. Palermo, P. Samori, and K. Mullen. Processing of giant graphene molecules by soft-landing mass spectrometry. *Nature Materials*, 5(4):276–280, 2006. 31.

[20] J. N. O'Shea, J. B. Taylor, J. C. Swarbrick, G. Magnano, L. C. Mayor, and K. Schulte. Electrospray deposition of carbon nanotubes in vacuum. *Nanotechnology*, 18(3):4, 2007. O'Shea, James N. Taylor, John B. Swarbrick, Janine C. Magnano, Graziano Mayor, Louise C. Schulte, Karina 17.

[21] J. C. Swarbrick, J. Ben Taylor, and J. N. O'Shea. Electrospray deposition in vacuum. *Applied Surface Science*, 252(15):5622–5626, 2006. 29.

[22] B. Davis and F.S. Goucher. Ionization and excitation of radiation by electron impact in mercury vapor and hydrogen. *Physical Review*, 10(2):101–115, 1917.

[23] J. J. Thomson. Bakerian lecture: Rays of positive electricity. *Proceedings of the Royal Society of London Series a-Containing Papers of a Mathematical and Physical Character*, 89(607):1, 1913. 0.

[24] M. Barber, R. S. Bordoli, R. D. Sedgwick, and A. N. Tyler. Fast atom bombardment of solids (FAB) - a new ion-source for mass-spectrometry. *Journal Of The Chemical Society-Chemical Communications*, 7:325–327, 1981.

[25] M. Yamashita and J. B. Fenn. Electrospray ion-source - another variation on the free-jet theme. *Journal of Physical Chemistry*, 88(20):4451–4459, 1984. 45.

[26] J. B. Fenn, M. Mann, C. K. Meng, S. F. Wong, and C. M. Whitehouse. Electrospray ionization-principles and practice. *Mass Spectrometry Reviews*, 9(1):37–70, 1990. 76.

[27] J. B. Fenn, M. Mann, and C. Meng. Method of producing multiply charged ions and for determining molecular weights of molecules by use of the multiply charged ions of molecules. *United States Patent*, (5,130,538), 1992. Patent.

[28] M. S. Wilm and M. Mann. Electrospray and taylor-cone theory, doles beam of macromolecules at last. *International Journal of Mass Spectrometry and Ion Processes*, 136(2-3):167–180, 1994. 22.

[29] V. G. Drozin. The electrical dispersion of liquids as aerosols. *J. Colloid Sci.*, 10:158, 1955.

[30] G. Taylor. Disintegration of water drops in electric field. *Proceedings of the Royal Society of London Series A - Mathematical and Physical Sciences*, 280(138):383, 1964. 11.

[31] M. Dole, H. L. Cox, and Gieniec J. Electrospray mass-spectroscopy. *Advances in Chemistry Series*, 125:73–84, 1973.

[32] C. S. Hoaglund-Hyzer, A. E. Counterman, and D. E. Clemmer. Anhydrous protein ions. *Chemical Reviews*, 99(10):3037–3079, 1999. 341.

[33] J. K. Eng, A. L. McCormack, and J. R. Yates. An approach to correlate tandem mass spectral data of peptides with amino acid sequences in a protein database. *Journal of the American Society for Mass Spectrometry*, 5(11):976–989, 1994.

[34] M.G. Ikonomou, A.T. Blades, and P. Kebarle. Investigations of the electrospray interface for liquid-chromatography mass-spectrometry. *Analytical Chemistry*, 62(9):957–967, 1990.

[35] M. Mann, C.K. MenG, and J. B. Fenn. Interpreting mass-spectra of multiply charged ions. *Analytical Chemistry*, 61(15):1702–1708, 1989.

[36] C. J. McNeal, R. D. Macfarlane, and E. L. Thurston. Thin-film deposition by the electrospray methos for CF-252 plasma desorption studies of involatile molecules. *Analytical Chemistry*, 51(12):2036–2039, 1979. 12.

[37] V. N. Morozov and T. Y. Morozova. Electrospray deposition as a method for mass fabrication of mono- and multicomponent microarrays of biological and biologically active substances. *Analytical Chemistry*, 71(15):3110–3117, 1999. 32.

[38] V. N. Morozov and T. Y. Morozova. Electrospray deposition as a method to fabricate functionally active protein films. *Analytical Chemistry*, 71(7):1415–1420, 1999. 37.

[39] M. Danek, K. F. Jensen, C. B. Murray, and M. G. Bawendi. Electrospray organometallic chemical-vapor-deposition - a novel technique for preparation of II-VI quantum-dot composites. *Applied Physics Letters*, 65(22):2795–2797, 1994. 16.

[40] I. W. Lenggoro, B. Xia, K. Okuyama, and J. F. de la Mora. Sizing of colloidal nanoparticles by electrospray and differential mobility analyzer methods. *Langmuir*, 18(12):4584–4591, 2002. 22.

[41] A. Gomez, D. Bingham, L. de Juan, and K. Tang. Production of protein nanoparticles by electrospray drying. *Journal of Aerosol Science*, 29(5-6):561–574, 1998. 34.

[42] A. M. Welle and H. O. Jacobs. Printing of organic and inorganic nanomaterials using electrospray ionization and coulomb-force-directed assembly. *Applied Physics Letters*, 87(26):3, 2005. 23.

[43] I. B. Rietveld, K. Kobayashi, H. Yamada, and K. Matsushige. Morphology control of poly(vinylidene fluoride) thin film made with electrospray. *Journal of Colloid and Interface Science*, 298(2):639–651, 2006. 42.

[44] M. Danek, K. F. Jensen, C. B. Murray, and M. G. Bawendi. Synthesis of luminescent thin-film cdse/znse quantum dot composites using cdse quantum dots passivated with an overlayer of znse. *Chemistry of Materials*, 8(1):173–180, 1996. 33.

[45] I. Uematsu, H. Matsumoto, K. Morota, M. Minagawa, A. Tanioka, Y. Yamagata, and K. Inoue. Surface morphology and biological activity of protein thin films produced by electrospray deposition. *Journal of Colloid and Interface Science*, 269(2):336–340, 2004. 21.

[46] T. Wyttenbach, G. vonHelden, and M. T. Bowers. Gas-phase conformation of biological molecules: Bradykinin. *Journal of the American Chemical Society*, 118(35):8355–8364, 1996. 88.

[47] M. Scalf, M. S. Westphall, J. Krause, S. L. Kaufman, and L. M. Smith. Controlling charge states of large ions. *Science*, 283(5399):194–197, 1999. 43.

[48] M. Gamero-Castano and J. F. de la Mora. Mechanisms of electrospray ionization of singly and multiply charged salt clusters. *Analytica Chimica Acta*, 406(1):67–91, 2000. 61.

[49] M. J. Ford, V. Kertesz, and G. J. Van Berkel. Thin-layer chromatography/electrospray ionization triple-quadrupole linear ion trap mass spectrometry system: Analysis of rhodamine dyes separated on reversed-phase C-8 plates. *Journal of Mass Spectrometry*, 40(7):866–875, 2005. 16.

[50] K. J. Kitching, H. N. Lee, W. T. Elam, E. E. Johnston, H. MacGregor, R. J. Miller, F. Turecek, and B. D. Ratner. Development of an electrospray approach to deposit complex molecules on plasma modified surfaces. *Review of Scientific Instruments*, 74(11):4832–4839, 2003. 35.

[51] G. Siuzdak, B. Bothner, M. Yeager, C. Brugidou, C. M. Fauquet, K. Hoey, and C. M. Chang. Mass spectrometry and viral analysis. *Chemistry and Biology*, 3(1):45–48, 1996. 20.

[52] S. A. Miller, H. Luo, S. J. Pachuta, and R. G. Cooks. Soft-landing of polyatomic ions at fluorinated self-assembled monolayer surfaces. *Science*, 275(5305):1447–1450, 1997. 23.

[53] Z. Ouyang, Z. Takats, T. A. Blake, B. Gologan, A. J. Guymon, J. M. Wiseman, J. C. Oliver, V. J. Davisson, and R. G. Cooks. Preparing protein microarrays by soft-landing of mass-selected ions. *Science*, 301(5638):1351–1354, 2003. 21.

[54] B. Gologan, Z. Takats, J. Alvarez, J. M. Wiseman, N. Talaty, Z. Ouyang, and R. G. Cooks. Ion soft-landing into liquids: Protein identification, separation, and purification with retention of biological activity. *Journal of the American Society for Mass Spectrometry*, 15(12):1874–1884, 2004. 44.

[55] R. J. Geiger, M. C. Melnyk, K. L. Busch, and M. G. Bartlett. Modifications to an analytical mass spectrometer for the soft-landing experiment. *International Journal of Mass Spectrometry*, 183:415–422, 1999. 21.

[56] M. Volny, W. T. Elam, A. Branca, B. D. Ratner, and F. Turecek. Preparative soft and reactive landing of multiply charged protein ions on a plasma-treated metal surface. *Analytical Chemistry*, 77(15):4890–4896, 2005. 27.

[57] M. Volny, A. Sengupta, C. B. Wilson, B. D. Swanson, E. J. Davis, and F. Turecek. Surface-enhanced raman spectroscopy of soft-landed polyatomic ions and molecules. *Analytical Chemistry*, 79(12):4543–4551, 2007. Volny, Michael Sengupta, Atanu Wilson, C. Brant Swanson, Brian D. Davis, E. James Turecek, Frantisek 48.

[58] H. Luo, S. A. Miller, R. G. Cooks, and S. J. Pachuta. Soft landing of polyatomic ions for selective modification of fluorinated self-assembled monolayer surfaces. *International Journal of Mass Spectrometry*, 174(1-3):193–217, 1998. 103.

[59] J. P. Biesecker, G. B. Ellison, H. Wang, M. J. Iedema, A. A. Tsekouras, and J. P. Cowin. Ion beam source for soft-landing deposition. *Review of Scientific Instruments*, 69(2):485–495, 1998. 25 Part 1.

[60] S. D. Fuerstenau, W. H. Benner, J. J. Thomas, C. Brugidou, B. Bothner, and G. Siuzdak. Mass spectrometry of an intact virus (vol 40, pg 542, 2001). *Angewandte Chemie-International Edition*, 40(6):982–982, 2001. 1.

[61] V. Franchetti, B. H. Solka, W. E. Baitinger, J. W. Amy, and R. G. Cooks. Soft landing of ions as a means of surface modification. *International Journal of Mass Spectrometry and Ion Processes*, 23(1):29–35, 1977. 12.

[62] S. A. Smith, T. A. Blake, D. R. Ifa, R. G. Cooks, and O. Y. Zheng. Dual-source mass spectrometer with MALDI-LIT-ESI configuration. *Journal of Proteome Research*, 6(2):837–845, 2007. Smith, Scott A. Blake, Thomas A. Ifa, Demian R. Cooks, R. Graham Zheng Ouyang 38.

[63] L. P. Smith, W. E. Parkins, and A. T. Forrester. On the separation of isotopes in quantity by electromagnetic means. *Physical Review*, 72(11):989–1002, 1947. 6.

[64] R. Campargue. Progress in overexpanded supersonic jets and skimmed molecular-beams in free-jet zones of silence. *Journal of Physical Chemistry*, 88(20):4466–4474, 1984. 77.

[65] D. Duft, T. Achtzehn, R. Muller, B. A. Huber, and T. Leisner. Coulomb fission - Rayleigh jets from levitated microdroplets. *Nature*, 421(6919):128–128, 2003. 9.

[66] T. A. Blake. *Instrumentation for Preparative Mass Spectrometry*. PhD thesis, Purdue University, West Lafayette, Indiana, 2006.

[67] R. B. Cole. *Electrospray Ionization Mass Spectrometry*. John Wiley and Sons, Inc., 1997.

[68] G. D. Wang and R. B. Cole. Charged residue versus ion evaporation for formation of alkali metal halide cluster ions in ESI. *Analytica Chimica Acta*, 406(1):53–65, 2000. 18.

[69] P. Kebarle. A brief overview of the present status of the mechanisms involved in electrospray mass spectrometry. *Journal of Mass Spectrometry*, 35(7):804–817, 2000. 47.

[70] P. Kebarle and M. Peschke. On the mechanisms by which the charged droplets produced by electrospray lead to gas phase ions. *Analytica Chimica Acta*, 406(1):11–35, 2000. 43.

[71] M. Labowsky, J. B. Fenn, and J. F. de la Mora. A continuum model for ion evaporation from a drop: Effect of curvature and charge on ion solvation energy. *Analytica Chimica Acta*, 406(1):105–118, 2000. 10.

[72] P. Milani and Iannotta S. *Cluster Beam Synthesis and Nanostructured Materials*. Springer, 1999.

[73] J. F. de la Mora. Electrospray ionization of large multiply charged species proceeds via dole's charged residue mechanism. *Analytica Chimica Acta*, 406(1):93–104, 2000. 44.

[74] S. J. Gaskell. Electrospray: Principles and practice. *Journal of Mass Spectrometry*, 32(7):677–688, 1997. 93.

[75] J. F. Anacleto, S. Pleasance, and R. K. Boyd. Calibration of ion spray mass-spetra using cluster ions. *Organic Mass Spectrometry*, 27(6):660–666, 1992. 33.

[76] D. W. Ledman and R. O. Fox. Water cluster calibration reduces mass error in electrospray ionization mass spectrometry of proteins. *Journal of the American Society for Mass Spectrometry*, 8(11):1158–1164, 1997. 34.

[77] K. Mori, D. Asakawa, J. Sunner, and K. Hiraoka. Electrospray droplet impact/secondary ion mass spectrometry: Cluster ion formation. *Rapid Communications in Mass Spectrometry*, 20(17):2596–2602, 2006. Mori, Kunihiko Asakawa, Dalki Sunner, Jan Hiraoka, Kenzo 16.

[78] D. X. Zhang and R. G. Cooks. Doubly charged cluster ions [(NaCl)(m)(Na)(2)](2+): Magic numbers, dissociation, and structure. *International Journal of Mass Spectrometry*, 196:667–684, 2000. 65 Sp. Iss. SI.

[79] S. L. Zhou and M. Hamburger. Formation of sodium cluster ions in electrospray mass spectrometry. *Rapid Communications in Mass Spectrometry*, 10(7):797–800, 1996. 19.

[80] C. Y. Hao, R. E. March, T. R. Croley, J. C. Smith, and S. P. Rafferty. Electrospray ionization tandem mass spectrometric study of salt cluster ions. Part 1 - investigations of alkali metal c chloride and sodium salt cluster ions. *Journal of Mass Spectrometry*, 36(1):79–96, 2001. 31.

[81] M. P. Ince, B. A. Perera, and M. J. Van Stipdonk. Production, dissociation, and gas phase stability of sodium fluoride cluster ions studied using electrospray ionization ion trap mass spectrometry. *International Journal of Mass Spectrometry*, 207(1-2):41–55, 2001. 65.

[82] P. H. Dawson. *Quadrupole Mass Spectrometry*. Elsevier Scientific Publishing Company, 1976.

[83] A. G. Marshall, C. L. Hendrickson, and G. S. Jackson. Fourier transform ion cyclotron resonance mass spectrometry: A primer. *Mass Spectrometry Reviews*, 17(1):1–35, 1998.

[84] Q. Z. Hu, R. J. Noll, H. Y. Li, A. Makarov, M. Hardman, and R. G. Cooks. The orbitrap: A new mass spectrometer. *Journal Of Mass Spectrometry*, 40(4):430–443, 2005.

[85] W. C. Wiley and I. H. McLaren. Time-of-flight mass spectrometer with improved resolution. *Review of Scientific Instruments*, 26(12):1150–1157, 1955. 7.

[86] R. G. Cooks and A. L. Rockwood. The Thomson - a suggested unit for mass spectroscopists. *Rapid Communications In Mass Spectrometry*, 5(2):93, 1991.

[87] T. Bergmann, T. P. Martin, and H. Schaber. High-resolution time-of-flight mass spectrometers .1. effects of field distortions in the vicinity of wire meshes. *Review of Scientific Instruments*, 3(60):347–349, 1989.

[88] T. Bergmann, T. P. Martin, and H. Schaber. High-resolution time-of-flight mass spectrometer. *Review of Scientific Instruments*, 60(4):792–793, 1989.

[89] T. Bergmann, T. P. Martin, and H. Schaber. High-resolution time-of-flight mass spectrometers .2. Reflector design. *Review of Scientific Instruments*, 61(10):2592–2600, 1990.

[90] T. Bergmann, H. Goehlich, T. P. Martin, and Schaber H. high-resolution time-of-flight mass spectrometers .2. cross beam ion optics. *Review of Scientific Instruments*, 61(10):2585–2591, 1990.

[91] B. A. Mamyrin, V. I. Karataev, D. V. Shmikk, and V. A. Zagulin. The mass-reflectron, a new nonmagnetic time-of-flight mass spectrometer with high resolution. *Sov. Phys. JETP*, 37(45), 1973.

[92] D. Gerlich. *Inhomogenous RF Fields: A Versatile Tool for the Study of Processes with Slow Ions*. John Wiley and Son, Inc., 1992.

[93] C. M. Lock and E. W. Dyer. Simulation of ion trajectories through a high pressure radio frequency only quadrupole collision cell by SIMION 6.0. *Rapid Communications in Mass Spectrometry*, 13:422–431, 1999.

[94] A. V. Tomachev, I. V. Chernushevich, A. F. Dodonov, and K. G. Standing. A collisional focusing ion guide for coupling an atmospheric pressure ion source to a mass spectrometer. *Nuclear Instruments and Methods in Physics Research*, 124:112–119, 1997.

[95] A. N. Krutchinsky, I. V. Chernushevich, V. L. Spicer, W. Ens, and K. G. Stand. Collisional damping interface for an electrospray ionization time-of-flight mass spectrometer. *American Society for Mass Spectrometry*, 9:569–579, 1998.

[96] M. D. Lunney and R. B. Moore. Cooling of mass-seperated beams using a radiofrequency quadropole ion guide. *International Journal of Mass Spectrometry*, 190/191:156–160, 1999.

[97] W. Petrich, M. Grieser, R. Grimm, A. Gruber, D. Habs, H. J. Miesner, D. Schwalm, B. Wanner, H. Wernoe, and A. Wolf. Laser cooling of stored high-velocity ions by means of the spontaneouse force. *Physical Review A*, 48(3):2127–2144, 1993.

[98] C. E. Sosolik, A. C. Lavery, E. B. Dahl, and B. H. Cooper. A technique for accurate measurements of ion beam current density using a Farraday cup. *Review of Scientific Instruments*, 71(9):3326–3330, 2000.

[99] C. K. Chao and S. Y. Su. Charged particles motion inside the retarding potential analyzer. *Phsyics of Plasmas*, 7(1):101–107, 2000.

[100] Volmer DA Sleno L. Ion activation methods for tandem mass spectrometry. *Journal of mass spectrometry*, 39(10):1091–112, 2004.

[101] R. D. Smith, J. A. Loo, C. G. Edmonds, C. J. Barinaga, and H. R. Udseth. New develpoments in biochemical mass-spectrometry - electrospray ionization. *Analytical Chemistry*, 62(9):882–899, 1990. 142.

[102] A. Schmidt, U. Bahr, and M. Karas. Influence of pressure in the first pumping stage on analyte desolvation and fragmentation in nano-esi ms. *Analytical Chemistry*, 73(24):6040–6046, 2001. 40.

[103] Arnold Sommerfeld. *Vorlesung ueber Theoretische Physik (Band V): Thermodynamik und Statistik*. Verlag Harri Deutsch, 1988.

[104] E. W. McDaniel. *Collision Phenomena in Ionized Gases*. John Wiley and Sons, New York, 1964.

[105] V. Grill, J. Shen, C. Evans, and R. G. Cooks. Collisions of ions with surfaces at chemically relevant energies: Instrumentation and phenomena. *Review of Scientific Instruments*, 72(8):3149–3179, 2001. 336.

[106] B. Gologan, J. R. Green, J. Alvarez, J. Laskin, and R. G. Cooks. Ion/surface reactions and ion soft-landing. *Physical Chemistry Chemical Physics*, 7(7):1490–1500, 2005. 92.

[107] R. G. Cooks, S. C. Jo, and J. Green. Collisions of organic ions at surfaces. *Applied Surface Science*, 231-2:13–21, 2004. 68 Sp. Iss. SI.

[108] J. P. Wang, S. O. Meroueh, Y. F. Wang, and W. L. Hase. Efficiency of energy transfer in protonated diglycine and dialanine SID - effects of collision angle, peptide ion size, and intramolecular potential. *International Journal of Mass Spectrometry*, 230(1):57–64, 2003. 41.

[109] S. B. Wainhaus, E. A. Gislason, and L. Hanley. Determination of activation energies for ion fragmentation by surface-induced dissociation. *Journal of the American Chemical Society*, 119(17):4001–4007, 1997. 46.

[110] M. Volny and F. Turecek. High efficiency in soft landing of biomolecular ions on a plasma-treated metal surface: are double-digit yields possible? *Journal of Mass Spectrometry*, 41(1):124–126, 2006. 16.

[111] K. Bromann, C. Felix, H. Brune, W. Harbich, R. Monot, J. Buttet, and K. Kern. Controlled dposition of size-selected silver nanoclusters. *Science*, 274(5289):956–958, 1996. 26.

[112] S. J. Carroll, S. Pratontep, M. Streun, R. E. Palmer, S. Hobday, and R. Smith. Pinning of size-selected Ag clusters on graphite surfaces. *Journal of Chemical Physics*, 113(18):7723–7727, 2000. 20.

[113] H. P. Cheng and U. Landman. Controlled deposition, soft landing, and glass-formation in nanocluster-surface collisions. *Science*, 260(5112):1304–1307, 1993. 38.

[114] A. Bötcher, P. Weis, A. Bihlmeier, and M. Kappes. C58 on HOPG: Soft-landing adsorption and thermal desorption. *Phys. Chem. Chem. Phys.*, 6:5213–5217, 2004.

[115] Nicha Thontasen. *Electrospray Ionization Mass Spectrometry and Vacuum Deposition of Very Low Energy Molecular Ion Beams*. PhD thesis, University of Stuttgart, 2006.

[116] J. J. Thomson. Cathode rays. *The London, Edinburgh, and Dublin Philosophical Magazine and Journal of Science*, 44(269):293, 1897.

[117] Poul Dahl. *Introduction to Electron and Ion Optics*. Academic Press, New York and London, 1973.

[118] M. E. Belov, A. W. Colburn, and P. J. Derrick. Design and performance of an electrospray ion source for magnetic-sector mass spectrometers. *Review of Scientific Instruments*, 69(3):1275–1281, 1998. 23.

[119] W. Paul, H. P. Reinhard, and U. Vonzahn. Der Elektrische Massenfilter als Massenspektrometer und Isotopentrenner. *Zeitschrift Fur Physik*, 152(2):143–182, 1958. 23.

[120] I. Cermak. Compact radio frequency power supply for ion and particle guides and traps. *Review of Scientific Instruments*, 76:063302, 2005.

[121] D. A. Dahl. SIMION for the personal computer in reflection. *International Journal of Mass Spectrometry*, 200:3–25, 2000.

[122] C. F. Quate G. Binnig and C. Gerber. Atomic force microscope. *Physical Review Letters*, 56:930–933, 1986.

[123] I. Horcas. WSXM: A software for scanning probe microscopy and a tool for nanotechnology. *Review of Scientific Instruments*, 78:013705, 2007.

[124] A. Benningh. Surface investigation of solids by statical method of secondary ion mass spectroscopy (SIMS). *Surface Science*, 35(1):427–457, 1973.

[125] Ch.K. Meng and J. B. Fenn. Formation of charged clusters during electrospray ionization of organic solute species. *Organic Mass Spectrometry*, 26, 1991.

[126] C. Y. Hao and R. E. March. Electrospray ionization tandem mass spectrometric study of salt cluster ions: Part 2 - Salts of polyatomic acid groups and of multivalent metals. *Journal of Mass Spectrometry*, 36(5):509–521, 2001. 29.

[127] U. Naher, S. Frank, N. Malinowski, U. Zimmermann, and T. P. Martin. Fission of highly-charged alkali-metal clusters. *Zeitschrift Fur Physik D-Atoms Molecules and Clusters*, 31(3):191–197, 1994. 23.

[128] U. Zimmermann, N. Malinowski, U. Naher, S. Frank, and T. P. Martin. Producing and detecting very large clusters. *Zeitschrift Fur Physik D-Atoms Molecules and Clusters*, 31(1-2):85–93, 1994. 20.

[129] K. Bromann, H. Brune, C. Felix, W. Harbich, R. Monot, J. Buttet, and K. Kern. Hard and soft landing of mass selected Ag clusters on Pt(111). *Surface Science*, 377(1-3):1051–1055, 1997. 16.

[130] S. Konig and H. M. Fales. Calibration of mass ranges up to m/z 10,000 in electrospray mass spectrometers. *Journal of the American Society for Mass Spectrometry*, 10(3):273–276, 1999. 14.

[131] J. A. Loo. Studying noncovalent protein complexes by electrospray ionization mass spectrometry. *Mass Spectrometry Reviews*, 16(1):1–23, 1997. 183.

[132] J. A. Loo. Electrospray ionization mass spectrometry: a technology for studying noncovalent macromolecular complexes. *International Journal of Mass Spectrometry*, 200(1-3):175–186, 2000. 82.

[133] P. C. Maria, L. Massi, N. S. Box, J. F. Gal, P. Burk, J. Tammiku-Tau, and M. Kutsar. Bonding energetics in clusters formed by cesium salts: a study by collision-induced dissociation and density functional theory. *Rapid Communications in Mass Spectrometry*, 20(13):2057–2062, 2006. Maria, Pierre-Charles Massi, Lionel Box, Natzaret Sindreu Gal, Jean-Francois Burk, Peeter Tammiku-Tau, Jaana Kutsar, Martin 53.

[134] J. M. Ding and R. J. Anderegg. Specific and nonspecific dimer formation in the electrospray-ionization mass-spectrometry of oligonucleotides. *Journal of the American Society for Mass Spectrometry*, 6(3):159–164, 1995. 21.

[135] E. C. Huang, B. N. Pramanik, A. Tsarbopoulos, P. Reichert, A. K. Ganguly, P. P. Trotta, T. L. Nagabhushan, and T. R. Covey. Application of electrospray mass-spectrometry in probing protein-protein and protein ligand noncovalent interactions. *Journal of the American Society for Mass Spectrometry*, 4(8):624–630, 1993. 41.

[136] J. C. Jurchen and E. R. Williams. Origin of asymmetric charge partitioning in the dissociation of gas-phase protein homodimers. *Journal of the American Chemical Society*, 125(9):2817–2826, 2003. 53.

[137] Y. T. Li, Y. L. Hsieh, J. D. Henion, M. W. Senko, F. W. McLafferty, and B. Ganem. Mass-spectrometric studies on noncovalent dimers of leucine-zipper peptides. *Journal of the American Chemical Society*, 115(18):8409–8413, 1993. 24.

[138] D. L. Zhan and J. B. Fenn. Gas phase hydration of electrospray ions from small peptides. *International Journal of Mass Spectrometry*, 219(1):1–10, 2002. 16.

[139] S. R. Feldman. *Kirk-Othmer Encyclopedia of Chemical Technology: Sodium Chloride*. John Wiley and Son, 2005.

[140] J. A. Zimmerman, J. R. Eyler, S. B. H. Bach, and S. W. McElvany. Magic number carbon clusters - ionization-potentials and selective reactivity. *Journal of Chemical Physics*, 94(5):3556–3562, 1991. 54.

[141] Toomre D Simons K. Lipid rafts and signal transduction. *Nature Reviews Molecular Cell Biology*, 1(1):31–39, 2000.

[142] Sackmann E Tanaka M. Polymer-supported membranes as models of the cell surface. *Nature*, 437(7059):656–663, 2005.

[143] J. L. Stephenson and S. A. McLuckey. Gaseous protein cations are amphoteric. *Journal of the American Chemical Society*, 119:1688–1696, 1997.

[144] L. Konermann and D. J. Douglas. Acid-induced unfolding of cytochrome c at different methanol concentrations: Electrospray ionization mass spectrometry specifically monitors changes in the tertiary structure. *Biochemistry*, 36(40):12296–12302, 1997. 51.

[145] D. E. Clemmer, R. R. Hudgins, and M. F. Jarrold. Naked protein conformations - cytochrome-c in the gas-phase. *Journal of the American Chemical Society*, 117(40):10141–10142, 1995. 50.

[146] Guillaume Vives, Alexandre Carella, Jean-Pierre Launay, and Gwenael Rapenne. A star-shaped ruthenium complex with five ferrocenyl-terminated arms bridged by trans-platinum fragments. *Chemical Communications*, pages 2283–2285, 2006.

[147] G. Rapenne, J. P. Launay, and C. Joachim. Design and synthesis of mono-molecular machines. *Journal Of Physics-Condensed Matter*, 18(33):S1797–S1808, 2006.

[148] C. D. Bain and Whitesides G. M. Molecular level control over surface order in self-assembled monolayer films of thiols on gold. *Science*, 240:62–63, 1988.

[149] K. A. Selanger, J. Falnes, and T. Sikkeland. Fluorescence lifetime studies of rhodamine 6G in methanol. *Journal of Physical Chemistry*, 81(20):1960, 1977.

[150] H. Du, R. A. Fuh, J. Li, A. Corkan, and J. S. Lindsey. Photochemcad: A computer-aided design and research tool in photochemistry. *Photochemistry and Photobiology*, 68:141–142, 1998.

[151] J. A. Titus, R. Haugland, S. O. Sharrow, and D. M. Segal. Texas Red, a hydorphilic, red-emitting flurophore for use with fluorescein in dual parameter flow micro-fluometric and fluorescence microscopic studies. *Journal of Immunological Methods*, 50(2):193–204, 1982. 5.

[152] D. Magde, R. Wong, and P. G. Seybold. Fluorescence quantum yields and their relation to lifetimes of rhodamine 6G and fluorescein in nine solvents: Improved absolute standards for quantum yields. *Photochemistry and Photobiology*, 75(4):327–334, 2002. 28.

[153] L. Allen and J. H. Eberly. *Optical Resonance and Two-Level Atoms*. Dover Publications, New York, 1975.

[154] G. Herzberg. *The Spectra and Structure of Simple Free Radicals*. Dover Publications, New York, 1971.

[155] Y. Uehara and S. Ushioda. Single molecule spectrum of rhodamine 6G on highly oriented pyrolytic graphite. *Applied Physics Letters*, 86(18):3, 2005. 16.

[156] M. Fujita, N. Fujita, K. Ogura, and K. Yamaguchi. Spontaneous assembly of ten components into two interlocked, identical coordination cages. *Nature*, 400, 1999.

[157] Sauvage J.P. and C. Dietrichbuchecker, editors. *Molecular Catenanes, Rotaxanes and Knots*. Wiely-VCH, Weinheim, 1999.

[158] D. B. Amabilino, P. R. Ashton, C. L. Brown, E. Cordova, L. A. Godinez, T. T. Goodnow, A. E. Kaifer, S. P. Newton, M. Pietraszkiewicz, D. Philp, F. M. Raymo, A. S. Reder, M. T. Rutland, A. M. Z. Slawin, N. Spencer, J. F. Stoddart, and D. J. Williams. Molecular meccano .2. self-assembly of [ETA]catenanes. *Journal of the American Chemical Society*, 117(4):1271–1293, 1995. 116.

[159] A. G. Johnston, D. A. Leigh, R. J. Pritchard, and M. D. Deegan. Facile synthesis and solid-state structure of a benzylic amide [2]catenane. *Angewandte Chemie-International Edition in English*, 34(11):1209–1212, 1995. 17.

[160] V. Balzani, Credi A., and Venturi M., editors. *Molecular Devices and Machines - A Journey into the Nano World*. Wiely-VCH, Weinheim, 2003.

[161] E. R. Kay, D. A. Leigh, and F. Zerbetto. Synthetic molecular motors and mechanical machines. *Angewandte Chemie-International Edition*, 46(1-2):72–191, 2007. Kay, Euan R. Leigh, David A. Zerbetto, Francesco 1607.

[162] W. R. Browne and B. L. Feringa. Making molecular machines work. *Nature Nanotechnology*, 1(1):25–35, 2006. Browne, Wesley R. Feringa, Ben L. 110.

[163] V. Balzani, A. Credi, F. M. Raymo, and J. F. Stoddart. Artificial molecular machines. *Angewandte Chemie-International Edition*, 39(19):3349–3391, 2000. 593.

[164] A. H. Flood, E. W. Wong, and J. F. Stoddart. Models of charge transport and transfer in molecular switch tunnel junctions of bistable catenanes and rotaxanes. *Chemical Physics*, 324(1):280–290, 2006. 67.

[165] Y. Liu, A. H. Flood, P. A. Bonvallett, S. A. Vignon, B. H. Northrop, H. R. Tseng, J. O. Jeppesen, T. J. Huang, B. Brough, M. Baller, S. Magonov, S. D. Solares, W. A. Goddard, C. M. Ho, and J. F. Stoddart. Linear artificial molecular muscles. *Journal of the American Chemical Society*, 127(27):9745–9759, 2005. 144.

[166] S. S. Jang, Y. H. Jang, Y. H. Kim, W. A. Goddard, A. H. Flood, B. W. Laursen, H. R. Tseng, J. F. Stoddart, J. O. Jeppesen, J. W. Choi, D. W. Steuerman, E. DeIonno, and J. R. Heath. Structures and properties of self-assembled monolayers of bistable [2]rotaxanes on Au(111) surfaces from molecular dynamics simulations validated with experiment. *Journal of the American Chemical Society*, 127(5):1563–1575, 2005. 156.

[167] H. R. Tseng, D. M. Wu, N. X. L. Fang, X. Zhang, and J. F. Stoddart. The metastability of an electrochemically controlled nanoscale machine on gold surfaces. *Chemphyschem*, 5(1):111–116, 2004. 70.

[168] D. Payer, S. Rauschenbach, M. Konuma, C. Virojanadara, U. Starke, C. Dietrich, J.P. Collin, J.P.and Sauvage, N. Lin, and K. Kern. Toward mechanical switching of surface-grafted [2]catenante by in-situ copper complexation. *(submitted)*, 0(0):0, 2007.

[169] C. Dietrichbuchecker, E. Leize, J. F. Nierengarten, J. P. Sauvage, and A. Vandorsselaer. Singly and doubly interlocked [2]-catenanes - influence of the degree of entangelment on chemical-stability as estimated by fast-atom-bombardement (FAB) and electrospray-ionization (ESI) mass spectrometries (MS). *Journal of the Chemical Society-Chemical Communications*, (19):2257–2258, 1994. 19.

[170] C. O. Dietrichbuchecker, J. P. Sauvage, and J. M. Kern. Templated synthesis of interlocked macrocyclic ligands - the catenands. *Journal of the American Chemical Society*, 106(10):3043–3045, 1984. 18.

[171] M. Cesario, C. O. Dietrichbuchecker, J. Guilhem, C. Pascard, and J. P. Sauvage. Molecular-structure of a catenand and it's copper(i) catenate - complete rearrangement of the interlocked macrocyclic ligands by complexation. *Journal of the Chemical Society-Chemical Communications*, (5):244–247, 1985. 11.

[172] O. Boussif, F. Lezoualch, M. Zanta, Mergny M., D. Scherman, B. Demeneix, and J. P. Behr. A versatile vector for gene and oligonucleotide transfer into cells in culture and in-vivo - polyethylenimine. *Proceedings Of The National Academy Of Sciences Of The United States Of America*, 92(16):7297–7301, 1995.

[173] A. G. Ludwick and C. G. Overberger. Synthesis and characterization of polyethylenimine backbone polynucleotide models. *Journal of Polymer Science, Part A, Polymer chemistry*, 20(8):2123–2138, 1982.

[174] M. J. Gething and J. Sambrook. Protein folding in the cell. *Nature*, 355(6355):33–45, 1992. 207.

[175] F. U. Hartl. Molecular chaperones in cellular protein folding. *Nature*, 381(6583):571–580, 1996. 154.

[176] Sigma. Albumine, bovine, CAS 9048-46-8. *Sigma Product Information*, pages 1–5, 1997.

[177] A.A. Bhattacharya, T. Grune, and S. Curry. Crystallographic analysis reveals common modes of binding of medium and long-chain fatty acids to human serum albumin. *J.Mol.Biol.*, 303:721–732, 2000.

[178] A. N. Verentchikov, W. Ens, and K. G. Standing. Reflecting time-of-flight mass-spectrometer with an electrospray ion-source and orthogonal extraction. *Analytical Chemistry*, 66(1):126–133, 1994. 37.

[179] R. D. Smith, Loo J. A., Loo R. R. O., Busman M., and Udseth H. R. Principles and practice of electrospray ionization - mass-spectrometry for large polypeptides and proteins. *Mass Spectrometry Reviews*, 10(5):359–451, 1991.

[180] Z. Y. Zhang and Lagally M. G. Atomistic processes in the early stages of thin-film growth. *Science*, 276(5311):377–383, 1997.

[181] T. Peters. *All about Albumine*. Academic Press, New York, 1996.

[182] A. P. Quist, J. Ahlbom, C. T. Reimann, and B. U. R. Sundqvist. Scanning force microscopy studies of surface-defects induced by incident energetic macromolecular ions. *Nuclear Instruments and Methods in Physics Research Section B-Beam Interactions with Materials and Atoms*, 88(1-2):164–169, 1994. 36.

[183] M. T. Bowers, A. G. Marshall, and F. W. McLafferty. Mass spectrometry: Recent advances and future directions. *Journal Of Physical Chemistry*, 100(31):12897–12910, 1996.

[184] J. Axelsson, C. T. Reimann, and B. U. R. Sundqvist. Secondary-electron emission from surfaces impacted by multiply-charged polyatomic ions. *Nuclear Instruments and Methods in Physics Research Section B-Beam Interactions with Materials and Atoms*, 88(1-2):131–137, 1994. 36.

[185] C. Leidy, T. Kaasgaard, J. H. Crowe, O. G. Mouritsen, and K. Jorgensen. Ripples and the formation of anisotropic lipid domains: Imaging two-component supported double bilayers by atomic force microscopy. *Biophys J*, 83(5):2625–2633, 2002.

[186] C. Richard, F. Balavoine, P. Schultz, T. W. Ebbesen, and Mioskowski C. Supramolecular self-assembly of lipid derivatives on carbon nanotubes. *Science*, 300(5620):775–778, 2003.

[187] D. Chandler. Interfaces and the driving force of hydrophobic assembly. *Nature*, 437:640, 2005.

[188] Scholtmeijer K. Hektor, H. J. Hydrophobins: proteins with potential. *Current Opinion In Biotechnology*, 16(4):434–439, 2005.

[189] H. M. McConnell. Structures and transitions in lipid monolayers at the air-water-interface. *Annual Review Of Physical Chemistry*, 42:171–195, 1991.

[190] F. A. Smidt. Use of ion-beam assisted deposition to modify the microstructure and properties of thin-films. *International Materials Reviews*, 53(2):61–128, 1990.

[191] G. Herzberg. *Atomic Spectra and Atomic Stucture*. Dover Publications, New York, 1937.

[192] Tsien R. Y. The green fluorescent protein. *Annu. Rev. Biochem.*, 67:509, 1998.

[193] J. J. Macklin, J. K. Trautman, T. D. Harris, and Brus L. E. Imaging and time-resolved spectroscopy of single molecules at an interface. *Science*, 272(5259):255–258, 1996.

[194] J. Alvarez, R. G. Cooks, S. E. Barlow, D. J. Gaspar, J. H. Futrell, and J. Laskin. Preparation and in situ characterization of surfaces using soft landing in a fourier transform ion cyclotron resonance mass spectrometer. *Analytical Chemistry*, 77(11):3452–3460, 2005. 36.

[195] F. Zondervan, R.and Kulzer, M. A. Kol'chenko, and M. Orrit. Photobleaching of rhodamine 6G in poly(vinyl alcohol) at the ensemble and single-molecule levels. *Journal of Physical Chemistry A*, 108(10):1657–1665, 2004.

[196] A. Sanchez, S. Abbet, U. Heiz, W. D. Schneider, H. Hakkinen, R. N. Barnett, and U. Landman. When gold is not noble: Nanoscale gold catalysts. *Journal Of Physical Chemistry A*, 103(48):9573–9578, 1999.

[197] S. Kar and S. Chaudhuri. Cadmium sulfide one-dimensional nanostructures: Syntheis, characterization and application. *Synthesis and Reactivity in Inorganic, Metal-Organic and Nano-Metal Chemistry*, 36:289–312, 2006.

[198] J. Muster, G.T. Kim, V. Krstic, J.G. Park, Y.W. Park, S. Roth, and M. Burghard. Electrical transport through individual vanadium pentoxide nanowires. *Advanced Materials*, 12(6):420, 2000.

[199] R.T. Weitz, U. Zschieschang, F. Effenberger, H. Klauk, M. Burghard, and K. Kern. High-performance carbon nanotube field effect transistors with a thin gate dielectric based on a self-assembled monolayer. *Nano Letters*, 7(1):22–27, 2007.

[200] Y. Li, H. Liao, Y. Ding, Y. Fan, Y. Zhang, and Y. Quian. Solvothermal elemental direct reaction to CdE (E=S, Se, Te) semiconductor nanorods. *Inorgainc Chemistry*, 38:1382, 1999.

[201] Brune H. Microscopic view of epitaxial metal growth: nucleation and aggregation. *Surface Science Reports*, 31(4-6):121–229, 1998.

[202] I.W. Chiang, B.E. Brinson, A.Y. Huang, P.A. Willis, M.J. Bronikowski, J.L. Margrave, R.E. Smalley, and R.H. Hauge. Purification and characterization of single-wall carbon nanotubes (SWNTs) obtained from the gas-phase decomposition of CO (HiPco process). *Journal Of Physical Chemistry B*, 105(35):8297–8301, 2001.

[203] G. Schatz and Weidinger A. *Nukleare Methoden der Festkoerperphysik*. Teubner Physik, Stuttgart, 1992.

Curriculum Vitae

Name	Stephan Rauschenbach
Birth	February 21st 1977 in Grossenhain (Sachsen)
Address	Filderbahnstr. 28 D-70567 Stuttgart
Telephone	+49-711-689 1418 (office) +49-711-358 9194 (home)
E-mail	s.rauschenbach@fkf.mpg.de

University Education

PhD (Feb 2004 - Sep 2007)	PhD student in Physics at EPFL (Ecole Polytechnique Federale de Lausanne) working at the Nanoscale Science Dept. of MPI-FKF Stuttgart (Max-Planck-Institute for Solid State Research), Fellow of the Hans-L.-Merkle program for excellence in science.
Diplom (Mar 2003)	Diplom in Physics, Universität Augsburg Grade: 1.2
Diploma Thesis (Okt 2001 - Nov 2002)	Diploma Thesis in the laboratory of Prof. Sackmann at Technische Universität München, Grade: 1.0
ETH Zürich (Feb 2001 - Okt 2001)	graduate Student in Physics; ETH Zürich
Universität Augsburg (Nov 1997 - Mar 2003)	Student of Physics at Universität Augsburg

School Education

Abitur (June 1996)	School Education finished with Abitur degree (Grade 2,0) (General Certificate of Education after 13 years)
Gymnasium (1993-1996)	*Wernher-von-Braun*-Gymnasium in Friedberg (Bayern)
Gymnasium (1991-1993)	*Martin-Anderson-Nexö-Spezialschule* Gymnasium for Mathematics and Science in Dresden
Elementary- and Highschool (1983-1991)	33. POS in Dresden

Work Experience

PhD Thesis (Feb 2004 - Dec 2007)	Planning, construction and setup of an electrospray ion beam deposition source. Main fields of work: Time-of-flight and quadrupole mass spectrometry, ultra-high vacuum ion beam deposition source, DC- and RF ion optics simulation, CAD construction, UHV technology, atomic force microscopy and TOF-SIMS.
Guest Scientist at TU München (Nov 2003 - Jan 2004)	Department of Physics, E22 Biophysics; Modelling of semiconductor sensor devices, development of a CMOS process for SOI biosensors;
Internship at Sony Japan (May - Okt 2003)	Internship at Sony Fusion Domain Laboratory, Tokyo; Conductive polymers, charge transport, polymer devices, biochemical sensors
Diploma Thesis (Nov 2001-Nov 2002)	Diploma Thesis in the laboratory of Prof. Sackmann at the Technische Universität München: *Development of a Surface Sensitive Semiconductor Resistor for the Detection of Biomolecules.*
Internship at Infineon (Aug 2001 - Okt 2001)	Internship at Infineon Technologies Corporate Center, business development ventures, biochip research and development group; macro- and mesoporous silicon, optical properties (deep UV, X-ray), DNA-sensors
Lab Student at Univ. Augsburg (May 2000 - Feb 2001)	Lab student at Universität Augsburg; Thin aluminium-nitride films, pulsed laser deposition, e-beam deposition of metal thin film, analysis (XRD, RBS, Channeling, SIMS)
Assistant Teacher at Univ. Augsburg (Okt 1998 - Mar 2000)	Mathematics teacher at Universität Augsburg, Institute for Mathematics and Computer Science;
Internship at Infineon (Mar, Apr 1999)	Internship at Infineon Technologies Corp. Research; building a prototype of an opto-electrochemical-etching-device for silicon wavers.
Internship at Siemens (Aug - Okt 1998)	Internship at Siemens AG, Corp. Research, Microelectronics; development of an opto-electrochemical-etching-device for silicon wavers.
Military Service (Nov 1996 - Aug 1997)	10 months Military Service as a flight dispatcher and Mission planer in German Air Force; Working in Lechfeld (Germany), Florennes (Belgium) and Piacenza (Italy)

Conferences / Summer Schools

Oct 2007	FRONTIERS in Nanoscience annual meeting, Leuven (Belgium)
Aug 2007	Workshop Ion Beams in Nanotechnology, Bochum, talk
Mar 2007	DPG (German Physical Society) Annual Meeting, poster presentation and talk, Regensburg
Oct 2006	FRONTIERS in Nanoscience annual meeting, Catania (Italy), poster presentation
Mar 2006	FRONTIERS workshop *Understanding processes at the molecular level* of the european excellence network in nanoscience and biology, oral presentation, Lenzerheide (Switzerland)
Okt 2005	iNano Autumn School on nanoscience and -technology, Aarhus
Mar 2005	DPG (German Physical Society) Annual Meeting, poster presentation, Berlin
Mar 2004	DPG (German Physical Society) Annual Meeting, poster presentation, Dresden
Okt 2003	Internat. Conference on Adv. Materials (MRS-J), poster presentation (electronic properties of PEDOT/PSS), Yokohama
May 2003	Nano-Bio-Interface Conference, Tokyo
Mar 2002	*Soft Matter* summer school at Jülich-National Laboratory
Mar 2001	*New Materials for Information Technology* summer school at Jülich National Laboratory
Aug 2000	Vacuum physics course at the Technical University Dresden

Publications

1. T. R. Weitz, L. Harnau, S. Rauschenbach, M. Burghard, K.Kern, *Polymer Nanofibres via Nozzle-Free Centrifugal Spinning*, submitted (2007)
2. D. Payer, S. Rauschenbach, M. Konuma, C. Virojanadara, U. Starke, C. Dietrich, J.P. Collin, J.P. Sauvage, N. Lin, K.Kern, *Toward Mechanical Switching of Surface-Grafted [2]catenante by In-Situ Copper Complexation.* J. Am. Chem. Soc., Vol. 129(50) (2007)
3. R.T. Weitz, S. Rauschenbach, A. Formenta-Aliaga, M. Burkhard, K. Kern, *Growth Mechanism of Solution-Deposited Layers of the Charge-Transfer salt CuDDQ.* Phys. Stat. Sol. B, Vol. 244(11), pg. 4346-4350(2007)
4. S. Rauschenbach, F. Stadler, E. Lunedei, N. Malinowski, S. Koltsov, G. Costantini, K. Kern, *Electrospray Ion Beam Depostion of Clusters and Biomolecules.* Small, Vol. 4 (2006)
5. M. Röttgen, K. Judai, J-M. Antonietti, S. Rauschenbach, K. Kern, U. Heiz *Conical Octopole Ion Guide Design, Focusing, and its Application to the Deposition Of Low Energetic Clusters.* Rev. Sci. Instrum., Vol. 77 (2006)
6. M. Oda, S. Rauschenbach, *Electronic Structure of Oligo-3,4-Ethylene- Dioxythiophene.* Trans. MRS-J, Vol. 29 (2004)
7. M. Nikolaides, S. Rauschenbach, M. Tornow, A. Bausch, *Characterisation of a SOI Based Thin Film Resistor in Electrolyte Solutions for Sensor Applications,* accepted, J. Appl. Phys. (2003)
8. M. Nikolaides, S. Rauschenbach, M. Tornow, A. Bausch, *Silicon-on-Insulator Based Thin-Film Resistor for Chemical and Biological Sensor Applications,* ChemPhysChem 4, 1104-1106 (2003)

9. G. Abstreiter, A. Bausch, S. Luber, M. Nikolaides, S. Rauschenbach, E. Sackmann, M. Tornow , *Silicon-on-insulator Biosensor Device,* international patent (2002)

Languages

German	native language
English	fluently
Russian	basic knowledge

Extracurricular Activities

Okt 2004 - Nov 2005	PhD representative for the Max-Planck-Institutes in Stuttgart Initiation of a supervision improvement initiative; PhD students seminars with guests from industry and distant scientific fields; PhD student field trip visiting FZ Jülich, Thyssen-Krupp, Phillips Eindhoven, TU Delft nuclear reactor; varous social events.
2004	participation in the *München Buissnes Plan Contest*
1999	Member of the physics-students representatives at Universität Augsburg
1997-2001	Basketball Player and Trainer for the 7 to 10 years old group at *Sportfreunde Friedberg* sports club

Acknowledgements

Many people contributed to this work in many different ways. Although not all of them can be acknowledged here, I want to express my gratefulness and thanks to them. However I want to single out those, whose contributions have been especially important or essential.

First I want to thank Prof. Klaus Kern, my supervisor, for giving me this amazing project, for providing the means to lead it to results and to have the chance to work on it beyond my thesis. I know that it is by far not common to trust a PhD student with such a big responsibility, for which I am grateful. I never missed anything I needed, be it either advice or equipment.

I want to express special thanks to the referees of the thesis Prof. T. Rizzo, Prof. M. Mayor, Prof. J. V. Barth and the president Prof. R. Schaller. Your great interest in the details of my thesis and the intense discussion in the exam convinced me that this work is relevant and also that it is not finished yet.

Dr. Nicola Malinowski deserves special credit. He not only worked with me every day in the lab but also I could profit from his vast experience in may areas. I learned that it is good to question every result, that it is good to start right away and that there are many experts in the institute that only waited for us to come and ask questions.

Similar credit has to be given to Dr. Giovanni Costantini who works on this project as my other direct supervisor. Thank you for the many open discussions and the constant encouragement. From Giovanni I learned how to write up results and how important this is for a scientist.

Such a work is impossible without all the other PhD students, postdocs, master students and interns who contributed to it. Therefore I have to thank my predecessor Dr. Frank Stadler who worked very hard on the first prototypes of the ion beam deposition source. I profited greatly from his work.

I want to thank Dr. Eugenio Lunedei, Nicha Thontasen, Dr. Yeliang Wang, Martin Paulig and Karsten Hinselmann for the great time working together in the laboratory. These coworkers have always been a source of inspiration and motivation.

Besides the people that worked with me in the lab every day, four other colleagues and friends greatly influenced this work. With Thomas Weitz, Dr. Sebastian Stepanow, Dr. Dietmar Payer and Dr. Ralf Vogelgesang I discussed almost every aspect of my thesis in great detail. They gave me general as well as practical advice and support.

Artur Kuester deserves special thanks since he supported me far beyond his duties as a technician. He taught me how to make CAD drawings, how to use the milling machine and the lathe and he was always there when we were testing our constructions in the lab.

A project like the setup of the ion beam deposition source requires a great deal of input from skilled experts which was provided from our technicians Wolfang Stiepany, Peter Andler and Andreas Koch as well as from the mechanical and electrical workshops. The amount and quality of their contribution might always be a guideline for my own work and I want to add many thanks for the things that I was allowed to learn along the way.

Also external collaborations played a great role in these last 3.5 years. Above all I want to thank Dr. Ivo Cermak who tough me the physics of RF-ion optics on the telephone. As a result of the gained knowledge I could not only successfully layout the ion beam deposition setup, but also support others. Like for instance the very fruitful collaboration with Dr. Martin Roettgen from the group of Prof. U. Heiz at TU Muenchen. Together we could analyze and understand their very special ion optical systems.

Moreover I want to thank Dr. Alfonz Luca, Prof. D. Gerlich and Prof. R. G. Cooks for the opportunity to speak in their group meetings and discuss my experiments and questions. The visits to their labs, which are famous with the ion beam and mass spectrometry community, were most inspiring to me.

A great deal of work as well as non-work happens not in the lab but in the office. During my thesis I shared it with Dr. Thomas Classen, Dr. Georgios Katsaros, Thomas Weitz, Jens Dorfmueller, Dr. Frank Stadler and Dr. Christina Gomez. Thank you for all the support in form of different activities, like for instance scientific discussions, non-scientific discussions, gossip, lunch breaks, dinner breaks, late-night-pizza breaks, beer breaks, other breaks, driving me around, office redecoration and art exhibitions.

Office and laboratory are not the only environments a PhD student is working in. Most probably the whole nanoscale science department contributed something to this work - one way or the other. I thank my colleagues in and outside of the department for all the times they helped me out when I came to them and asked questions or was in need of support.

I want to thank Mrs. Bucurescu, Mrs. Roux and Mrs. Nguyen from the EPFL administration for their care about my PhD studies, especially because I was a student which spent most of his time away from the campus.

Finally many thanks are owed to my friends and family, especially to my sister Katrin, my parents and my wife Sabine. Their unconditional support finally enabled and motivated me to work on and finish this project. Especially very much I owe to my wife, because her support went as far as proofreading this thesis on the highest professional level.